

Distribution Agreement:

In presenting this thesis or dissertation as a partial fulfillment of the requirements for an advanced degree from Emory University, I hereby grant to Emory University and its agents the non-exclusive license to archive, make accessible, and display my thesis or dissertation in whole or in part in all forms of media, now or hereafter known, including display on the world wide web. I understand that I may select some access restrictions as part of the online submissions of this thesis or dissertation. I retain all ownership rights to the copyright of the thesis or dissertation. I also retain the right to use in future works (such as articles or books) all or part of this thesis or dissertation.

Signature:

Omar Villanueva

Date

Design and Development of Novel Bis(amidophenyl)amine Redox-active Ligands to
Promote Novel Reactivity at First-row Transition Metal Centers

By

Omar Villanueva

Doctor of Philosophy

Chemistry

Cora E. MacBeth, Ph.D.
Advisor

Craig L. Hill, Ph.D.
Committee Member

Khalid Salaita, Ph.D.
Committee Member

Accepted:

Lisa A. Tedesco, Ph.D.
Dean of the James T. Laney School of Graduate Studies

Date

Design and Development of Novel Bis(amidophenyl)amine Redox-active Ligands to
Promote Novel Reactivity at First-row Transition Metal Centers

By

Omar Villanueva

B.S., University of Georgia, 2009

B.S.Ed., University of Georgia, 2009

Advisor: Cora E. MacBeth, Ph.D.

An abstract of

A dissertation submitted to the Faculty of the
James T. Laney School of Graduate Studies of Emory University
in partial fulfillment of the requirements for the degree of
Doctor of Philosophy

in Chemistry

2015

Abstract

Design and Development of Novel Bis(amidophenyl)amine Redox-active Ligands to Promote Novel Reactivity at First-row Transition Metal Centers

By

Omar Villanueva

To address the Nation's environmental and energy challenges, chemical catalysis research has shifted its focus to discover new methodologies that can produce alternative fuels and reduce the use of harmful pollutants. At the center of this grand challenge lies the need to discover sustainable transition metal catalysts that utilize environmentally benign reagents for the activation of strong bonds. Developing such systems will bring upon significant technological advances. In Chapter 1, the significance of using earth-abundant first-row transition metal ions in catalysis is highlighted and the role of redox-active ligands in promoting this reactivity is discussed. In chapter 2, the development of coordinatively versatile bis(amidophenyl)amine redox-active ligands as novel motifs to control catalyst structure and reactivity is described. Chapter 3 discloses fundamental spectroscopic, mechanistic, and structural investigations on the reactivity of cobalt(II) complexes of bis(amidophenyl)amine ligands with dioxygen to carry out aerobic oxidation reactions. Given the multi-electron reactivity observed with dioxygen, cobalt(II) complexes were investigated as catalysts for C–H amination catalysis. This dissertation concludes with chapter 4, which deliberates the selective catalytic C–H amination of aryl azides facilitated by a robust and versatile cobalt(II) catalyst to form medicinally relevant heterocycles. The results presented herein constitute a significant advance in sustainable catalysis technology.

Design and Development of Novel Bis(amidophenyl)amine Redox-active Ligands to
Promote Novel Reactivity at First-row Transition Metal Centers

By

Omar Villanueva

B.S., University of Georgia, 2009

B.S.Ed., University of Georgia, 2009

Advisor: Cora E. MacBeth, Ph.D.

An abstract of

A dissertation submitted to the Faculty of the
James T. Laney School of Graduate Studies of Emory University

in partial fulfillment of the requirements for the degree of

Doctor of Philosophy

in Chemistry

2015

Acknowledgements

Graduate school was definitely challenging for me. I would have never been able to do go through it without the help, guidance, and support from many people around me. First and foremost, I would like to thank my advisor, Dr. Cora MacBeth, for being such a supportive, encouraging, and enthusiastic advisor. The work presented in this dissertation is the result of her deep commitment to science, immense support, and high expectations. She has been nothing but supportive in both my professional and scientific goals while in graduate school. Dr. MacBeth has given me the confidence I needed to gain which led me to be the scientist and mentor that I am today. I hope that we continue to work together throughout the years.

I would also like to acknowledge my committee members, Dr. Craig Hill and Dr. Khalid Salaita, for always being there for me in all of my yearly reports and always giving me constructive feedback. Dr. Hill, I have deeply enjoyed taking your inorganic graduate courses. Dr. Salaita, being a young successful scientist as yourself, thank you for allowing me to always pop into your office and advising me despite your busy schedule. It has been a privilege to interact with both of you throughout my graduate career at Emory.

Other people that have had an impact in my research have been Dr. Kenneth Hardcastle, Dr. John Bacsa and Dr. Karl Hagen. These three individuals have allowed me to sit in their offices to get help with X-ray crystallography. All three of them, in different forms and in different capacities, have given me so much help and guidance with respect to X-ray crystallography and have helped define the work presented herein.

I would also like to acknowledge all Blakey group members, in specific Nina Weldy; it has been a pleasure working with you in the C–H amination project. This project would not have been possible without the substrates you synthesized. I am also honored to have gotten the opportunity to work with Dr. Simon Blakey. I would have never imagined gaining so much organic chemistry knowledge and skills if it was not for the MacBeth-Blakey collaboration and long discussions we had in the past.

Various people not directly involved in my research have impacted my career path. For example, Dr. Pat Marsteller, it was a privilege to work with you in various aspects of science education. Additionally, all the chemistry department staff and faculty that have helped me while I was teaching my own general chemistry course. Thank you for willing to always be there for me and helping me out. I am also grateful for meeting many friends and other colleagues at Emory. Current and previous MacBeth group members (Savita, Matt, Kelly) who had a huge impact my early graduate school years. Also Felicia Fullilove, who has been a colleague in research and a true friend – I look forward to collaborating with her in the near future. There are other people/friends that I would like to thank, many of you know who you are.

Finally, I would like to thank my family for their immense support. My parents Jorge and Ody Villanueva: *Ustedes dos han sido los padres más comprensivos que jamás habría pedido. Gracias por todo su amor y apoyo todos estos años.* Especially, I would like to thank my wife Dimple Villanueva, without her support and love, I would have never made it. I look forward to our new life and spending more time with you and little Arvind Villanueva.

Table of Contents

Chapter 1	Introduction to Redox-active Ligands and Their Role in Promoting Novel Reactivity at First-row Transition Metal Centers.....	1
Section 1-1	Introduction.....	1
Section 1-2	A Historical Perspective on Redox-active Ligands and Their Metal Complexes.....	3
Section 1-3	Redox-active Ligands in Biology.....	12
Section 1-4	Utility of Redox-active Ligands in Catalysis.....	16
Section 1-4	Dissertation Overview.....	20
Chapter 2	First-row Transition Metal Complexes of Coordinatively Versatile Bis(amidophenyl)amine Ligands.....	30
Section 2-1	Introduction.....	30
Section 2-2	Background and Significance.....	41
Section 2-3	Results.....	44
Section 2-3-1	Synthesis of Bis(amidophenyl)amine Ligands.....	44
Section 2-3-2	Synthesis of Metal Complexes with NH(<i>o</i> -PhNHC(O)R) ₂ Ligands.....	47
Section 2-3-3	X-ray Crystallographic Studies.....	54
Section 2-3-4	Electronic and Magnetic Characterization of Metal Complexes.....	66
Section 2-3-5	Electrochemical Properties of Metal Complexes.....	74
Section 2-4	Discussion.....	81
Section 2-5	Conclusion.....	85

Section 2-6	Experimental Section.....	86
Section 2-6-1	General Considerations.....	86
Section 2-6-2	Ligand Syntheses.....	87
Section 2-6-3	Complex Syntheses.....	91
Section 2-6-4	X-ray Crystallographic Data of Complexes.....	102
Chapter 3	Mechanistic, Spectroscopic, and Structural Investigations on the Activation of Dioxygen by Cobalt Complexes Incorporating Redox-active Ligands.....	113
Section 3-1	Introduction.....	113
Section 3-2	Background and Significance.....	117
Section 3-3	Results.....	122
Section 3-3-1	Stoichiometric Oxygenation and Oxygen-atom Transfer Reaction Studies.....	125
Section 3-3-2	Spectroscopic Studies on the Activation of Dioxygen by Cobalt Complexes.....	128
Section 3-3-3	Chemical Oxidation of Mononuclear Complex (Et ₄ N) ₂ [Co(HL ^{iPr}) ₂].....	133
Section 3-3-4	Synthetic Studies to Probe Possible Catalyst Structure.....	136
Section 3-3-5	Synthetic Studies to Probe the Role of The Ligand Backbone.....	147
Section 3-3-6	Synthetic Studies to Establish the Redox Non-innocence of Tridentate, Trianionic Ligand [L ^{iPr}] ³⁻	151

Section 3-3-7	Synthetic and Spectroscopic Studies Using Zinc(II) To Probe Possible Decomposition Pathway of Bidentate, Dianionic Ligand $[L^{Mod}]^{2-}$	158
Section 3-3-8	Expanding The Aerobic Oxidation Reactivity Profile of Dinuclear Cobalt(II) Complex, $(Et_4N)_2[Co_2(L^{iPr})_2]$	165
Section 3-4	Discussion.....	169
Section 3-5	Conclusion.....	175
Section 3-6	Experimental Section.....	176
Section 3-6-1	General Considerations and Materials.....	177
Section 3-6-2	Ligand Syntheses.....	178
Section 3-6-3	Complex Syntheses.....	182
Section 3-6-4	Reactivity Studies.....	189
Section 3-6-5	Crystallographic Data.....	199
Chapter 4	Intramolecular sp^3 C–H Amination of Aryl Azides Catalyzed by a Cobalt(II) Complex.....	209
Section 4-1	Introduction.....	209
Section 4-2	Background and Significance.....	224
Section 4-3	Results.....	228
Section 4-3-1	Initial Investigations on the C–H Amination of an Aryl Azide by Dinuclear Cobalt(II) Complex $(Et_4N)_2[Co_2(L^{iPr})_2]$	229
Section 4-3-2	C–H Amination of An Aryl Azide Using Dinuclear Cobalt(II) Complexes With Varying Acyl Substituents.....	231
Section 4-3-3	Optimization of Cobalt(II)-Catalyzed C–H amination Reaction.....	233
Section 4-3-4	Substrate Scope and Limitations.....	235

Section 4-3-5 Kinetic Isotope Effect Study.....	240
Section 4-4 Discussion.....	241
Section 4-5 Conclusion.....	249
Section 4-6 Experimental Section.....	250
Section 4-6-1 General Considerations and Materials.....	250
Section 4-6-2 General Procedures.....	251
Section 4-6-3 Additional Experiments.....	259
Section 4-6-4 Crystallographic Data.....	262

List of Figures

Chapter 1

- Figure 1-1 Selected examples of classical Werner-type complexes.....1
- Figure 1-2 Dithiobenzyl ligand (**1**) and its nickel(II) complex (**2**) reported by Schrauzer and Mayweg.....3
- Figure 1-3 Tetrachloro-1,2-semiquinonate ligand Cl₄(SQ) (**13**) and its corresponding V^{III}, Cr^{III}, Mn^{III}, Fe^{III}, and Co^{III} tris(*o*-semiquinone) complexes.....6
- Figure 1-4 Other nitrogen-donor based redox-active ligands.....10
- Figure 1-7 Redox-active ligands containing phenol moieties.....11

Chapter 2

- Figure 2-1 Early examples of metal complexes with tetradentate ligands that offered open coordination sites.....31
- Figure 2-2 Selected tridentate pincer ligands.....34
- Figure 2-3 Ligands used in this study.....43
- Figure 2-4 Solid-state structures of **A**) (Et₄N)₂[Co₂(L^{*i*Pr})₂], **B**) K₂[Co₂(L^{*t*Bu})₂], **C**) (Et₄N)₂[Co₂(L^{Ph})₂] and **D**) (Et₄N)₂[Co₂(L^{CF₃})₂]. Thermal ellipsoids drawn at 40% probability. Hydrogen atoms and counteranions have been omitted for clarity.....54
- Figure 2-5 Solid-state structures of **A**) (Et₄N)₂[Co₂(L^{*i*Pr})₂] and **B**) K₂[Co₂(L^{*i*Pr})₂]. Thermal ellipsoids drawn at 40% probability. Tetraethylammonium counteranions (for complex (Et₄N)₂[Co₂(L^{*i*Pr})₂]) and hydrogen atoms for both complexes have been omitted for clarity.....58

- Figure 2-6 Solid-state structures of **A**) $(\text{Et}_4\text{N})_2[\text{Co}(\text{HL}^{i\text{Pr}})_2]$, **B**) $(\text{PPh}_4)_2[\text{Co}(\text{HL}^{t\text{Bu}})_2]$, **C**) $\text{K}_2[\text{Co}(\text{HL}^{\text{Ph}})_2]$ and **D**) $(\text{Et}_4\text{N})_2[\text{Co}(\text{HL}^{\text{Ad}})_2]$. Thermal ellipsoids drawn at 40 % probability. Hydrogen atoms (except the amide hydrogens on each complex) and counteranions have been omitted for clarity.....60
- Figure 2-7 Solid-state structures of **A**) $(\text{PPh}_4)_2[\text{Fe}_2(\text{L}^{i\text{Pr}})_2]$, **B**) $(\text{Et}_4\text{N})_2[\text{Ni}_2(\text{L}^{i\text{Pr}})_2]$, **C**) $(\text{PPh}_4)_2[\text{Cu}_2(\text{L}^{i\text{Pr}})_2]$, and **D**) $(\text{Et}_4\text{N})_2[\text{Zn}_2(\text{L}^{i\text{Pr}})_2]$. Thermal ellipsoids drawn at 40% probability. Hydrogen atoms and counteranions have been omitted for clarity.....62
- Figure 2-8 UV-visible absorption spectra of dinuclear cobalt(II) complexes $\text{K}_2[\text{Co}_2(\text{L}^{i\text{Pr}})_2]$ (black line), $\text{K}_2[\text{Co}_2(\text{L}^{t\text{Bu}})_2]$ (blue line), $(\text{Et}_4\text{N})_2[\text{Co}_2(\text{L}^{\text{Ph}})_2]$ (green line), and $(\text{Et}_4\text{N})_2[\text{Co}_2(\text{L}^{\text{CF}_3})_2]$ (teal line). Recorded in CH_3CN at room temperature.....68
- Figure 2-9 UV-visible absorption spectra of mononuclear cobalt(II) complexes $(\text{Et}_4\text{N})_2[\text{Co}(\text{HL}^{i\text{Pr}})_2]$ (black line), $(\text{PPh}_4)_2[\text{Co}(\text{HL}^{t\text{Bu}})_2]$ (blue line), $\text{K}_2[\text{Co}(\text{HL}^{\text{Ph}})_2]$ (green line), and $(\text{Et}_4\text{N})_2[\text{Co}(\text{HL}^{\text{Ad}})_2]$ (red line). Recorded in CH_3CN at room temperature.....69
- Figure 2-10 UV-visible absorption spectra of $(\text{PPh}_4)_2[\text{Fe}_2(\text{L}^{i\text{Pr}})_2]$ (brown line), $(\text{Et}_4\text{N})_2[\text{Ni}_2(\text{L}^{i\text{Pr}})_2]$ (orange line), $(\text{PPh}_4)_2[\text{Cu}_2(\text{L}^{i\text{Pr}})_2]$ (purple line), and $(\text{Et}_4\text{N})_2[\text{Zn}_2(\text{L}^{i\text{Pr}})_2]$ (yellow line). Recorded in CH_3CN at room temperature. Spectrum for $(\text{PPh}_4)_2[\text{Cu}_2(\text{L}^{i\text{Pr}})_2]$ is plotted on the secondary y-axis to the left.....70

- Figure 2-11 UV-visible absorption spectra of mononuclear species $(Et_4N)_2[Ni(HL^{iPr})_2]$ (orange line) and dinuclear species $(Et_4N)_2[Ni_2(L^{iPr})_2]$ (red line). Recorded in CH_3CN at room temperature.....71
- Figure 2-12 UV-visible NIR absorption spectrum of $(PPh_4)_2[Cu_2(L^{iPr})_2]$. Recorded in CH_3CN at room temperature. Spectral noise at ~ 1700 nm is resultant from the quartz from the cuvettes (noted by *).....73
- Figure 2-13 Cyclic voltammograms of **A**) $K_2[Co_2(L^{tBu})_2]$, **B**) $(Et_4N)_2[Co_2(L^{Ph})_2]$ and **C**) $(Et_4N)_2[Co_2(L^{CF_3})_2]$. Conditions: 10 mV/s, with 0.2 M TBAPF₆TBA in CH_2Cl_2 as the supporting electrolyte, referenced vs. Fc/Fc⁺, Ag/Ag⁺ as the reference electrode, using a glassy carbon working electrode, with scans initially negative.....75
- Figure 2-14 Cyclic voltammograms of **A**) $(PPh_4)_2[Co(HL^{tBu})_2]$, **B**) $K_2[Co(HL^{Ph})_2]$, and **C**) $(Et_4N)_2[Co(HL^{Ad})_2]$. Conditions: 10 mV/s, with 0.2 M TBAPF₆TBA in CH_2Cl_2 as the supporting electrolyte, referenced vs. Fc/Fc⁺, Ag/Ag⁺ as the reference electrode, using a glassy carbon-working electrode, with scans initially negative.....77
- Figure 2-15 Cyclic voltammograms of **A**) $(PPh_4)_2[Fe_2(L^{iPr})_2]$, **B**) $(Et_4N)_2[Ni_2(L^{iPr})_2]$, **C**) $(PPh_4)_2[Cu_2(L^{iPr})_2]$ and **D**) $(Et_4N)_2[Zn_2(L^{iPr})_2]$. Conditions: 10 mV/s, with 0.2 M TBAPF₆TBA in CH_2Cl_2 as the supporting electrolyte, referenced vs. Fc/Fc⁺, Ag/Ag⁺ as the reference electrode, using a glassy carbon-working electrode, with scans initially negative.....79
- Figure 2-16 Cyclic voltammogram of mononuclear nickel(II) complex, $(Et_4N)_2[Ni(HL^{iPr})_2]$. Conditions: 10 mV/s, with 0.2 M TBAPF₆TBA in

DMF as the supporting electrolyte, referenced vs. Fc/Fc^+ , Ag/Ag^+ as the reference electrode, using a glassy carbon-working electrode, with scans initially negative.....80

Chapter 3

- Figure 3-1 Schematic representations of possible cobalt-oxygen containing species formed during the reaction of cobalt(II) with dioxygen.....120
- Figure 3-2 **A)** Dinuclear and **B)** mononuclear cobalt(II) complexes supported by the bis(phenylamido)amine ligand $\text{NH}(o\text{-PhNHC(O)}^i\text{Pr})_2$ ($\text{H}_3\text{L}^{i\text{Pr}}$), and their solid-state X-ray structures (**C** and **D**) and electrochemical profiles (**E** and **F**), respectively.....123
- Figure 3-3 UV-Visible absorption spectra of the products isolated from the reaction of **A)** $(\text{Et}_4\text{N})_2[\text{Co}_2(\text{L}^{i\text{Pr}})_2]$ with two equivalents of dioxygen gas and **B)** $(\text{Et}_4\text{N})_2[\text{Co}(\text{HL}^{i\text{Pr}})_2]$ with one equivalent of dioxygen gas. Both spectra recorded at room temperature in CH_3CN from isolated oxygenated compounds.....126
- Figure 3-4 Changes in the UV-visible absorption spectrum of $(\text{Et}_4\text{N})_2[\text{Co}_2(\text{L}^{i\text{Pr}})_2]$ (green trace, prior to oxygenation) upon addition of dioxygen into the headspace above a solution of $(\text{Et}_4\text{N})_2[\text{Co}_2(\text{L}^{i\text{Pr}})_2]$ in CH_3CN at 25 °C. Scan rate of 1 scan/min. Orange trace corresponds to *Intermediate 1* and burgundy trace corresponds to the final oxygenated species *C* upon reaction with dioxygen.....129
- Figure 3-5 Changes in the UV-visible absorption spectrum of $(\text{Et}_4\text{N})_2[\text{Co}(\text{HL}^{i\text{Pr}})_2]$ (red trace, prior to oxygenation) upon addition of dioxygen into the headspace

above a solution of $(\text{Et}_4\text{N})_2[\text{Co}(\text{HL}^{i\text{Pr}})_2]$ in CH_3CN at $25\text{ }^\circ\text{C}$. Scan rate of 1 scan/min. Blue trace corresponds to *Intermediate 1* and orange trace corresponds to *Intermediate 2*. Burgundy trace corresponds to the final oxygenated species *C* upon reaction with dioxygen.....131

Figure 3-6 Changes in the UV-visible NIR absorption spectrum of $(\text{Et}_4\text{N})_2[\text{Co}(\text{HL}^{i\text{Pr}})_2]$ (red trace, prior to oxygenation) upon addition of dioxygen into the headspace above a solution of $(\text{Et}_4\text{N})_2[\text{Co}(\text{HL}^{i\text{Pr}})_2]$ in CH_3CN at $25\text{ }^\circ\text{C}$. Scan rate of 1 scan/ 3 min. Blue trace corresponds to *Intermediate 1* and orange trace corresponds to *Intermediate 2*. Burgundy trace corresponds to the final oxygenated species *C* upon reaction with dioxygen. Quartz from cuvette is marked by an asterisk (*).....131

Figure 3-7 Changes in the UV-visible NIR absorption spectrum of $(\text{Et}_4\text{N})_2[\text{Co}_2(\text{L}^{i\text{Pr}})_2]$ (green trace, prior to oxygenation) upon addition of dioxygen into the headspace above a solution of $(\text{Et}_4\text{N})_2[\text{Co}_2(\text{L}^{i\text{Pr}})_2]$ in CH_3CN at $25\text{ }^\circ\text{C}$. Scan rate of 1 scan/3 min. Orange trace corresponds to *Intermediate 1*. Burgundy trace corresponds to the final oxygenated species *C* upon reaction with dioxygen. Quartz from cuvette is marked by an asterisk (*).....133

Figure 3-8 UV-visible NIR absorption spectrum of $(\text{Et}_4\text{N})_2[\text{Co}(\text{HL}^{i\text{Pr}})_2]$. Recorded in CH_3CN at room temperature. Quartz from cuvette is marked by an asterisk (*).....135

Figure 3-9 **A)** Solid-state structure of $(\text{Et}_4\text{N})_2[\text{Co}(\text{L}^{i\text{Pr}})(\text{CN})]$. **B)** Side view of $(\text{Et}_4\text{N})_2[\text{Co}(\text{L}^{i\text{Pr}})(\text{CN})]$ showing the orientation of the cyano ligand with respect to the tridentate ligand. Thermal ellipsoids are drawn at 40%

	probability. Hydrogen atoms and tetraethylammonium counteranions have been omitted for clarity.....	138
Figure 3-10	UV-visible absorption spectrum of $(Et_4N)_2[Co(L^{iPr})(CN)]$ in CH_3CN . Recorded at room temperature.....	140
Figure 3-11	Cyclic voltammogram of $(Et_4N)_2[Co(L^{iPr})(CN)]$. Conditions: 10 mV/s, with 0.1 M TBAPF ₆ TBA in CH_2Cl_2 as the supporting electrolyte, referenced vs. Fc/Fc ⁺ , Ag/Ag ⁺ as the reference electrode, using a glassy carbon-working electrode, with scans initially negative.....	141
Figure 3-12	Solid-state structure of $(PPh_4)_2[Co(L^{Mod})_2]$. Thermal ellipsoids are drawn at 40% probability. Hydrogen atoms and tetraphenylphosphonium counteranions have been omitted for clarity.....	143
Figure 3-13	UV-visible absorption of $(PPh_4)_2[Co(L^{Mod})_2]$. Spectrum recorded in CH_3CN at room temperature.....	145
Figure 3-14	Cyclic voltammogram of $(PPh_4)_2[Co(L^{Mod})_2]$. Conditions: 10 mV/s, with 0.1M TBAPF ₆ TBA in CH_2Cl_2 as the supporting electrolyte, referenced vs. Fc/Fc ⁺ , Ag/Ag ⁺ as the reference electrode, using a glassy carbon working electrode, with scans initially negative.....	146
Figure 3-15	Solid-state structure of $K_2[Zn(L^{Mod})_2]$. Thermal ellipsoids are drawn at 40% probability. Hydrogen atoms and potassium counteranions have been omitted for clarity.....	149
Figure 3-16	Cyclic voltammogram of $K_2[Zn(L^{Mod})_2]$. Conditions: 10 mV/s, with 0.1M TBAPF ₆ TBA in CH_2Cl_2 as the supporting electrolyte, referenced vs.	

- Fc/Fc⁺, Ag/Ag⁺ as the reference electrode, using a glassy carbon working electrode, with scans initially negative.....150
- Figure 3-17 Solid-state structure of (Et₄N)₂[Co₂(μ-OH)₂(Me-L^{iPr})₂]. Thermal ellipsoids are drawn at 40% probability. Hydrogen atoms (with the exception of the hydrogen atoms on two μ-bridging-hydroxo ligands) and tetraethylammonium counteranions have been omitted for clarity.....155
- Figure 3-18 UV-visible absorption of (Et₄N)₂[Co₂(μ-OH)₂(Me-L^{iPr})₂]. Spectrum recorded in DMF at room temperature.....156
- Figure 3-19 Cyclic voltammogram of (Et₄N)₂[Co₂(μ-OH)₂(Me-L^{iPr})₂]. Conditions: 25 mV/s, with 0.1M TBAPF₆TBA in DMF as the supporting electrolyte, referenced vs. Fc/Fc⁺, Ag/Ag⁺ as the reference electrode, using a glassy carbon working electrode, with scans initially negative.....157
- Figure 3-20 UV-visible absorption spectra of K₂[Zn(L^{Mod})₂] (gray line), K₂[Zn(L^{Mod})₂] after its reaction with dioxygen gas (green line), and K₂[Zn(L^{Mod})₂] after its reaction with dioxygen gas followed by slow evaporation in air (red line). All spectra were recorded from isolated compounds in CH₃CN at room temperature.....159
- Figure 3-21 Solid-state structure of the ligand decomposition product, [L^{Mod}]^{Decomp.}, obtained from the reaction of K₂[Zn(L^{Mod})₂] with dioxygen after open-air evaporation. Thermal ellipsoids are drawn at 40 % probability.....161
- Figure 3-22 UV-visible absorption spectra of the products from one-electron (purple line) and two-electron (green line) oxidations of K₂[Zn(L^{Mod})₂] resulting from treatment with one and two equivalents of FcBF₄, respectively.

	Spectra were recorded from isolated compounds in CH ₃ CN at room temperature.....	162
Figure 3-23	EPR spectra of A) one-electron oxidized species, K[Zn(L ^{Mod}) ₂] ^{ox} (room temperature, toluene), B) two-electron oxidized species, K[Zn(L ^{Mod}) ₂] ^{ox} (Toluene glass, 10K), and C) the product isolated from the reaction of K ₂ [Zn(L ^{Mod}) ₂] with dioxygen gas. Spectra recorded at room temperature in toluene (10K).....	164
Figure 3-24	Increase in absorbance band at λ _{max} = 400 nm, after addition of dioxygen into the headspace above a [7.192 x 10 ⁻⁴] M solution of 3,5-DTBC (initial black trace) containing 1 mol% of (Et ₄ N) ₂ [Co ₂ (L ^{iPr}) ₂] in CH ₃ CN at 25 °C. Scan rate of 1 scan/min. Final red trace corresponds to 3,5-DTBQ (λ _{max} = 400 nm).....	168
Figure 3-25	Deprotonated ligand, (Et ₄ N) ₂ [HL ^{Ph}], obtained as a byproduct from the reaction of (Et ₄ N) ₂ [Co(HL ^{iPr}) ₂] and dioxygen gas.....	172
Figure 3-26	Solid-state structure of (Et ₄ N) ₂ [HL ^{Ph}]. Thermal ellipsoids are drawn at 40 % probability. Hydrogen atoms (with the exception of central amide hydrogen) and tetraethylammonium counterions have been omitted for clarity.....	173
Chapter 4		
Figure 4-1	Mechanism for the formation of a metallonitrene and its insertion into a C–H bond.....	212
Figure 4-2	Commonly used sources of nitrene precursors.....	212

Figure 4-4	General scheme for the formation of a metallonitrene and its insertion into a C–H bond using an organic azide (resonance formulas for RN ₃ are shown).....	216
Figure 4-5	Proposed mechanism for catalytic intermolecular cobalt(II)-catalyzed nitrene insertion with TrocN.....	221
Figure 4-6	A) Dinuclear cobalt(II) complex, (Et ₄ N) ₂ [Co ₂ (L ^{iPr}) ₂], used in the investigation for C–H amination reactions with aryl azides and B) its solid-state X-ray structure.....	228
Figure 4-7	UV-visible absorption spectrum of A) (Et ₄ N) ₂ [Co ₂ (L ^{iPr}) ₂] (λ _{max} = 596 nm) and B) product formed from the reaction of (Et ₄ N) ₂ [Co ₂ (L ^{iPr}) ₂] with 2.0 equivalents of azide 47a (λ _{max} = 773 nm). Both spectra recorded in CH ₃ CN at 25 °C.....	246
Figure 4-8	ESI-MS (negative mode) spectrum of the product formed from the reaction of (Et ₄ N) ₂ [Co ₂ (L ^{iPr}) ₂] with 2.0 equivalents of azide 47a	247
Figure 4-9	A) cyclized ligand L ^{Cyc} and B) its solid-state X-ray structure (thermal ellipsoids drawn at 40 % probability. Hydrogen atoms omitted for clarity).....	248
Figure 4-10	¹ H NMR spectra for A) deuterated azide 50a , B) indoline product 50b , C) aniline precursor to azide 50a , ¹ and D) reaction mixture of indoline products 50b-D and 50b-H	263

List of Tables

Chapter 2

Table 2-1	Solid-state FTIR and mass spectrometry data of synthesized ligands H_3L^R ($R = tBu, Ph, adamantyl, \text{ and } CF_3$).....	47
Table 2-2	Selected bond lengths (\AA) and angles ($^\circ$) for $(Et_4N)_2[Co_2(L^{iPr})_2]$, $K_2[Co_2(L^{tBu})_2]$, $(Et_4N)_2[Co_2(L^{Ph})_2]$, and $(Et_4N)_2[Co_2(L^{CF_3})_2]$. Torsion angle is defined as $N_{amido}-Co-N_{amido}-Co$	55
Table 2-3	Selected bond lengths (\AA) and angles ($^\circ$) for $(Et_4N)_2[Co_2(L^{iPr})_2]$, and $K_2[Co_2(L^{iPr})_2]$. The torsion angle is defined as $N_{Amido}-Co-N_{Amido}-Co$	58
Table 2-4	Selected bond lengths (\AA) and angles ($^\circ$) for $(Et_4N)_2[Co(HL^{iPr})_2]$, $(PPh_4)_2[Co(HL^{tBu})_2]$, $K_2[Co(HL^{Ph})_2]$, and $(Et_4N)_2[Co(HL^{Ad})_2]$	61
Table 2-5	Selected bond lengths (\AA) and angles ($^\circ$) for $(PPh_4)_2[Fe_2(L^{iPr})_2]$, $(Et_4N)_2[Ni_2(L^{iPr})_2]$, $(PPh_4)_2[Cu_2(L^{iPr})_2]$, and $(Et_4N)_2[Zn_2(L^{iPr})_2]$. The torsion angle is defined as $N_{Amido}-M-N_{Amido}-M$	63
Table 2-6	Magnetic and spectral properties of synthesized metal complexes.....	67
Table 2-7	Summary of electrochemical half-potentials ($E_{1/2}$) for mononuclear cobalt(II) complexes $(Et_4N)_2[Co(HL^{Ad})_2]$, $(PPh_4)_2[Co(HL^{tBu})_2]$, $(Et_4N)_2[Co_2(L^{iPr})_2]$, and $K_2[Co(HL^{Ph})_2]$	76
Table 2-8	Structural refinement data for dinuclear cobalt(II) complexes $K_2[Co_2(L^{tBu})_2]$, $(Et_4N)_2[Co_2(L^{Ph})_2]$ and $(Et_4N)_2[Co_2(L^{CF_3})_2]$	103
Table 2-9	Structural refinement data for dinuclear cobalt(II) complex $K_2[Co_2(L^{iPr})_2]$	104

Table 2-10	Structural refinement data for mononuclear cobalt(II) complexes (PPh ₄) ₂ [Co(HL ^{iBu}) ₂], K ₂ [Co(HL ^{Ph}) ₂] and (Et ₄ N) ₂ [Co(HL ^{Ad}) ₂].....	105
Table 2-11	Structural refinement data for dinuclear complexes (PPh ₄) ₂ [Fe ₂ (L ^{iPr}) ₂] and (Et ₄ N) ₂ [Ni ₂ (L ^{iPr}) ₂].....	106
Table 2-12	Structural refinement data for dinuclear complexes (PPh ₄) ₂ [Cu ₂ (L ^{iPr}) ₂] and (Et ₄ N) ₂ [Zn ₂ (L ^{iPr}) ₂].....	107

Chapter 3

Table 3-1	Catalytic aerobic O-atom transfer to triphenylphosphine carried out by (Et ₄ N) ₂ [Co ₂ (L ^{iPr}) ₂] and (Et ₄ N) ₂ [Co(HL ^{iPr}) ₂]	124
Table 3-2	Selected bond lengths (Å) and angles (°) for (Et ₄ N) ₂ [Co(L ^{iPr})(CN)].....	139
Table 3-3	Selected bond lengths (Å) and angles (°) for (PPh ₄) ₂ [Co(L ^{Mod}) ₂].....	144
Table 3-4	Selected bond lengths (Å) and angles (°) for K ₂ [Zn(L ^{Mod}) ₂].....	149
Table 3-5	Selected bond lengths (Å) and angles (°) for (Et ₄ N) ₂ [Co ₂ (μ-OH) ₂ (MeL ^{iPr}) ₂].....	155
Table 3-6	Crystal data and structure refinement parameters for (Et ₄ N) ₂ [Co(CN)(L ^{iPr}) ₂] and (Et ₄ N) ₂ [Co ₂ (m-OH) ₂ (Me-L ^{iPr}) ₂].....	200
Table 3-7	Crystal data and structure refinement parameters for (PPh ₄) ₂ [Co(L ^{Mod}) ₂] and K ₂ [Zn(L ^{Mod}) ₂] complexes.....	201
Table 3-8	Crystal data and structure refinement parameters for [L ^{Mod}] ^{Decomp.} and (Et ₄ N) ₂ [L ^{Ph}].....	202

Chapter 4

Table 4-1	Initial reaction conditions of cobalt(II) complex, (Et ₄ N) ₂ [Co ₂ (L ^{iPr}) ₂], with aryl azide 39a	230
-----------	--	-----

Table 4-2	Performance of cobalt(II) dinuclear complexes bearing redox-active ligands with varying acyl substituents for intramolecular C–H amination of aryl azide 39a	232
Table 4-3	Optimization for the conversion of aryl azide 39a to indoline 39b catalyzed by $(\text{Et}_4\text{N})_2[\text{Co}_2(\text{L}^{\text{iPr}})_2]$	234
Table 4-4	Electronic effect on the cobalt(II)-catalyzed benzylic C–H bond amination of aryl azides.....	236
Table 4-5	Substrate scope on the cobalt(II)-catalyzed benzylic C–H bond amination of aryl azides to form N-heterocycles.....	239
Table 4-6	Data refinement for the solid-state structure of cycled ligand (L^{Cyc}).....	265

List of Schemes

Chapter 1

Scheme 1-1	Neutral (3), monoanionic (2), and dianionic (5) dithiolene metal complexes.....	4
Scheme 1-2	Schematic representations of the different oxidation states in A) <i>ortho</i> -catecholate ligands and B) their metal complexes.....	5
Scheme 1-3	Different redox states of A) amidophenolate and B) diimine ligand systems.....	7
Scheme 1-4	Possible oxidation states of the 2,2'-dipyridine ligand system.....	8
Scheme 1-5	A) Schematic representation of the different oxidation states of α -iminopyridine ligands and B) complexes supported by two monoanionic π -radicals of the α -iminopyridine ligand 24 (Ni(COD) ₂ was used in the synthesis of the Ni ^{II} complex).....	9
Scheme 1-6	Catalytic cycle for intradiol cleavage by catechol dioxygenase.....	13
Scheme 1-7	Catalytic cycle for extradiol cleavage by catechol dioxygenase.....	14
Scheme 1-8	Proposed mechanism in the oxidation of primary alcohols carried out by galactose oxidase.....	15
Scheme 1-9	A) [2+2] cycloaddition and B) olefin isomerization and hydrosilylation of unfunctionalized alkenes carried out by the iron(II) bis(imino)pyridine complex [FeII(PDI)] ²⁻ 50	17
Scheme 1-10	Negishi-type C–C bond formation carried out by cobalt(III) redox-active amino/imino phenolate.....	19

Chapter 2

- Scheme 2-1 General reaction mechanism for substrate oxidation, reversible formation of an inert $M-\mu-O-M$ species, and product inhibition.....32
- Scheme 2-2 Tridentate pincer ligand **[PCP]**, (2,6-bis[(di-*tert*-butylphosphino)methyl]phenyl), and its metal complexes, **[M(PCP)X]**, reported by Moulton and Shaw.....33
- Scheme 2-3 **A)** Metalation of $H_3[ONO^{red}]$ with Ta(V), **B)** generation of a bis(μ -imido) tantalum dimer and **C)** its reactivity with $PhICl_2$ in the formation of diazene product (scheme adapted from reference)36
- Scheme 2-4 **A)** Metalation of $H_3[ONO^{red}]$ with Zr(IV) and **B)** O_2 reduction by its complex $[ONO^{red}](Zr^{IV}Cl_2)THF$ to form a Zr(IV) bis- μ -hydroxo dimer...37
- Scheme 2-5 **A)** Degradation of a tripodal ligand to form a pincer-ligated Ta(V) complex and **B)** incorporation of phenyl backbones to the tridentate trianionic pincer ligand.....39
- Scheme 2-6 **A)** Metalation of the tridentate ligand $H_3[NNN^{Red}]$ with Ta(V) and **B)** reaction of its Ta(V) complex with an aryl azide to yield a Ta(V)-nitrene species.....40
- Scheme 2-7 Synthetic route for the preparation of $NH(o-PhNHC(O)^{iPr})_2 (H_3L^{iPr})$44
- Scheme 2-8 Synthesis of $NH(o-PhNHC(O)R)_2$ ligands (H_3L^R , where R = ^tBu, Ph, Adamantyl and CF_3).....46
- Scheme 2-9 Metalation strategy of H_3L^{iPr} with cobalt(II) ions to form the mononuclear cobalt(II) complex, $(Et_4N)_2[Co(HL^{iPr})_2]$, and dinuclear cobalt(II) complex, $(Et_4N)_2[Co_2(L^{iPr})_2]$48

Scheme 2-10	Synthesis of dinuclear cobalt(II) complexes $K_2[Co_2(L^{tBu})_2]$, $K_2[Co_2(L^{Ph})_2]$, and $K_2[Co_2(L^{CF_3})_2]$ (counterion exchange not shown)	49
Scheme 2-11	Synthesis of cobalt(II) mononuclear complexes $K_2[Co(HL^{tBu})_2]$, $K_2[Co(HL^{Ph})_2]$, and $K_2[Co(HL^{Ad})_2]$ (counter ion exchange for each complex not shown).....	51
Scheme 2-12	Synthesis of dinuclear complexes $K_2[Fe_2(L^{iPr})_2]$, $K_2[Ni_2(L^{iPr})_2]$, $K_2[Cu_2(L^{iPr})_2]$, and $K_2[Zn_2(L^{iPr})_2]$ (counterion exchange with each complex is not shown).....	52
Scheme 2-13	Synthesis of mononuclear nickel(II) complex $(Et_4N)_2[Ni_2(L^{iPr})_2]$	53
Chapter 3		
Scheme 3-1	Aerobic ethylene oxidation to acetaldehyde by $PdCl_2$ and $CuCl_2$ in the Wacker process.....	114
Scheme 3-2	Aerobic oxidations carried out by A) monooxygenases, B) dioxygenases, and C) oxidases.....	116
Scheme 3-4	Synthetic functional models for galactose oxidase: (Top) Catalytic aerobic alcohol oxidation by copper(II) and zinc(II) complexes of tetradentate ligand (L^1), and (bottom) five possible redox states of ligand, [L^1].....	118
Scheme 3-5	Schematic representation of reversible dioxygen binding to cobalt(II)....	119
Scheme 3-6	A) Synthesis of a cobalt(III)-peroxo complex supported by 13-TMC ligand and B) its ability to perform deformylation of 2-phenylpropionaldehyde.....	121
Scheme 3-7	Stoichiometric O-atom transfer reactions by A) $(Et_4N)_2[Co_2(L^{iPr})_2]$ and B) $(Et_4N)_2[Co(HL^{iPr})_2]$ to PPh_3	127

Scheme 3-8	One-electron chemical oxidation of $(\text{Et}_4\text{N})_2[\text{Co}(\text{HL}^{i\text{Pr}})_2]$ to generate $(\text{Et}_4\text{N})[\text{Co}(\text{HL}^{i\text{Pr}})_2]^{\text{ox}}$	135
Scheme 3-9	Synthesis of mononuclear cobalt(II)-cyano complex, $(\text{Et}_4\text{N})_2[\text{Co}(\text{L}^{i\text{Pr}})(\text{CN})]$	136
Scheme 3-10	A) Synthesis of bidentate ligand $[\text{HN}(\text{Ph})(o\text{-PhNHC}(\text{O})^i\text{Pr})]$ ($\text{H}_2\text{L}^{\text{Mod}}$) and B) its metalation with cobalt(II) to form mononuclear cobalt(II) complex $(\text{PPh}_4)_2[\text{Co}(\text{L}^{\text{Mod}})_2]$	142
Scheme 3-11	Synthesis of mononuclear zinc(II) complex, $\text{K}_2[\text{Zn}(\text{L}^{\text{Mod}})_2]$	148
Scheme 3-12	Possible oxidation states of the trianionic ligand platform $[\text{L}^{i\text{Pr}}]^{3-}$	151
Scheme 3-13	Synthesis of the ligand $\text{MeN}(o\text{-PhNHC}(\text{O})^i\text{Pr})_2$ ($\text{Me-H}_2\text{L}^{i\text{Pr}}$).....	152
Scheme 3-14	Synthesis of dinuclear cobalt(II) complex $(\text{Et}_4\text{N})_2[\text{Co}_2(\mu\text{-OH})_2(\text{Me-L}^{i\text{Pr}})_2]$	153
Scheme 3-15	Decomposition pathway of $\text{K}_2[\text{Zn}(\text{L}^{\text{Mod}})_2]$ observed after exposing a solution of the fully oxidized complex to air.....	160
Scheme 3-16	Catalytic aerobic deformylation of 2-phenylpropionaldehyde (2-PPA) by $(\text{Et}_4\text{N})_2[\text{Co}_2(\text{L}^{i\text{Pr}})_2]$	166
Scheme 3-17	Catalytic aerobic oxidation of 3,5-di- <i>tert</i> -butylcatechol (3,5-DTBC) carried out by dinuclear cobalt(II) complex, $(\text{Et}_4\text{N})_2[\text{Co}_2(\text{L}^{i\text{Pr}})_2]$	167
Scheme 3-18	A) One- and B) two-electron chemical oxidations of mononuclear zinc(II) complex $\text{K}_2[\text{Zn}(\text{L}^{\text{Mod}})_2]$ using FcBF_4	174
Chapter 4		
Scheme 4-1	C–H insertion by metallocarbenes and metallonitrenes.....	210

Scheme 4-2	Catalytic intramolecular C–H amination by Mn(III)- and Fe(III)-porphyrins and dirhodium(II) acetate.....	211
Scheme 4-3	C–H amination of carbamates by dirhodium(II) tetracarboxylate.....	213
Scheme 4-4	Intramolecular rhodium(II)-catalyzed C–H amination of A) sulfamates and B) sulfamides.....	214
Scheme 4-5	Ruthenium(II)-catalyzed enantioselective intramolecular C–H amination of sulfamate esters.....	215
Scheme 4-6	Cobalt(II)-porphyrin catalyzed C–H amination with sulfonyl azides.....	217
Scheme 4-7	Cobalt(II)-porphyrin catalyzed C–H amination with A) sulfonyl and B) sulfamoyl azides.....	219
Scheme 4-8	Intramolecular C–H amination catalyzed by Co ^{II} (TPP) 14 using azide Troc-N ₃	220
Scheme 4-9	Stoichiometric intramolecular C–H amination by an iron(II) dipyrromethene complex.....	222
Scheme 4-10	Catalytic intermolecular C–H amination by an iron(II) dipyrromethene complex.....	223
Scheme 4-11	Catalytic intramolecular C–H amination of linear alkyl azides by an iron(II) dipyrromethene complex.....	224
Scheme 4-12	Iridium(I)-catalyzed C–H amination of aryl azides to form indolines and indoles.....	225
Scheme 4-13	Reactions of cobalt(I) dipyrromethene complex 35 with A) alkyl and B) aryl azides.....	227

Scheme 4-14 C–H amination reaction in the presence of pyridine using azide	
39a	237
Scheme 4-15 Intramolecular KIE for the C–H amination of benzylic C–H bonds of aryl	
azide 50a carried out by $(\text{Et}_4\text{N})_2[\text{Co}_2(\text{L}^{\text{iPr}})_2]$	241

Chapter 1:

Introduction to Redox-active Ligands and Their Role in Promoting Novel Reactivity at First-row Transition Metal Centers

Section 1-1. Introduction

In 1905, Alfred Werner reported his investigations that defined the basics of modern coordination chemistry.¹ Since his early studies, significant advances to the development of transition metal catalysts for small molecule activation leading to the discovery of novel compounds for a wide range of applications have been made.² Typical Werner-type complexes are shown in Figure 1-1.¹ Tracking oxidation state changes at the metal center in classical Werner-type transition metal catalysts throughout their catalytic cycles is a key factor.^{1b}

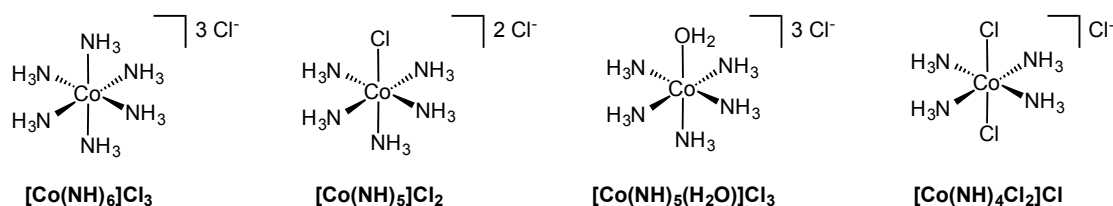


Figure 1-1. Selected examples of classical Werner-type complexes.¹

Traditionally, these catalysts consist of second- and third-row metal ions. First-row transition metal ions, however, remain far less used, as they tend to favor one-electron oxidations rather than the two-electron transfer sequence that is often the hallmark of an

effective second- or third-row transition metal catalyst. In recent years, redox-active ligands have demonstrated to be promising coordination motifs that enhance the ability of first-row metal centers to carry out multi-electron redox processes.

Metal-mediated redox processes are traditionally viewed as changes in the metal's oxidation state. However this view only holds true if the supporting ligand acts as a spectator. If the ligand is capable of undergoing a redox change it is termed redox-active.³ More recently, redox-active or non-innocent ligands have been coordinated to metal centers. In these cases, the ligand can undergo redox activity while the metal oxidation state remains unchanged.

In 1966, Jørgensen was among the first persons to recognize that ligands were capable of undergoing redox changes.^{3b} The ambiguity in metal versus ligand oxidation has since been a topic of great scrutiny over the past 50 years. This ambiguity lies in the fact that these types of ligands have frontier molecular orbitals (highest occupied molecular orbitals, HOMOs, and lowest unoccupied molecular orbitals, LUMOs) that are similar in energy as the metal that they are coordinated to. As a result, one common feature shared among transition metal complexes of redox-active ligands is the ability of these ligands to undergo redox changes in oxidation state without changing the oxidation state of the metal center. For first-row transition metal ions, which typically display one-electron sequences that are detrimental for catalysis, these types of ligands become beneficial. The focus of this introduction is to give a brief historical perspective on the origin of redox-active ligands, their ubiquity in biological systems, and recent uses to promote novel reactivity at first-row transition metal centers.

Section 1-2. A Historical Perspective on Redox-active Ligands and Their Metal Complexes

Recognized in the early 1960s, dithiolene ligands were some of the first ligand systems to be classified as redox-active. Schrauzer and Mayweg initially reported the synthesis of neutral nickel complex **2** supported by two dithiobenzyl ligands (**1**) (Figure 1-2).⁴ Given the neutral nature of each dithiobenzyl ligand, it was initially believed that the oxidation state of nickel in this complex was Ni(0). Spectroscopic data collected of this complex, however, implied a square planar nickel(II) center, which suggested that each ligand was singly reduced by one electron. These observations led to the synthesis and characterization of similar Pd(II), Pt(II), Co(II), Cu(II), and Zn(II) complexes supported by dithiolene ligands with various ligand substituents, as reported by Gray and co-workers.⁵ In their work, spectroscopic investigations demonstrated that these complexes shared electronic properties and almost identical geometries. More importantly, through a series of electron paramagnetic spectroscopy (EPR) studies, it was observed that radicals could be delocalized on the π -molecular orbitals of these complexes, a previously unexplored concept.

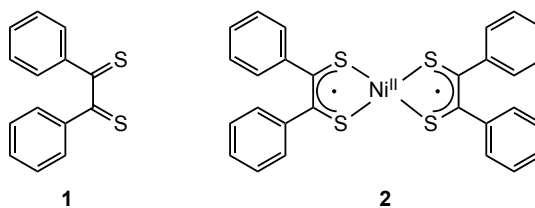
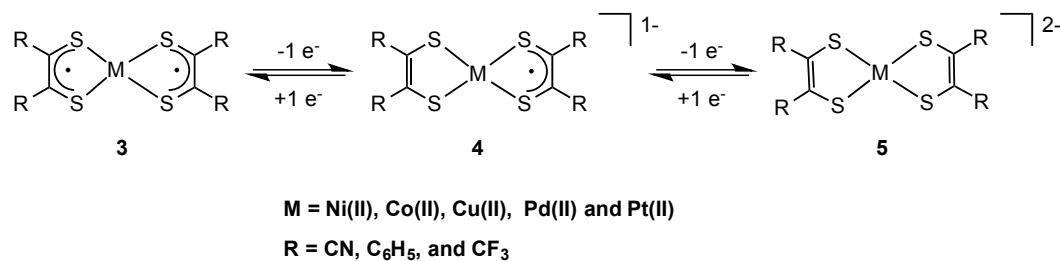


Figure 1-2. Dithiobenzyl ligand (**1**) and its nickel(II) complex (**2**) reported by Schrauzer and Mayweg.⁴

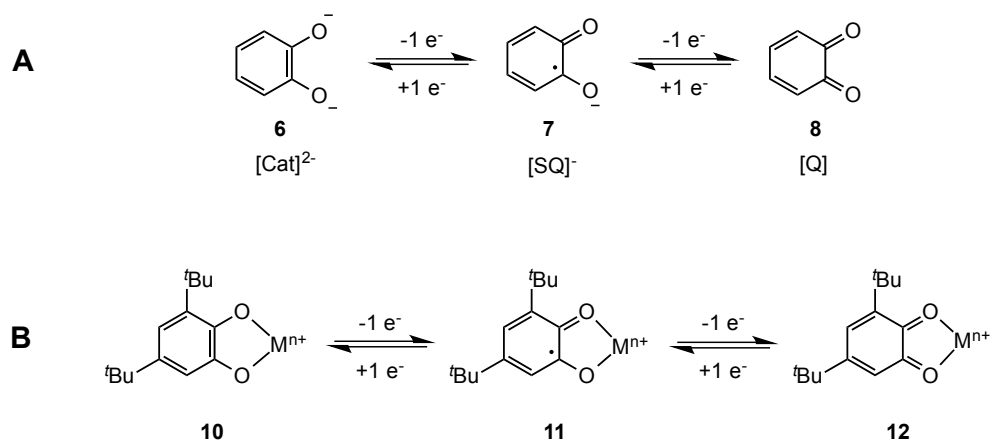
Davison and co-workers contributed to this body of work through further investigation of Grey's unusual observations. In their studies, dithiolene Ni(II), Co(II), Cu(II), Pd(II) and Pt(II) neutral complexes (**3**) were prepared as well as their respective monoanionic (**4**) and dianionic (**5**) analogues by a series of electron transfer reactions (Scheme 1-1).⁶ The assignments shown in Scheme 1-1 were derived by the investigation of the structural, electrochemical, spectroscopic, and magnetic properties of each independent species. From these experiments, it was concluded that the metal complexes could undergo sequential redox events whereby the redox process could selectively take place at the ligand backbone instead of the metal center. The dithiolene ligand systems provided early evidence for non-classical electronic structures in metal complexes and became the very first bidentate redox-active ligands.⁷



Scheme 1-1. Neutral (**3**), monoanionic (**2**), and dianionic (**5**) dithiolene metal complexes.⁶

The rapid interest in dithiolene systems led to the discovery of their oxygen analogues, dioxolenes. One of the most widely studied dioxolene systems is the *ortho*-benzoquinones, also referred to as catecholates.⁸ Similarly to dithiolene ligands, catecholates are capable of coordinating to a metal ion in three different modes (Scheme 1.2A). When coordinated, the fully oxidized dianionic catecholate ($[\text{Cat}]^{2-}$, **6**) can undergo sequential redox

processes; a one electron oxidation to become a monoanionic semiquinone ($[SQ]^{-1}$, **7**) and the subsequent additional one electron oxidation reduces **6** to a fully-reduced quinone ($[Q]$, **8**). Metal complexes of catecholates and semiquinones tend to exhibit unique spectroscopic properties resulting from electronic metal-ligand charge localization compared to their dithiolene analogues.^{3a} Substitutions at the 3 and 5 positions in the *ortho*-benzoquinone ligands and advances in X-ray crystallography have resulted in the structural characterization of compounds **10**, **11**, and **12** (Scheme 1-2B).⁸⁻⁹ The formal identification of such compounds were confirmed by examining the C–N and C–O bond lengths, which provided crucial evidence about ligand radical localization and has allowed for the assignment and diversification of these types of compounds over the past 40 years.¹⁰



Scheme 1-2. Schematic representations of the different oxidation states in **A**) *ortho*-catecholate ligands and **B**) their metal complexes.^{3a}

The majority of the spectroscopic and electrochemical properties known about semiquinone metal complexes have come from the investigations of the ligand with first-row transition metals. The close HOMO and LUMO ligand and metal energies, found in these

complexes has allowed for detailed spectroscopic and electrochemical investigations. One of the most widely studied [SQ]⁻ ligand systems is that derived from tetrachloro-1,2-benzoquinone (Cl₄BQ), 3,5-di-*tert*-butyl-1,2-benzoquinone (3,5-DBBQ).¹¹ This ligand was shown to coordinate to a series of first-row transition metal ions in a 3 to 1, ligand to metal ratio to form six-coordinate pseudo-octahedral complexes **14** (Figure 1-3). The electrochemical and magnetic properties of complexes **14** revealed that the electron transfer process could occur either at the metal center or at the ligand.

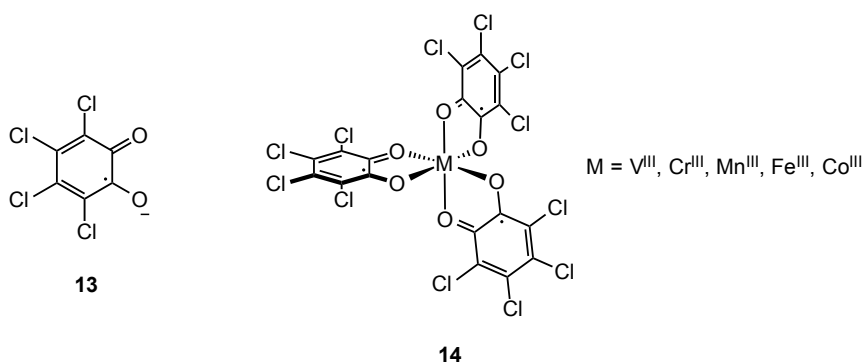
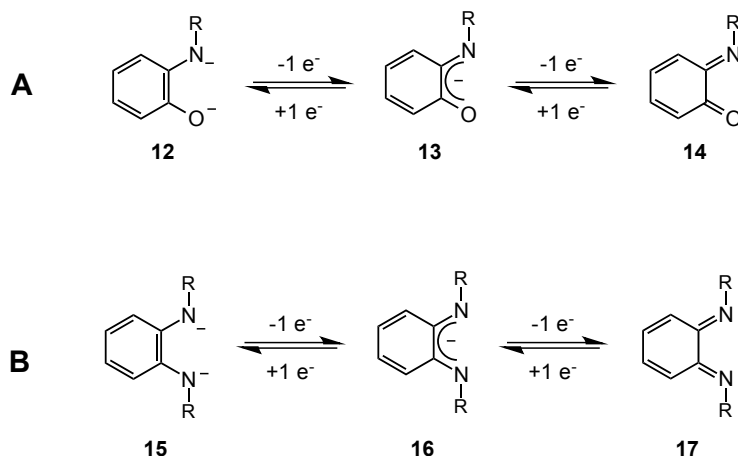


Figure 1-3. Tetrachloro-1,2-semiquinonate ligand Cl₄(SQ) (**13**) and its corresponding V^{III}, Cr^{III}, Mn^{III}, Fe^{III}, and Co^{III} tris(*o*-semiquinone) complexes.¹¹

As more spectroscopic and crystallographic evidence for ligand-centered radicals became available from the catecholate, semiquinone, and quinone systems, their nitrogen analogues began emerging. The corresponding amidophenolate and diimine ligands complexes displayed similar redox profiles as their catecholate analogues. First reported by Holm and co-workers in 1966, first-row complexes of the amidophenolate and diimine ligands have been heavily investigated for their electronic properties over the past four

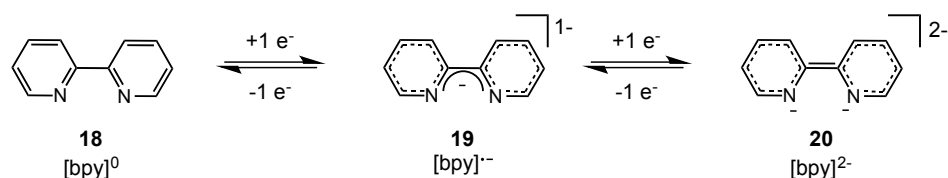
decades.¹² Until the reports from Wieghardt and co-workers in 2001, the formal oxidation state of these ligands and their metal center remained ambiguous for the past four decades.¹³



Scheme 1-3. Different redox states of **A**) amidophenolate and **B**) diimine ligand systems.¹²⁻¹³

One of the most widely used classes of bidentate redox-active nitrogen-donor ligands in coordination chemistry is the 2,2'-dipyridine ligand. First reported by Fritz Blau in 1888¹⁴, it has been extensively used as a chelating ligand for the synthesis of a number of metal complexes,¹⁵ supramolecular compounds,¹⁶ and devices for optoelectronic applications.¹⁷ Similarly to the dithiolene and dioxolene ligand systems, the 2,2'-dipyridine ligand consists of an alkene motif that would suggest that it is redox-active (Scheme 1-4). Despite its initial discovery more than 100 year ago, its redox-active flexibility was not reported until recently.¹⁸ Wieghardt and co-workers, pioneers in establishing its redox-active properties, has shown that tris-2,2'-bipyridine complexes of Y, Ti, V, Cr, Mo, Mn, Fe and Ru can undergo ligand based reduction to form stable ligand radical species.¹⁹ More importantly, Wieghardt and co-workers have presented a wide array of density functional theory (DFT) data demonstrating that complexes with neutral tris-2,2'-dipyridine ligands ([bpy]⁰, **18**) can

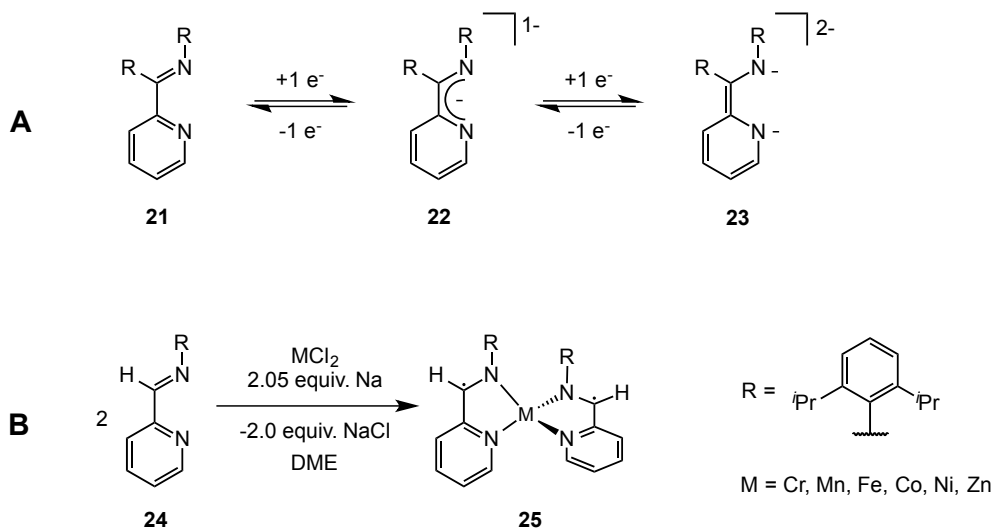
undergo a one-electron reduction to generate its one-electron reduced radical species ($[\text{bpy}]^{\cdot-}$, **19**). A further one-electron reduction of **19** yields the dianionic, fully reduced ($[\text{bpy}]^{2-}$, **20**). Interestingly, these studies have concluded that the radical anion **19**, when coordinated to a transition metal ion with an open-shell configuration, is capable of forming singlet diradicals by anti-ferromagnetic coupling. The studies by Wieghardt and co-workers have provided fundamental insights on the electronic assignment of complexes supported by these widely chelating used ligands.



Scheme 1-4. Possible oxidation states of the 2,2'-dipyridine ligand system.

A derivation of the 2,2'-dipyridine system, the α -iminopyridine redox-active ligand, has been extensively studied with first-row transition metal ions. Their unusual redox-activity is the result of an electron-accepting π -system ligand backbone composed from the combination of bipyridine and 1,4-diazabutadiene (Scheme 1-5A). Wieghardt and co-workers have prepared Cr, Mn, Fe, Co, Ni, and Zn complexes of the α -iminopyridine ligand **24** and investigated their spectroscopic properties.²⁰ In these studies, ligand **24** was used as a chelating scaffold to support complexes **25** of divalent metal centers with two π -radical ligands (Scheme 1-5B). The results from these studies provided evidence of their π -radical monoanionic nature in coordination complexes as well as mixed ligand valency, a concept that was previously unexplored in metal complexes with two bis- π -radical monoanionic

ligands. Subsequent studies of this ligand system, utilizing X-ray crystallographic analysis, have revealed significant differences in bonding parameters between complexes containing neutral, monoanionic and dianionic α -iminopyridine ligands.²¹



Scheme 1-5. **A)** Schematic representation of the different oxidation states of α -iminopyridine ligands and **B)** complexes supported by two monoanionic π -radicals of the α -iminopyridine ligand **24** ($\text{Ni}(\text{COD})_2$ was used in the synthesis of the Ni^{II} complex).²⁰

Initially developed during the 1960s, bis(imino)pyridines have become an important type of redox-active ligands. Primarily, bis(imino)pyridines, analogous to α -iminopyridines, can undergo sequential one-electron reductions in a similar manner (**26**, Figure 1-6). Initially investigated by Wieghardt and co-workers,²² these ligands have been extensively targeted due to their wide use in promoting multi-electron reactions at first-row transition metals.²³ Other ligands of interest that display similar behavior to the bis(imino)pyridines include terpyridines (**27**, Figure 1-6)²⁴, which have also been extensively studied for the unique electronic and electrochemical properties of the resulting metal complexes.

The combination of spectroscopy, X-ray crystallography, and theory has served as a foundation to understand the properties of redox-active ligands and their metal complexes. Other recent and emerging nitrogen-based redox-active ligands, shown in Figure 1-4, include porphyrin-derived dipyrromethenes (**28**)²⁵ and phthalocyanines (**29**),²⁶ 9,10-diaminophenanthrenes (**30**),^{26b} and bis(2-isopropyl-4-methoxyphenyl)amine ligand, H₃[NNN^{red}] (**31**).²⁷

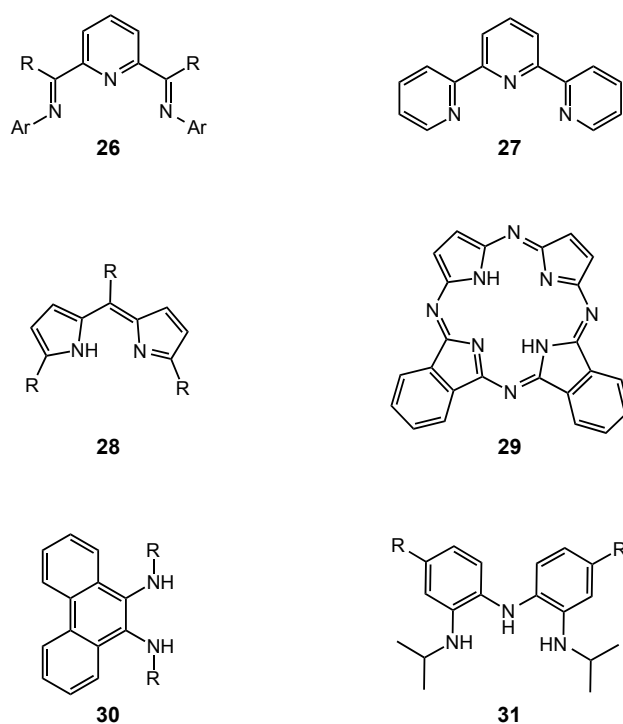


Figure 1-4. Other nitrogen-donor based redox-active ligands.²⁵⁻²⁷

Phenol-containing ligands have also been a target for discussion over the past few years. Phenol-containing redox-active ligands are highly attractive scaffolds due to their ability to stabilize one-electron oxidized phenoxyl radical species.²⁸ Included in this ligand scaffold are bidentate *o*-aminophenol (**32**),²⁹ *o*-aminothiols (**33**),²⁹ trianionic bis(phenol)amines

(**34**),³⁰ bis(phenol)thioethers (**35**),³¹ bis(phenol)selenoethers (**36**),³² tetradentate bis(phenol)-*ortho*-phenylenediamines (**37**)³³ and salen ligands (**38**)³⁴ (Figure 1-5).

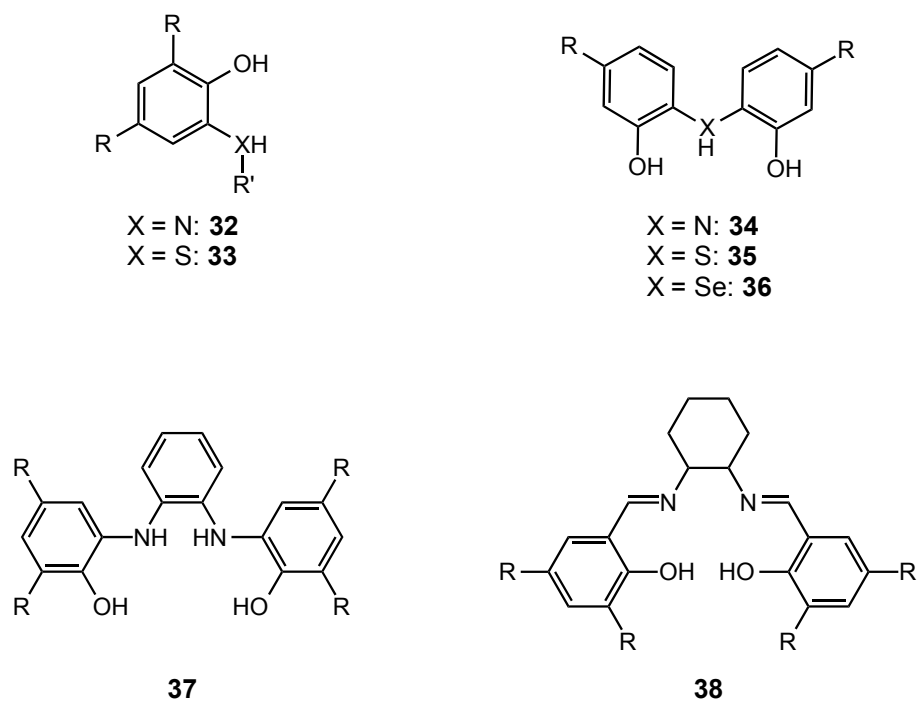
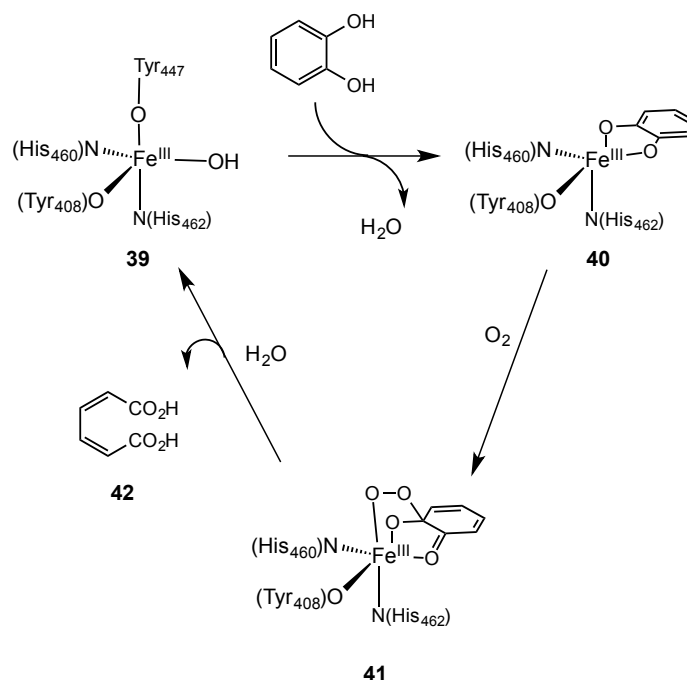


Figure 1-5. Redox-active ligands containing phenol moieties.²⁸⁻³⁴

Section 1-3. Redox-active Ligands in Biology

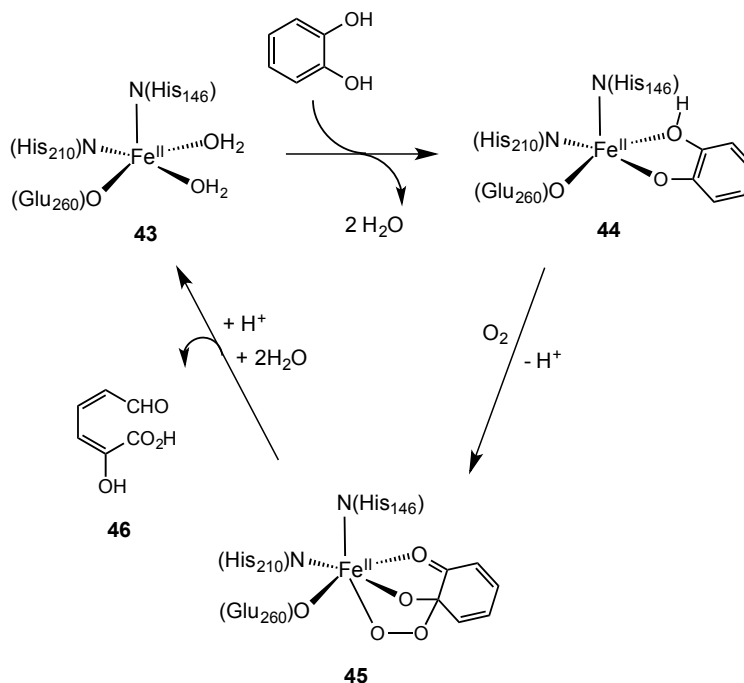
First-row transition metal-catalyzed redox reactions facilitated by redox-active ligands are found in a variety of enzymes including the cytochrome *c* oxidase,³⁵ glyoxal oxidase,³⁶ ribonucleotide reductases,³⁷ catechol dioxygenases,³⁸ and galactose oxidase.³⁹ These enzymes take the advantage of a redox-active moiety in its active site to promote multi-electron reactions at metals that preferentially react via one-electron redox pathways.⁴⁰ Advances in spectroscopic techniques over the past five decades have provided evidence for the role of redox-active moieties embedded within the active sites of several enzymes.³⁷

Catechol dioxygenases are non-heme iron-dependent enzymes that catalyze the oxidative cleavage of catechols in bacterial aromatic degradation pathway.^{38, 41} Spectroscopic and X-ray crystallography studies have concluded that a single non-heme iron center chelated by the catecholate substrates is responsible for this intramolecular electron exchange event. Catechol dioxygenases are divided into two different classes depending on their position of bond cleavage – intradiols and extradiols.⁴¹⁻⁴² Intradiol cleavage uses an iron(III) metal center in a bipyramidal geometry coordinated by two histidine moieties, two tyrosine moieties, and a hydroxide ligand (Scheme 1-6, **39**).⁴³ As the catechol substrate binds to the iron(III), one tyrosine and hydroxide ligands dissociate to form species **40**. Iron(III) species **40** then activates substrate as semiquinone using dioxygen, to form peroxide intermediate **41**, which after rearrangement cleaves the C–C bond of the catechol substrate to yield *cis,cis*-muconic acid product **42**.



Scheme 1-6. Catalytic cycle for intradiol cleavage by catechol dioxygenase.⁴²⁻⁴³

The mechanism for extradiol cleavage differs in the oxidation state of the iron cofactor.^{38b} In this case, a five-coordinate iron(II) center situated in a square pyramidal geometry ligated by two histidine, one glutamate, and two water ligands initiates the extradiol cleavage (Scheme 1-7, **43**).⁴⁴ As a result of the differences in the ligand environment, the catechol substrate binds as a bidentate monoanion.⁴⁵ The concomitant release of two water molecules in the primary coordination sphere allows for the catechol to coordinate and generate species **44**. This species then activates dioxygen to form iron(II) superoxide **45** which reacts directly with the bound catechol to promote the C–C cleavage and release 2-hydroxymucaldehyde acid as the product (**46**).

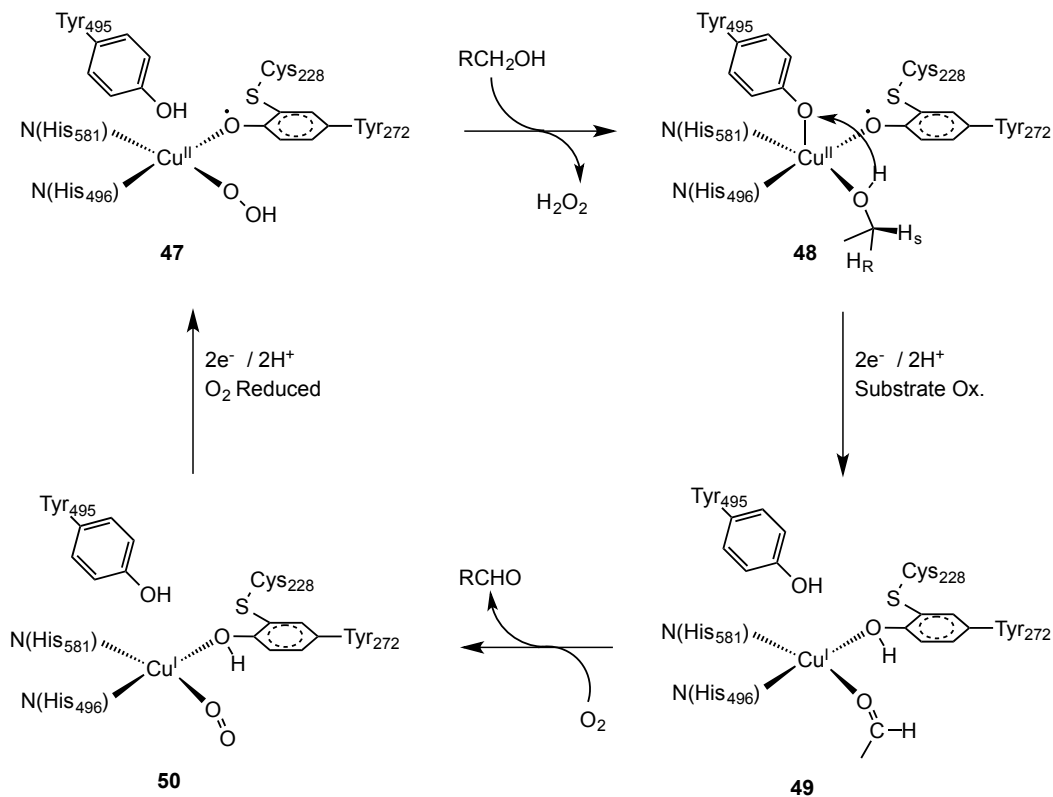


Scheme 1-7. Catalytic cycle for extradiol cleavage by catechol dioxygenase.^{42, 45}

Synthetic systems for both intradiol and extradiol catechol dioxygenases have been reported. Most of these examples employ tetradentate ligands (for intradiol)⁴⁶ and tridentate ligands (for extradiol),⁴⁷ which have given spectroscopic insights into the redox-active ligand of the catechol substrate and its selectivity in this enzyme.

Another widely studied enzymatic reaction that is facilitated by a redox-active ligand is the reaction involving the aerobic oxidation of primary alcohols by galactose oxidase.^{39, 48} Galactose oxidase utilizes dioxygen to convert primary alcohols to aldehydes alongside the production of H₂O₂. Detailed spectroscopic studies have made this enzymatic process be one of the best-understood systems involving a redox-active ligand. In its active form, a coordinated and magnetically coupled copper(II)-tyrosinate radical species (**47**) is responsible for the completion of this two-electron oxidation process (Scheme 1-8).⁴⁹ While copper is ubiquitous in many biological enzymes, its Cu^I/Cu^{II}

couple limits its redox activity, however the tyrosinate radical in galactose oxidase provides the second oxidizing equivalent required to promote the alcohol oxidation carried out by this enzyme.



Scheme 1-8. Proposed mechanism in the oxidation of primary alcohols carried out by galactose oxidase.⁴⁹

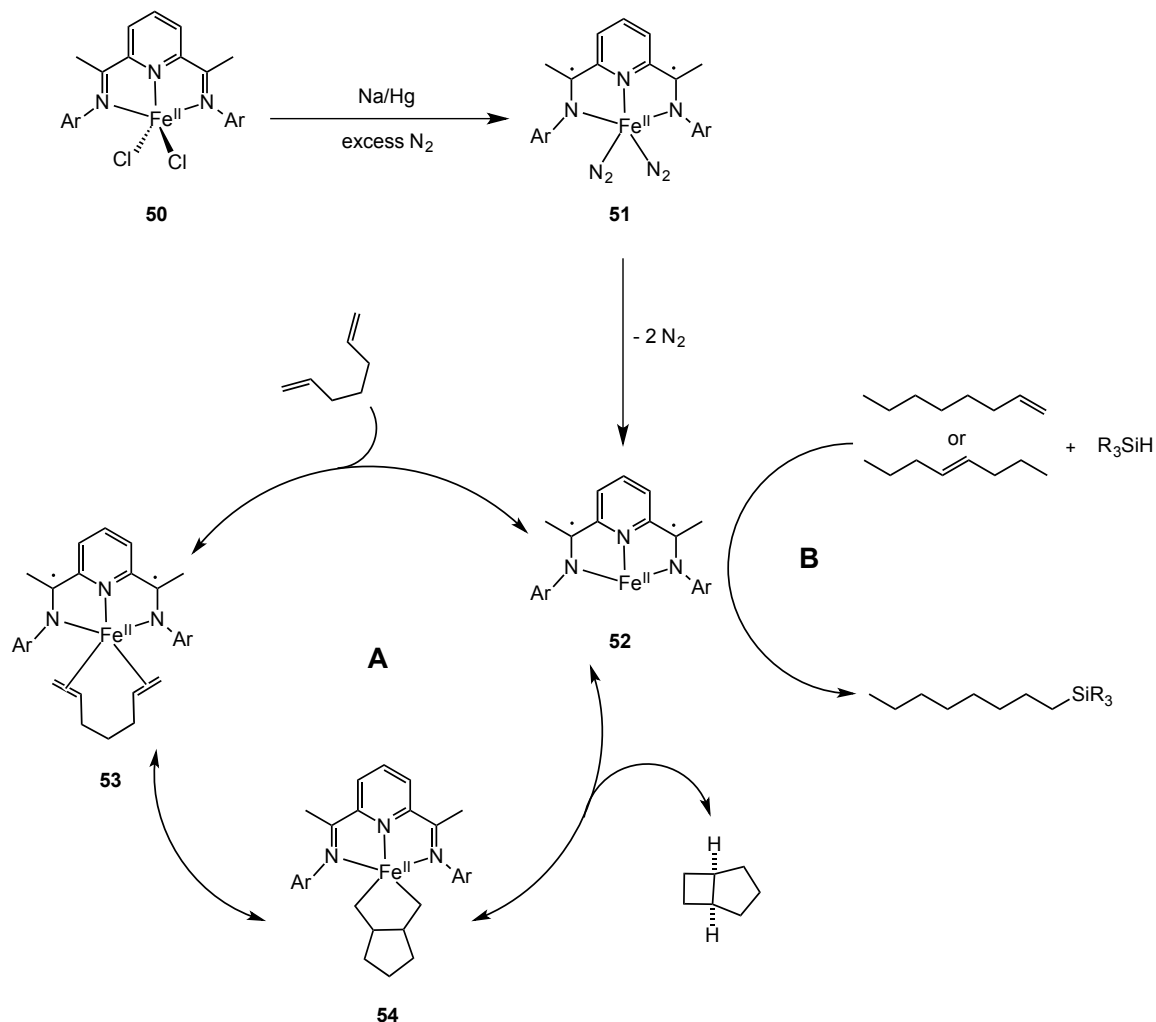
Section 1-4. Utility of Redox-active Ligands in Catalysis

The interest in redox-active ligands has transformed from a spectroscopic curiosity to an application concept in catalysis. Mechanistic evidence for their crucial role in the biological systems mentioned above led to the use of redox-active ligands for catalysis. Synthetic studies reported within the past decade have illustrated the ability of redox-active ligands to promote catalysis at first-row transition metals.⁵⁰ In all of the examples presented herein, the reactions involve the transfer of two or more electrons requiring multiple accessible ligand-based electronic states.

One of the most widely employed ligand in the last decade used to promote catalysis at first-row transition metals has been the bis(imino)pyridine ligand family. Chirik and co-workers have been the leading pioneers in demonstrating the ability of these ligands to promote formal [2+2] cycloadditions,⁵¹ hydrogenation⁵² and hydrosilylation⁵³ reactions, oxidative additions into C–C bonds,⁵⁴ and hydrogen-mediated reductive cyclization of 1,6-enynes and diynes.⁵⁵

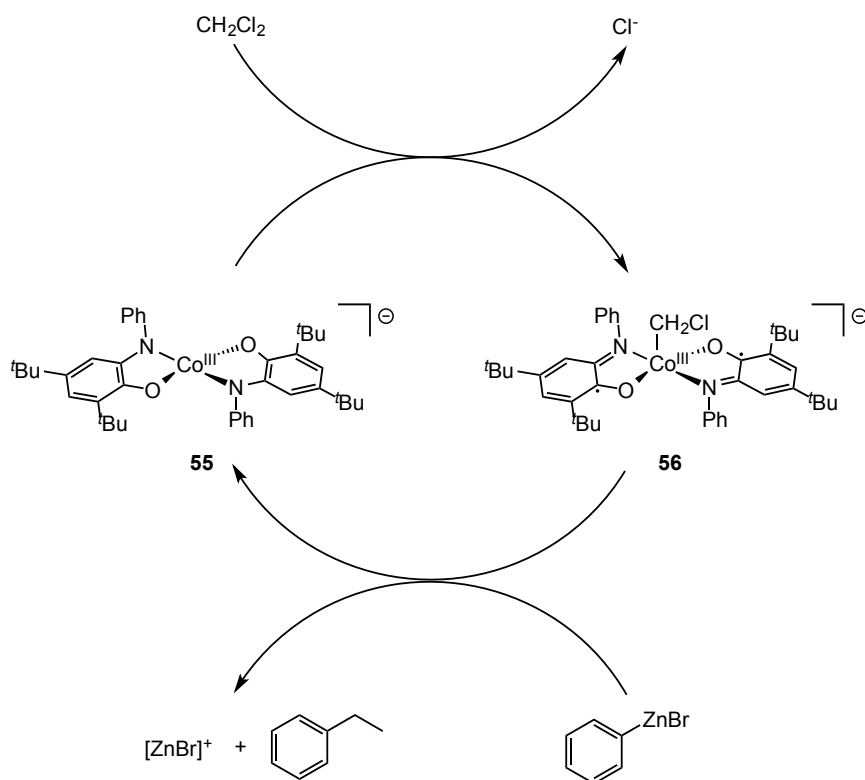
First reported by Brookhart and co-workers,⁵⁶ the iron(II) bis(imino)pyridine complex $[\text{Fe}^{\text{II}}(\text{PDI})]^{2-}$ **50** has been shown to carry out highly efficient [2+2] cycloadditions and selective terminal alkene hydrosilylation (Scheme 1-9).⁵¹ In this work, carried out by Chirik and co-workers, complex **50** can be reduced with sodium amalgam (Na/Hg) to obtain the bis(dinitrogen) complex **51** under a reduced nitrogen pressure. Complex **51** is defined as a formally two-electron reduced iron(II) complex whereby the reduction takes place on the bis(imino)pyridine backbone rather than on the iron center. Complex **51** then dissociates two of its dinitrogen ligands to become the active catalyst

52, capable of carrying out the [2+2] cycloaddition of diynes (Scheme 1-9A). Catalyst **52** was also shown by the same group to be the active catalyst for the hydrosilylation of unfunctionalized olefins (Scheme 1-9B).⁵³ The reactivity profile of this system is due to the ability of the ligand to store two reducing equivalents.⁵⁷



Scheme 1-9. A) [2+2] cycloaddition and B) olefin isomerization and hydrosilylation of unfunctionalized alkenes carried out by the iron(II) bis(imino)pyridine complex $[\text{Fe}^{\text{II}}(\text{PDI})]^{2-}$ **50**.^{51, 53}

Amidophenolate ligands have also demonstrated their usefulness to promote catalysis at first-row transition metal centers. Synthetic and mechanistic studies by Soper and co-workers have found amidophenolate redox-active ligands useful in promoting bond-forming redox reactions at square planar cobalt(III) centers. In this work, the unusual square planar cobalt(III) bis-iminophenolate complex **55** was found to react with alkyl halides to generate a stable five-coordinate alkylcobalt(III) bis-iminophenolate complex **56** (Scheme 1-10).⁵⁸ Complex **56** was shown to carry out the Negishi-type C–C cross coupling. Interestingly, the cobalt(III) center remains +3, with each amidophenolate ligand providing the overall two-electron reducing equivalents necessary for this reaction. Complex **56** is best described as a cobalt(III)-bis(imino)semiquinone.



Scheme 1-10. Negishi-type C–C bond formation carried out by cobalt(III) redox-active amino/imino phenolate.⁵⁸

The synthetic systems discussed in this chapter constitute only two of the many synthetic models, which have exemplified the utility of redox-active ligands in promoting catalysis at first-row transition metals. Examples of other redox-active ligand systems utilized for multi-electron transformations and efficient catalytic reactions will be discussed throughout the chapters of this dissertation. All examples presented herein indicate that redox-active ligands can be utilized in conjunction with first-row transition metals, in which one or two electron redox changes can occur on the ligand backbone. This tactic has been a topic of recent interest and growth in catalysis.

Section 1-5. Dissertation Overview

In this thesis, three different projects will be highlighted with the overarching theme of using redox-active ligands to promote novel reactivity at first-row transition metal centers. Each chapter represents an individual, yet related cohesive project.

In Chapter 2, the preparation and characterization of a series of cobalt(II) complexes with coordinatively bis(amidophenyl)amine ligands $[\text{NH}(o\text{-PhNHC(O)R})_2]$ ($R = \text{'Bu, Ph, Ad, CF}_3$) capable of acting as bidentate (dianionic) or tridentate (trianionic) is presented. Structural and spectroscopic data collected on complexes formed by these ligands will be presented to showcase key factors that influence the assembly of mononuclear versus dinuclear cobalt(II) species. In addition, this chapter will present a synthetic scheme for the synthesis and stabilization of dinuclear Fe^{II} , Ni^{II} , Cu^{II} , and Zn^{II} complexes supported by the tridentate, trianionic ligand $[\text{N}(o\text{-PhNC(O)}^{\text{iPr}})_2]^{3-}$. The structural, magnetic, spectroscopic, and electrochemical properties of these complexes will be explained.

In Chapter 3, the utility of cobalt(II) complexes of redox-active bis(amidophenyl)amine ligands for the activation of dioxygen is illustrated. This chapter will highlight the spectroscopic, mechanistic, and structural investigations carried out to understand how a mononuclear and dinuclear cobalt(II) complex, individually, react with dioxygen to carry out aerobic oxidation reactions. Key insights into the role of the ligand backbone will be illustrated using a zinc(II) complex of a related ligand scaffold.

This dissertation will conclude with the results presented in Chapter 4. This chapter will discuss the selective C–H amination of aryl azides by the dinuclear cobalt(II) complex, $(\text{Et}_4\text{N})_2[\text{Co}_2(\text{L}^{\text{iPr}})_2]$. The utility of using aryl azides with a sustainable and highly modular

cobalt(II) catalyst for the selective synthesis of indolines, a biologically-relevant type of compounds will be presented. The scope of the C–H amination reactivity of this complex is illustrated and a brief discussion into potential mechanism pathways of this reaction will be deliberated.

References

1. (a) Werner, A., *Berichte der deutschen chemischen Gesellschaft*. **1905**, 38 (1), 914; (b) Constable, E. C.; Housecroft, C. E., *Chem Soc Rev*. **2013**, 42 (4), 1429.
2. John C, B.; H, I.; M. J, C.; J, G., Some Recent Developments in Coordination Chemistry. In *Werner Centennial*, AMERICAN CHEMICAL SOCIETY: 1967; Vol. 62, pp 103.
3. (a) Pierpont, C. G., *Coordin Chem Rev*. **2001**, 219–221 (0), 415; (b) Jørgensen, C. K., *Coordin Chem Rev*. **1966**, 1 (1–2), 164.
4. Schrauzer, G. N.; Mayweg, V., *Journal of the American Chemical Society*. **1962**, 84 (16), 3221.
5. (a) Gray, H. B.; Williams, R.; Bernal, I.; Billig, E., *Journal of the American Chemical Society*. **1962**, 84 (18), 3596; (b) Gray, H. B.; Billig, E., *Journal of the American Chemical Society*. **1963**, 85 (13), 2019.
6. Davison, A.; Edelstein, N.; Holm, R. H.; Maki, A. H., *Inorg Chem*. **1963**, 2 (6), 1227.
7. Sproules, S.; Wieghardt, K., *Coordin Chem Rev*. **2011**, 255 (7–8), 837.
8. Pierpont, C. G.; Buchanan, R. M., *Coordin Chem Rev*. **1981**, 38 (1), 45.
9. (a) Carugo, O.; Castellani, C. B.; Djinovic, K.; Rizzi, M., *Journal of the Chemical Society, Dalton Transactions*. **1992**, (5), 837; (b) Bhattacharya, S.; Boone, S. R.; Fox, G. A.; Pierpont, C. G., *Journal of the American Chemical Society*. **1990**, 112 (3), 1088; (c) Boone, S. R.; Pierpont, C. G., *Inorg Chem*. **1987**, 26 (11), 1769.
10. Zanello, P.; Corsini, M., *Coordin Chem Rev*. **2006**, 250 (15–16), 2000.

11. (a) Pierpont, C. G.; Kelly, J. K., *Coordination Chemistry of o-Semiquinones*. In *PATAI'S Chemistry of Functional Groups*, John Wiley & Sons, Ltd: 2009; (b) Pierpont, C. G.; Downs, H. H., *Journal of the American Chemical Society*. **1975**, 97 (8), 2123; (c) Pierpont, C. G.; Downs, H. H.; Rukavina, T. G., *Journal of the American Chemical Society*. **1974**, 96 (17), 5573; (d) Pierpont, C. G.; Downs, H. H., *Journal of the American Chemical Society*. **1976**, 98 (16), 4834; (e) Buchanan, R. M.; Downs, H. H.; Shorthill, W. B.; Pierpont, C. G.; Kessel, S. L.; Hendrickson, D. N., *Journal of the American Chemical Society*. **1978**, 100 (13), 4318.
12. Balch, A. L.; Holm, R. H., *Journal of the American Chemical Society*. **1966**, 88 (22), 5201.
13. Chaudhuri, P.; Verani, C. N.; Bill, E.; Bothe, E.; Weyhermüller, T.; Wiegardt, K., *Journal of the American Chemical Society*. **2001**, 123 (10), 2213.
14. (a) Blau, F., *Monatshefte für Chemie*. **1889**, 10 (1), 375; (b) Blau, F., *Berichte der deutschen chemischen Gesellschaft*. **1888**, 21 (1), 1077.
15. Constable, E. C., Homoleptic Complexes of 2,2'-Bipyridine. In *Advances in Inorganic Chemistry*, Sykes, A. G., Ed. Academic Press: 1989; Vol. Volume 34, pp 1.
16. Ward, M. D.; White, C. M.; Barigelletti, F.; Armaroli, N.; Calogero, G.; Flamigni, L., *Coordination Chemistry Reviews*. **1998**, 171 (0), 481.
17. (a) Kalyanasundaram, K.; Grätzel, M., *Coordination Chemistry Reviews*. **1998**, 177 (1), 347; (b) Baxter, S. M.; Jones Jr, W. E.; Danielson, E.; Worl, L.; Strouse, G.; Younathan, J.; Meyer, T. J., *Coordination Chemistry Reviews*. **1991**, 111 (0), 47.

18. (a) Schultz, M.; Boncella, J. M.; Berg, D. J.; Tilley, T. D.; Andersen, R. A., *Organometallics*. **2001**, *21* (3), 460; (b) Kraft, S. J.; Fanwick, P. E.; Bart, S. C., *Inorg Chem*. **2010**, *49* (3), 1103; (c) Booth, C. H.; Kazhdan, D.; Werkema, E. L.; Walter, M. D.; Lukens, W. W.; Bauer, E. D.; Hu, Y.-J.; Maron, L.; Eisenstein, O.; Head-Gordon, M.; Andersen, R. A., *Journal of the American Chemical Society*. **2010**, *132* (49), 17537.
19. (a) Scarborough, C. C.; Sproules, S.; Weyhermüller, T.; DeBeer, S.; Wieghardt, K., *Inorg Chem*. **2011**, *50* (24), 12446; (b) Bowman, A. C.; Sproules, S.; Wieghardt, K., *Inorg Chem*. **2012**, *51* (6), 3707; (c) Wang, M.; Weyhermüller, T.; England, J.; Wieghardt, K., *Inorg Chem*. **2013**, *52* (21), 12763; (d) England, J.; Scarborough, C. C.; Weyhermüller, T.; Sproules, S.; Wieghardt, K., *Eur J Inorg Chem*. **2012**, *2012* (29), 4605; (e) Wang, M.; England, J.; Weyhermüller, T.; Wieghardt, K., *Inorg Chem*. **2014**, *53* (4), 2276.
20. Lu, C. C.; Bill, E.; Weyhermüller, T.; Bothe, E.; Wieghardt, K., *Journal of the American Chemical Society*. **2008**, *130* (10), 3181.
21. (a) Lu, C. C.; DeBeer George, S.; Weyhermüller, T.; Bill, E.; Bothe, E.; Wieghardt, K., *Angewandte Chemie International Edition*. **2008**, *47* (34), 6384; (b) Lu, C. C.; Weyhermüller, T.; Bill, E.; Wieghardt, K., *Inorg Chem*. **2009**, *48* (13), 6055; (c) van Gastel, M.; Lu, C. C.; Wieghardt, K.; Lubitz, W., *Inorg Chem*. **2009**, *48* (6), 2626.
22. de Bruin, B.; Bill, E.; Bothe, E.; Weyhermüller, T.; Wieghardt, K., *Inorg Chem*. **2000**, *39* (13), 2936.

23. (a) Bart, S. C.; Chłopek, K.; Bill, E.; Bouwkamp, M. W.; Lobkovsky, E.; Neese, F.; Wieghardt, K.; Chirik, P. J., *Journal of the American Chemical Society*. **2006**, *128* (42), 13901; (b) Scott, J.; Gambarotta, S.; Korobkov, I.; Knijnenburg, Q.; de Bruin, B.; Budzelaar, P. H. M., *Journal of the American Chemical Society*. **2005**, *127* (49), 17204; (c) Zhu, D.; Budzelaar, P. H. M., *Organometallics*. **2008**, *27* (12), 2699; (d) Zhu, D.; Thapa, I.; Korobkov, I.; Gambarotta, S.; Budzelaar, P. H. M., *Inorg Chem*. **2011**, *50* (20), 9879; (e) Scott, J.; Vidyaratne, I.; Korobkov, I.; Gambarotta, S.; Budzelaar, P. H. M., *Inorg Chem*. **2008**, *47* (3), 896; (f) Vidyaratne, I.; Scott, J.; Gambarotta, S.; Budzelaar, P. H. M., *Inorg Chem*. **2007**, *46* (17), 7040.
24. Constable, E. C., The Coordination Chemistry of 2,2':6',2''-Terpyridine and Higher Oligopyridines. In *Advances in Inorganic Chemistry*, Emeléus, H. J., Ed. Academic Press: 1986; Vol. Volume 30, pp 69.
25. (a) Cohen, S. M.; Halper, S. R., *Inorg Chim Acta*. **2002**, *341* (0), 12; (b) King, E. R.; Betley, T. A., *Inorg Chem*. **2009**, *48* (6), 2361; (c) King, E. R.; Betley, T. A., *Journal of the American Chemical Society*. **2009**, *131* (40), 14374.
26. (a) Kobayashi, N.; Nakajima, S.-i.; Ogata, H.; Fukuda, T., *Chemistry – A European Journal*. **2004**, *10* (24), 6294; (b) Shaffer, D. W.; Ryken, S. A.; Zarkesh, R. A.; Heyduk, A. F., *Inorg Chem*. **2010**, *50* (1), 13.
27. Nguyen, A. I.; Blackmore, K. J.; Carter, S. M.; Zarkesh, R. A.; Heyduk, A. F., *Journal of the American Chemical Society*. **2009**, *131* (9), 3307.
28. Chaudhuri, P.; Wieghardt, K.; In Progress, n., *John Wiley & Sons: New York*. **2001**, *50*, 151.

29. Poddel'sky, A. I.; Cherkasov, V. K.; Abakumov, G. A., *Coordin Chem Rev.* **2009**, 253 (3–4), 291.
30. (a) Bruni, S.; Caneschi, A.; Cariati, F.; Delfs, C.; Dei, A.; Gatteschi, D., *Journal of the American Chemical Society.* **1994**, 116 (4), 1388; (b) Larsen, S. K.; Pierpont, C. G., *Journal of the American Chemical Society.* **1988**, 110 (6), 1827; (c) Simpson, C. L.; Boone, S. R.; Pierpont, C. G., *Inorg Chem.* **1989**, 28 (24), 4379; (d) Girgis, A. Y.; Balch, A. L., *Inorg Chem.* **1975**, 14 (11), 2724.
31. (a) Paine, Tapan K.; Rentschler, E.; Weyhermüller, T.; Chaudhuri, P., *Eur J Inorg Chem.* **2003**, 2003 (17), 3167; (b) Paine, Tapan K.; Weyhermüller, T.; Bill, E.; Bothe, E.; Chaudhuri, P., *Eur J Inorg Chem.* **2003**, 2003 (24), 4299; (c) Weyhermüller, T.; Paine, T. K.; Bothe, E.; Bill, E.; Chaudhuri, P., *Inorg Chim Acta.* **2002**, 337 (0), 344.
32. (a) Paine, T. K.; Weyhermüller, T.; Slep, L. D.; Neese, F.; Bill, E.; Bothe, E.; Wieghardt, K.; Chaudhuri, P., *Inorg Chem.* **2004**, 43 (23), 7324; (b) Paine, T. K.; Weyhermüller, T.; Wieghardt, K.; Chaudhuri, P., *Inorg Chem.* **2002**, 41 (25), 6538; (c) Paine, T. K.; Weyhermüller, T.; Bothe, E.; Wieghardt, K.; Chaudhuri, P., *Dalton T.* **2003**, (15), 3136; (d) Paine, T. K.; Weyhermüller, T.; Wieghardt, K.; Chaudhuri, P., *Dalton T.* **2004**, (14), 2092.
33. Chaudhuri, P.; Hess, M.; Müller, J.; Hildenbrand, K.; Bill, E.; Weyhermüller, T.; Wieghardt, K., *Journal of the American Chemical Society.* **1999**, 121 (41), 9599.
34. (a) Baleizão, C.; Garcia, H., *Chem Rev.* **2006**, 106 (9), 3987; (b) Cozzi, P. G., *Chem Soc Rev.* **2004**, 33 (7), 410.

35. Chen, Y.-R.; Gunther, M. R.; Mason, R. P., *Journal of Biological Chemistry*. **1999**, *274* (6), 3308.
36. Whittaker, M. M.; Kersten, P. J.; Nakamura, N.; Sanders-Loehr, J.; Schweizer, E. S.; Whittaker, J. W., *Journal of Biological Chemistry*. **1996**, *271* (2), 681.
37. Stubbe, J.; van der Donk, W. A., *Chem Rev*. **1998**, *98* (2), 705.
38. (a) Bugg, T. D. H., *Tetrahedron*. **2003**, *59* (36), 7075; (b) Lipscomb, J. D., *Current Opinion in Structural Biology*. **2008**, *18* (6), 644.
39. Whittaker, J. W., *Chem Rev*. **2003**, *103* (6), 2347.
40. Jazdzewski, B. A.; Tolman, W. B., *Coordin Chem Rev*. **2000**, *200–202* (0), 633.
41. Que, L.; Ho, R. Y. N., *Chem Rev*. **1996**, *96* (7), 2607.
42. Bugg, T. D. H.; Ramaswamy, S., *Current Opinion in Chemical Biology*. **2008**, *12* (2), 134.
43. Whittaker, J. W.; Lipscomb, J. D., *Journal of Biological Chemistry*. **1984**, *259* (7), 4487.
44. Sato, N.; Uragami, Y.; Nishizaki, T.; Takahashi, Y.; Sasaki, G.; Sugimoto, K.; Nonaka, T.; Masai, E.; Fukuda, M.; Senda, T., *Journal of Molecular Biology*. **2002**, *321* (4), 621.
45. Vaillancourt, F. H.; Barbosa, C. J.; Spiro, T. G.; Bolin, J. T.; Blades, M. W.; Turner, R. F. B.; Eltis, L. D., *Journal of the American Chemical Society*. **2002**, *124* (11), 2485.
46. Velusamy, M.; Palaniandavar, M.; Gopalan, R. S.; Kulkarni, G. U., *Inorg Chem*. **2003**, *42* (25), 8283.

47. Jo, D.-H.; Que, J. L., *Angewandte Chemie International Edition*. **2000**, 39 (23), 4284.
48. Lyons, C. T.; Stack, T. D. P., *Coordin Chem Rev*. **2013**, 257 (2), 528.
49. Wachter, R. M.; Montague-Smith, M. P.; Branchaud, B. P., *Journal of the American Chemical Society*. **1997**, 119 (33), 7743.
50. (a) Chirik, P. J.; Wieghardt, K., *Science*. **2010**, 327 (5967), 794; (b) Praneeth, V. K. K.; Ringenberg, M. R.; Ward, T. R., *Angewandte Chemie International Edition*. **2012**, 51 (41), 10228.
51. Russell, S. K.; Lobkovsky, E.; Chirik, P. J., *Journal of the American Chemical Society*. **2011**, 133 (23), 8858.
52. (a) Bart, S. C.; Lobkovsky, E.; Chirik, P. J., *Journal of the American Chemical Society*. **2004**, 126 (42), 13794; (b) Bart, S. C.; Lobkovsky, E.; Bill, E.; Chirik, P. J., *Journal of the American Chemical Society*. **2006**, 128 (16), 5302.
53. (a) Trovitch, R. J.; Lobkovsky, E.; Bill, E.; Chirik, P. J., *Organometallics*. **2008**, 27 (7), 1470; (b) Aaron, M. T.; Atienza, C. C. H.; Weller, K. J.; Nye, S. A.; Lewis, K. M.; Delis, J. G. P.; Chirik, P. J., *Science*. **2012**, 335 (6068), 567.
54. Darmon, J. M.; Stieber, S. C. E.; Sylvester, K. T.; Fernández, I.; Lobkovsky, E.; Semproni, S. P.; Bill, E.; Wieghardt, K.; DeBeer, S.; Chirik, P. J., *Journal of the American Chemical Society*. **2012**, 134 (41), 17125.
55. Sylvester, K. T.; Chirik, P. J., *Journal of the American Chemical Society*. **2009**, 131 (25), 8772.
56. Small, B. L.; Brookhart, M.; Bennett, A. M. A., *Journal of the American Chemical Society*. **1998**, 120 (16), 4049.

57. Bouwkamp, M. W.; Bowman, A. C.; Lobkovsky, E.; Chirik, P. J., *Journal of the American Chemical Society*. **2006**, *128* (41), 13340.
58. (a) Smith, A. L.; Clapp, L. A.; Hardcastle, K. I.; Soper, J. D., *Polyhedron*. **2010**, *29* (1), 164; (b) Smith, A. L.; Hardcastle, K. I.; Soper, J. D., *Journal of the American Chemical Society*. **2010**, *132* (41), 14358.

Chapter 2:

First-row Transition Metal Complexes of Coordinatively Versatile Bis(amidophenyl)amine Ligands

Section 2-1. Introduction

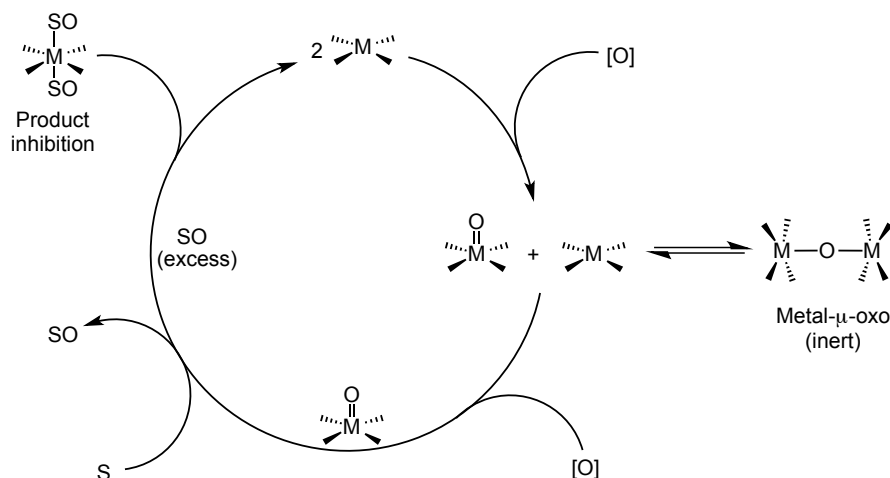
The development of ligand architectures capable of stabilizing transition metal complexes for homogeneous catalysts was first recognized as a vital area of research over 50 years ago. To this day, this area remains a very active field. A variety of novel ligands have been synthesized that can influence the primary coordination sphere around the central metal, leading to a wide variety of unprecedented reactivity. As the field of catalytic bond activation faces new challenges in the synthesis and functionalization of novel organic compounds, innovative ligand scaffolds must emerge to bolster the development of next-generation sustainable transition metal catalysts. Consequently, tridentate, trianionic redox-active pincer ligands have been viewed as versatile ligand scaffolds for carrying out a number of unprecedented transformations.

Tetradentate ligands were some of the earliest examples of supporting ligands employed in catalytic oxidation reactions. This ligand family includes salen, corrole, and porphyrin systems (Figure 2-1) that were highly sought after because their tetradentate coordination mode stabilized transition metal complexes as biomimetic models for cytochrome P450 in a wide spectrum of oxygen-atom insertion reactions.¹ In particular, these three ligand systems offered one major advantage versus other chelating ligands – at least one open coordination site when bound to a metal ion.



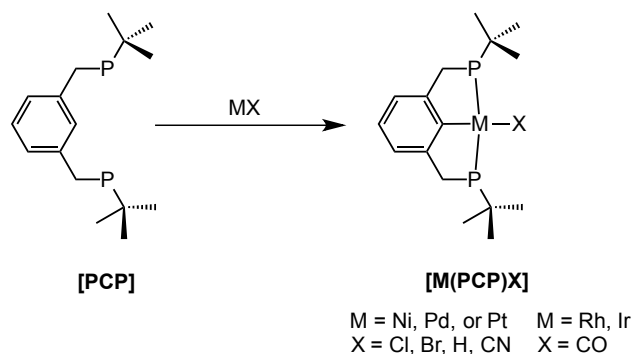
Figure 2-1. Early examples of metal complexes with tetradentate ligands that offered open coordination sites.

Additionally, these ligands systems have allowed for the generation of high-valent metal-oxo species, proposed to be the active intermediates in cytochrome P450 responsible for oxidizing C–H bonds.^{1b} The presence of an open coordination sphere at a metal center (M^{n+}) is advantageous, as an oxidant can coordinate the metal center and generate a reactive high-valent metal-oxo ($M^{(n+2)}=O$). Although several metal complexes of these ligands have shown to carry out successful oxidation reactions, a major drawback with the tetradentate salen, corrole, and porphyrin systems has been the reversible formation of an inert metal- μ -oxo species that constrains reactivity (Scheme 2-1).² In addition, irreversible coordination of the oxidized substrate (product inhibition) has also been observed as a common problem in these catalytic systems, making them highly inefficient, yielding low turnover numbers (TONs). The development of new ligand systems that prevent this phenomenon is a crucial area of pending investigation.^{1b}



Scheme 2-1. General reaction mechanism for substrate oxidation, reversible formation of an inert $\text{M-}\mu\text{-O-M}$ species, and product inhibition.^{1b}

Different strategies to circumvent the formation of the inert bridging metal- μ -oxo species and avoid substrate inhibition have emerged over the past decades. One of these strategies involves utilizing a tridentate pincer ligand scaffold in place of a tetradentate system. Initially reported by Moulton and Shaw in 1976, pincer ligands were originally described as tridentate meridionally-coordinating ligands that contained an anionic carbon between two pendant neutral donors (Scheme 2-2).³ Although incorporating a tridentate ligand system would open an additional coordination site and allow one more oxidized substrate (SO) to coordinate during oxidation reactions, the strong *trans* effect caused by the pincer carbon-metal bond would weaken ligation. For this same reason, if a bridging metal- μ -oxo intermediate were formed during the catalytic cycle, the weak metal-O bond would allow for the dissociation of such μ -oxo dimers.⁴ As a result, pincer metal complexes have been recently targeted as potential robust catalysts in oxidation reactions.⁵



Scheme 2-2. Tridentate pincer ligand **[PCP]**, (2,6-bis[(di-*tert*-butylphosphino)methyl]phenyl), and its metal complexes, **[M(PCP)X]**, reported by Moulton and Shaw.³

Throughout the years, pincer ligands have evolved to incorporate a variety of donor and central atoms and have diversified in their design to include various backbones (Figure 2-2).⁶ Given their wide diversification, tridentate pincer ligands have become popular as useful chelating ligands to support highly robust transition metal catalysts for various chemical transformations in catalysis and materials science.⁷ Pincer metal complexes are typically described as "robust" with "high thermal stability," making them ideal catalysts for a large spectrum of catalytic conditions. More importantly, these types of ligands have recently gained immense amount of attention in part due to their high modularity, which in effect, provides a wide scope of ligand platforms capable of tailoring the activity of metal centers towards the activation of strong unreactive bonds.⁸

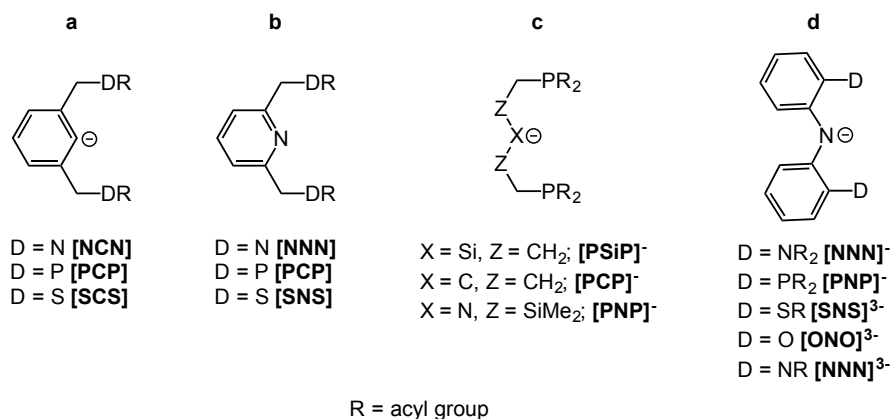
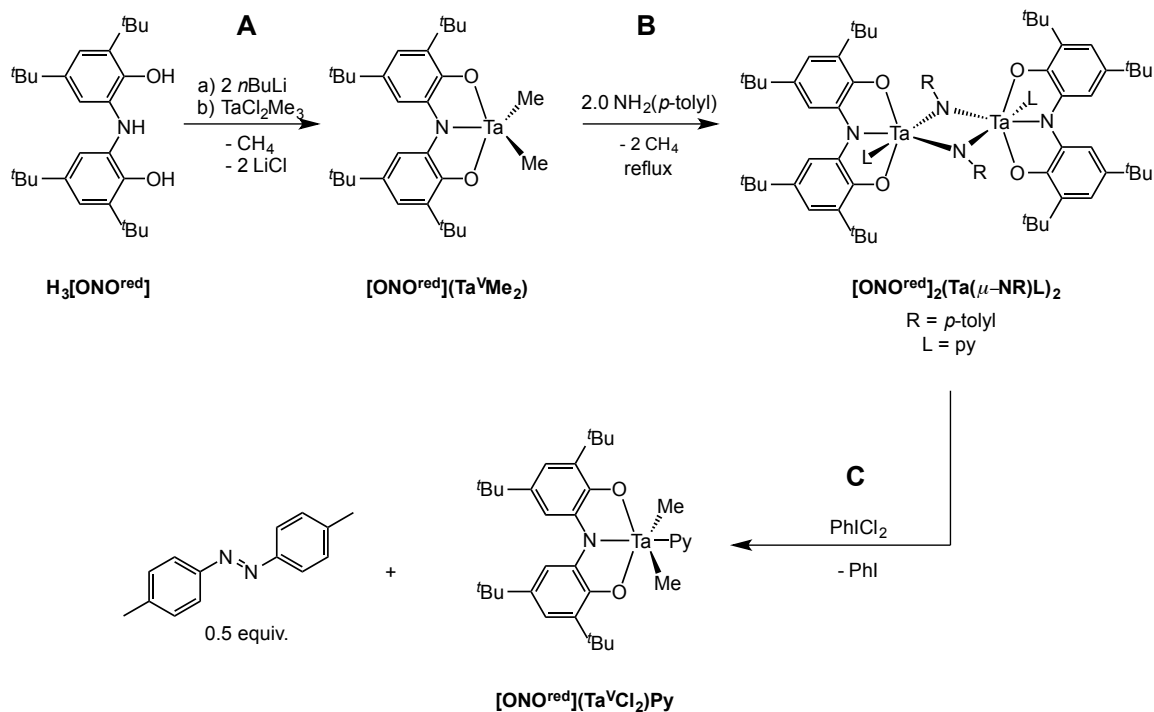


Figure 2-2. Selected tridentate pincer ligands.⁹

Of the ligands shown in Figure 2-2, perhaps the most recently targeted pincer ligands for catalysis have been the tridentate, trianionic [SNS]³⁻, [ONO]³⁻, and [NNN]³⁻ systems. Initially chosen for their high anionic charge (3-) to stabilize metal centers in high oxidation states (M^{n+} , $n^+ \geq 3^+$), these systems have recently been shown to access multiple oxidation states, shuttling between trianionic, dianionic, and monoanionic forms without changing their coordination with the metal center.⁹ More importantly, complexes of these ligands are capable of undergoing successive oxidation changes without a formal change in oxidation at the metal center, proving these systems to be, by definition, redox-active. As mentioned in Chapter 1, the incorporation of redox-active ligands has become a useful tactic for promoting multi-electron reactivity at first-row and redox-inactive metals.¹⁰

The tridentate, trianionic *N,N*-bis(3,5-di-*tert*-butyl-2phenosoxide)amide [ONO]³⁻ ligand was first reported by Girgis and Balch in 1975.¹¹ Recent work by Heyduk and co-workers has established the ligand redox-active and explored its use in multi-electron redox reactions. For example, this ligand was found to stabilize the five-coordinate,

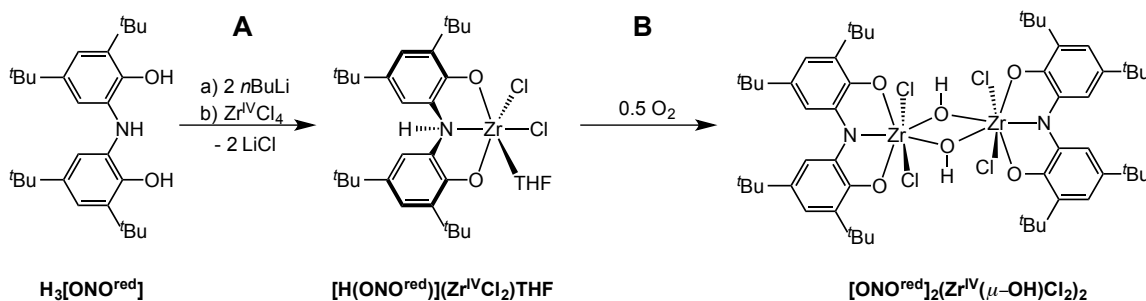
pseudo-octahedral Ta(V) complex, $[\text{ONO}^{\text{red}}](\text{Ta}^{\text{V}}\text{Me}_2)$ (Scheme 2-3, A).¹² Here, this complex reacts with two equivalents of $\text{NH}_2(p\text{-tolyl})$ to afford the seven-coordinate bis(μ -imido) tantalum dimer, $[\text{ONO}^{\text{red}}]_2(\text{Ta}(\mu\text{-NR})\text{L})_2$ (where R = *p*-tolyl, L = pyridine) (Scheme 2-3, B) with loss of two molecules of methane (CH_4). Upon treatment with two equivalents of iodobenzene dichloride (PhICl_2), this dimer was capable of releasing the corresponding aryl diazene (Scheme 2-3c). This work ultimately demonstrated that the tridentate, trianionic ligand $[\text{ONO}]^{3-}$ was capable of promoting multi-electron reactions at Ta(V) centers. In subsequent reports, this same system was shown to react with aryl azides and 1,2-diphenylhydrazines to obtain bis(triazenido) complexes of tantalum, a previously unprecedented reaction.¹³ Although attempts to expand similar Ta(V)[ONO] systems in catalytic carbene transfer reactions using diazoalkanes have been carried out, it was observed that adding excess diazoalkane simply resulted in low product yields and modest turnover numbers ($\text{TON} = 30$).¹⁴



Scheme 2-3. **A**) Metalation of $\text{H}_3[\text{ONO}^{\text{red}}]$ with Ta(V), **B**) generation of a bis(μ -imido) tantalum dimer and **C**) its reactivity with PhICl_2 in the formation of diazene product (scheme adapted from reference).¹²

Trianionic redox-active $[\text{ONO}]^{3-}$ pincer ligands have also found applicability in dioxygen activation. Inspired by the work of Abu-Omar and co-workers,¹⁵ Heyduk and co-workers set out to activate dioxygen using Zr(IV) complexes supported by the $[\text{ONO}]^{3-}$ ligand framework. In a recent report, it was observed that the $[\text{ONO}]^{3-}$ ligand scaffold was capable of promoting dioxygen activation at Zr(IV) centers.¹⁶ In this work, the $\text{H}_3[\text{ONO}]$ ligand was selectively deprotonated with two equivalents of $n\text{BuLi}$ and subsequently treated with one equivalent of $\text{Zr}^{\text{IV}}\text{Cl}_4$ to generate the six-coordinate Zr(IV) complex, $[\text{H}(\text{ONO}^{\text{red}})](\text{Zr}^{\text{IV}}\text{Cl}_2(\text{THF}))$. The complex was capable of reducing dioxygen to form the Zr(IV) bis- μ -hydroxo dimer, $[\text{ONO}^{\text{red}}]_2(\text{Zr}^{\text{IV}}(\mu\text{-OH})\text{Cl}_2)_2$ (Scheme 2-4). As a d¹⁰

metal, Zr(IV) typically would not be expected to participate in the two-electron activation of dioxygen, however in this case, the [ONO] ligand served as a reservoir for both protons and electrons, allowing this transformation to occur. Additionally, recent structural and spectroscopic studies carried out on aluminum(III)¹⁷ and iron(III)¹⁸ complexes of the [ONO] ligand system suggest the ability of these ligands to carry out unexpected multi-electron transformations at metal centers with limited redox capabilities.

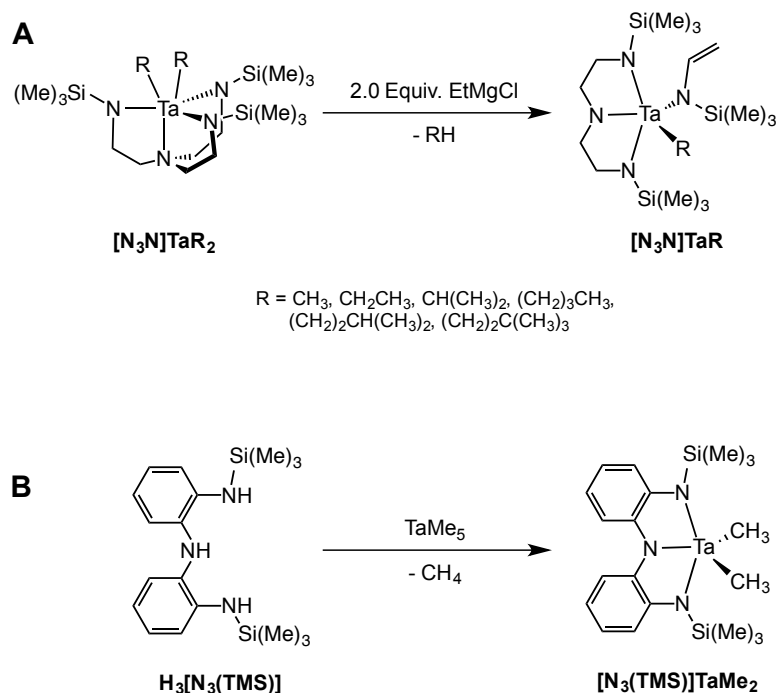


Scheme 2-4. A) Metalation of $\text{H}_3[\text{ONO}^{\text{red}}]$ with Zr(IV) and B) O_2 reduction by its complex $[\text{ONO}^{\text{red}}](\text{Zr}^{\text{IV}}\text{Cl}_2)\text{THF}$ to form a Zr(IV) bis- μ -hydroxo dimer.¹⁶

Tridentate nitrogen-donor redox-active pincer ligands (NNN) can stabilize transition metal complexes with unique structural, spectroscopic, and reactivity profiles. One of the best known neutral tridentate NNN redox-active ligand systems is the bis(imino)-pyridine (PDI) framework shown in Figure 2-3a.¹⁹ First reported by Wieghardt and co-workers, the coordination and redox-active nature of this ligand has been widely investigated.²⁰ Two distinctive features of this ligand include its electronic flexibility and variety of accessible redox states. These features enable coordinated metal centers to

readily adjust to the ligand's imposed environment. Numerous systems have illustrated the effectiveness of the redox-active pincer NNN ligand.

The coordination chemistry of trianionic, tridentate redox-active $[\text{NNN}]^{3-}$ pincer ligands with various metal ions has also recently been reported. Schrock and co-workers, reported the five-coordinate Ta(V) complex, $[\text{N}_3\text{N}]\text{TaR}$ (Scheme 2-5, A), which was the result of an unexpected modification of their original tetradentate tripodal tris(amido)amine ligand $[\text{N}_3\text{N}]^{3-}$.²¹ When $[\text{N}_3\text{N}]\text{TaR}$ was treated with a Grignard reagent, the six-coordinate complex $[\text{N}_3\text{N}]\text{TaR}_2$ decomposed via C–N bond cleavage, yielding the trianionic $[\text{NNN}]^{3-}$ pincer-type five-coordinate complex $[\text{N}_3\text{N}]\text{TaR}$ (Scheme 2-5, A). These results led to the synthesis and characterization of the first trianionic tris-amido ligands of this kind.

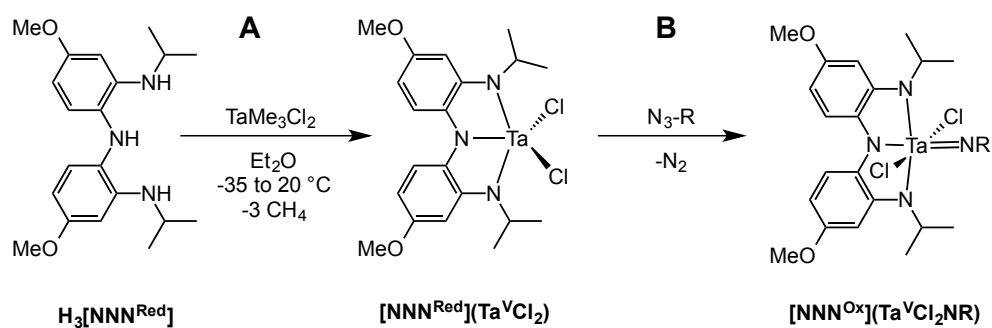


Scheme 2-5. **A)** Degradation of a tripodal ligand to form a pincer-ligated Ta(V) complex and **B)** incorporation of phenyl backbones to the tridentate trianionic pincer ligand.²¹

One of Schrock's ligand design strategies that impacted the field of trianionic, tridentate redox-active ligands ($[NNN]^{3-}$) was the incorporation of phenyl rings in the backbone of a tris-amido ligand.²² This ligand was believed to be more rigid than its corresponding diethylenetriamine analogue, capable of stabilizing robust catalysts for group transfer reactions. The metalation of the tridentate bis(2-aminophenyl)amine ligand $H_3[N_3(TMS)]$ with Ta(V) is shown in Scheme 2-5A.²²

In 2009, Heyduk and co-workers reported a Ta(V) complex supported by the bis(2-isopropyl-4-methoxyphenyl)amine ligand, $H_3[NNN^{red}]$.²³ The Ta(V) complex, $[NNN^{red}](Ta^VCl_2)$ reacts with organic azides to form the corresponding Ta(V)-nitrene ($Ta=NR$) species, $[NNN^{ox}](Ta^VCl_2R)$ (Scheme 2-6). Here, the electrons are sequestered from

the ligand backbone and thus used in the bond forming reaction. These observations were supported by the isolation of the $\text{Ta}^{\text{V}}=\text{NR}$ species in which the supporting ligand was described as a fully oxidized quinone. Recently it has been reported that this ligand system can promote catalytic nitrene transfer reactions at $\text{Zr}(\text{IV})$ centers.²⁴



Scheme 2-6. A) Metalation of the tridentate ligand $\text{H}_3[\text{NNN}^{\text{Red}}]$ with Ta(V) and B) reaction of its Ta(V) complex with an aryl azide to yield a Ta(V)-nitrene species.²³

Section 2-2. Background and Significance

Increased emphasis has been placed on using sustainable transition metal complexes as catalysts for oxidation reactions. Moreover, catalysts capable of utilizing dioxygen as a terminal oxidant would represent significant advancement in this research area. First-row transition metal complexes that incorporate redox-active ligands for aerobic oxidation reactions can address these issues. In spite of the numerous reports of tridentate, trianionic $[\text{ONO}]^{3-}$ and $[\text{NNN}]^{3-}$ redox-active pincer ligands and their metal complexes, there are relatively few studies involving late first-row transition metal complexes. More specifically, tridentate, trianionic NNN redox-active ligands are significantly under-developed in the area of aerobic oxidation reactions. The paucity of well-defined trianionic NNN redox-active ligands in aerobic oxidation reactions inspired the us to investigate a ligand system that would facilitate aerobic oxidation reactions at late, first-row transition ions.

Our group has developed a family of robust, NNN pincer-type ligands capable of acting as both dianionic or trianionic and that incorporate the *o*-phenylenediamine ligand backbone as well as carboxamide (amide = $[\text{RNHC}(\text{O})\text{R}']$) functional groups. Carboxamide functional groups are highly attractive in designing ligands for oxidation catalysis for a number of reasons: (1) acyl (R) substituents on amide-based ligand frameworks can be varied to regulate both electronic and steric properties of the resulting transition metal complexes;²⁵ (2) the strong sigma-donor capacity of the carboxamide functionality allows for the stabilization of metal ions in high oxidation states;²⁶ and (3) carboxamide-based ligands are well known to be robust under oxidizing conditions.²⁶

The ligand design approach was inspired by the highly-rigid tripodal tetradentate, tris(amidate) ligand ($[N(o\text{-PhNC(O)R})_3]^{3-}$) reported by our group,²⁷ and redesigning it into a tridentate, trianionic redox-active bis(amidate) ligand platform ($[NH(o\text{-PhNC(O)R})_2]^{3-}$).

In an effort to understand the ability of the bis(phenylamido)amine ligand system to promote catalytic aerobic oxidation reactions at late first-row metals, we sought to first explore the coordination properties of this ligand. A handful of synthetic systems have shown that performing structural and electronic modifications on ligands can control the redox processes of the resulting metal complex.²⁸ The ability to tailor the steric and electronic effects within the ligand design allows for the utilization of its metal complexes for a wide range of organic transformations.

It was envisaged that bis(phenylamido)amine ligands of this type would engender stable complexes with first-row transition metals as potential homogeneous catalysts for atom-transfer reactions. To address this issue, a series of cobalt(II) complexes with different bis(amidophenyl)amine ligands $NH(o\text{-PhNHC(O)}^R)_2$ ((H_3L^R) $R = \text{'Bu, Ph, Ad, CF}_3$) were synthesized (Figure 2-3). The ligands differ in both steric and electronic character on the carboxamide arms of the ligands and allowed for the examination of how these modifications correlate to the formation of mononuclear versus dinuclear cobalt(II) systems. Our findings illustrated that the electrochemical properties of these cobalt(II) complexes can be tuned predictably through modulation of the ligand. Additionally, a family of dinuclear complexes containing late first-row transition metal ions (i.e., Fe^{II} , Ni^{II} , Cu^{II} , and Zn^{II}) were synthesized using the isopropyl-substituted ligand, $NH(o\text{-PhNHC(O)}^{iPr})_2$ (H_3L^{iPr}).

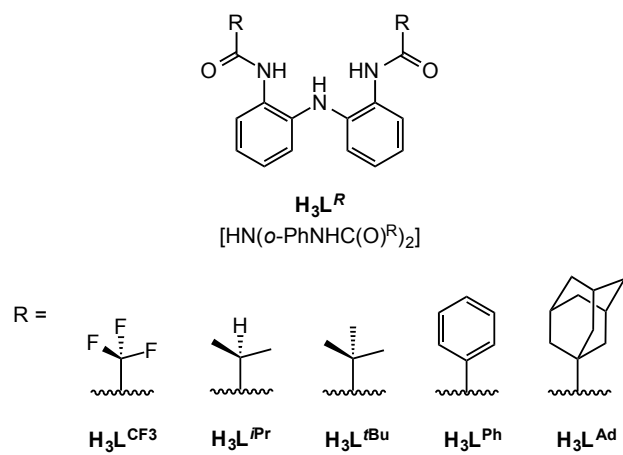
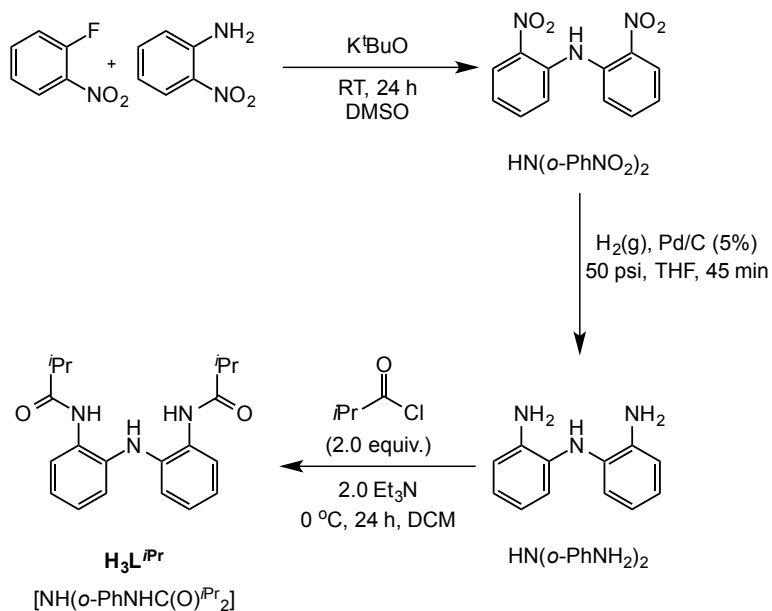


Figure 2-3. Ligands used in this study.

Section 2-3. Results

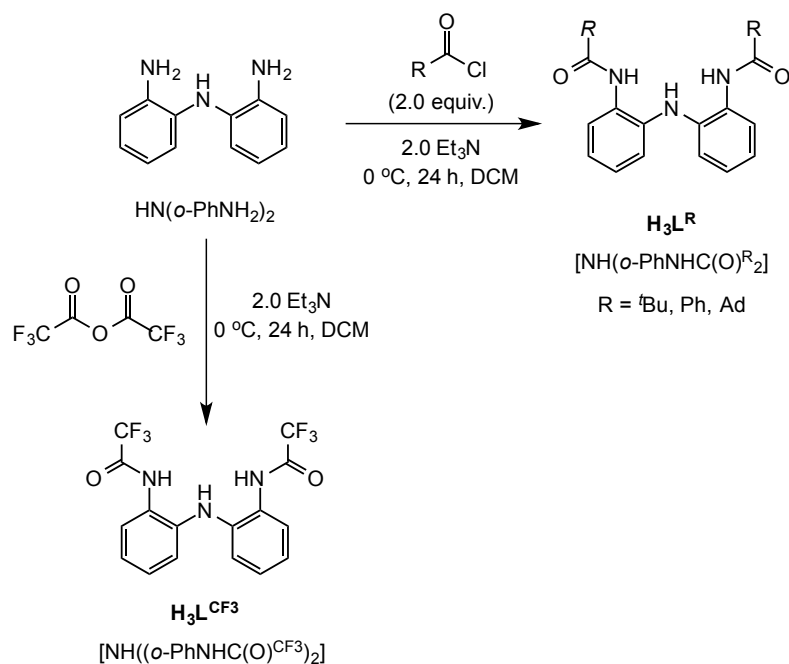
Section 2-3-1. Synthesis of Bis(amidophenyl)amine Ligands

The three-step synthesis of the coordinatively versatile tridentate bis(2-isobutyrylamidophenyl)amine ligand scaffold, $\text{NH}(o\text{-PhNHC(O)}^i\text{Pr})_2$ ($\text{H}_3\text{L}^{i\text{Pr}}$), was previously reported by our group (Scheme 2-7).²⁹ A nucleophilic aromatic substitution reaction was carried out using 1-fluoro-2-nitrobenzene and 2-nitroaniline to obtain $\text{HN}(o\text{-PhNO}_2)_2$. Catalytic hydrogenation using palladium-on-charcoal (Pd/C, 5%) of $\text{HN}(o\text{-PhNO}_2)_2$ yields bis(2-aminophenyl)amine $\text{HN}(o\text{-PhNH}_2)_2$.³⁰ Subsequent acylation of $\text{HN}(o\text{-PhNH}_2)_2$ with isobutyryl chloride yields the bis(2-isobutyrylamidophenyl)amine ligand scaffold, $\text{NH}(o\text{-PhNHC(O)}^i\text{Pr})_2$ ($\text{H}_3\text{L}^{i\text{Pr}}$) as a white, air-stable microcrystalline powder in high yield (85 %).



Scheme 2-7. Synthetic route for the preparation of $\text{NH}(o\text{-PhNHC(O)}^i\text{Pr})_2$ ($\text{H}_3\text{L}^{i\text{Pr}}$).²⁹

A key synthetic advantage of the bis(amidophenyl)amine ligand design is its high modularity. It was speculated that diversifying the acyl chloride reagent would allow for the straightforward synthesis of new ligand derivatives, hosting a variety of electronic and steric modifications. In order to investigate the electronic and steric properties of the bis(amidophenyl)amine ligand platform, a family of $\text{NH}(o\text{-PhNHC(O)R})_2$ ($\text{H}_3\text{L}^{\text{R}}$) ligands were prepared (where $\text{R} = \text{CF}_3$, $t\text{Bu}$, Ph and adamantyl). Using a modified procedure previously reported by our laboratory to synthesize $\text{H}_3\text{L}^{i\text{Pr}}$, the bis(2-aminophenyl)amine $\text{HN}(o\text{-PhNH}_2)_2$, was acylated using two equivalents of pivaloyl chloride, benzoyl chloride, or 1-adamantanecarbonyl chloride in the presence of two equivalents triethylamine to generate the corresponding *tert*-butyl, phenyl, and adamantane-substituted ligands, respectively. The trifluoromethyl substituted ligand, $\text{H}_3\text{L}^{\text{CF}_3}$, was generated by treating the parent amine, $\text{HN}(o\text{-PhNH}_2)_2$, with one equivalent of trifluoroacetic anhydride in the presence of triethylamine under similar reaction conditions. Using the synthetic route outlined in Scheme 2-8, these ligands were isolated in multigram quantities and in good yield (70 – 80%). In contrast to related NNN bis(amidophenyl)amine pincer ligand frameworks reported by Heyduk and co-workers,^{23, 31} the ligand scaffolds presented in this work are air-stable, easily-handled microcrystalline solids. We reason that this oxidizing stability is owed to the incorporation of the amidate group functionality, moieties are known to be highly stable under oxidizing conditions.²⁶



Scheme 2-8. Synthesis of $\text{NH}(\text{o-PhNHC}(\text{O})\text{R})_2$ ligands ($\text{H}_3\text{L}^{\text{R}}$, where $\text{R} = \text{'Bu, Ph, Adamantyl and CF}_3$).

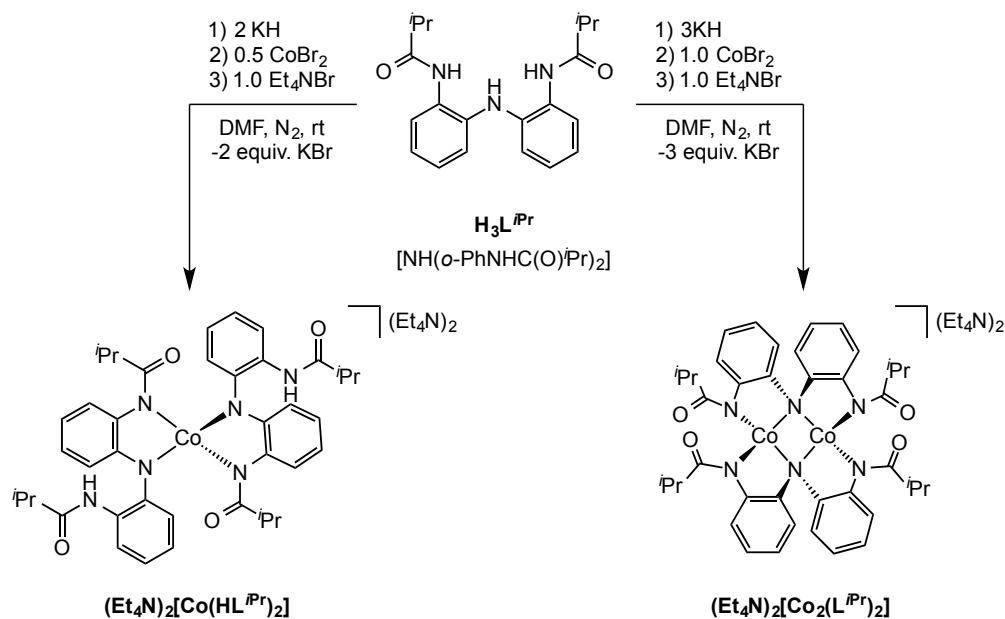
The bis(amidophenyl)amine ($\text{H}_3\text{L}^{\text{R}}$) ligands were characterized by ^1H and ^{13}C NMR spectroscopy, solid-state FTIR spectroscopy, and mass spectrometry. ^1H and ^{13}C NMR analyses confirmed the solution-state, two-fold symmetry of these ligands. In their mass spectrum, the presence of the expected parent peaks corresponding to the appropriate mass-to-charge (m/z) ratio of each ligand confirmed the structural assignments. The N-H stretching frequencies observed in the solid-state FTIR are consistent with the assignment of the $\nu(\text{NH})_{\text{Amine}}$ and $\nu(\text{NH})_{\text{Amide}}$ stretches of each corresponding ligand. This data are summarized in Table 2-1.

Table 2-1. Solid-state FTIR and mass spectrometry data of synthesized ligands H_3L^R ($R = tBu, Ph, adamantyl, \text{and } CF_3$).

Characterization Details of Ligands				
	FTIR (KBr, cm^{-1})			ESI-MS
	$\nu(NH)_{Amine}$	$\nu(NH)_{Amide}$	$\nu(C=O)$	$m/z [H^+ + L]$
H_3L^{tBu}	3343	3428	1685	368.2
H_3L^{Ph}	3386	3292	1658	408.4
H_3L^{Ad}	3410	3318	1655	524.3
$H_3L^{CF_3}$	3298	3298	1702	392.1

Section 2-3-2. Synthesis of Metal Complexes with $NH(o\text{-}PhNHC(O)R)_2$ Ligands

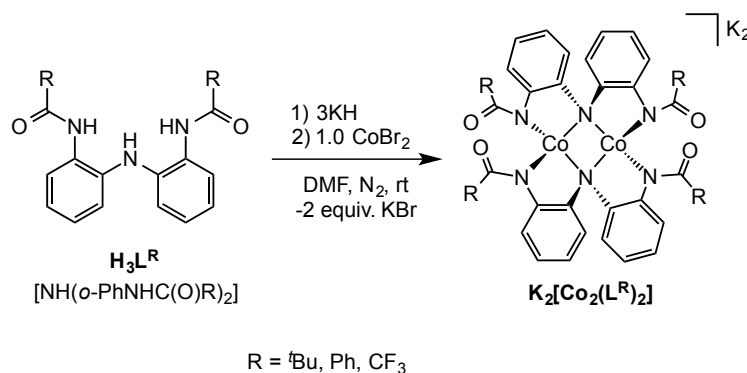
Our group has previously reported on the metalation of the H_3L^{iPr} ligand with cobalt(II).²⁹ In this work, it was observed that the deprotonation state of the ligand framework dictates the nuclearity of the resulting cobalt(II) complex. As illustrated in Scheme 2-9, the deprotonation of H_3L^{iPr} in dimethylformamide (DMF) with two equivalents of potassium hydride (KH) followed by transmetalation with 0.5 equivalents of cobalt(II) bromide ($CoBr_2$) and *in situ* salt metathesis with tetraethylammonium bromide (Et_4NBr) results in the formation of an isolable four-coordinate dianionic cobalt(II) complex in a 2:1 ligand to metal ratio. In contrast, treatment of H_3L^{iPr} in DMF with three equivalents of KH followed by transmetalation with one equivalent of $CoBr_2$ and *in situ* salt metathesis with Et_4NBr results in the formation of a four-coordinate dianionic cobalt(II) dinuclear complex in a 2:2 ligand to metal ratio, whereby two deprotonated amido donors and the two cobalt ions constitute a Co_2N_2 diamond core structure.



Scheme 2-9. Metalation strategy of $\text{H}_3\text{L}^{i\text{Pr}}$ with cobalt(II) ions to form the mononuclear cobalt(II) complex, $(\text{Et}_4\text{N})_2[\text{Co}(\text{HL}^{i\text{Pr}})_2]$, and dinuclear cobalt(II) complex, $(\text{Et}_4\text{N})_2[\text{Co}_2(\text{L}^{i\text{Pr}})_2]$.²⁹

In collaboration with Dr. Savita Sharma, a postdoctoral fellow in our laboratory credited with initiating this work, efforts to metalate the bis(amidophenyl)amine ligands $\text{NH}(o\text{-PhNHC}(\text{O})^{\text{R}})_2$ ($\text{H}_3\text{L}^{\text{R}}$, where $\text{R} = \text{CF}_3, \text{tBu}, \text{Ph}$ and adamantyl), with cobalt(II) ions were carried out. Using the same metalation strategy as with $\text{H}_3\text{L}^{i\text{Pr}}$, we attempted to synthesize a family of cobalt(II) complexes supported by these ligands. Our synthetic studies began with the syntheses of the dianionic cobalt(II) dinuclear complexes analogous to $(\text{Et}_4\text{N})_2[\text{Co}_2(\text{L}^{i\text{Pr}})_2]$. Addition of three equivalents of KH to a DMF solution of $\text{H}_3\text{L}^{\text{R}}$, followed by transmetalation with one equivalent of CoBr_2 afforded the corresponding dianionic cobalt(II) dinuclear complexes $\text{K}_2[\text{Co}_2(\text{L}^{\text{Ph}})_2]$, $\text{K}_2[\text{Co}_2(\text{L}^{\text{CF}_3})_2]$, and $\text{K}_2[\text{Co}_2(\text{L}^{\text{tBu}})_2]$ (Scheme 2-10). Subsequent *in*

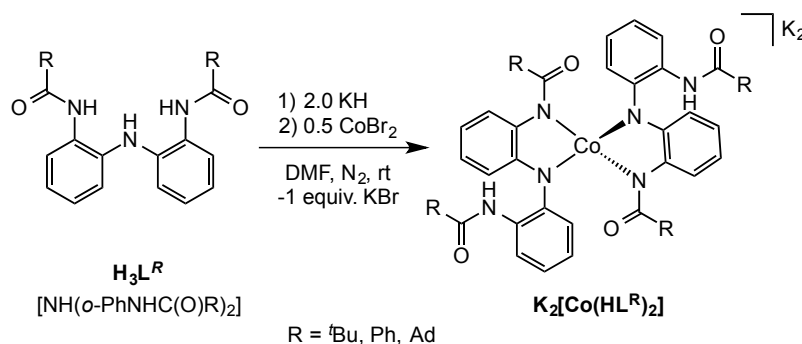
situ salt metatheses with Et_4NBr for counterion exchange afforded salts of $(\text{Et}_4\text{N})_2[\text{Co}_2(\text{L}^{\text{Ph}})_2]$, and $(\text{Et}_4\text{N})_2[\text{Co}_2(\text{L}^{\text{CF}_3})_2]$, where $\text{K}_2[\text{Co}_2(\text{L}^{\text{tBu}})_2]$ was isolated as the dipotassium salt. The complexes $(\text{Et}_4\text{N})_2[\text{Co}_2(\text{L}^{\text{Ph}})_2]$ and $\text{K}_2[\text{Co}_2(\text{L}^{\text{tBu}})_2]$ were isolated as dark green blocks by recrystallization from diffusion of diethyl ether into an acetonitrile (CH_3CN) solution of the product in 75 % and 65 % yield, respectively. The complex $(\text{Et}_4\text{N})_2[\text{Co}_2(\text{L}^{\text{CF}_3})_2]$ was isolated as dark teal blocks by recrystallization from diffusion of diethyl ether into a CH_3CN solution of the product in 70 % yield. Attempts to generate and isolate the dinuclear cobalt(II) adamantyl analogue, $\text{K}_2[\text{Co}_2(\text{L}^{\text{Ad}})_2]$, were unsuccessful. The formation of the dinuclear complexes was confirmed by the disappearance of the N-H stretching frequencies exhibited by the free ligands and a shift in the C=O stretching frequencies observed in the solid-state FTIR spectrum of each complex.



Scheme 2-10. Synthesis of dinuclear cobalt(II) complexes $\text{K}_2[\text{Co}_2(\text{L}^{\text{tBu}})_2]$, $\text{K}_2[\text{Co}_2(\text{L}^{\text{Ph}})_2]$, and $\text{K}_2[\text{Co}_2(\text{L}^{\text{CF}_3})_2]$ (counterion exchange not shown).

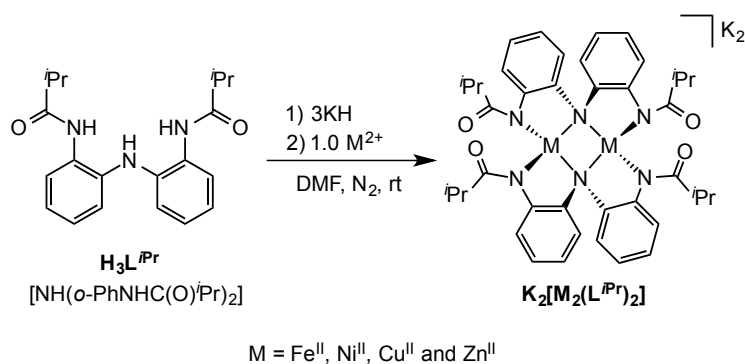
Similarly, the mononuclear cobalt(II) analogues of $(\text{Et}_4\text{N})_2[\text{Co}(\text{HL}^{\text{iPr}})_2]$, were synthesized using ligands $\text{H}_3\text{L}^{\text{iBu}}$, $\text{H}_3\text{L}^{\text{Ph}}$, $\text{H}_3\text{L}^{\text{Ad}}$ and $\text{H}_3\text{L}^{\text{CF}_3}$. Addition of two equivalents of KH to a DMF solution of $\text{H}_3\text{L}^{\text{R}}$ ($\text{R} = \text{iBu}, \text{Ph}$ and adamantyl) followed by transmetalation with 0.5 equivalents of CoBr_2 afforded the corresponding dianionic cobalt(II) mononuclear complexes $\text{K}_2[\text{Co}(\text{HL}^{\text{iBu}})_2]$, $\text{K}_2[\text{Co}(\text{HL}^{\text{Ph}})_2]$, and $\text{K}_2[\text{Co}(\text{HL}^{\text{Ad}})_2]$ (Scheme 2-11). Subsequent *in situ* salt metathesis with Et_4NBr afforded the salt of $(\text{Et}_4\text{N})_2[\text{Co}(\text{HL}^{\text{Ad}})_2]$. *In situ* salt metathesis with tetraphenylphosphonium bromide (PPh_4Br) afforded the $(\text{PPh}_4)_2[\text{Co}(\text{HL}^{\text{iBu}})_2]$ complex. The complex $\text{K}_2[\text{Co}(\text{HL}^{\text{Ph}})_2]$ was isolated as a potassium salt. These mononuclear cobalt(II) complexes, were isolated as deep red blocks by recrystallization from diffusion of diethyl ether into an acetonitrile (CH_3CN) solution of the product in 70 %, 55 %, and 75 % yield, respectively. Efforts to generate the trifluoromethyl-substituted mononuclear cobalt(II) complex, $(\text{Et}_4\text{N})_2[\text{Co}(\text{HL}^{\text{CF}_3})_2]$, however, were unsuccessful. In this case, addition of two equivalents of KH to a DMF solution of $\text{H}_3\text{L}^{\text{CF}_3}$ followed by the transmetalation with 0.5 equivalents of CoBr_2 afforded a dark teal solution. Absence of the N-H stretching frequency in the solid-state FTIR spectrum and ^1H NMR of the solid recovered from this reaction proved to not be $(\text{Et}_4\text{N})_2[\text{Co}(\text{HL}^{\text{CF}_3})_2]$, but instead the dinuclear complex $(\text{Et}_4\text{N})_2[\text{Co}_2(\text{L}^{\text{CF}_3})_2]$.

To distinguish between the formation of dinuclear versus mononuclear cobalt(II) complexes of these ligands solid-state FT-IR spectroscopy was utilized. The formation of mononuclear complexes was readily confirmed by the disappearance of the N-H stretching frequencies observed for the free ligands, a shift in the C=O stretching frequencies, and a diagnostic $\text{N-H}_{\text{Amide}}$ stretching frequency corresponding to the uncoordinated (or dangling) carboxamide moiety of each ligand around the cobalt(II) center.



Scheme 2-11. Synthesis of cobalt(II) mononuclear complexes $\text{K}_2[\text{Co}(\text{HL}^{\text{tBu}})_2]$, $\text{K}_2[\text{Co}(\text{HL}^{\text{Ph}})_2]$, and $\text{K}_2[\text{Co}(\text{HL}^{\text{Ad}})_2]$ (counter ion exchange for each complex not shown).

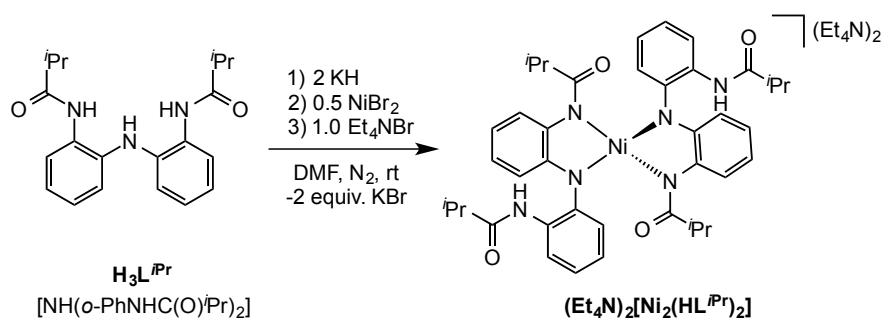
With these results for the cobalt(II) complexes at hand, it was envisaged that bis(amidophenyl)amine ligands of this type could engender stable mononuclear and dinuclear complexes with other late first-row transition metals (e.g. Fe^{II} , Ni^{II} , Cu^{II} and Zn^{II}). Developing a synthetic route for such complexes would afford us the opportunity to prepare a wide scope of mono- and bimetallic complexes as potential catalysts for a variety of multi-electron processes. Initially, the syntheses of dinuclear first-row transition metal (Fe^{II} , Ni^{II} , Cu^{II} and Zn^{II}) complexes supported by $\text{H}_3\text{L}^{\text{iPr}}$ were pursued. Following the same approach for generating the dinuclear cobalt(II) complex $(\text{Et}_4\text{N})_2[\text{Co}_2(\text{L}^{\text{iPr}})_2]$ as a standard metalation procedure, reaction of a DMF solution of $\text{H}_3\text{L}^{\text{iPr}}$ with three equivalents of KH and subsequent addition of a corresponding divalent metal salt in a 3:1 (ligand to metal) molar ratio at ambient temperature afforded the complexes $\text{K}_2[\text{M}_2(\text{L}^{\text{iPr}})_2]$ ($\text{M} = \text{Fe}^{\text{II}}$, Ni^{II} , Cu^{II} and Zn^{II}) (Scheme 2-12). *In situ* salt metathesis with PPh_4Br afforded the Fe^{II} and Cu^{II} complexes, $(\text{PPh}_4)_2[\text{Fe}_2(\text{L}^{\text{iPr}})_2]$ and $(\text{PPh}_4)_2[\text{Cu}_2(\text{L}^{\text{iPr}})_2]$, respectively. The Ni^{II} and Zn^{II} complexes, $(\text{Et}_4\text{N})_2[\text{Ni}_2(\text{L}^{\text{iPr}})_2]$ and $(\text{Et}_4\text{N})_2[\text{Zn}_2(\text{L}^{\text{iPr}})_2]$, were isolated as Et_4N^+ salts after *in situ* salt metathesis with Et_4NBr .



Scheme 2-12. Synthesis of dinuclear complexes $K_2[Fe_2(L^{iPr})_2]$, $K_2[Ni_2(L^{iPr})_2]$, $K_2[Cu_2(L^{iPr})_2]$, and $K_2[Zn_2(L^{iPr})_2]$ (counterion exchange with each complex is not shown).

Attempts to synthesize the mononuclear Fe^{II}, Ni^{II}, Cu^{II} and Zn^{II} complexes of H₃L^{iPr} proved to be a challenge. Reacting a DMF solution of H₃L^{iPr} with two equivalents of KH and subsequent addition of 0.5 equivalents of a corresponding divalent metal salt at ambient temperature did not afford the desired mononuclear complexes $K_2[M(HL^{iPr})_2]$ (M = Fe^{II}, Cu^{II} and Zn^{II}). This conclusion was supported by the absence of the diagnostic N-H_{Amide} stretching frequency, which would correspond to the uncoordinated carboxamide moiety of each ligand around the metal(II) center in the solid-state FTIR spectrum of each product. Using the synthetic strategy outlined in Scheme 2-13, only the monomeric nickel(II) complex, (Et₄N)₂[Ni(HL^{iPr})₂], was attained. In its solid-state FTIR spectrum, (Et₄N)₂[Ni(HL^{iPr})₂] exhibits a diagnostic N-H_{Amide} stretching frequency at 3392 cm⁻¹, which is very similar to that exhibited by the mononuclear cobalt(II) complexes $K_2[Co(HL^R)_2]$. However, X-ray diffraction-quality crystals could not be obtained for further characterization. After several days in solution, (Et₄N)₂[Ni(HL^{iPr})₂] converted into the dimer complex (Et₄N)₂[Ni₂(L^{iPr})₂], as confirmed by ¹H NMR and UV-visible absorption spectroscopy analysis. The dimerization of

$(\text{Et}_4\text{N})_2[\text{Ni}(\text{HL}^{\text{iPr}})_2]$ into $(\text{Et}_4\text{N})_2[\text{Ni}_2(\text{L}^{\text{iPr}})_2]$ could explain the aforementioned lack of crystals suitable for X-ray diffraction.



Scheme 2-13. Synthesis of mononuclear nickel(II) complex $(\text{Et}_4\text{N})_2[\text{Ni}_2(\text{L}^{\text{iPr}})_2]$.

Section 2-3-3. X-ray Crystallographic Studies

The molecular structures of the dinuclear cobalt(II) complexes were characterized by X-ray diffraction methods. Selected bond lengths and bond angles are given in Table 2-2 and representative thermal ellipsoid diagrams of $(\text{Et}_4\text{N})_2[\text{Co}_2(\text{L}^{\text{tBu}})_2]$, $\text{K}_2[\text{Co}_2(\text{L}^{\text{tBu}})_2]$, $(\text{Et}_4\text{N})_2[\text{Co}_2(\text{L}^{\text{Ph}})_2]$ and $(\text{Et}_4\text{N})_2[\text{Co}_2(\text{L}^{\text{CF}_3})_2]$ are shown in Figure 2-4.

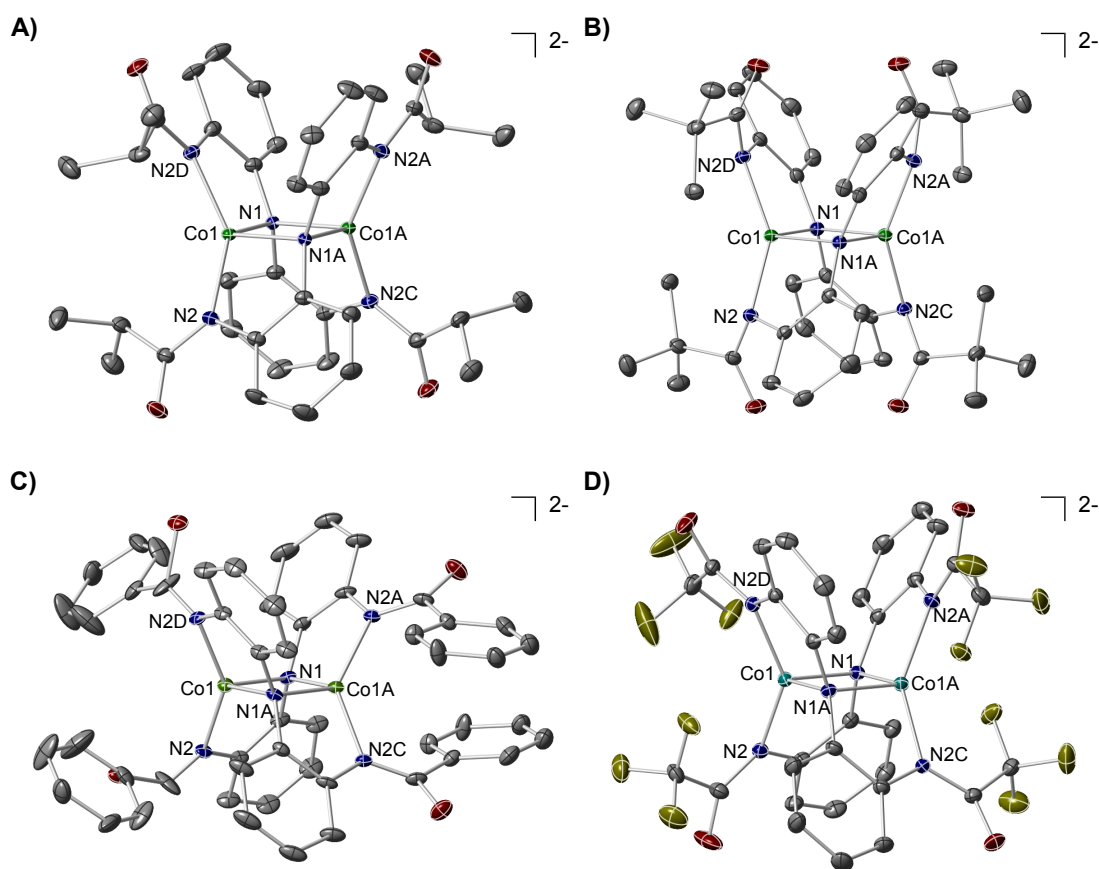


Figure 2-4. Solid-state structures of **A)** $(\text{Et}_4\text{N})_2[\text{Co}_2(\text{L}^{\text{iPr}})_2]$,²⁹ **B)** $\text{K}_2[\text{Co}_2(\text{L}^{\text{tBu}})_2]$, **C)** $(\text{Et}_4\text{N})_2[\text{Co}_2(\text{L}^{\text{Ph}})_2]$ and **D)** $(\text{Et}_4\text{N})_2[\text{Co}_2(\text{L}^{\text{CF}_3})_2]$. Thermal ellipsoids drawn at 40% probability. Hydrogen atoms and counterions have been omitted for clarity.

Table 2-2. Selected bond lengths (Å) and angles (°) for $(\text{Et}_4\text{N})_2[\text{Co}_2(\text{L}^{\text{iPr}})_2]$,²⁹ $\text{K}_2[\text{Co}_2(\text{L}^{\text{tBu}})_2]$, $(\text{Et}_4\text{N})_2[\text{Co}_2(\text{L}^{\text{Ph}})_2]$, and $(\text{Et}_4\text{N})_2[\text{Co}_2(\text{L}^{\text{CF}_3})_2]$. Torsion angle is defined as $\text{N}_{\text{amido}}-\text{Co}-\text{N}_{\text{amido}}-\text{Co}$.

Bond Lengths (Å) and Angles (°)				
R =	ⁱ Pr	^t Bu	Ph	CF ₃
Co···Co	2.6807(9)	2.6586(7)	2.666(4)	2.631(6)
Co–N _{Amidate}	1.975(2)	1.9639(14)	1.963(9)	1.986(3)/1.982(3)
Co–N _{Amido}	2.040(2)	2.1123(16)	2.0407(1)	2.038(3)/2.043(3)
N _{Amido} –Co–N _{Amido}	97.84(11)	102.00(7)	97.50(6)	100.13(11)
N _{Amidat} –Co–N _{Amidate}	143.85(14)	146.66(8)	141.8(6)	141.55(12)
N _{Amido} –Co–N _{Amidate}	86.08(7)	86.15(4)	85.5(4)	86.82(12)
Torsion Angle	0.028	0.00	0.00	0.371
τ_4	0.69	0.69	0.69	0.70

Dinuclear cobalt(II) complexes $(\text{Et}_4\text{N})_2[\text{Co}_2(\text{L}^{\text{tBu}})_2]$, $\text{K}_2[\text{Co}_2(\text{L}^{\text{Ph}})_2]$, and $(\text{Et}_4\text{N})_2[\text{Co}_2(\text{L}^{\text{CF}_3})_2]$ crystallized with two crystallographically independent but geometrically similar molecules in their asymmetric units. Similar to the isopropyl-substituted dinuclear cobalt(II) complex, $(\text{Et}_4\text{N})_2[\text{Co}_2(\text{L}^{\text{iPr}})_2]$ (shown in Figure 2-5A), the *tert*-butyl, phenyl, and trifluoromethyl-substituted complexes also form a Co_2N_2 diamond core in which the atoms are related by inversion. The solid-state structures of $\text{K}_2[\text{Co}_2(\text{L}^{\text{tBu}})_2]$, $(\text{Et}_4\text{N})_2[\text{Co}_2(\text{L}^{\text{Ph}})_2]$, and $(\text{Et}_4\text{N})_2[\text{Co}_2(\text{L}^{\text{CF}_3})_2]$, show that the four-coordinate cobalt(II) ions in each complex have near identical distorted seesaw geometries, quantified by their τ_4 values of 0.69, 0.69, and 0.70 respectively. First described by Houser, et al, the τ_4 value is a parameter to describe four-coordinate geometries based on a 0.0 – 1.00 scale, where 0.0 is described as an ideal square planar geometry, and 1.00 is an idealized tetrahedral geometry.³² τ_4 values that fall within this range are typically described as trigonal pyramidal, distorted tetrahedral, or seesaw

geometries. The cobalt–cobalt through-space separation distances in these complexes fall within 0.1 Å of each other, demonstrating that varying the R-group on the ligand scaffolds do not significantly affect the geometry of the Co₂N₂ diamond core. The Co–N (amidate and bridging amido) distances of these complexes are comparable to the distances observed in other known dinuclear cobalt(II) complexes that also form a Co₂N₂ diamond core.³³ The Co⋯Co through-space distances are large enough to rule out the possibility of a Co–Co bond, but short enough to consider possible interactions between the two metal centers.

One notable incongruence between the molecular structures of the dinuclear cobalt(II) complexes is observed in the molecular structure of K₂[Co₂(L^{iBu})₂]. In the molecular structure of K₂[Co₂(L^{iBu})₂], the two potassium counterions are positioned directly on top of the anionic complex and have a close interaction to the *O*-amidate arms of the ligand backbone, as evidenced by the close K⋯O_{Amidate} through-space distance of 2.682(14) Å. This structural difference sparked our interest as a number of studies have shown that varying the counterion of charged complexes may modulate their magnetic and structural characteristics.³⁴ In order to better correlate the structural effect imposed by the potassium counterions on the overall structure, the analogous K₂[Co₂(L^{iPr})₂] was prepared using the same general procedure used for K₂[Co₂(L^{iBu})₂] and suitable crystals for X-ray diffraction of K₂[Co₂(L^{iPr})₂] were obtained by slow diffusion of diethyl ether into a concentrated acetonitrile solution of K₂[Co₂(L^{iPr})₂]. According to the crystallographic data, K₂[Co₂(L^{iPr})₂] crystallizes in the triclinic P-1 space group. The molecular structures of K₂[Co₂(L^{iPr})₂] and (Et₄N)₂[Co₂(L^{iPr})₂] are shown in Figure 2-5. As expected, the two potassium counterions in the molecular structure of K₂[Co₂(L^{iPr})₂] have a close interaction to the *O*-amidate arms of the ligand backbone, with K⋯O_{Amidate} through-space distances of 2.671(3) Å. This is not

observed in the corresponding $(\text{Et}_4\text{N})_2[\text{Co}_2(\text{L}^{\text{iPr}})_2]$ complex in which the tetraethylammonium counterions exhibit no interaction with the anionic molecule. When the molecular structures of $\text{K}_2[\text{Co}_2(\text{L}^{\text{iPr}})_2]$ and $(\text{Et}_4\text{N})_2[\text{Co}_2(\text{L}^{\text{iPr}})_2]$ are carefully compared, it is observed that the potassium ions instigate slight changes in bond lengths and bond angles throughout the entire molecule as shown in Table 2-3. Most notably, the $\text{Co}\cdots\text{Co}$ through-space distance in $\text{K}_2[\text{Co}_2(\text{L}^{\text{iPr}})_2]$ is slightly shorter (2.6363(6) Å) than in $(\text{Et}_4\text{N})_2[\text{Co}_2(\text{L}^{\text{iPr}})_2]$ (2.66807(9) Å). The shortening of the $\text{Co}\cdots\text{Co}$ distance in $\text{K}_2[\text{Co}_2(\text{L}^{\text{iPr}})_2]$ may be attributed to a strain within the ligand backbone from the *O*-amidates interacting with the potassium counter ions. This strain can be quantified by analyzing the torsion angle of the Co_2N_2 diamond cores in each complex, whereby the torsion angle is described as the $\text{N}_{\text{Amide}}\text{-Co-N}_{\text{Amidate}}\text{-Co}$ angle. The torsion angle in the diamond core of $(\text{Et}_4\text{N})_2[\text{Co}_2(\text{L}^{\text{iPr}})_2]$ is 0.028° whereas the torsion angle in $\text{K}_2[\text{Co}_2(\text{L}^{\text{iPr}})_2]$ increases to 4.775° as a result of the counter ions interacting with the *O*-amidate moieties.

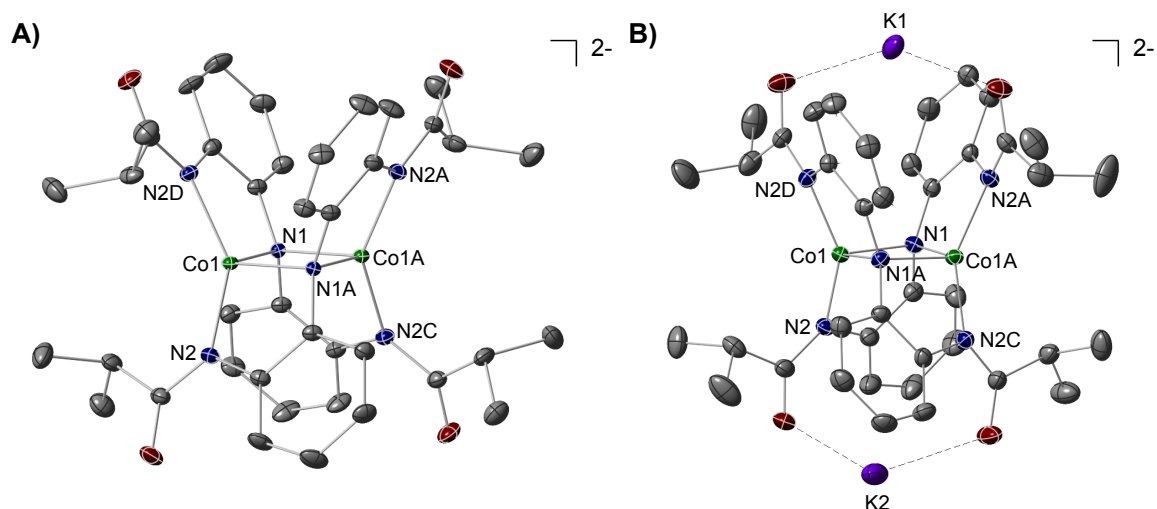


Figure 2-5. Solid-state structures of **A)** $(\text{Et}_4\text{N})_2[\text{Co}_2(\text{L}^{\text{iPr}})_2]^{29}$ and **B)** $\text{K}_2[\text{Co}_2(\text{L}^{\text{iPr}})_2]$. Thermal ellipsoids drawn at 40% probability. Tetraethylammonium counteranions (for complex $(\text{Et}_4\text{N})_2[\text{Co}_2(\text{L}^{\text{iPr}})_2]$) and hydrogen atoms for both complexes have been omitted for clarity.

Table 2-3. Selected bond lengths (Å) and angles (°) for $(\text{Et}_4\text{N})_2[\text{Co}_2(\text{L}^{\text{iPr}})_2]^{29}$ and $\text{K}_2[\text{Co}_2(\text{L}^{\text{iPr}})_2]$. The torsion angle is defined as $\text{N}_{\text{Amido}}-\text{Co}-\text{N}_{\text{Amido}}-\text{Co}$.

Bond Lengths (Å) and Angles (°)		
	$(\text{Et}_4\text{N})_2[\text{Co}_2(\text{L}^{\text{iPr}})_2]$	$\text{K}_2[\text{Co}_2(\text{L}^{\text{iPr}})_2]$
Co...Co	2.6807(9)	2.6586(7)
Co- $\text{N}_{\text{Amidate}}$	1.975(2)	1.9639(14)
Co- N_{Amido}	2.040(2)	2.1123(16)
$\text{N}_{\text{Amido}}-\text{Co}-\text{N}_{\text{Amido}}$	97.84(11)	102.00(7)
$\text{N}_{\text{Amidate}}-\text{Co}-\text{N}_{\text{Amidate}}$	141.63(13)	146.66(8)
$\text{N}_{\text{Amido}}-\text{Co}-\text{N}_{\text{Amidate}}$	86.08(7)	115.35(4)
$\text{K}\cdots\text{O}_{\text{Amidate}}$	—	2.671(3)
Torsion Angle	0.028	4.775
τ_4	0.69	0.69

The molecular structures of mononuclear cobalt(II) complexes were determined by X-ray diffraction. The results are shown in Figure 2-6 and the metrical parameters for these complexes are listed in Table 2-4. Similar to the isopropyl-substituted mononuclear cobalt(II) complex, $(\text{Et}_4\text{N})_2[\text{Co}(\text{HL}^{\text{iPr}})_2]$, the solid-state structure of complexes $(\text{PPh}_4)_2[\text{Co}(\text{HL}^{\text{iBu}})_2]$, $\text{K}_2[\text{Co}(\text{HL}^{\text{Ph}})_2]$, and $(\text{Et}_4\text{N})_2[\text{Co}(\text{HL}^{\text{Ad}})_2]$ demonstrate that the cobalt(II) ion is coordinated by one amido and one *N*-amidate donor from each ligand with relatively similar $\text{Co}-\text{N}_{\text{amido}}$ and $\text{C}-\text{N}_{\text{amidate}}$ bond lengths. In each solid-state structure, the cobalt(II) ion is four-coordinate and situated in a distorted trigonal pyramidal geometry with τ_4 values of 0.72, 0.73, and 0.70 for complexes $(\text{PPh}_4)_2[\text{Co}(\text{HL}^{\text{iBu}})_2]$, $\text{K}_2[\text{Co}(\text{HL}^{\text{Ph}})_2]$ and $(\text{Et}_4\text{N})_2[\text{Co}(\text{HL}^{\text{Ad}})_2]$, respectively. These three complexes have nearly the same geometry, suggesting that subtle changes in the carboxamide substituents do not significantly alter the coordination geometries of the cobalt(II) complexes.

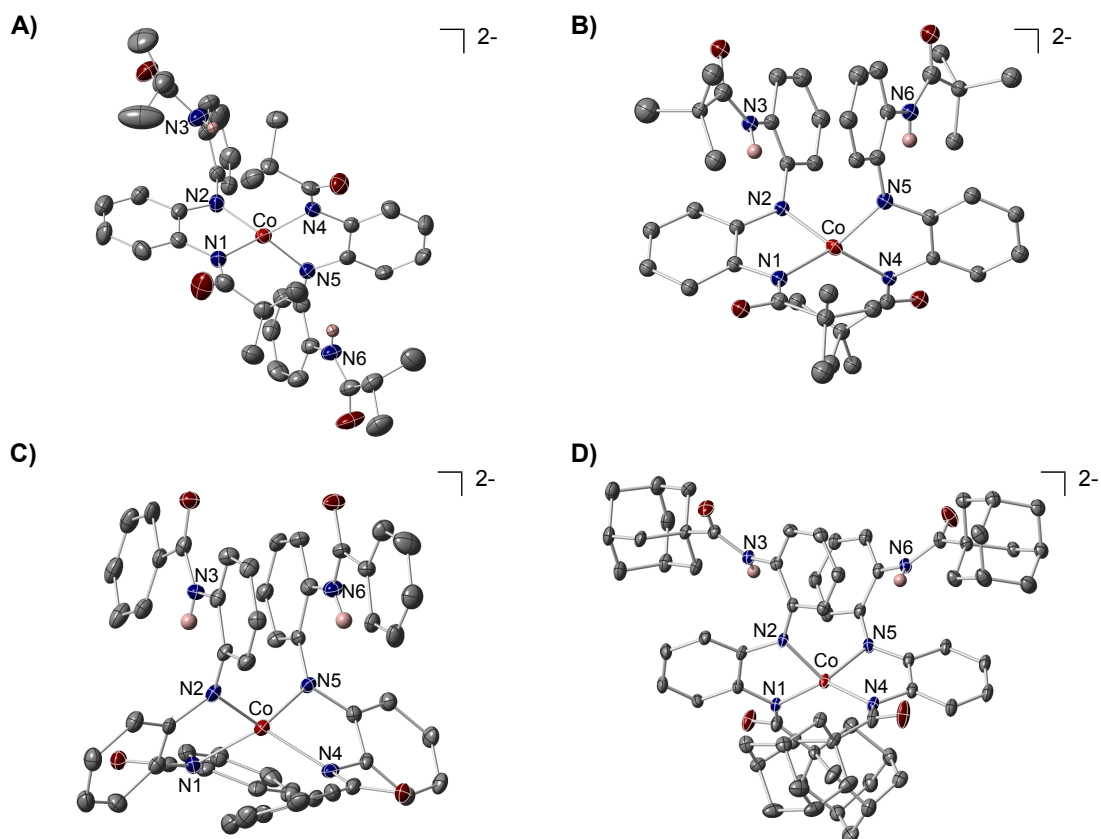


Figure 2-6. Solid-state structures of **A)** $(\text{Et}_4\text{N})_2[\text{Co}(\text{HL}^{\text{tPr}})_2]^{2-}$, **B)** $(\text{PPh}_4)_2[\text{Co}(\text{HL}^{\text{tBu}})_2]^{2-}$, **C)** $\text{K}_2[\text{Co}(\text{HL}^{\text{Ph}})_2]^{2-}$ and **D)** $(\text{Et}_4\text{N})_2[\text{Co}(\text{HL}^{\text{Ad}})_2]^{2-}$. Thermal ellipsoids drawn at 40 % probability. Hydrogen atoms (except the amide hydrogens on each complex) and counterions have been omitted for clarity.

Table 2-4. Selected bond lengths (Å) and angles (°) for $(\text{Et}_4\text{N})_2[\text{Co}(\text{HL}^{\text{iPr}})_2]$,²⁹ $(\text{PPh}_4)_2[\text{Co}(\text{HL}^{\text{iBu}})_2]$, $\text{K}_2[\text{Co}(\text{HL}^{\text{Ph}})_2]$, and $(\text{Et}_4\text{N})_2[\text{Co}(\text{HL}^{\text{Ad}})_2]$.

Bond Lengths (Å) and Angles (°)				
R =	ⁱ Pr	^t Bu	Ph	Ad
Co–N _{Amidate}	2.029(3)	2.045(14)	2.020(7)	2.017(5)
	2.035(3)	2.031(14)	2.046(8)	2.024(6)
Co–N _{Amido}	1.966(3)	1.968(15)	1.925(9)	1.965(5)
		1.940(14)	1.955(9)	1.960(6)
N _{Amido} –Co–N _{Amido}	123.5(1)	105.8(6)	121.4(3)	103.5(2)
	132.0(1)			
N _{Amidate} –Co–N _{Amidate}	117.1(1)	130.3(5)	118.5(3)	136.2(2)
			82.6(6)	80.6(3)
N _{Amido} –Co–N _{Amidate}	83.0(1)	83.1(6)	85.3(3)	84.6(2)
	123.4(1)	126.9(6)	126.2(4)	123.2(4)
		130.3(5)	130.2(4)	125.0(2)
τ_4	0.69	0.72	0.73	0.7

The molecular structures of dinuclear Fe^{II} , Ni^{II} , Cu^{II} and Zn^{II} complexes supported by the isopropyl-substituted ligand ($\text{H}_3\text{L}^{\text{iPr}}$) were determined by X-ray diffraction. The results are shown in Figure 2-7 and the metrical parameters for these complexes are listed in Table 2-5. The structural data obtained from these studies reveal that similar to the dinuclear cobalt(II) systems, these complexes also form a M_2N_2 (where $\text{M} = \text{Fe}^{\text{II}}$, Ni^{II} , Cu^{II} and Zn^{II}) diamond core in which the atoms are related by inversion. Analyses of the molecular structures of these complexes show the overall arrangement of the ligands around each core to be very similar. In spite of the similar overall structural architecture of each complex, major differences in the M_2N_2 diamond core are observed within this series of complexes.

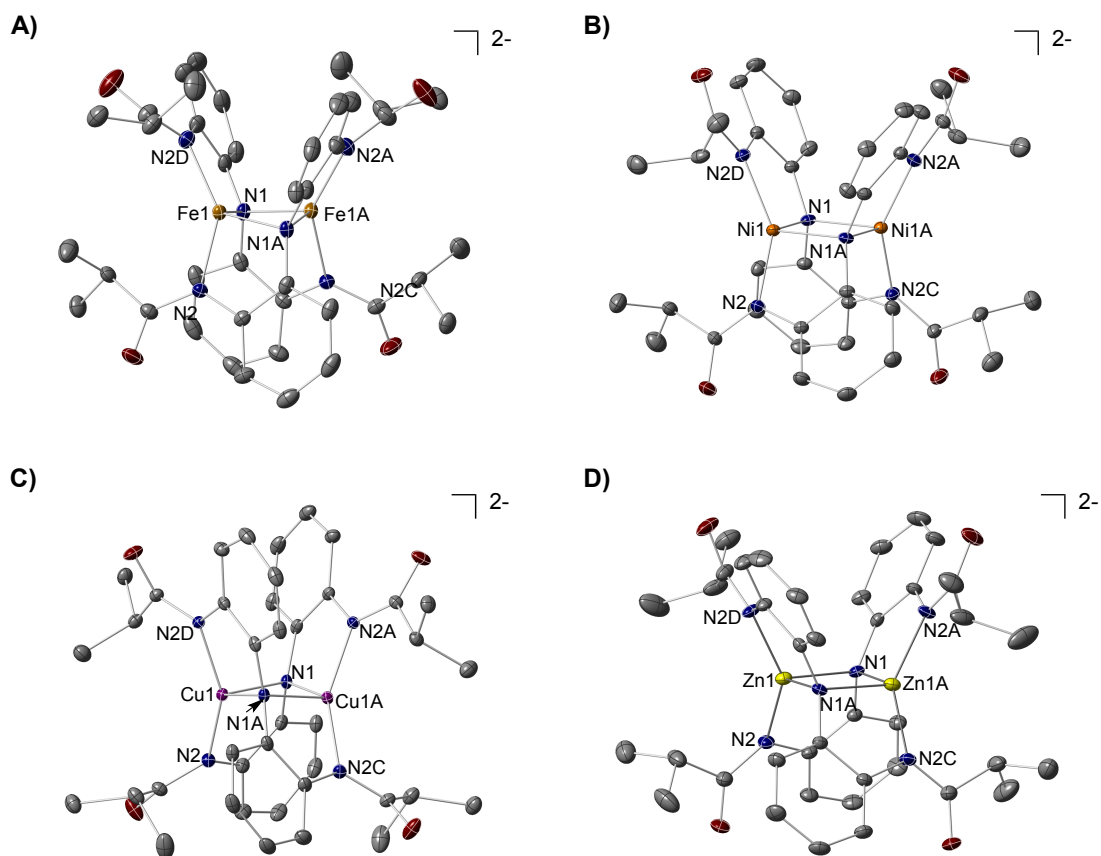


Figure 2-7. Solid-state structures of **A)** $(\text{PPh}_4)_2[\text{Fe}_2(\text{L}^{i\text{Pr}})_2]$, **B)** $(\text{Et}_4\text{N})_2[\text{Ni}_2(\text{L}^{i\text{Pr}})_2]$, **C)** $(\text{PPh}_4)_2[\text{Cu}_2(\text{L}^{i\text{Pr}})_2]$, and **D)** $(\text{Et}_4\text{N})_2[\text{Zn}_2(\text{L}^{i\text{Pr}})_2]$. Thermal ellipsoids drawn at 40% probability. Hydrogen atoms and counteranions have been omitted for clarity.

Table 2-5. Selected bond lengths (Å) and angles (°) for $(\text{PPh}_4)_2[\text{Fe}_2(\text{L}^{\text{iPr}})_2]$, $(\text{Et}_4\text{N})_2[\text{Ni}_2(\text{L}^{\text{iPr}})_2]$, $(\text{PPh}_4)_2[\text{Cu}_2(\text{L}^{\text{iPr}})_2]$, and $(\text{Et}_4\text{N})_2[\text{Zn}_2(\text{L}^{\text{iPr}})_2]$. The torsion angle is defined as $\text{N}_{\text{Amido}}-\text{M}-\text{N}_{\text{Amido}}-\text{M}$.

Bond Lengths (Å) and Angles (°)				
M =	Fe ^{II}	Ni ^{II}	Cu ^{II}	Zn ^{II}
M···M	2.3507(19)	2.716(1)	2.5617(8)	2.7403(9)
M–N _{Amidate}	2.0897(19)	1.9602(14)	1.933(2)	2.021(2)
	2.0971(19)	1.9603(14)	1.944(2)	2.008(2)
M–N _{Amido}	2.020(2)	2.0144(13)	2.09(19)	2.078(2)
	2.008(2)	2.0144(13)	2.131(9)	2.084(2)
N _{Amido} –M–N _{Amido}	108.01(8)	95.261(1)	104.29(6)	97.62(8)
N _{Amidate} –M–N _{Amidate}	143.20(8)	145.97(9)	148.89(9)	141.85(11)
N _{Amido} –M–N _{Amidate}	81.29(8)	85.66(4)	82.80(8)	86.314
Torsion Angle	13.018	0.028	10.483	1.468
τ_4	0.62	0.65	0.62	0.69

Dark brown single crystals of iron(II) complex $(\text{PPh}_4)_2[\text{Fe}_2(\text{L}^{\text{iPr}})_2]$ can be obtained by diffusing diethyl ether into a CH_3CN solution of the complex. $(\text{PPh}_4)_2[\text{Fe}_2(\text{L}^{\text{iPr}})_2]$ crystallizes in the orthorhombic crystal system C2221 space group. The four-coordinate iron(II) center has a distorted seesaw coordination geometry, as evidenced by its τ_4 value of 0.62 (Figure 2-7A). The Fe–N bond lengths of this complex are within the expected ranges for iron(II) complexes hosting four anionic nitrogen ligands. Most notably, the Fe···Fe through-space distance (2.3507(19) Å) is short enough to imply a possible Fe–Fe bond. This short distance imposes a major distortion throughout the molecule, causing its diamond core to have the largest torsion angle, ($\text{N}_{\text{amido}}-\text{Fe}-\text{N}_{\text{amido}}-\text{Fe}$), (13.018°) in this series.

The nickel(II) complex $(\text{Et}_4\text{N})_2[\text{Ni}_2(\text{L}^{\text{iPr}})_2]$ can be crystallized as deep brown blocks by the slow diffusion of diethyl ether into a concentrated acetonitrile solution of the complex.

$(\text{Et}_4\text{N})_2[\text{Ni}_2(\text{L}^{\text{iPr}})_2]$ crystallizes in the tetragonal $I4_122$ space group. In the molecular structure of $(\text{Et}_4\text{N})_2[\text{Ni}_2(\text{L}^{\text{iPr}})_2]$, each nickel(II) ion is situated in a distorted seesaw geometry ($\tau_4 = 0.65$) and displays Ni–N average bond lengths that are in the typical range for complexes with a central nickel(II) ion in a distorted seesaw geometry (Figure 2-7B). The Ni \cdots Ni through-space distance is 2.716(1) Å, which is significantly shorter than previously reported for $\text{Ni}^{\text{II}}_2\text{N}_2$ diamond cores, but long enough to preclude any direct Ni–Ni bonding.³⁵ Interestingly, the bond angles about the diamond core and its torsion angle (0.028°) resemble that of the cobalt(II) dinuclear complex, $(\text{Et}_4\text{N})_2[\text{Co}_2(\text{L}^{\text{iPr}})_2]$. The very similar ionic radii of Co^{2+} and Ni^{2+} could reason these similarities, affording these two complexes to possess near-identical distorted four-coordinate seesaw geometries with almost identical metrical parameters.

The copper(II) complex $(\text{PPh}_4)_2[\text{Cu}_2(\text{L}^{\text{iPr}})_2]$ can be crystallized as deep purple blocks by the slow diffusion of diethyl ether into a concentrated acetonitrile solution of the complex. The complex crystallizes in the orthorhombic $C2221$ space group, similarly to $(\text{PPh}_4)_2[\text{Fe}_2(\text{L}^{\text{iPr}})_2]$. In its molecular structure, the copper(II) ions in the Cu_2N_2 diamond core are situated 2.5617(8) Å apart (Figure 2-7C), a distance slightly longer than Cu \cdots Cu separations found in similar $\text{Cu}^{\text{II}}_2\text{N}_2$ structures.³⁶ The Cu \cdots Cu through-space distance in $(\text{PPh}_4)_2[\text{Cu}_2(\text{L}^{\text{iPr}})_2]$ is large enough to rule out a possible Cu–Cu bond, but short enough to support possible metal–metal interactions between the two d^9 metal ions. The copper(II) centers are related by inversion and are equally situated in a distorted tetrahedral (seesaw) geometry ($\tau_4 = 0.69$). As a result of the short Cu \cdots Cu separation, the angle of distortion about the diamond core plane is 10.483° . Work by Peters and co-workers has reported on the structural characterization of Cu_2N_2 and Cu_2P_2 systems, but to our knowledge,

$(\text{PPh}_4)_2[\text{Cu}_2(\text{L}^{\text{iPr}})_2]$ is the first structurally characterized four-coordinate amido-bridged copper(II) complex with a $\text{Cu}^{\text{II}}_2\text{N}_2$ diamond core structure.³⁶⁻³⁷

The zinc(II) complex $(\text{Et}_4\text{N})_2[\text{Zn}_2(\text{L}^{\text{iPr}})_2]$ can be crystallized as light yellow needles by the slow diffusion of diethyl ether into a concentrated acetonitrile solution of the complex. The complex crystallizes in the orthorhombic C2221 space group. The molecular structure of $(\text{Et}_4\text{N})_2[\text{Zn}_2(\text{L}^{\text{iPr}})_2]$ is shown in Figure 2-7D and its corresponding metrical parameters are listed in Table 2-5 show that each zinc(II) ion is situated in a distorted seesaw geometry ($\tau_4 = 0.69$). The $\text{Zn}\cdots\text{Zn}$ through-space separation (2.7403(9) Å) in this complex is the largest of this series. This is not surprising as Zn^{2+} possesses the largest ionic radii of the metal ions constituting this synthetic series. The large $\text{Zn}\cdots\text{Zn}$ separations cause the overall torsion angle ($\text{N}_{\text{amido}}-\text{Zn}-\text{N}_{\text{amido}}-\text{Zn}$) about the diamond core to be relatively low (1.468°).

Section 2-3-4. Electronic and Magnetic Characterization of Metal Complexes

The electronic nature of the metal complexes supported by the bis(amidophenyl)amine ligands was investigated using UV-visible absorption spectroscopy and the magnetic properties were examined through magnetic susceptibility measurements, using solution phase ^1H NMR Evan's method. This data is summarized in Table 2-6.³⁸ For the dinuclear complexes, because the two metal ions in these compounds are crystallographically equivalent, the magnetic results are presented per metal ion.³⁹

Table 2-6. Magnetic and spectral properties of synthesized metal complexes

Spin State (<i>S</i>), Magnetic Moments (μ_{eff}), and Absorption Values			
Complex	<i>S</i>	μ_{eff} (μ_B) ^a	λ_{max}/nm ($\epsilon/M^{-1}\cdot cm^{-1}$) ^b
(Et ₄ N) ₂ [Co ₂ (L ^{CF3}) ₂]	3/2	4.82(7)	597 (360), 876 (31)
(Et ₄ N) ₂ [Co ₂ (L ^{Ph}) ₂]	3/2	4.48(4)	597 (764), 936 (276)
K ₂ [Co ₂ (L ^{tBu}) ₂]	3/2	4.67(6)	587 (764), 820 (245) (sh)
K ₂ [Co ₂ (L ^{iPr}) ₂]	3/2	4.72(1)	598 (765), 927 (160)
(Et ₄ N) ₂ [Co(HL ^{Ad}) ₂]	3/2	4.30(6)	573 (636), 557 (594) (sh)
K ₂ [Co(HL ^{Ph}) ₂]	3/2	4.39(5)	588 (652), 552 (622) (sh)
(PPh ₄) ₂ [Co(HL ^{tBu}) ₂]	3/2	4.42(4)	588 (606), 553 (563) (sh)
(PPh ₄) ₂ [Fe ₂ (L ^{iPr}) ₂]	2	4.50(9)	510 (640), 625 (281)
(Et ₄ N) ₂ [Ni ₂ (L ^{iPr}) ₂]	1	2.51(9)	460 (1942), 601 (560) (sh), 740 (330) (sh)
(Et ₄ N) ₂ [Ni(HL ^{iPr}) ₂]	1	2.07(1)	480 (1862), 620 (348) (sh), 708 (150) (sh)
(PPh ₄) ₂ [Cu ₂ (L ^{iPr}) ₂]	0	—	522 (4775), 595 (4065), 735 (2959), 962 (780)
(Et ₄ N) ₂ [Zn ₂ (L ^{iPr}) ₂]	0	—	—

^a Measured at 295 K using the Evan's Method.³⁸^b Recorded at room temperature.

The ¹H NMR spectra of the synthesized dinuclear and mononuclear cobalt(II) complexes give rise to paramagnetically shifted peaks at 295K. The number of paramagnetic peaks indicates that these species maintain their C₂-symmetry in solution. Magnetic susceptibility measurements confirmed that the cobalt(II) ions in all complexes are high-spin (*S* = 3/2) with magnetic moments typical of a cobalt(II) ion in a high-spin ground state with three unpaired electrons. The UV-visible absorption spectra of the cobalt(II) complexes were recorded at room temperature as acetonitrile (CH₃CN) solutions. In their UV-visible absorption spectra, the dinuclear cobalt(II) complexes K₂[Co₂(L^{iPr})₂], K₂[Co₂(L^{tBu})₂],

$(\text{Et}_4\text{N})_2[\text{Co}_2(\text{L}^{\text{Ph}})_2]$, and $(\text{Et}_4\text{N})_2[\text{Co}_2(\text{L}^{\text{CF}_3})_2]$ exhibit very similar broad bands between $\lambda_{\text{max}} = 500$ and 597 nm, which correspond to d–d transitions (Figure 2-8). The mononuclear cobalt(II) complexes $(\text{PPh}_4)_2[\text{Co}(\text{HL}^{\text{tBu}})_2]$, $\text{K}_2[\text{Co}(\text{HL}^{\text{Ph}})_2]$, and $(\text{Et}_4\text{N})_2[\text{Co}(\text{HL}^{\text{Ad}})_2]$ exhibit bands between $\lambda_{\text{max}} = 543$ and 588 nm, which also correspond to d–d transitions (Figure 2-9). The UV-visible absorptions of the mononuclear species are consistent with the cobalt(II) ion oriented in a distorted tetrahedral geometry. The spectra of these complexes are solvent-independent, suggesting that these species retain their respective geometries even in the presence of coordinating solvents.

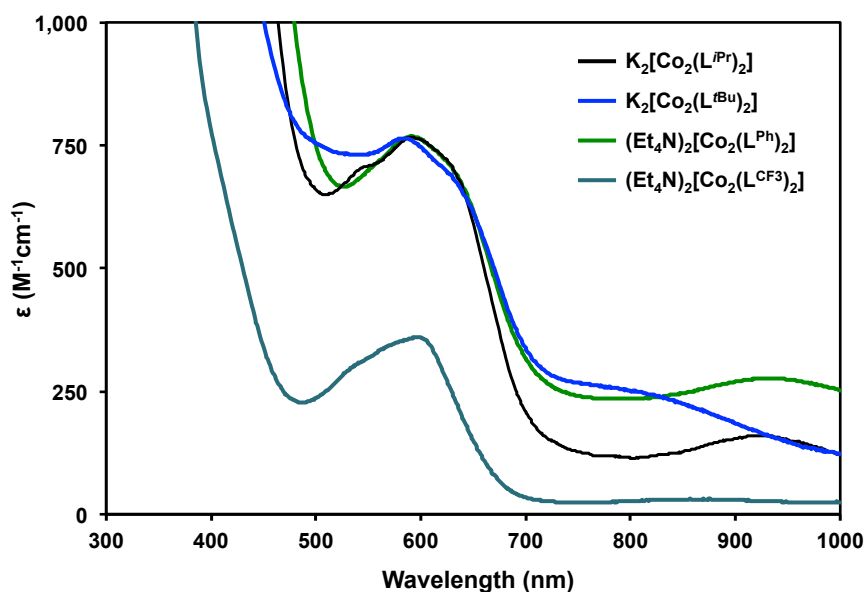


Figure 2-8. UV-visible absorption spectra of dinuclear cobalt(II) complexes $\text{K}_2[\text{Co}_2(\text{L}^{\text{tPr}})_2]$ (black line), $\text{K}_2[\text{Co}_2(\text{L}^{\text{tBu}})_2]$ (blue line), $(\text{Et}_4\text{N})_2[\text{Co}_2(\text{L}^{\text{Ph}})_2]$ (green line), and $(\text{Et}_4\text{N})_2[\text{Co}_2(\text{L}^{\text{CF}_3})_2]$ (teal line). Recorded in CH_3CN at room temperature.

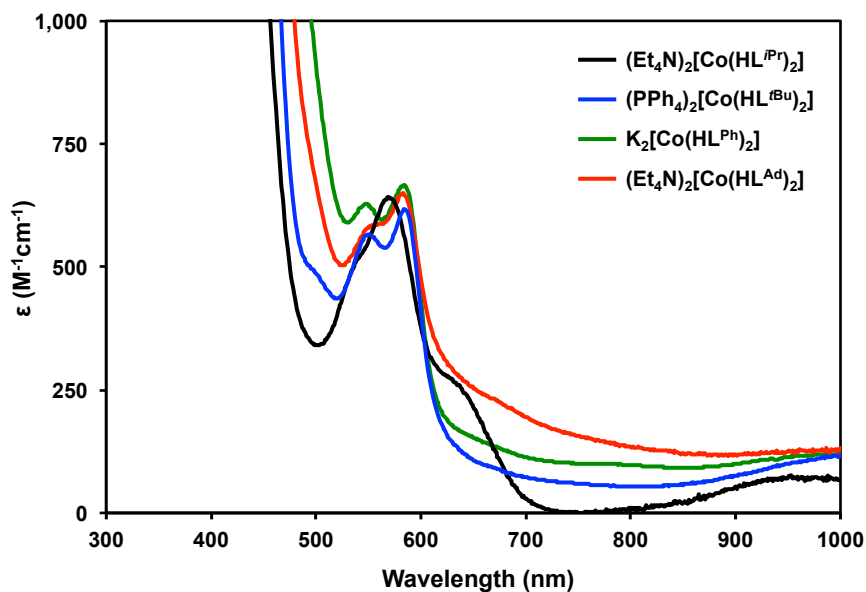


Figure 2-9. UV-visible absorption spectra of mononuclear cobalt(II) complexes $(\text{Et}_4\text{N})_2[\text{Co}(\text{HL}^{\text{iPr}})_2]$ (black line),²⁹ $(\text{PPh}_4)_2[\text{Co}(\text{HL}^{\text{tBu}})_2]$ (blue line), $\text{K}_2[\text{Co}(\text{HL}^{\text{Ph}})_2]$ (green line), and $(\text{Et}_4\text{N})_2[\text{Co}(\text{HL}^{\text{Ad}})_2]$ (red line). Recorded in CH_3CN at room temperature.

The UV-visible absorption spectra of the dinuclear complexes $[\text{M}_2(\text{L}^{\text{iPr}})_2]^{2-}$ (where $\text{M} = \text{Fe}^{\text{II}}, \text{Ni}^{\text{II}}, \text{Cu}^{\text{II}}$ and Zn^{II}) are shown in Figure 2-10. The solution magnetic moment of the iron(II) complex, $(\text{PPh}_4)_2[\text{Fe}_2(\text{L}^{\text{iPr}})_2]$, was measured to be $4.50(9) \mu_{\text{B}}/\text{metal ion}$ (298K, CD_3CN). This magnetic moment indicates a high-spin $S = 2$ iron(II) center, with a value typical of four-coordinate high-spin iron(II) complexes. Additionally, in its UV-visible absorption spectrum, the complex displays weak, broad absorption bands at $\lambda_{\text{max}} = 510 \text{ nm}$ ($\epsilon = 640 \text{ M}^{-1} \text{ cm}^{-1}$) and 625 nm ($\epsilon = 681 \text{ M}^{-1} \text{ cm}^{-1}$). These values are of the appropriate magnitude for spin-allowed d—d transitions expected for a high-spin iron(II) complex.

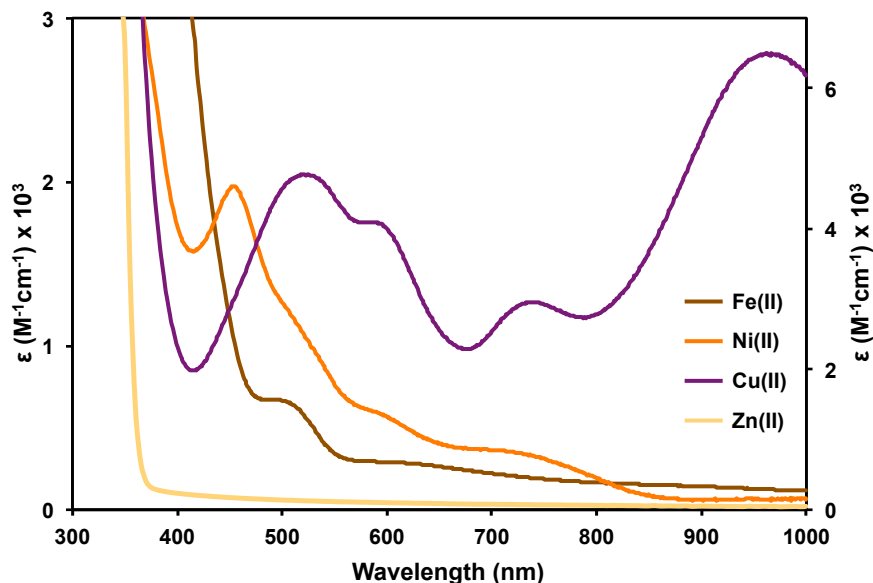


Figure 2-10. UV-visible absorption spectra of $(\text{PPh}_4)_2[\text{Fe}_2(\text{L}^{i\text{Pr}})_2]$ (brown line), $(\text{Et}_4\text{N})_2[\text{Ni}_2(\text{L}^{i\text{Pr}})_2]$ (orange line), $(\text{PPh}_4)_2[\text{Cu}_2(\text{L}^{i\text{Pr}})_2]$ (purple line), and $(\text{Et}_4\text{N})_2[\text{Zn}_2(\text{L}^{i\text{Pr}})_2]$ (yellow line). Recorded in CH_3CN at room temperature. Spectrum for $(\text{PPh}_4)_2[\text{Cu}_2(\text{L}^{i\text{Pr}})_2]$ is plotted on the secondary y-axis to the left.

The four-coordinate dimeric species $(\text{Et}_4\text{N})_2[\text{Ni}_2(\text{L}^{i\text{Pr}})_2]$ exhibits a μ_{eff} of $2.51(9) \mu_{\text{B}}$ (298K, CDCl_3), indicative of a high-spin $S = 1$ ground state. A paramagnetic high-spin ground state with $S = 1$ in nickel(II) ($3d^8$) complexes is typical for four-coordinate tetrahedral and distorted tetrahedral geometries.⁴⁰ In its UV-visible absorption spectrum, $(\text{Et}_4\text{N})_2[\text{Ni}_2(\text{L}^{i\text{Pr}})_2]$ exhibits a ligand-to-metal charge transfer (LMCT) band at $\lambda_{\text{max}} = 460 \text{ nm}$ ($\epsilon = 1942 \text{ M}^{-1} \text{ cm}^{-1}$) followed by weak energy, low intensity shoulders at $\lambda_{\text{max}} = 601 \text{ nm}$ ($\epsilon = 560 \text{ M}^{-1} \text{ cm}^{-1}$) and $\lambda_{\text{max}} = 740 \text{ nm}$ ($\epsilon = 330 \text{ M}^{-1} \text{ cm}^{-1}$), characteristic of a four-coordinate nickel(II) complex with a distorted tetrahedral geometry. Although a solid-state molecular structure of the monomeric nickel(II) species $(\text{Et}_4\text{N})_2[\text{Ni}(\text{HL}^{i\text{Pr}})_2]$ was not obtained during our

studies, comparing its UV-visible absorption spectrum, shown in Figure 2-11, to that of the dimeric species, $(\text{Et}_4\text{N})_2[\text{Ni}_2(\text{L}^{i\text{Pr}})_2]$, clearly shows its distinct presence in solution. $(\text{Et}_4\text{N})_2[\text{Ni}(\text{HL}^{i\text{Pr}})_2]$ exhibits values at $\lambda_{\text{max}} = 480 \text{ nm}$ ($\epsilon = 1862 \text{ M}^{-1} \text{ cm}^{-1}$) followed by weak energy, low intensity shoulders at $\lambda_{\text{max}} = 620 \text{ nm}$ ($\epsilon = 348 \text{ M}^{-1} \text{ cm}^{-1}$) and $\lambda_{\text{max}} = 708 \text{ nm}$ ($\epsilon = 3150 \text{ M}^{-1} \text{ cm}^{-1}$). Its solution-state magnetic moment was measured to be $2.07 \mu_{\text{B}}$ (298K, CDCl_3), consistent with a high-spin $S = 1$ ground state.

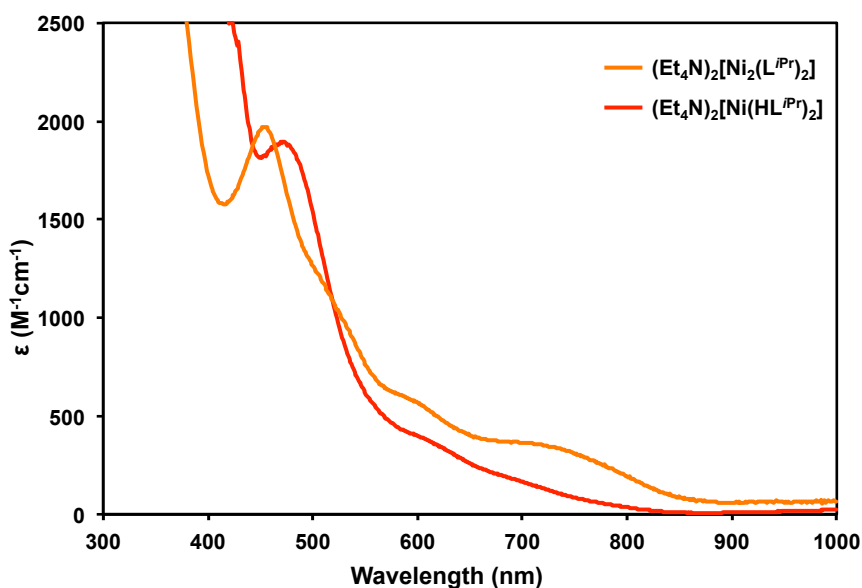


Figure 2-11. UV-visible absorption spectra of mononuclear species $(\text{Et}_4\text{N})_2[\text{Ni}(\text{HL}^{i\text{Pr}})_2]$ (orange line) and dinuclear species $(\text{Et}_4\text{N})_2[\text{Ni}_2(\text{L}^{i\text{Pr}})_2]$ (red line). Recorded in CH_3CN at room temperature.

The ^1H NMR spectrum of dinuclear copper(II) complex $(\text{PPh}_4)_2[\text{Cu}_2(\text{L}^{i\text{Pr}})_2]$ gives rise to diamagnetically shifted peaks at 295K, indicative of strong antiferromagnetic coupling between the two d^9 metal ions in the Cu_2N_2 diamond core. Its absorption spectrum displays

bands at $\lambda_{\text{max}} = 522, 595, \text{ and } 735 \text{ nm}$, with high molar extinction coefficients ($\epsilon, \text{M}^{-1} \text{cm}^{-1}$) of 4775, 4065 and 2959, respectively. This pattern of one high energy absorbance accompanied by a lower energy, lower intensity shoulder indicates that a distorted tetrahedral coordination geometry about the copper(II) center is being maintained in solution. Moreover, the UV-visible near-infrared (UV-vis NIR) spectrum of this complex exhibits an intense broad intervalence charge transfer (IVCT) band centered at $\lambda_{\text{max}} = 962 \text{ nm}$ ($\epsilon = 6,500 \text{ M}^{-1} \text{cm}^{-1}$) followed by a very low intensity broad band at $\lambda_{\text{max}} = 1697 \text{ nm}$ ($\epsilon = 780 \text{ M}^{-1} \text{cm}^{-1}$) (Figure 2-12). This characteristic supports the diamagnetic behavior observed via NMR for the complex, indicating a strong interaction between the two d^9 metal ions. Additionally, the bridging angle between the two copper(II) centers is known to affect the magnitude of the antiferromagnetic coupling.⁴¹ $(\text{PPh}_4)_2[\text{Cu}_2(\text{L}^{\text{iPr}})_2]$ exhibits a bridging angle ($\text{Cu}^{\text{II}}-\text{N}_{\text{amido}}-\text{Cu}^{\text{II}} = 74.77(6)^\circ$) consistent with previously reported copper(II) dimers displaying strong antiferromagnetic coupling.⁴¹

The light yellow complex $(\text{Et}_4\text{N})_2[\text{Zn}_2(\text{L}^{\text{iPr}})_2]$ displays no transitions in the visible or NIR regions. This is expected for a Zn(II) metal center with a d^{10} configuration as this compound exhibits diamagnetic peaks in its ^1H NMR spectrum.

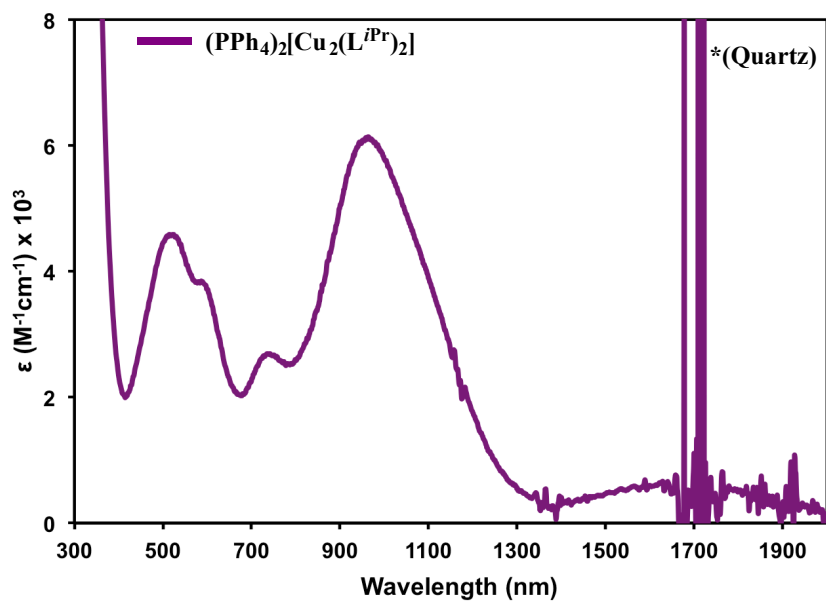


Figure 2-12. UV-visible NIR absorption spectrum of $(\text{PPh}_4)_2[\text{Cu}_2(\text{L}^{i\text{Pr}})_2]$. Recorded in CH_3CN at room temperature. Spectral noise at ~ 1700 nm is resultant from the quartz from the cuvettes (noted by *).

Section 2-3-5. Electrochemical Properties of Metal Complexes

The electrochemical properties of the prepared metal complexes were investigated using cyclic voltammetry. The electrochemical profiles of the dinuclear cobalt(II) complexes were found to give rise to rich electrochemical responses. Additionally, the cyclic voltammograms of dinuclear cobalt(II) complexes $K_2[Co_2(L^{tBu})_2]$, $(Et_4N)_2[Co_2(L^{Ph})_2]$, and $(Et_4N)_2[Co_2(L^{CF_3})_2]$ display a number of irreversible responses in their cyclic voltammograms that we were unable to assign (Figure 2-13). This was not surprising to us as the isopropyl-substituted dinuclear cobalt(II) complex $(Et_4N)_2[Co_2(L^{iPr})_2]$ displays a very complex electrochemical profile also containing electrochemical responses unable to be isolated.²⁹ It is worth mentioning, however, that the trifluoromethyl-substituted cobalt(II) complex, $(Et_4N)_2[Co_2(L^{CF_3})_2]$ exhibits a number of irreversible responses whose features are shifted to more positive potentials. This observation is explained by the presence of a strong electron-withdrawing acyl substituent on the ligand backbone.

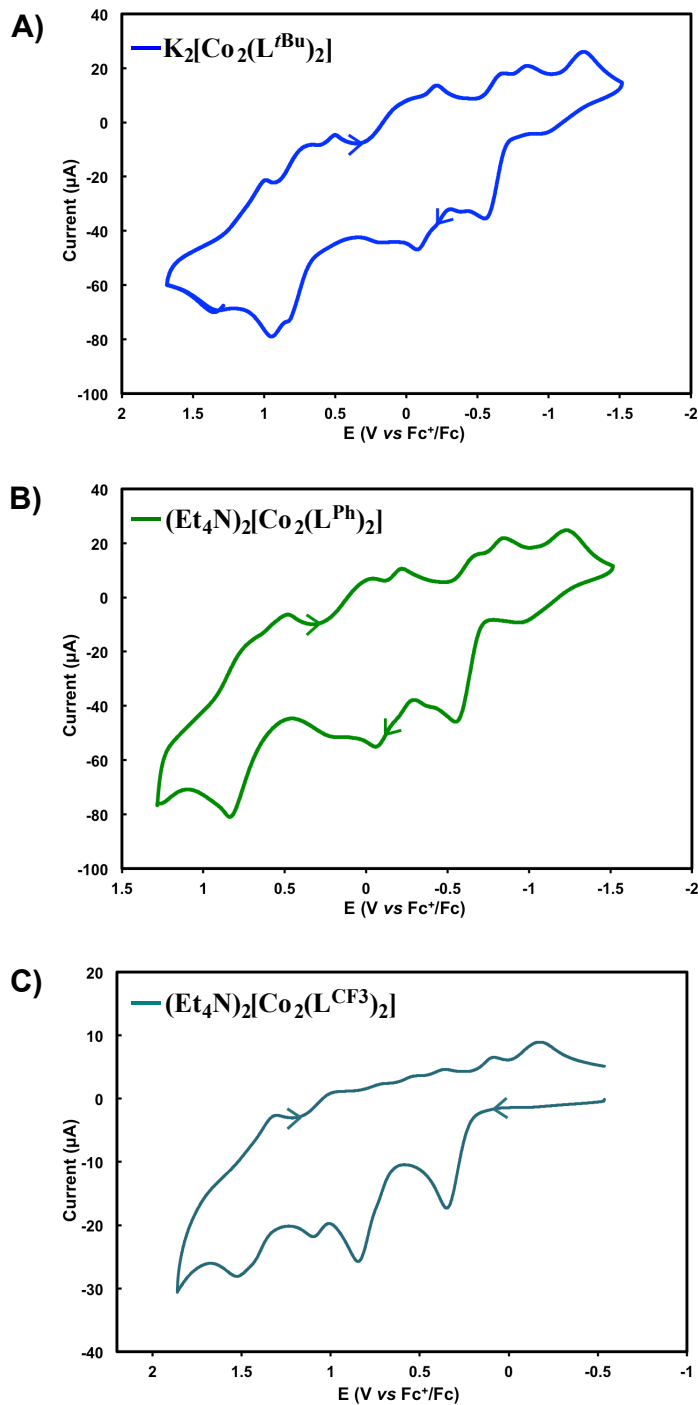


Figure 2-13. Cyclic voltammograms of **A)** $K_2[Co_2(L^{tBu})_2]$, **B)** $(Et_4N)_2[Co_2(L^{Ph})_2]$ and **C)** $(Et_4N)_2[Co_2(L^{CF_3})_2]$. Conditions: 10 mV/s, with 0.2 M TBAPF₆TBA in CH₂Cl₂ as the supporting electrolyte, referenced vs. Fc/Fc⁺, Ag/Ag⁺ as the reference electrode, using a glassy carbon working electrode, with scans initially negative.

The cyclic voltammograms of mononuclear cobalt(II) complexes $(\text{PPh}_4)_2[\text{Co}(\text{HL}^{\text{tBu}})_2]$, $\text{K}_2[\text{Co}(\text{HL}^{\text{Ph}})_2]$, and $(\text{Et}_4\text{N})_2[\text{Co}(\text{HL}^{\text{Ad}})_2]$ were recorded in CH_2Cl_2 ; the results of these studies are shown in Figure 2-14. These mononuclear species give rise to three reversible electrochemical events. Similarly to the cyclic voltammogram of $(\text{Et}_4\text{N})_2[\text{Co}_2(\text{L}^{\text{iPr}})_2]$,²⁹ the *tert*-butyl, phenyl, and adamantyl-substituted complexes display three reversible oxidation events. While the third of these events is quasi-reversible in $(\text{PPh}_4)_2[\text{Co}(\text{HL}^{\text{tBu}})_2]$, $\text{K}_2[\text{Co}(\text{HL}^{\text{Ph}})_2]$, and $(\text{Et}_4\text{N})_2[\text{Co}(\text{HL}^{\text{Ad}})_2]$. The formal potentials ($E_{1/2}$) for these complexes are shown within their cyclic voltammograms and are referenced against the $[\text{Cp}_2\text{Fe}]^{+/0}$ redox couple.⁴² A shift to more negative potentials is expected, as the electron donation from the acyl substituents increase. Comparing the potentials of the first electrochemical event (E_1) in this series shown in Table 2-7, it is observed that these complexes follow the expected trend — more negative potentials are observed as the electron donating ability of the acyl substituent on the carboxamide ligand arms is increased.

Table 2-7. Summary of electrochemical half-potentials ($E_{1/2}$) for mononuclear cobalt(II) complexes $(\text{Et}_4\text{N})_2[\text{Co}(\text{HL}^{\text{Ad}})_2]$, $(\text{PPh}_4)_2[\text{Co}(\text{HL}^{\text{tBu}})_2]$, $(\text{Et}_4\text{N})_2[\text{Co}_2(\text{L}^{\text{iPr}})_2]$,²⁹ and $\text{K}_2[\text{Co}(\text{HL}^{\text{Ph}})_2]$.

Electrochemical Properties of Mononuclear $[\text{Co}(\text{HL}^{\text{R}})_2]^{2-}$ Complexes			
R =	E^0 (V vs Fc/Fc⁺)		
	E_1	E_2	E_3
Ad	-1.12	-0.69	0.24
^t Bu	-1.10	-0.71	0.13
ⁱ Pr	-1.06	-0.45	0.01
Ph	-1.04	-0.63	-0.17

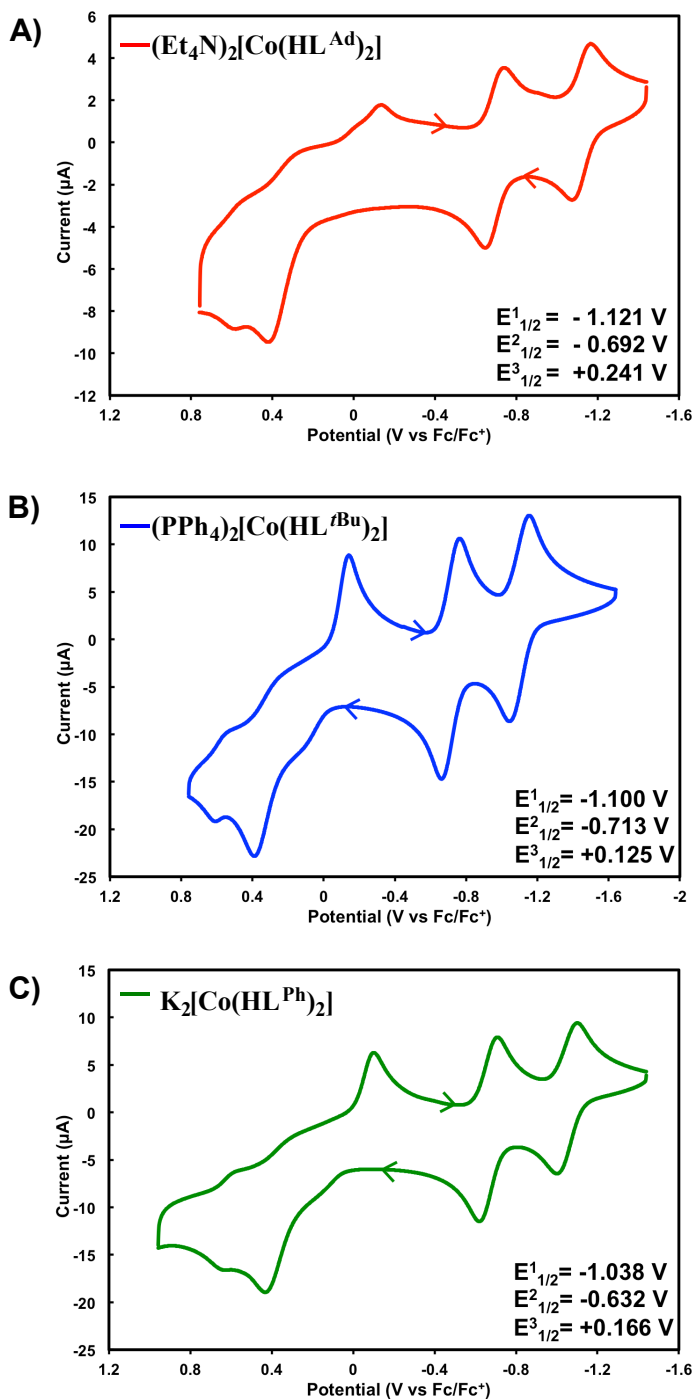


Figure 2-14. Cyclic voltammograms of **A)** $(\text{PPh}_4)_2[\text{Co}(\text{HL}^{\text{tBu}})_2]$, **B)** $\text{K}_2[\text{Co}(\text{HL}^{\text{Ph}})_2]$, and **C)** $(\text{Et}_4\text{N})_2[\text{Co}(\text{HL}^{\text{Ad}})_2]$. Conditions: 10 mV/s, with 0.2 M TBAPF₆TBA in CH₂Cl₂ as the supporting electrolyte, referenced vs. Fc/Fc⁺, Ag/Ag⁺ as the reference electrode, using a glassy carbon-working electrode, with scans initially negative.

The cyclic voltammograms of the dinuclear complexes $(\text{PPh}_4)_2[\text{Fe}_2(\text{L}^{i\text{Pr}})_2]$, $(\text{Et}_4\text{N})_2[\text{Ni}_2(\text{L}^{i\text{Pr}})_2]$, $(\text{PPh}_4)_2[\text{Cu}_2(\text{L}^{i\text{Pr}})_2]$ and $(\text{Et}_4\text{N})_2[\text{Zn}_2(\text{L}^{i\text{Pr}})_2]$ were recorded in CH_2Cl_2 ; the results of these studies are shown in Figure 2-15. The cyclic voltammograms of $(\text{PPh}_4)_2[\text{Fe}_2(\text{L}^{i\text{Pr}})_2]$, $(\text{Et}_4\text{N})_2[\text{Ni}_2(\text{L}^{i\text{Pr}})_2]$, and $(\text{Et}_4\text{N})_2[\text{Zn}_2(\text{L}^{i\text{Pr}})_2]$ all display complex and irreversible electrochemical responses which we were unable to assign. The dicopper complex $(\text{PPh}_4)_2[\text{Cu}_2(\text{L}^{i\text{Pr}})_2]$, however, displays a reversible oxidation event, as shown in Figure 2-15C, with $E_{1/2} = -0.688 \text{ V vs. Fc/Fc}^+$.

The cyclic voltammogram of the mononuclear Ni(II) complex, $(\text{Et}_4\text{N})_2[\text{Ni}_2\text{HL}^{i\text{Pr}})_2]$ differs significantly from the cyclic voltammogram of the dinuclear species, $(\text{Et}_4\text{N})_2[\text{Ni}_2(\text{L}^{i\text{Pr}})_2]$. Whereas the dinuclear complex $(\text{Et}_4\text{N})_2[\text{Ni}_2(\text{L}^{i\text{Pr}})_2]$ displays a number of irreversible electrochemical responses which we were unable to assign, $(\text{Et}_4\text{N})_2[\text{Ni}_2\text{HL}^{i\text{Pr}})_2]$ displays two, one-electron oxidation events at $E_{1/2} = -0.870 \text{ V}$ and $-0.463 \text{ V vs. Fc/Fc}^+$ (Figure 2-16). These results reinforce the fact that a mononuclear Ni(II) complex is present. The results presented in the cyclic voltammogram of mononuclear nickel(II) complex, $(\text{Et}_4\text{N})_2[\text{Ni}_2\text{HL}^{i\text{Pr}})_2]$, are in line with those recently observed by Gardinier and co-workers, where additional electrochemical responses were observed in a nickel(II) complex bearing a redox-active ligand.⁴³

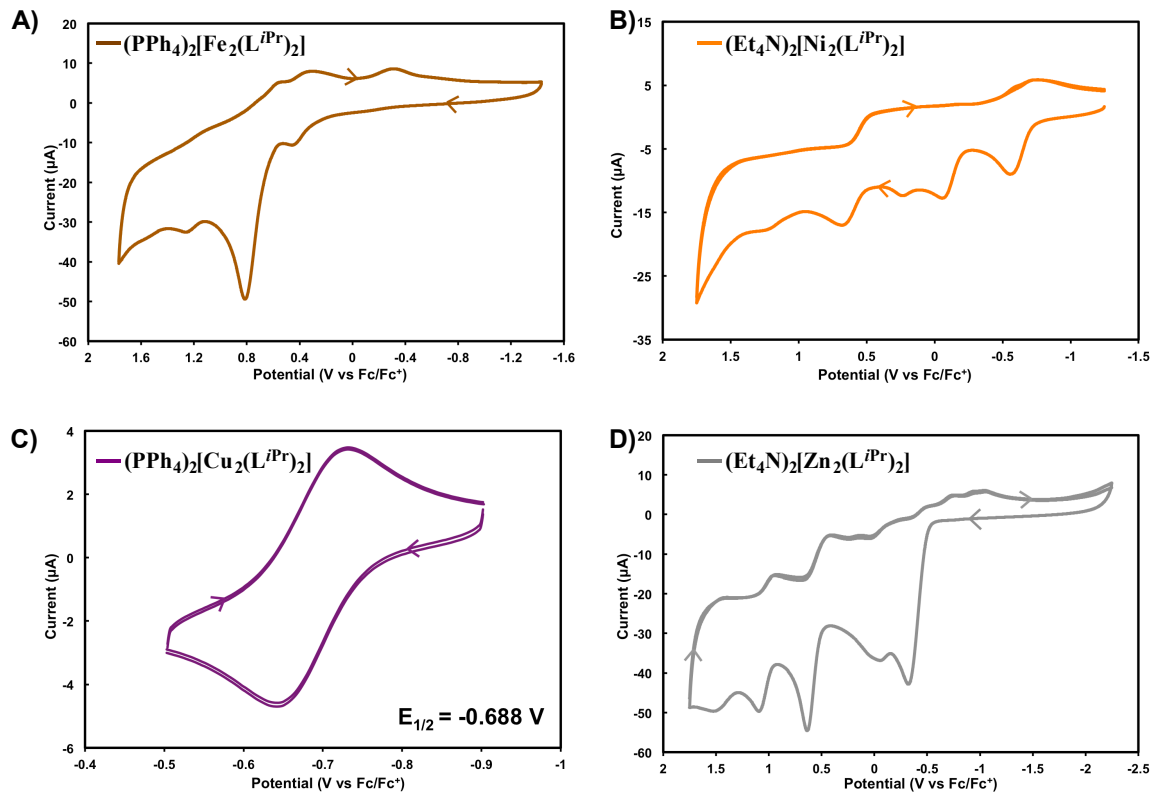


Figure 2-15. Cyclic voltammograms of **A)** (PPh₄)₂[Fe₂(L^{iPr})₂], **B)** (Et₄N)₂[Ni₂(L^{iPr})₂], **C)** (PPh₄)₂[Cu₂(L^{iPr})₂] and **D)** (Et₄N)₂[Zn₂(L^{iPr})₂]. Conditions: 10 mV/s, with 0.2 M TBAPF₆TBA in CH₂Cl₂ as the supporting electrolyte, referenced vs. Fc/Fc⁺, Ag/Ag⁺ as the reference electrode, using a glassy carbon-working electrode, with scans initially negative.

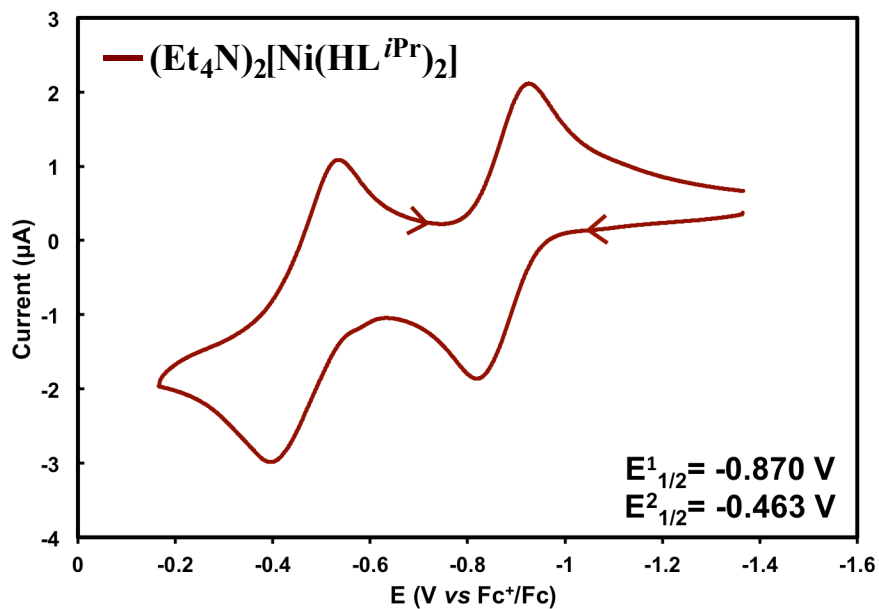


Figure 2-16. Cyclic voltammogram of mononuclear nickel(II) complex, $(\text{Et}_4\text{N})_2[\text{Ni}(\text{HL}^{i\text{Pr}})_2]$. Conditions: 10 mV/s, with 0.2 M TBAPF_6TBA in DMF as the supporting electrolyte, referenced vs. Fc/Fc^+ , Ag/Ag^+ as the reference electrode, using a glassy carbon-working electrode, with scans initially negative.

Section 2-4. Discussion

The coordination versatility of tridentate bis(amidophenyl)amine ligands $\text{NH}(o\text{-PhNHC(O)R})_2$ ($(\text{H}_3\text{L}^{\text{R}})$ $\text{R} = \text{'Bu, Ph, Ad, CF}_3$) with cobalt(II) was demonstrated and key factors involved in the assembly of mononuclear versus dinuclear metal complexes of these ligands were observed. In these studies, it was observed that only the $\text{H}_3\text{L}^{\text{iPr}}$, $\text{H}_3\text{L}^{\text{tBu}}$, $\text{H}_3\text{L}^{\text{Ph}}$, $\text{H}_3\text{L}^{\text{CF}_3}$ were able to form dinuclear species. We propose that the steric bulk of the carboxamide substituents in these ligands can regulate the coordination motifs adopted by these complexes. For example, the adamantyl substituted ligand ($\text{H}_3\text{L}^{\text{Ad}}$) did not form a dinuclear species with cobalt(II). This suggests that very bulky R-groups are required to prevent the formation of dinuclear species.

The trifluoromethyl-substituted ligand ($\text{H}_3\text{L}^{\text{CF}_3}$) provided insights into the electronic factors involved in controlling the assembly of mononuclear versus dinuclear metal complexes of these ligands. The use of this ligand was limited to the formation of a dinuclear species. We speculate that the monomeric species $[\text{Co}(\text{HL}^{\text{CF}_3})_2]^{2-}$ could not be successfully assembled due to the inductive effect that the electron-withdrawing groups induced on each *N*-amidate group. Placing this electron-withdrawing group on the carboxamide arms of the ligand substantially lowers the pKa on the acidic $\text{N-H}_{\text{Amidate}}$ protons making them more labile for deprotonation with a base. This effect is quite common, as it has been shown to considerably have an effect on the deprotonation of acyl-substituted amino acid derivatives and other reported ligand moieties.⁴⁴ Additionally, an electron-withdrawing group on the carboxamide would decrease electron donation into the metal center, making the metal more electrophilic.

It was speculated that the carboxamide substituents in these ligands could be used to regulate the redox properties, through inductive effects, of the resulting metal complexes. Using the redox potentials observed in the cobalt(II) mononuclear complexes, we can firmly say that the ligand redox potentials can be adjusted over an 83 mV range through varying the acyl substitution at the carboxamide arms of the ligand. More importantly, the coordination chemistry for the mononuclear complexes at the bound cobalt(II) center remains unchanged, suggesting that these ligand modifications can be used to tune the redox potentials for a particular substrate of interest.

The molecular structures of the cobalt dimers are remarkably similar. Structurally, the dinuclear cobalt(II) complexes, $[\text{Co}_2(\text{L}^{\text{R}})_2]^{2-}$ ($\text{R} = \text{Ph}, \text{'Bu}$ and CF_3), have nearly the same distorted see-saw geometry with minor metrical differences in their primary coordination spheres. The preceding X-ray diffraction studies demonstrate that bis(amidophenyl)amine ligands $\text{NH}(\text{o-PhNHC(O)R})_2$ ($(\text{H}_3\text{L}^{\text{R}})$ $\text{R} = \text{'Bu}, \text{Ph}, \text{Ad}, \text{CF}_3$) can be used to stabilize four-coordinate cobalt(II) complexes with distorted seesaw geometries (for the dimers) and distorted tetrahedral geometries (in the case of the monomers). Bimetallic cores are ubiquitous in nature and they are known to carry out a wide scope of enzymatic processes.⁴⁵ Although bimetallic complexes with diamond cores are ubiquitous, those that exhibit well-characterized interactions between the metals are much less common. We have explored the coordination chemistry of the $(\text{HN}(\text{o-PhNHC(O)}^i\text{Pr})_2)$ ligand ($\text{H}_3\text{L}^{i\text{Pr}}$) with a host of inexpensive and redox-active metal ions ($\text{Fe}^{\text{II}}, \text{Ni}^{\text{II}}, \text{Cu}^{\text{II}}, \text{Zn}^{\text{II}}$). The $(\text{HN}(\text{o-PhNHC(O)}^i\text{Pr})_2)$ ligand ($\text{H}_3\text{L}^{i\text{Pr}}$) was metalated with these ions and found to stabilize a series of dimeric complexes, in which the deprotonated amine of the ligand backbone bridges the two metal ion ($\text{Fe}^{\text{II}}, \text{Ni}^{\text{II}}, \text{Cu}^{\text{II}}, \text{Zn}^{\text{II}}$) centers. These studies demonstrate that bis(amidophenyl)amine

ligands systems show different coordination chemistry than their previously reported bis(amido)amine counterparts reported by Schrock and co-workers.²² The molecular structures of the dinuclear Fe^{II}, Ni^{II}, Cu^{II}, Zn^{II} species are architecturally similar to the cobalt(II) dinuclear complexes. A limited number of well-characterized solid-state structures of dinuclear late, first-row metal complexes with amido-bridging ligands have been reported, and none of them involve an iron(II) species with such a short Fe...Fe through-space distance as observed in (PPh₄)₂[Fe₂(L^{Pr})₂] (2.3507(19) Å). Diiron systems formed by chelating ligand scaffolds and carboxylate bridging ligands as functional models for non-heme iron enzymes are perhaps the most common type of diiron systems, most of which have large Fe...Fe through-space separation distances (greater than 2.7 Å).⁴⁶

Structurally characterized synthetic dicopper systems of the Cu₂N₂ diamond core system are typically rare. From a structural point of view, the molecular structure of the dinuclear copper(II) complex, (PPh₄)₂[Cu₂(L^{Pr})₂] in this study, is distinctive and is of great relevance to small molecule model complexes for the Cu_A site in cytochrome *c* oxidase. Only a small number of synthetic systems have been able to achieve a diamond core coordination environment that brings two copper ions at close proximity to reproduce the short Cu...Cu distance observed in the enzyme (~2.5 Å).⁴⁷ Peters and co-workers have made a significant contribution to this field with their reports on an amido-bridged Cu₂N₂ system supported by the bis(2-*tert*-butylsulfanylphenyl)amide tridentate ligand,^{37b} and phosphido-bridged dicopper systems supported by bis(phosphinophenyl)phosphide ligands.³⁶⁻³⁷ Their studies provided structural, spectroscopic, and electrochemical information on these systems and its resemblance to the enzyme. In spite of the results, amido-bridged Cu₂N₂ dicopper systems supported by bis(amidophenyl)amine ligands, to our knowledge, have never been

synthesized and structurally characterized. The structural and electrochemical results reported here suggest that the complex $(\text{PPh}_4)_2[\text{Cu}_2(\text{L}^{i\text{Pr}})_2]$ can be a suitable synthetic model for the CuA active site, capable of facilitating reversible redox behavior.

The results presented herein demonstrate the tridentate, trianionic ligand $\text{N}(o\text{-PhNHC(O)}^i\text{Pr})_2]^{3-}$ ($[\text{H}_3\text{L}^{i\text{Pr}}]^{3-}$) as an architectural scaffold that can stabilize amido-bridging bimetallic complexes with M_2N_2 diamond core. These types of species are highly sought after for their potential to generate robust metal centers capable of carrying out bond activation reactions. Though a number of similar synthetic systems have previously been reported, bimetallic complexes with M_2N_2 diamond cores that incorporate redox-active ligands remains far less explored.^{33a, 33b, 39, 48}

Section 2-5. Conclusion

This study describes the synthesis and characterization of a series of cobalt(II) complexes with coordinatively versatile bis(amidophenyl)amine pincer ligands. These ligands demonstrate their ability of acting as tridentate (trianionic) or bidentate (dianionic) and are designed to vary the properties at the cobalt(II) centers via modifying the sterics and electronics of the acyl group on the ligand amidate arms. These modifications prove to control the assembly of mononuclear versus dinuclear cobalt(II) complexes. Additionally, these studies report the synthesis of dinuclear complexes of late-first-row transition metal ions (Fe^{II} , Ni^{II} , Cu^{II} , Zn^{II}) supported by the bis(2-isobutyrylamidophenyl)amine ($\text{HN}(o\text{-PhNHC(O)}^i\text{Pr})_2$) ligand ($\text{H}_3\text{L}^i\text{Pr}$). The results presented herein demonstrate that the trianionic, tridentate NNN redox-active pincer bis(amidophenyl)amine ligand system is a highly attractive scaffold to generate bimetallic diamond core systems.

These systems are particularly interesting, as they have been made with the intention to develop novel late first-row transition metal complexes capable of performing catalytic aerobic oxidations. We believe these species may be uniquely poised for dioxygen activation to carry out aerobic oxidation reactions. The $\text{M}\cdots\text{M}$ through-space distances in the diamond cores may allow both metal centers to interact with a single dioxygen ligand. For these reasons, we envisage the bimetallic complexes of Fe^{II} , Ni^{II} , Cu^{II} , and Zn^{II} to be robust oxidation catalysts. Detailed mechanistic, spectroscopic, and structural investigations on the reactivity of the mononuclear and dinuclear cobalt(II) systems with dioxygen are described in Chapter 3.

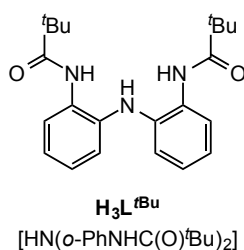
Section 2-6. Experimental Section

Section 2-6-1. General Considerations and Materials

All manipulations were carried out using standard Schlenk techniques or conducted in an MBraun Labmaster 130 drybox under a nitrogen atmosphere. All reagents used were purchased from commercial vendors and used as received unless otherwise noted. Anhydrous solvents were purchased from Sigma-Aldrich and further purified by sparging with Ar gas followed by passage through activated alumina columns. Midwest Microlab, LLC, performed elemental analyses. ^1H , ^{13}C , and ^{19}F NMR spectra were recorded on an Inova 400 MHz spectrometer at ambient temperature. ^1H and ^{13}C chemical shifts were referenced to residual solvent peaks. ^{19}F NMR chemical shifts were referenced relative to an external reference ($\text{C}_6\text{H}_5\text{CF}_3$). Solid-state infrared spectra were recorded as KBr pellets on a Varian Scimitar 800 Series FTIR spectrophotometer. UV-Visible absorption spectra were recorded on a Cary50 spectrophotometer using 1.0 cm quartz cuvettes. UV-Visible near-infrared absorption spectra were recorded on a UV-3101PC Shimadzu UV-Vis NIR scanning spectrophotometer using 1.0 cm quartz cuvettes. Solution-state magnetic moments were measured using the method of Evans.³⁸ Mass spectra were recorded in the Mass Spectrometry Center at Emory University on a JEOL JMS-SX102/SX102A/E mass spectrometer. X-ray diffraction studies were carried out in the X-ray Crystallography Laboratory at Emory University on a Bruker Smart 1000 CCD diffractometer. Cyclic voltammetry experiments were carried out using a CH Instruments (Austin, TX) Model 660C potentiostat. All experiments were conducted in CH_2Cl_2 (unless indicated) with 0.10 M tetrabutylammonium hexafluorophosphate as the supporting electrolyte. Electrochemical experiments were

conducted in a three-component cell consisting of a Pt auxiliary electrode, a non-aqueous reference electrode (Ag/AgNO₃), and a glassy carbon-working electrode. All electrochemical measurements are referenced and reported versus the ferrocene/ferrocenium (Fc/Fc⁺) couple.

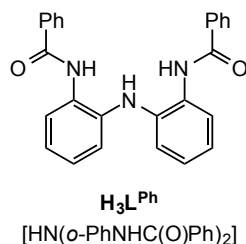
Section 2-6-2. Ligand Syntheses



2,2'-Bis(*tert*-butylacetamido)diphenylamine (HN(*o*-PhNHC(O)^{tBu})₂) [H₃L^{tBu}]:

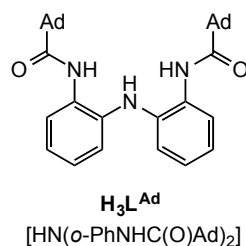
A suspension of HN(*o*-PhNH₂)₂²⁹ (3.50 g, 0.0176 mmol) in dichloromethane (DCM, 50 mL) was lowered to 0 °C under an atmosphere of N₂. Triethylamine (4.90 mL, 0.00352 mmol) was then added, followed by the drop-wise addition pivaloyl chloride (4.30 mL, 0.0352 mmol) via a dropper funnel. The mixture was stirred at 0 °C for 1 h. The reaction mixture was slowly warmed to room temperature and stirred for an additional 24 h. The resulting pale brown-colored solution was extracted with saturated aqueous NaHCO₃ (3 x 30 mL) and brine (2 x 20 mL), and the organic layer was dried over magnesium sulfate, filtered, and concentrated in vacuo. The crude solid was recrystallized by slow diffusion of diethyl ether into a concentrated DCM solution of the product (5.20 g, 80 %). ¹H NMR (δ, CDCl₃, 400 MHz): (ppm) 7.71 - 7.69 (m, 1H), 7.69 - 7.65 (m, 3H), 7.11 - 7.00 (m, 4H), 6.90 (dd, *J* = 7.8

Hz, 1.6 Hz, 2H), 6.15 - 6.07 (m, 1H), 1.21 (d, $J = 0.6$ Hz, 19H); ^{13}C NMR (CDCl_3 , 75.5 MHz): (δ , ppm) 177.32, 135.75, 129.203, 126.00, 123.47, 122.99, 121.013, 39.54, 27.48. FTIR (KBr, cm^{-1}): $\nu(\text{NH})_{\text{Amine}}$ 3343, $\nu(\text{NH})_{\text{Amide}}$ 3428, $\nu(\text{CO})$ 1685. HRESI-MS: $\text{C}_{22}\text{H}_{30}\text{N}_3\text{O}_2$ m/z Calcd. 368.233 Found 368.23305 $[\text{M} + \text{H}]^+$.



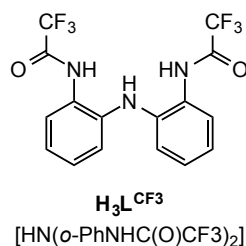
2,2'-Bis(diphenylacetamido)diphenylamine ($\text{HN}(o\text{-PhNHC(O)Ph})_2$) [$\text{H}_3\text{L}^{\text{Ph}}$]:

A suspension of $\text{HN}(o\text{-PhNH}_2)_2$ ²⁹ (6.312 g, 31.68 mmol) in dichloromethane (DCM, 50 mL) was lowered to 0 °C under an atmosphere of N_2 . Triethylamine (9.75 mL, 63.36 mmol) was then added, followed by benzoyl chloride (8.10 mL, 63.36 mmol). The mixture was stirred at 0 °C for 1 h. The reaction mixture was slowly warmed to room temperature and stirred for an additional 20 h. The resulting pale brown solution was extracted with saturated aqueous NaHCO_3 (3 x 30 mL), and the organic layer was dried over magnesium sulfate, filtered, and concentrated in vacuo. The crude solid was recrystallized by layering hexanes over a concentrated DCM solution of the product (10.98 g, 85 %). ^1H NMR (δ , CDCl_3 , 400 MHz): (ppm) 8.35 (s, 1H, $\text{NH}(\text{CO})$), 7.73 - 7.80 (m, 6H, ArH), 7.49 (t, 2H $J = 4.4$ Hz, $J = 9.6$ Hz, ArH), 7.38 (t, 2H, $J = 10.4$ Hz, $J = 9.6$ Hz ArH), 7.13 - 7.01 (m, 6H, ArH), 6.12 (s, 1H, NH); ^{13}C NMR (δ , CDCl_3 , 75.5 MHz): (ppm) 166.39, 136.22, 134.23, 132.07, 129.063, 128.77, 127.62, 126.72, 124.53, 123.05, 120.95. FTIR (KBr, cm^{-1}): $\nu(\text{NH})$ 3386, 3292, $\nu(\text{CO})$ 1658. HRESI-MS: $\text{C}_{26}\text{H}_{21}\text{N}_3\text{O}_2$ m/z Calcd. 407.1634, Found 407.1626 $[\text{M}]^+$.



2,2'-Bis(adamantylacetamido)diphenylamine (HN(*o*-PhNHC(O)Ad)₂) [H₃L^{Ad}]:

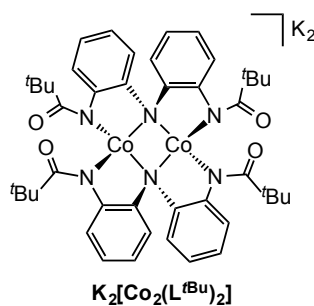
The parent amine HN(*o*-PhNH₂)₂²⁹ (3.10 g, 15.56 mmol) and 1-adamantanecarbonyl chloride (6.20 g, 31.12 mmol) were placed in a 250 mL round bottom flask and was placed under an atmosphere of N₂. Anhydrous dichloromethane (DCM, 100 mL) was added via cannula and the suspension was lowered to 0 °C. Triethylamine (2.60 mL, 31.12 mmol) was then added dropwise throughout the duration of 1 h. After all triethylamine was added, the mixture was stirred at 0 °C for an additional 2 h. The reaction mixture was slowly warmed to room temperature and stirred for an additional 20 h. The resulting pale brown solution was extracted with saturated aqueous NaHCO₃ (3 x 30 mL), and the organic layer was dried over magnesium sulfate, filtered, and concentrated in vacuo. The crude solid was recrystallized by layering hexanes over a concentrated DCM solution of the product (6.60 g, 81 %). ¹H NMR (δ, CDCl₃, 400 MHz): (ppm) 7.71 (dd, J = 2.0 Hz, J = 2.4 Hz, 2H, ArH), 7.08 - 6.97 (m, 4H), 6.90 (dd, J = 2.8 Hz, 2.4 Hz, 2H, ArH), 7.66 (s, 1H, NH(CO)), 7.08 - 6.97 (m, 4H, ArH), 6.09 (s, 1H, NH), 2.02 (s, 2H, CH), 1.85 (d, J = 3.6 Hz, CH₂), 1.69 (dd, J = 28.4 Hz, 27.6 Hz); ¹³C NMR (δ, CDCl₃, 75.5 MHz): (ppm) 176.93, 135.84, 129.40, 125.97, 123.62, 123.07, 1210.15, 41.63, 39.23, 36.54, 28.27. FTIR (KBr, cm⁻¹): ν(NH) 3410, 3318, ν(CO) 1655. HRESI-MS: C₃₄H₄₁N₃O₂ m/z Calcd. 524.3277, Found 524.3235 [M+1]⁺.



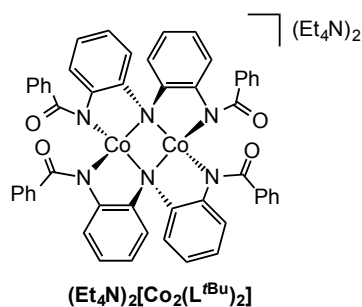
2,2'-Bis(trifluoroacetamido)diphenylamine (HN(*o*-PhNHC(O)CF₃)₂) [$\text{H}_3\text{L}^{\text{CF}_3}$]:

A suspension of HN(*o*-PhNH₂)₂ (2.55 g, 12.8 mmol) in dichloromethane (DCM, 50 mL) was lowered to 0 °C under an atmosphere of N₂. Triethylamine (3.60 mL, 25.8 mmol) was then added, followed by trifluoroacetic anhydride (3.60 mL, 14.5 mmol). The mixture was stirred at 0 °C for 1 h. The reaction mixture was slowly warmed to room temperature and stirred for an additional 20 h. The resulting pale brown solution was extracted with saturated aqueous NaHCO₃ (3 x 30 mL), and the organic layer was dried over magnesium sulfate, filtered, and concentrated in vacuo. The crude solid was recrystallized by layering hexanes over a concentrated DCM solution of the product (1.78 g, 80 %). ¹H NMR (δ, CDCl₃, 400 MHz): (ppm) 8.33 (s, 1H, NH(CO)), 7.67 (d, 2H, J = 1.6 Hz, ArH), 7.04 (m, 4H, ArH), 6.88 (d, 2H, J = 1.2 Hz, ArH), 5.52 (s, 1H, NH); ¹³C NMR (δ, CDCl₃, 75.5 MHz): (ppm) 131.93, 129.50, 127.73, 127.20, 125.29, 123.90, 1122.36, 110.73; ¹⁹F NMR (δ, CDCl₃, 400 MHz): (ppm) 75.88. FTIR (KBr, cm⁻¹): ν(NH) 3298, ν(CO) 1701. HRESI-MS: C₁₆H₁₁F₆N₃O₂ m/z Calcd. 392.083, Found 392.083 [M+1]⁺.

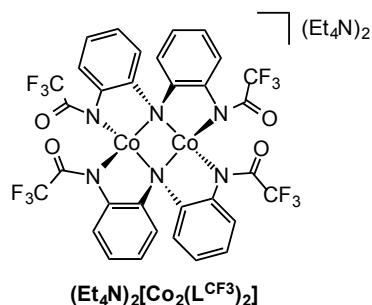
Section 2-6-3. Complex Syntheses



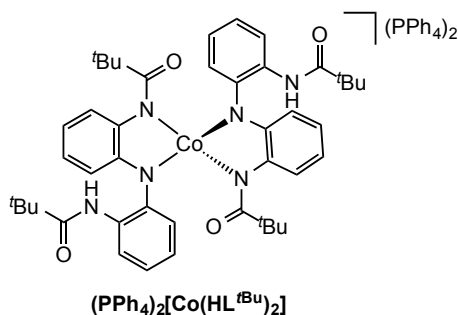
$\text{K}_2[\text{Co}_2(\text{L}^{\text{tBu}})_2]$: To a solution of $[\text{HN}(o\text{-PhNHC}(\text{O})^{\text{tBu}})_2]$ ($\text{H}_3\text{L}^{\text{tBu}}$) (120.0 mg, 0.3265 mmol) in dry dimethylformamide (DMF, 10 mL) was added potassium hydride (39.30 mg, 0.9705 mmol). When gas evolution ceased, CoBr_2 (71.43 mg, 0.3265 mmol) was added as a solid and the mixture stirred for 1 h. After stirring for 3 h, DMF was removed under high vacuum and the resulting solid was dissolved in CH_3CN (15 mL), filtered through a medium porosity frit, and the filtrate was concentrated to dryness. Deep green X-ray diffraction quality crystals were obtained by slow diffusion of diethyl ether into a concentrated CH_3CN solution of $\text{K}_2[\text{Co}_2(\text{L}^{\text{tBu}})_2]$ (65 %, 128.4 mg). ^1H NMR (δ , CD_3CN , 400 MHz): (ppm) -1.372 (s), 38.753 (s), 44.278 (s), 54.962(s). FTIR (KBr, cm^{-1}): $\nu(\text{CO})$ 1664. $\mu_{\text{eff}} = 4.67(6)$ μB (Evans Method, CD_2Cl_2 , 298K). λ_{max} , nm (ϵ , $\text{M}^{-1}\text{cm}^{-1}$) (CH_3CN): 587 (764), 820 (245) sh. ESI-MS: for $(\text{K}[\text{Co}_2(\text{L}^{\text{tBu}})_2])^-$ m/z Calcd. 1024.1310, Found 1024.16936; for $[\text{Co}_2(\text{L}^{\text{tBu}})_2]^{1-}$ m/z Calcd. 846.29 Found 846.27.



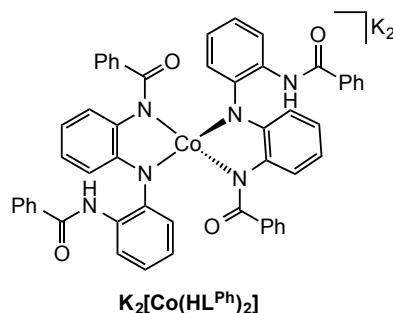
$(\text{Et}_4\text{N})_2[\text{Co}_2(\text{L}^{\text{Ph}})_2]$: To a solution of $[\text{HN}(o\text{-PhNHC(O)Ph})_2]$ ($\text{H}_3\text{L}^{\text{Ph}}$) (150.0 mg, 0.3681 mmol) in dry dimethylformamide (DMF, 10 mL) was added potassium hydride (44.30 mg, 1.104 mmol). When gas evolution ceased, CoBr_2 (80.52 mg, 0.3681 mmol) was added as a solid and the mixture stirred for 1 h. Tetraethylammonium bromide (77.37 mg, 0.3681 mmol) was then added to the deep green solution. After stirring for 3 h, DMF was removed under high vacuum and the resulting solid was dissolved in CH_3CN (15 mL), filtered through a medium porosity frit, and the filtrate was concentrated to dryness. Deep green X-ray diffraction quality crystals were obtained by slow diffusion of diethyl ether into a concentrated CH_3CN solution of $(\text{Et}_4\text{N})_2[\text{Co}_2(\text{L}^{\text{Ph}})_2]$ (75 %, 164 mg). ^1H NMR (δ , CD_3CN , 400 MHz): (ppm) -106.72 (s), -9.521 (s), -3.736 (s), 6.87 (s), 25.93 (s), 28.78 (s), 61.89 (s). Solid-state FTIR (KBr, cm^{-1}): $\nu(\text{CO})$ 1655. $\mu_{\text{eff}} = 4.48(4)$ μB (Evans Method, CD_2Cl_2 , 298K). λ_{max} , nm (ϵ , $\text{M}^{-1}\text{cm}^{-1}$) (CH_3CN): 597 (764), 936 (276). ESI-MS: for $[\text{Co}_2(\text{L}^{\text{Ph}})_2]^{2-}$ m/z Calcd. 463.073, Found 463.073.



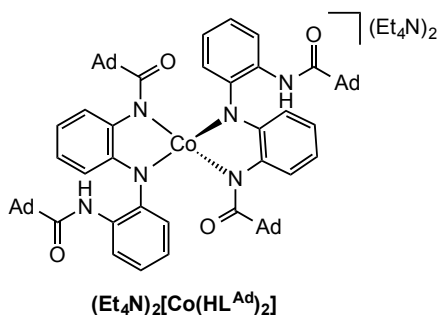
$(\text{Et}_4\text{N})_2[\text{Co}_2(\text{L}^{\text{CF}_3})_2]$: To a solution of $\text{HN}(o\text{-PhNHC(O)CF}_3)_2$ ($\text{H}_3\text{L}^{\text{CF}_3}$) (140.0 mg, 0.3578 mmol) in anhydrous dimethylformamide (DMF, 10 mL) was added potassium hydride (43.10 mg, 1.075 mmol). When gas evolution ceased, CoBr_2 (78.30 mg, 0.3579 mmol) was added as a solid and the mixture was stirred for 1 h. Tetraethylammonium bromide (75.20 mg, 0.3579 mmol) was then added to the deep magenta-teal solution. After stirring for 3 h, DMF was removed under high vacuum and the resulting solid was dissolved in CH_3CN (15 mL), filtered through a medium porosity frit, and the filtrate was concentrated to dryness. Deep teal X-ray diffraction quality crystals were obtained by slow diffusion of diethyl ether into a concentrated CH_3CN solution of $(\text{Et}_4\text{N})_2[\text{Co}_2(\text{L}^{\text{CF}_3})_2]$ (65%, 134 mg). ^1H NMR (CD_3CN , 400 MHz): (δ , ppm) -1.372 (s), 38.753 (s), 44.278 (s), 54.962(s). ^{19}F NMR (CD_3CN , 400 MHz): (δ , ppm) -57.139 (s). Solid-state FTIR (KBr, cm^{-1}): $\nu(\text{CO})$ 1637. $\mu_{\text{eff}} = 4.82(7)$ μB (Evans Method, CD_3CN , 298K). λ_{max} , nm (ϵ , $\text{M}^{-1}\text{cm}^{-1}$) (CH_3CN): 597 (360), 876 (31). ESI-MS: for $(\text{Et}_4\text{N})[\text{Co}_2(\text{L}^{\text{CF}_3})_2]^-$ m/z Calcd. 1024.1310 Found 1024.16936; for $[\text{Co}_2(\text{L}^{\text{CF}_3})_2]^{2-}$ m/z Calcd. 446.986, Found 446.99085; Anal. Calcd (found) for $(\text{Et}_4\text{N})_2[\text{Co}_2(\text{L}^{\text{CF}_3})_2]$: C, 49.92 (48.88); H, 4.82 (4.72); N, 9.70 (9.30).



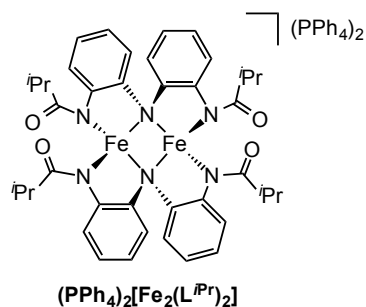
(PPh₄)₂[Co(HL^{tBu})₂]: To a solution of [HN(*o*-PhNHC(O)^{tBu})₂] (H₃L^{tBu}) (165.0 mg, 0.4280 mmol) in dry dimethylformamide (DMF, 10 mL) was added potassium hydride (34.33 mg, 0.8560 mmol). When gas evolution ceased, CoBr₂ (46.81 mg, 0.2140 mmol) was added as a solid and the mixture stirred for 1 h. Tetraphenylphosphonium bromide (179.50 mg, 0.4280 mmol) was then added to the deep red solution. After stirring for 3 h, DMF was removed under high vacuum and the resulting solid was dissolved in CH₃CN (15 mL), filtered through a medium porosity frit, and the filtrate was concentrated to dryness. Deep red X-ray diffraction quality crystals were obtained by slow diffusion of diethyl ether into a concentrated CH₃CN solution of (PPh₄)₂[Co(HL^{tBu})₂] (70%, 220 mg). ¹H NMR (CD₃CN, 400 MHz): (δ, ppm) -63.61 (s), -56.85 (s), -53.79 (s), -52.48 (s), -48.69 (s), -13.87 (s), -11.25 (s), -2.73 (s), 12.55 (s), 17.43 (s), 18.16 (s), 19.16 (s), 22.90 (s), 23.83 (s), 30.62 (s), 32.50 (s), 37.26 (s), 42.31 (s), 62.75 (s), 66.54 (s), 71.98 (s), 82.85 (s). FTIR (KBr, cm⁻¹): ν(NH) 3381, ν(CO) 1655. μ_{eff} = 4.42(4) μB (Evans Method, CD₂Cl₂, 298K). λ_{max}, nm (ε, M⁻¹cm⁻¹) (CH₃CN): 588 (606), 553 (563) sh. ESI-MS: for (PPh₄)[Co(HL^{tBu})₂]⁻ m/z Calcd. 1024.1310 Found 1024.16936; for [Co(HL^{tBu})₂]²⁻ m/z Calcd. 446.986 Found 446.99085.



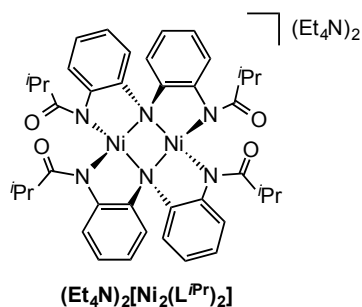
$\text{K}_2[\text{Co}(\text{HL}^{\text{Ph}})_2]$: To a solution of $[\text{HN}(o\text{-PhNHC(O)Ph})_2]$ ($\text{H}_3\text{L}^{\text{Ph}}$) (130.0 mg, 0.3190 mmol) in dry dimethylformamide (DMF, 10 mL) was added potassium hydride (25.6 mg, 0.6381 mmol). When gas evolution ceased, CoBr_2 (34.9 mg, 0.1595 mmol) was added as a solid and the mixture stirred for 1 h. After stirring for 3 h, DMF was removed under high vacuum and the resulting solid was dissolved in CH_3CN (15 mL), filtered through a medium porosity frit, and the filtrate was concentrated to dryness. Deep red X-ray quality crystals were obtained by slow diffusion of diethyl ether into a concentrated CH_3CN solution of $\text{K}_2[\text{Co}(\text{HL}^{\text{Ph}})_2]$ (55%, 83.1 mg). $^1\text{H NMR}$ (CD_3CN , 400 MHz): (δ , ppm) -70.03 (s), -63.80 (s), -46.48 (s), -37.23 (s), -16.31 (s), -14.7 (s), -4.11 (s), 1.32 (s), 3.60 (s), 4.90 (s), 6.36 (s), 8.56 (s), 9.22 (s), 12.39 (br), 17.67 (br), 23.44 (s), 27.01 (s), 56.50 (s), 60.54 (s). FTIR (KBr, cm^{-1}): $\nu(\text{NH})$ 3371, 3294, $\nu(\text{CO})$ 1660. $\mu_{\text{eff}} = 4.39(5) \mu\text{B}$ (Evans Method, CD_2Cl_2 , 298K). λ_{max} , nm (ϵ , $\text{M}^{-1}\text{cm}^{-1}$) (CH_3CN): 588 (652), 552 (622) sh. ESI-MS: for $[\text{Co}(\text{HL}^{\text{Ph}})_2]^-$ m/z Calcd. 869.230 Found 869.251, for $[\text{Co}(\text{HL}^{\text{Ph}})_2]^{2-}$ m/z Calcd. 434.615 Found 434.625.



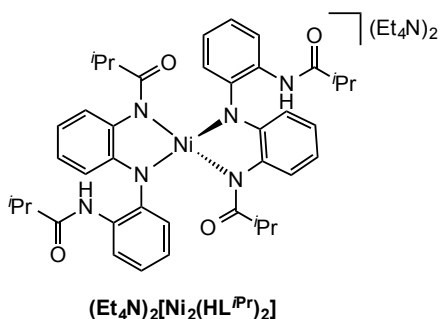
(Et₄N)₂[Co(HL^{Ad})₂]: To a solution of [HN(*o*-PhNHC(O)Ad)₂] (H₃L^{Ad}) (125 mg, 0.2387 mmol) in dry dimethylformamide (DMF, 10 mL) was added potassium hydride (19.2 mg, 0.4774 mmol). When gas evolution ceased, CoBr₂ (26.1 mg, 0.1193 mmol) was added as a solid and the mixture stirred for 1 h. Tetraethylammonium bromide (50.2 mg, 0.2387 mmol) was then added to the deep magenta-teal solution. After stirring for 3 h, DMF was removed under high vacuum and the resulting solid was dissolved in CH₃CN (15 mL), filtered through a medium porosity frit, and the filtrate was concentrated to dryness. Deep red X-ray diffraction quality crystals were obtained by slow diffusion of diethyl ether into a concentrated CH₃CN solution of (Et₄N)₂[Co₂HL^{Ad}]₂] (75%, 197 mg). ¹H NMR (CD₃CN, 400 MHz): (δ, ppm) -80.92 (s), -75.31 (s), -49.28 (s), -13.55 (s), -12.18 (s), -6.74 (s), 7.129 (s), 9.05 (s) 10.32 (s), 24.95 (s), 20.48 (s), 13.72 (s), 38.753 (s), 57.33 (s), 78.09(s). FTIR (KBr, cm⁻¹): ν(NH) 3387, ν(CO) 1655. μ_{eff} = 4.30(6) μB (Evans Method, CD₂Cl₂, 298K). λ_{max}, nm (ε, M⁻¹cm⁻¹) (CH₃CN): 573 (636), 557 (594) sh. ESI-MS: for (Et₄N)[Co(HL^{Ad})₂]⁻ m/z Calcd. 1024.1310 Found 1024.16936; for [Co(HL^{Ad})₂]²⁻ m/z Calcd. 446.986 Found 446.99085.



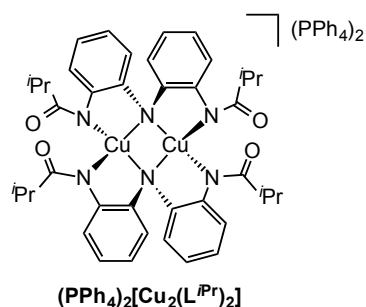
$(PPh_4)_2[Fe_2(L^{iPr})_2]$: To a solution of $[HN(o\text{-}PhNHC(O)^iPr)_2]$ (H_3L^{iPr}) (206.0 mg, 0.6076 mmol) in dry dimethylformamide (DMF, 10 mL) was added potassium hydride (73.12 mg, 1.823 mmol). When gas evolution ceased, $Fe(OAc)_2$ (105.67 mg, 0.607 mmol) was added as a solid and the mixture stirred for 1 h. Tetraphenylphosphonium bromide (254.7 mg, 0.607 mmol) was then added to the yellow solution. After stirring for 3 h, DMF was removed under high vacuum and the resulting solid was dissolved in CH_3CN (15 mL), filtered through a medium porosity frit, and the filtrate was concentrated to dryness. Dark brown X-ray diffraction quality crystals were obtained by slow diffusion of diethyl ether into a concentrated CH_3CN solution of $(PPh_4)_2[Fe_2(L^{iPr})_2]$ (260.5 mg, 59%). 1H NMR (CD_3CN , 400 MHz): (δ , ppm) -63.947 (s), -8.529 (s), 1.12 (s), 3.41 (s), 5.46 (s), 8.00 (s), 24.54 (s), 57.72 (s), 76.11 (s). FTIR (KBr, cm^{-1}): $\nu(CO)$ 1663. $\mu_{eff} = 4.50(9)$ μ_B (Evans Method, CD_3CN , 298K). λ_{max} , nm (ϵ , $M^{-1}cm^{-1}$) (CH_3CN): 510 (640), 625 (281). Anal. Calcd (found) for $(PPh_4)_2[Fe_2(L^{iPr})_2]$: C, 63.98 (63.64); H, 8.05 (7.95); N, 10.66 (11.01).



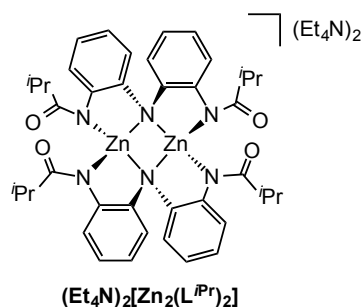
$(\text{Et}_4\text{N})_2[\text{Ni}_2(\text{L}^{\text{iPr}})_2]$: To a solution of $[\text{HN}(o\text{-PhNHC}(\text{O})^{\text{iPr}})_2]$ ($\text{H}_3\text{L}^{\text{iPr}}$) (166.0 mg, 0.4896 mmol) in dry dimethylformamide (DMF, 10 mL) was added potassium hydride (68.73 mg, 0.1714 mmol). When gas evolution ceased, NiBr_2 (106.98 mg, 0.4896 mmol) was added as a solid. After stirring for 3 h, the DMF was removed under high vacuum and the resulting solid was dissolved in CH_3CN (15 mL), filtered through a medium porosity frit, and the filtrate was concentrated to dryness. Deep brown X-ray diffraction quality crystals were obtained by slow diffusion of diethyl ether into a concentrated DMF solution of $\text{K}_2[\text{Ni}_2(\text{L}^{\text{iPr}})_2]$ (140.0 mg, 55%). ^1H NMR (CD_3CN , 400 MHz): (δ , ppm) -6.33 (s), -4.83 (s), 5.17 (s), 12.93 (s), 13.93 (s), 32.5 (s). FTIR (KBr, cm^{-1}): $\nu(\text{CO})$ 1664. $\mu_{\text{eff}} = 2.51(9)$ μB (Evans Method, CDCl_3 , 298K). λ_{max} , nm (ϵ , $\text{M}^{-1}\text{cm}^{-1}$) (CH_3CN): 299 (18800), 452 (1970), 602 (sh), 740 (sh). HRESI-MS: for $[\text{H}^+ + \text{K}[\text{Ni}_2(\text{L}^{\text{iPr}})_2]]^-$ m/z Calcd. 827.177 Found 827.17831. Anal. Calcd (found) for $\text{K}_2[\text{Ni}_2(\text{L}^{\text{iPr}})_2]$: C, 63.98 (63.64); H, 8.05 (7.95); N, 10.66 (11.01).



$(\text{Et}_4\text{N})_2[\text{Ni}(\text{HL}^{\text{iPr}})_2]$: To a solution of $[\text{HN}(o\text{-PhNHC(O)}^{\text{iPr}})_2]$ ($\text{H}_3\text{L}^{\text{iPr}}$) (140.8 mg, 0.4150 mmol) in DMF, (8 mL) was added potassium hydride (36.64 mg, 0.9136 mmol). When gas evolution ceased, NiBr_2 (45.37 mg, 0.2076 mmol) was added as a solid. When the reaction mixture became homogenous, tetraethylammonium bromide (87.27 mg, 0.4150 mmol) was added to the reddish brown solution. After stirring for 3 h, the DMF was removed under high vacuum and the resulting solid was dissolved in CH_3CN (15 mL), filtered through a medium porosity frit, and the filtrate was concentrated to dryness. Reddish-brown crystals were obtained by slow diffusion of diethyl ether into a concentrated CH_3CN solution of $(\text{Et}_4\text{N})_2[\text{Ni}(\text{HL}^{\text{iPr}})_2]$ (47.5 mg, 48%). ^1H NMR (CD_3CN , 400 MHz): (δ , ppm) -70.03 (s), -63.80 (s), -46.48 (s), -37.23 (s), -16.31 (s), -14.7 (s), -4.11 (s), 1.32 (s), 3.60 (s), 4.90 (s), 6.36 (s), 8.56 (s), 9.22 (s), 12.39 (br), 17.67 (br), 23.44 (s), 27.01 (s), 56.50 (s), 60.54 (s). FTIR (KBr, cm^{-1}): $\nu(\text{NH})$ 3396, $\nu(\text{CO})$ 1667. $\mu_{\text{eff}} = 2.07(1) \mu\text{B}$ (Evans Method, CDCl_3 , 298K). λ_{max} , nm (ϵ , $\text{M}^{-1}\text{cm}^{-1}$) (DCM): 636 (sh), 573 (570), 534 (sh).



$(\text{PPh}_4)_2[\text{Cu}_2(\text{L}^{\text{iPr}})_2]$: To a solution of $[\text{HN}(o\text{-PhNHC(O)}^{\text{iPr}})_2]$ ($\text{H}_3\text{L}^{\text{iPr}}$) (185.4 mg, 0.5469 mmol) in dry dimethylformamide (DMF, 10 mL) was added potassium hydride (65.80 mg, 1.640 mmol). When gas evolution ceased, $\text{Cu}(\text{OAc})_2$ (99.30 mg, 0.5469 mmol) was added as a solid and the mixture stirred for 1 h. Tetraphenylphosphonium bromide (229.3 mg, 0.5469 mmol) was then added to the deep purple solution. After stirring for 3 h, DMF was removed under high vacuum and the resulting solid was dissolved in CH_3CN (15 mL), filtered through a medium porosity frit, and the filtrate was concentrated to dryness. Deep purple X-ray diffraction quality crystals were obtained by slow diffusion of diethyl ether into a concentrated CH_3CN solution of $(\text{PPh}_4)_2[\text{Cu}_2(\text{L}^{\text{iPr}})_2]$ (269 mg, 67%). ^1H NMR, (CD_3CN , 400 MHz): (δ , ppm) 0.217 (s, $-\text{CH}_3$), 1.27 (s, $-\text{CH}_3$), 2.14 (s, $-\text{CH}$), 3.071 (s, $-\text{CH}$), 6.50 (s, ArH), 6.688 (s, ArH), 6.993 (s, ArH), 7.77 (m, $-\text{PPh}_4$), 8.36 (s, ArH). FTIR (KBr, cm^{-1}): $\nu(\text{CO})$ 1669. λ_{max} , nm (ϵ , $\text{M}^{-1}\text{cm}^{-1}$) (CH_3CN): 522 (4775), 595 (sh, 4065), 735 (2959), 962 (6500), 1697 (780). HRESI-MS: for $[\text{H}^+ + (\text{Cu}_2(\text{L}^{\text{iPr}})_2)^{-}]^{\text{m/z}}$ Calcd. 799.210 Found 799.22845. Anal. Calcd (found) for $(\text{PPh}_4)_2[\text{Cu}_2(\text{L}^{\text{iPr}})_2]$: C, 71.48 (71.26); H, 5.73 (5.87); N, 5.68 (5.72).



$(\text{Et}_4\text{N})_2[\text{Zn}_2(\text{L}^{\text{iPr}})_2]$: To a solution of $[\text{HN}(o\text{-PhNHC}(\text{O})^{\text{iPr}})_2]$ ($\text{H}_3\text{L}^{\text{iPr}}$) (88.5 mg, 0.261 mmol) in dry dimethylformamide (DMF, 5 mL) was added potassium hydride (31.4 mg, 0.7830 mmol). When gas evolution ceased, ZnBr_2 (59.0 mg, 0.261 mmol) was added as a solid and the mixture stirred for 1 h. Tetraethylammonium bromide (54.85 mg, 0.2610 mmol) was then added to the yellow solution. After stirring for 3 h, DMF was removed under high vacuum and the resulting solid was dissolved in CH_3CN (10 mL), filtered through a medium porosity frit, and the filtrate was concentrated to dryness. Colorless X-ray diffraction quality crystals were obtained by layering diethyl ether into a concentrated CH_3CN solution of $(\text{Et}_4\text{N})_2[\text{Zn}_2(\text{L}^{\text{iPr}})_2]$ (120 mg, 86%). ^1H NMR, (CD_3CN , 400 MHz): (δ , ppm) 0.64 (d, -CH₃), 1.06 (d, CH₃), 1.13 (m, -NEt₄), 2.41 (m, -CH), 3.01 (m, -NEt₄), 6.55 (m, ArH), 6.74 (m, ArH), 6.52 (m, ArH). FTIR (KBr, cm^{-1}): $\nu(\text{CO})$ 1664. HRESI-MS: for $[\text{H}^+ + (\text{Zn}_2(\text{L}^{\text{iPr}})_2)]^{-1}$ m/z Calcd. 803.205 Found 803.213. Anal. Calcd (found) for $(\text{Et}_4\text{N})_2[\text{Zn}_2(\text{L}^{\text{iPr}})_2]$: C, 63.21 (61.92); H, 7.96 (7.84); N, 10.53 (10.35).

Section 2-6-4. X-ray Crystallographic Data of Complexes

Data were collected using a Bruker APEX-II CCD diffractometer equipped with an Oxford cryosystems low-temperature apparatus operating at the indicated temperature. All structures were solved in their respective space groups and crystal systems by direct methods using the XT (Sheldrick, 2008) structure solution program and refined by Least Squares using version of ShelXL-97 (Sheldrick, 2008). All non-hydrogen atoms were refined anisotropically. Hydrogen atom positions were calculated geometrically and refined using the riding model.

Table 2-8. Structural refinement data for dinuclear cobalt(II) complexes $K_2[Co_2(L^{tBu})_2]$, $(Et_4N)_2[Co_2(L^{Ph})_2]$ and $(Et_4N)_2[Co_2(L^{CF_3})_2]$.

	$K_2[Co_2(L^{tBu})_2]$	$(Et_4N)_2[Co_2(L^{Ph})_2]^a$	$(Et_4N)_2[Co_2(L^{CF_3})_2]$
Formula	$C_{44}H_{52}N_6O_4K_2Co_2$	$C_{70}H_{79}N_9O_4Co_2$	$C_{52}H_{66}Co_2F_{12}N_8O_5$
Form. Wt.			
(g/mol)	924.98	1228.28	1228.99
T (K)	293(2)	110(2)	293(2)
Crystal system	Orthorhombic	Trigonal	Monoclinic
Space group	Fddd	$P3_21$	$P21/n$
<i>a</i> (Å)	10.8136(3)	14.064(3)	10.072(2)
<i>b</i> (Å)	27.5330(7)	14.064(3)	38.683(8)
<i>c</i> (Å)	29.5266(8)	27.143(5)	14.706(3)
α (°)	90	90	90
β (°)	90	90	98.28(3)
γ (°)	90	120	90
V (Å³)	8791.0(4)	4649(2)	5670.2(19)
Z	8	3	4
ρ, calcd (g/cm³)	1.398	1.672	1.4396
m/mm-1	7.994	0.59	0.677
Crystal size			
(mm³)	$0.27 \times 0.13 \times 0.12$	$0.40 \times 0.35 \times 0.28$	$0.37 \times 0.13 \times 0.12$
Theta range	8.78 to 135.82	3.34 to 54.26°	3.5 to 57.4°
Reflns. Collected	15480	20628	101428
Unique reflns.	1971	4466	14606
Data/rest./par.	1971/0/133	6831/15/487	14606/0/722
GOF	1.028	1.052	1.02
Final R indexes			
[I>2σ (I)]	R1 = 0.0288	R1 = 0.0814	R1 = 0.0609
All data	wR2 = 0.0811	wR2 = 0.2493	wR2 = 0.1705

^aThe structure of $(Et_4N)_2[Co_2(L^{Ph})_2]$ refines with very large elongated ellipsoids giving a completely disordered species. For this inversion twinned crystal, each reflection is a composite of a cluster of reflections corresponding to the disordered species. The disorder was refined as two dependent molecules that are shifted 0.8 Å from each other.

Table 2-9. Structural refinement data for dinuclear cobalt(II) complex $K_2[Co_2(L^{iPr})_2]$.

$K_2[Co_2(L^{iPr})_2]$	
Formula	$C_{41.7}H_{45.8}Co_2K_2N_{7.1}O_4$
Form. Wt. (g/mol)	906.51
T (K)	446(2)
Crystal system	triclinic
Space group	P-1
<i>a</i> (Å)	10.5531(2)
<i>b</i> (Å)	11.4727(2)
<i>c</i> (Å)	19.0998(4)
α (°)	73.6670(10)
β (°)	80.5950(10)
γ (°)	87.5600(10)
V (Å³)	2189.30(7)
Z	2
ρ, calcd (g/cm³)	1.375
μ (mm⁻¹)	8.023
Crystal size (mm³)	0.24 × 0.22 × 0.17
Theta range (°)	4.88 to 136.36
Reflns. Collected	22768
Unique reflns.	7264
Data/rest./par.	7264/0/524
GOF	1.061
Final R indexes [$I > 2\sigma$ (I)]	R1 = 0.0437
All data	wR2 = 0.1333

Table 2-10. Structural refinement data for mononuclear cobalt(II) complexes (PPh₄)₂[Co(HL^{tBu})₂], K₂[Co(HL^{Ph})₂] and (Et₄N)₂[Co(HL^{Ad})₂].

	(PPh ₄) ₂ [Co(HL ^{tBu}) ₂]	K ₂ [Co(HL ^{Ph}) ₂]	(Et ₄ N) ₂ [Co(HL ^{Ad}) ₂]
Formula	C ₉₂ H ₉₄ CoN ₆ O ₄ P ₂	C ₅₂ H ₃₈ CoK ₂ N ₆ O ₄	C ₉₀ H ₁₂₅ CoN ₁₁ O ₄
Form. Wt. (g/mol)	1468.6	948.01	1483.93
T (K)	173(2)	173(2)	110(2)
Crystal system	Monoclinic	Monoclinic	Triclinic
Space group	Cc	P2(1)	P-1
a (Å)	14.76(2)	11.6149(4)	14.6893(9)
b (Å)	27.54(4)	23.3837(9)	17.1524(13)
c (Å)	38.06(6)	19.9487(7)	17.8784(11)
α (°)	90	90	95.338(5)
β (°)	86.132(18)	95.605(3)	112.499(5)
γ (°)	90	90	96.941(5)
V (Å³)	15438(41)	5392.1(3)	4083.3(5)
Z	8	4	2
ρ, calcd (g/cm³)	1.264	1.168	1.207
m/mm-1	0.321	4.24	2.091
Crystal size (mm³)	0.07 x 0.03 x 0.02	0.12 x 0.08 x 0.04	0.2 x 0.14 x 0.09
Theta range(°)	1.07 to 20.81	2.23 to 69.59	5.412 to 139.744
Reflns. Collected	70626	29852	34077
Unique reflns.	16161	16418	14030
Data/rest./par.	16161 / 2 / 873	16418 / 7 / 1173	14030/923/966
GOF	1.006	1.013	1.025
Final R indexes [I>2σ (I)]	R1 = 0.0919	R1 = 0.0889	R1 = 0.1149
All data	R1 = 0.2257	R1 = 0.1357	R1 = 0.2274

Table 2-11. Structural refinement data for dinuclear complexes $(\text{PPh}_4)_2[\text{Fe}_2(\text{L}^{i\text{Pr}})_2]$ and $(\text{Et}_4\text{N})_2[\text{Ni}_2(\text{L}^{i\text{Pr}})_2]$.

	$(\text{PPh}_4)_2[\text{Fe}_2(\text{L}^{i\text{Pr}})_2]$	$(\text{Et}_4\text{N})_2[\text{Ni}_2(\text{L}^{i\text{Pr}})_2]$
Formula	$\text{C}_{89}\text{H}_{84}\text{N}_{6.5}\text{O}_4\text{P}_2\text{Fe}_2$	$\text{C}_{62}\text{H}_{98}\text{N}_{10}\text{Ni}_2\text{O}_6$
Form. Wt. (g/mol)	1482.34	1196.92
T (K)	173.15	110(2)
Crystal system	orthorhombic	tetragonal
Space group	C2221	I4 ₁ 22
<i>a</i> (Å)	13.6251(12)	18.6962(13)
<i>b</i> (Å)	22.596(2)	18.6962(13)
<i>c</i> (Å)	25.348(2)	35.625(2)
α (°)	90	90
β (°)	90	90
γ (°)	90	90
<i>V</i> (Å³)	7803.9(12)	12452.6(19)
<i>Z</i>	4	8
ρ, calcd (g/cm³)	1.2616	1.277
<i>m</i>/mm-1	0.468	0.662
Crystal size (mm³)	0.409 × 0.256 × 0.144	0.74 × 0.56 × 0.47
Theta range(°)	3.5 to 61.02	1.23 to 31.04
Reflns. Collected	84143	75953
Unique reflns.	11924	9967
Data/rest./par.	11924/0/471	75953/60/423
<i>GOF</i>	1.023	1.04
Final R indexes [<i>I</i>>2σ(<i>I</i>)]	R1 = 0.0484	0.0315
All data	wR2 = 0.1393	wR2 = 0.0783

Table 2-12. Structural refinement data for dinuclear complexes $(\text{PPh}_4)_2[\text{Cu}_2(\text{L}^{i\text{Pr}})_2]$ and $(\text{Et}_4\text{N})_2[\text{Zn}_2(\text{L}^{i\text{Pr}})_2]$

	$(\text{PPh}_4)_2[\text{Cu}_2(\text{L}^{i\text{Pr}})_2]$	$(\text{Et}_4\text{N})_2[\text{Zn}_2(\text{L}^{i\text{Pr}})_2]$
Formula	$\text{C}_{89}\text{H}_{85.5}\text{Cu}_2\text{N}_{6.5}\text{O}_4\text{P}_2$	$\text{C}_{56}\text{H}_{84}\text{N}_8\text{O}_4\text{Zn}_2$
Form. Wt. (g/mol)	1499.16	1064.13
T (K)	173(2)	173.15
Crystal system	orthorhombic	orthorhombic
Space group	C2221	C2221
<i>a</i> (Å)	13.597(3)	13.256(4)
<i>b</i> (Å)	22.642(5)	21.102(6)
<i>c</i> (Å)	25.303(5)	20.266(6)
α (°)	90	90
β (°)	90	90
γ (°)	90	90
<i>V</i> (Å³)	7790(3)	5669(3)
<i>Z</i>	4	4
ρ, calcd (g/cm³)	1.278	1.2467
<i>m</i>/mm-1	0.643	0.897
Crystal size (mm³)	0.46 × 0.19 × 0.14	0.292 × 0.291 × 0.228
Theta range(°)	3.22 to 61.02	3.62 to 55.74
Reflns. Collected	79119	60067
Unique reflns.	11899	6776
Data/rest./par.	11899/1/473	6776/0/317
<i>GOF</i>	1.046	1.124
Final R indexes [<i>I</i>>2σ (<i>I</i>)]	R1 = 0.0459	R1 = 0.0459
All data	wR2 = 0.1181	wR2 = 0.1207

References

1. (a) Murahashi, S.-I.; Zhang, D., *Chem Soc Rev.* **2008**, *37* (8), 1490; (b) Meunier, B.; de Visser, S. P.; Shaik, S., *Chem Rev.* **2004**, *104* (9), 3947.
2. Momenteau, M.; Reed, C. A., *Chem Rev.* **1994**, *94* (3), 659.
3. Moulton, C. J.; Shaw, B. L., *Journal of the Chemical Society, Dalton Transactions.* **1976**, (11), 1020.
4. O'Reilly, M. E.; Del Castillo, T. J.; Falkowski, J. M.; Ramachandran, V.; Pati, M.; Correia, M. C.; Abboud, K. A.; Dalal, N. S.; Richardson, D. E.; Veige, A. S., *Journal of the American Chemical Society.* **2011**, *133* (34), 13661.
5. (a) O'Reilly, M.; Falkowski, J. M.; Ramachandran, V.; Pati, M.; Abboud, K. A.; Dalal, N. S.; Gray, T. G.; Veige, A. S., *Inorg Chem.* **2009**, *48* (23), 10901; (b) O'Reilly, M. E.; Del Castillo, T. J.; Abboud, K. A.; Veige, A. S., *Dalton T.* **2012**, *41* (8), 2237.
6. (a) Wanniarachchi, S.; Liddle, B. J.; Lindeman, S. V.; Gardinier, J. R., *J Organomet Chem.* **2011**, *696* (23), 3623; (b) van der Vlugt, J. I.; Reek, J. N. H., *Angewandte Chemie International Edition.* **2009**, *48* (47), 8832.
7. van Koten, G.; Gebbink, R. J. M. K., *Dalton T.* **2011**, *40* (35), 8731.
8. Albrecht, M.; Lindner, M. M., *Dalton T.* **2011**, *40* (35), 8733.
9. O'Reilly, M. E.; Veige, A. S., *Chem Soc Rev.* **2014**, *43* (17), 6325.
10. Luca, O. R.; Crabtree, R. H., *Chem Soc Rev.* **2013**, *42* (4), 1440.
11. Girgis, A. Y.; Balch, A. L., *Inorg Chem.* **1975**, *14* (11), 2724.
12. Zarkesh, R. A.; Ziller, J. W.; Heyduk, A. F., *Angewandte Chemie International Edition.* **2008**, *47* (25), 4715.

13. Zarkesh, R. A.; Heyduk, A. F., *Organometallics*. **2011**, *30* (18), 4890.
14. Zarkesh, R. A.; Heyduk, A. F., *Organometallics*. **2009**, *28* (23), 6629.
15. Stanciu, C.; Jones, M. E.; Fanwick, P. E.; Abu-Omar, M. M., *Journal of the American Chemical Society*. **2007**, *129* (41), 12400.
16. Lu, F.; Zarkesh, R. A.; Heyduk, A. F., *Eur J Inorg Chem*. **2012**, *2012* (3), 467.
17. Szigethy, G.; Heyduk, A. F., *Dalton T*. **2012**, *41* (26), 8144.
18. Wong, J. L.; Sanchez, R. H.; Logan, J. G.; Zarkesh, R. A.; Ziller, J. W.; Heyduk, A. F., *Chemical Science*. **2013**, *4* (4), 1906.
19. Knijnenburg, Q.; Gambarotta, S.; Budzelaar, P. H. M., *Dalton T*. **2006**, (46), 5442.
20. (a) de Bruin, B.; Bill, E.; Bothe, E.; Weyhermüller, T.; Wieghardt, K., *Inorg Chem*. **2000**, *39* (13), 2936; (b) Budzelaar, P. H. M.; de Bruin, B.; Gal, A. W.; Wieghardt, K.; van Lenthe, J. H., *Inorg Chem*. **2001**, *40* (18), 4649.
21. Freundlich, J. S.; Schrock, R. R.; Davis, W. M., *Journal of the American Chemical Society*. **1996**, *118* (15), 3643.
22. Schrock, R. R.; Lee, J.; Liang, L.-C.; Davis, W. M., *Inorg Chim Acta*. **1998**, *270* (1–2), 353.
23. Nguyen, A. I.; Blackmore, K. J.; Carter, S. M.; Zarkesh, R. A.; Heyduk, A. F., *Journal of the American Chemical Society*. **2009**, *131* (9), 3307.
24. Nguyen, A. I.; Zarkesh, R. A.; Lacy, D. C.; Thorson, M. K.; Heyduk, A. F., *Chemical Science*. **2011**, *2* (1), 166.
25. Bossu, F. P.; Margerum, D. W., *Journal of the American Chemical Society*. **1976**, *98* (13), 4003.

26. Collins, T. J., *Accounts Chem Res.* **1994**, 27 (9), 279.
27. Jones, M. B.; MacBeth, C. E., *Inorg Chem.* **2007**, 46 (20), 8117.
28. (a) Hong, S.; Hill, L. M. R.; Gupta, A. K.; Naab, B. D.; Gilroy, J. B.; Hicks, R. G.; Cramer, C. J.; Tolman, W. B., *Inorg Chem.* **2009**, 48 (10), 4514; (b) Sjödin, M.; Gätjens, J.; Tabares, L. C.; Thuéry, P.; Pecoraro, V. L.; Un, S., *Inorg Chem.* **2008**, 47 (7), 2897; (c) Buttafava, A.; Fabbrizzi, L.; Perotti, A.; Poggi, A.; Poli, G.; Seghi, B., *Inorg Chem.* **1986**, 25 (9), 1456; (d) Chambers, J.; Eaves, B.; Parker, D.; Claxton, R.; Ray, P. S.; Slattery, S. J., *Inorg Chim Acta.* **2006**, 359 (8), 2400; (e) Lau, N.; Ziller, J. W.; Borovik, A. S., *Polyhedron.* (0).
29. Sharma, S. K.; May, P. S.; Jones, M. B.; Lense, S.; Hardcastle, K. I.; MacBeth, C. E., *Chem Commun.* **2011**, 47 (6), 1827.
30. Black, D. S. C.; Rothnie, N. E., *Aust J Chem.* **1983**, 36 (6), 1141.
31. Munhá, R. F.; Zarkesh, R. A.; Heyduk, A. F., *Inorg Chem.* **2013**, 52 (19), 11244.
32. Yang, L.; Powell, D. R.; Houser, R. P., *Dalton T.* **2007**, (9), 955.
33. (a) Mund, G.; Gabert, A. J.; Batchelor, R. J.; Britten, J. F.; Leznoff, D. B., *Chem Commun.* **2002**, (24), 2990; (b) Murray, B. D.; Power, P. P., *Inorg Chem.* **1984**, 23 (26), 4584; (c) Hope, H.; Olmstead, M. M.; Murray, B. D.; Power, P. P., *Journal of the American Chemical Society.* **1985**, 107 (3), 712.
34. Kahn, O.; Martinez, C. J., *Science.* **1998**, 279 (5347), 44.
35. Arriortua, M. I.; Cortes, A. R.; Lezam, L.; Rojo, T.; Solans, X.; Font-Bardia, M., *Inorg Chim Acta.* **1990**, 174 (2), 263.
36. Mankad, N. P.; Rivard, E.; Harkins, S. B.; Peters, J. C., *Journal of the American Chemical Society.* **2005**, 127 (46), 16032.

37. (a) Harkins, S. B.; Peters, J. C., *Journal of the American Chemical Society*. **2005**, *127* (7), 2030; (b) Harkins, S. B.; Peters, J. C., *Journal of the American Chemical Society*. **2004**, *126* (9), 2885.
38. Evans, D. F., *Journal of the Chemical Society (Resumed)*. **1959**, (0), 2003.
39. Ni, C.; Long, G. J.; Grandjean, F.; Power, P. P., *Inorg Chem*. **2009**, *48* (24), 11594.
40. Desrochers, P. J.; Telser, J.; Zvyagin, S. A.; Ozarowski, A.; Krzystek, J.; Vicic, D. A., *Inorg Chem*. **2006**, *45* (22), 8930.
41. (a) Charlot, M. F.; Jeannin, S.; Jeannin, Y.; Kahn, O.; Lucrece-Abaul, J.; Martin-Frere, J., *Inorg Chem*. **1979**, *18* (6), 1675; (b) Crawford, V. H.; Richardson, H. W.; Wasson, J. R.; Hodgson, D. J.; Hatfield, W. E., *Inorg Chem*. **1976**, *15* (9), 2107; (c) Hay, P. J.; Thibeault, J. C.; Hoffmann, R., *Journal of the American Chemical Society*. **1975**, *97* (17), 4884.
42. Connelly, N. G.; Geiger, W. E., *Chem Rev*. **1996**, *96* (2), 877.
43. Hewage, J. S.; Wanniarachchi, S.; Morin, T. J.; Liddle, B. J.; Banaszynski, M.; Lindeman, S. V.; Bennett, B.; Gardinier, J. R., *Inorg Chem*. **2014**, *53* (19), 10070.
44. Graddon, D. P.; Rochani, S.; Way, H., *Inorg Chim Acta*. **1985**, *104* (2), 87.
45. (a) Wu, A. J.; Penner-Hahn, J. E.; Pecoraro, V. L., *Chem Rev*. **2004**, *104* (2), 903; (b) Schenk, G.; Mitić, N.; Gahan, L. R.; Ollis, D. L.; McGeary, R. P.; Guddat, L. W., *Accounts Chem Res*. **2012**, *45* (9), 1593.
46. Fontecave, M.; Ménage, S.; Duboc-Toia, C., *Coordin Chem Rev*. **1998**, *178–180*, Part 2 (0), 1555.

47. (a) Blackburn, N. J.; Barr, M. E.; Woodruff, W. H.; van der Oost, J.; de Vries, S., *Biochemistry*. **1994**, *33* (34), 10401; (b) Wilmanns, M.; Lappalainen, P.; Kelly, M.; Sauer-Eriksson, E.; Saraste, M., *Proceedings of the National Academy of Sciences*. **1995**, *92* (26), 11955.
48. (a) Ni, C.; Lei, H.; Power, P. P., *Organometallics*. **2010**, *29* (8), 1988; (b) Merrill, W. A.; Wright, R. J.; Stanciu, C. S.; Olmstead, M. M.; Fettingner, J. C.; Power, P. P., *Inorg Chem*. **2010**, *49* (15), 7097.

Chapter 3:
Mechanistic, Spectroscopic, and Structural Investigations on the
Activation of Dioxygen by Cobalt Complexes Incorporating
Redox-active Ligands.

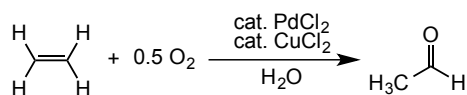
Section 3-1. Introduction

The catalytic aerobic oxidation of organic substrates has long been an important goal in catalysis and remains one of the most active research areas in modern chemistry. Centered at the focal point of this field is the development of synthetic transition metal catalysts that can efficiently and selectively promote such processes. Recently, emphasis has been placed on discovering new methodologies that utilize dioxygen as a terminal oxidant in aerobic oxidations. In the wake of increasingly stringent environmental reform and economic changes, earth-abundant first-row transition metal ions for aerobic oxidation reactions are becoming increasingly attractive.

Achieving sustainable and environmentally benign conversion of petroleum-based feedstocks to more synthetically useful oxygen-containing organic substrates is of great importance. In this context, an ideal and highly attractive approach for such transformations is the use of dioxygen as an oxidant.¹ Dioxygen is a readily available oxidant from the atmosphere and its byproducts are environmentally benign.

Homogeneous aerobic oxidations are widely utilized in industrial applications, with one of the most successful processes being the Wacker process. In the Wacker oxidation, co-catalysts PdCl₂ and CuCl₂ utilize dioxygen to convert methylene to

acetaldehyde, a process yielding millions of tons of acetaldehyde annually (Scheme 3-1).² Another industrialized aerobic oxidation process is the synthesis of terephthalic acid (TPA), a precursor in the production of polyethylene terephthalate (PET).³ In spite of its efficiency, the reaction scope of this process remains limited to substrates prone to reacting via radical pathways.



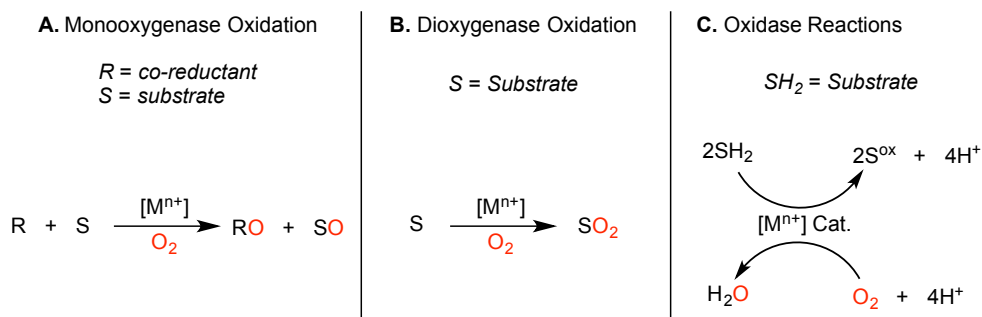
Scheme 3-1. Aerobic ethylene oxidation to acetaldehyde by PdCl₂ and CuCl₂ in the Wacker process.²

In addition to large-scale industrialized processes, homogeneous aerobic oxidations are highly sought after for the synthesis of fine chemicals. The main advantage lies in performing these reactions without using stoichiometric quantities of harsh inorganic oxidants, such as dichromates⁴ and permanganates.⁵ Though these methods work well, the production of large amounts of waste makes them unattractive for environmental and atom economical reasons. Developing catalysts that can effectively use dioxygen as a terminal oxidant would yield important advancements for the field of homogeneous catalysis.

In the recent *Technology Vision 2020 Catalysis Report*, the Council for Chemical Research highlighted the need to develop novel catalysts that can activate dioxygen and selectively oxidize alkanes, olefins, and aromatics.⁶ Among the most widely studied catalytic systems for dioxygen activation are those that incorporate palladium. Recent advances in palladium-catalyzed homogeneous aerobic oxidations have led to the

discovery of convenient and synthetically versatile systems for dioxygen activation. Practical uses in palladium-catalyzed aerobic oxidations include oxidative C–C, C–N, and C–O coupling of alkenes,⁷ alcohol and amine oxidation,⁸ and aerobic oxidative amination.⁹ Despite these advances, efforts to utilize first-row transition metals for aerobic oxidation processes have emerged over the past several decades.

The use of first-row metals to carry out a wide range of aerobic enzymatic chemical transformations via dioxygen activation is very common. Metalloenzymes that utilize first-row transition metal ions and dioxygen as a terminal oxidant for substrate oxidation include mononuclear¹⁰ and dinuclear¹¹ non-heme oxygenases, copper monooxygenases,¹² cytochrome P450 monooxygenases,^{12b} and non-heme oxidases.¹³ Oxygenase-type reactions occur when oxygen atoms from dioxygen are incorporated into the oxidized substrate. Enzymes that participate in these processes can be further classified as either monooxygenases (Scheme 3-2A), which incorporate one oxygen atom from dioxygen into the substrate, or dioxygenases (Scheme 3-2B), which deliver both oxygen atoms of dioxygen to the substrate. On the other hand, in oxidase systems, dioxygen functions as both an electron and proton acceptor to form water or hydrogen peroxide (H₂O₂) as a byproduct (Scheme 3-2C).



Scheme 3-2. Aerobic oxidations carried out by **A)** monooxygenases, **B)** dioxygenases, and **C)** oxidases.¹⁰⁻¹³

A large number of synthetic systems utilizing first-row metal ions that are capable of carrying out homogeneous aerobic oxidations have been reported in past decades. However, only a handful of these systems can be regarded as truly biomimetic.¹⁴ To date, mimicking the aerobic oxidation reactivity and selectivity achieved by metalloenzymes has been one of the biggest challenges in synthetic inorganic chemistry.¹⁵ Embedded into the active sites of metalloenzymes are highly organized intermolecular interactions that help facilitate substrate oxidation. Synthetic systems incorporating porphyrins^{14b} and C₃-symmetric tripodal cavities¹⁶ have attempted to shape the microenvironment surrounding first-row metal ions by influencing geometry and secondary coordination sphere interactions in ways that promote dioxygen activation. While significant advances have been made, most synthetic analogues of these ligand systems have demonstrated to yield low turnover numbers (TON = moles of substrate/moles of catalyst) and low turnover frequencies (TOF = moles of substrate/moles of catalyst per hour), with low selectivity.

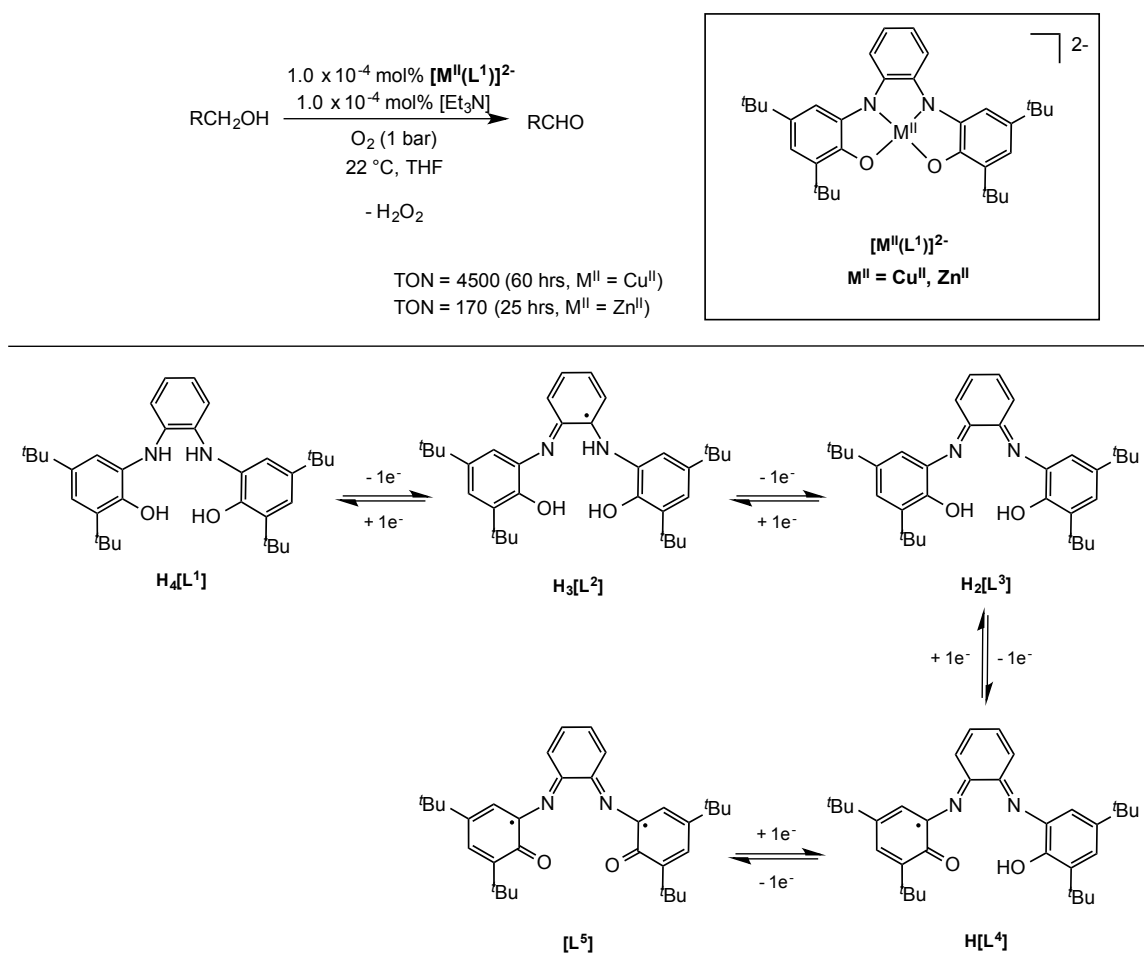
Additionally, designing first-row transition metal catalysts for efficient catalytic aerobic oxidation processes is especially challenging because the activation of dioxygen is a multi-electron process. For example, the reduction of dioxygen to peroxide is

formally a two-electron process and the complete reduction of dioxygen to water is a four-electron process. First-row transition metal catalysts that utilize dioxygen must, therefore, be able to facilitate multiple electron transfer events. In recent literature, an emerging tactic to promote multi-electron transfer processes at first-row transition metals in catalysis has been the use of redox-active ligands.¹⁷ In this context, redox-active ligands comprise promising scaffolds capable of promoting catalytic dioxygen activation at first-row metal ions.

Section 3-2. Background and Significance

The ubiquity of redox-active ligands in biological systems has shown that they can be used with first-row transition metal ions in dioxygen activation.¹⁸ Inspired by biological systems that use redox-active ligands, synthetic systems have been able to achieve biomimetic catalytic reactivity. For example, one of the most widely studied biological systems that use a redox-active ligand is galactose oxidase.¹⁹ A limited number of biomimetic synthetic systems as functional models for galactose oxidase have been reported.¹⁹ One seminal example reported by Wieghardt and co-workers has shown that redox-active ligands are appealing scaffolds for the aerobic oxidation of primary alcohols.²⁰ In their studies, a tetradentate ligand framework, ($H_4[L^1]$) shown in Scheme 3-4, with phenolic donor groups stabilizing copper(II) and zinc(II) complexes are capable of oxidizing primary alcohols, including methanol, in the presence of dioxygen and triethylamine (Et_3N) at unprecedented catalyst TONs (4500 TON for copper(II) and 170 TON for zinc(II)). Detailed spectroscopic and electrochemical experiments provided

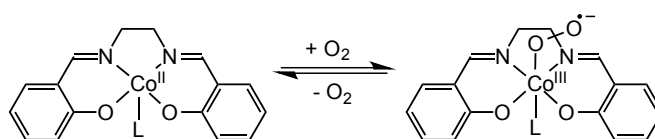
evidence that this ligand was capable of existing in five different oxidation states (Scheme 3-4, bottom). This work established that catalytic dioxygen activation by metal complexes containing redox-active ligands is feasible.



Scheme 3-4. Synthetic functional models for galactose oxidase: (Top) Catalytic aerobic alcohol oxidation by copper(II) and zinc(II) complexes of tetradentate ligand (L¹), and (bottom) five possible redox states of ligand, [L¹].²⁰

Our group targeted the use of cobalt(II) to design catalysts for aerobic oxidation reactions. Cobalt(II) complexes of chelating ligands have been known to bind dioxygen.²¹

Early reports, dating back to 1938 by Tsumaki, report that Schiff base complexes of cobalt(II) are capable of binding and transporting dioxygen.²² For this reason, cobalt(II) complexes have been widely studied as potential catalysts in a large number of aerobic oxidation reactions. Examples of homogeneous cobalt(II)-catalyzed aerobic oxidations include sulfide oxidation, epoxidation and allylic oxidation of alkenes, partial oxidation of alkanes to alcohols and ketones, and C–H oxidation of alkylbenzenes.¹³ These processes, however, require high temperatures and pressures that often result in low TOF and TON. More importantly, cobalt(II)-catalyzed aerobic oxidations require the use of stoichiometric amounts of co-reductants. Due to the inaccessible Co(III)/Co(IV) redox couple, these co-reductants are needed in the reaction of cobalt(II) with dioxygen in order to reduce the cobalt(III)-superoxide radical species that is initially formed. In the absence of co-reductants, the cobalt(III)-superoxide species reaches an equilibrium affording reversible dioxygen binding (Scheme 3-5).²³ As a result, cobalt(II) complexes that use dioxygen for aerobic oxidations in ambient conditions (without the use of co-reductants) are very limited.



Scheme 3-5. Schematic representation of reversible dioxygen binding to cobalt(II).²⁴

Designing cobalt(II) complexes capable of driving the reaction shown in Scheme 3-5 forward is of great interest due to the generation of possible cobalt-oxygen containing compounds. The paucity of well-defined cobalt-oxygen containing species that could

form in the reaction of cobalt(II) with dioxygen has raised interest in the inorganic community over the past decade.²⁵ Figure 3-1 depicts possible cobalt-oxygen containing species that could result from the reaction of cobalt(II) with dioxygen.²⁴ Mononuclear and dinuclear metal-dioxygen intermediates have been generally considered as the reactive species responsible for oxygenation reactions by many non-heme systems.²⁶ Out of the systems shown in Figure 3-1, only a limited number of well-characterized examples have been reported.^{26d, 27} Furthermore, there are less examples of structurally characterized cobalt-oxygen containing species derived from cobalt(II) and dioxygen.^{26b, 27b, 28}

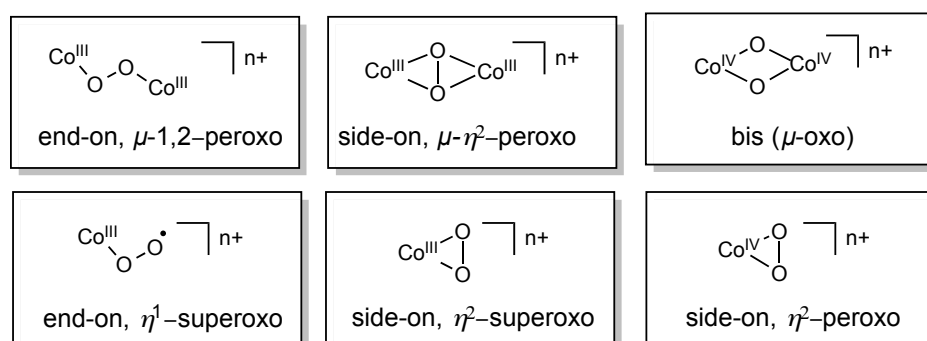
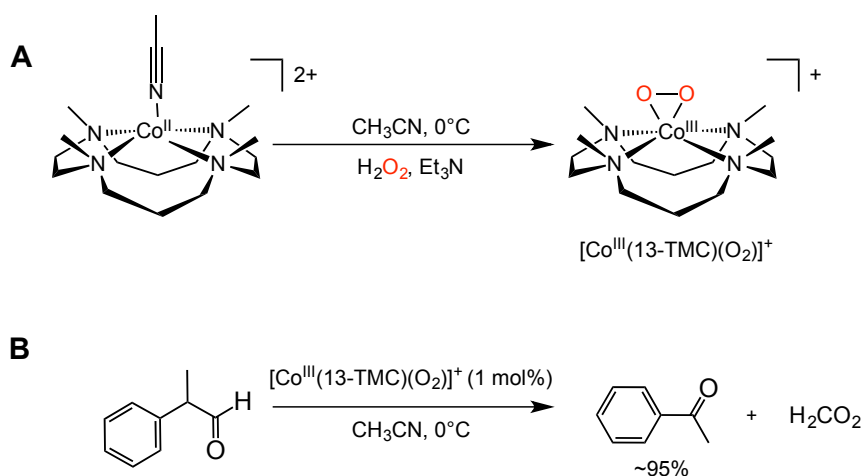


Figure 3-1. Schematic representations of possible cobalt-oxygen containing species formed during the reaction of cobalt(II) with dioxygen.²⁴

Recent interest has been placed on generating cobalt(III)-peroxo complexes, as these species have been shown to be active species in a number of substrate oxidation.^{26a, 29} Extensive work by Nam and co-workers has reported a synthetic route to prepare side-on, cobalt(III)- η^2 -peroxo complexes supported by tetraazamacrocyclic (TMC) ligands.³⁰ To this date, these are the only cobalt(III)- η^2 -peroxo species with a high-resolution crystal structure available. It was reported that these species are capable of carrying out

the deformylation of 2-phenylpropionaldehyde (2-PPA), a typical substrate used in testing the deformylation ability of metal(III)- η^2 -peroxos (Scheme 3-6).³⁰ The source of the peroxo ligand in this type of complex, however, is derived from H_2O_2 , a reduced form of dioxygen, in the presence of excess base. Examples of such complexes derived from dioxygen remain scarce. We hypothesized that cobalt(II) complexes of redox-active ligands could be good candidates for such an array of reactivity using dioxygen.



Scheme 3-6. **A)** Synthesis of a cobalt(III)-peroxo complex supported by 13-TMC ligand and **B)** its ability to perform deformylation of 2-phenylpropionaldehyde.³⁰

In Chapter 2, the coordination of the bis(phenylamido)amine ligand $\text{NH}(o\text{-PhNHC}(\text{O})^i\text{Pr})_2$ ($\text{H}_3\text{L}^{i\text{Pr}}$) was explored with cobalt(II) ions. This chapter will outline mechanistic, spectroscopic, and structural studies carried out on the activation of dioxygen by cobalt(II) complexes of this ligand system.

Section 3-3. Results

In 2011, work by Sharma et al. demonstrated that the oxidatively robust, tridentate, trianionic redox-active bis(phenylamido)amine ligand scaffold $\text{NH}(o\text{-PhNHC(O)}^i\text{Pr})_2$ ($\text{H}_3\text{L}^{i\text{Pr}}$) is capable of stabilizing dinuclear complex, $(\text{Et}_4\text{N})_2[\text{Co}_2(\text{L}^{i\text{Pr}})_2]$, and mononuclear complex, $(\text{Et}_4\text{N})_2[\text{Co}(\text{HL}^{i\text{Pr}})_2]$ (Figure 3-2, A and B, respectively).³¹ The cyclic voltammogram of mononuclear complex $(\text{Et}_4\text{N})_2[\text{Co}(\text{HL}^{i\text{Pr}})_2]$, shown in Figure 3-1F, indicates that these complexes are capable of reacting with dioxygen and potentially carrying out its four-electron reduction. In these studies, it was observed that under ambient conditions and in the presence of excess dioxygen, both $(\text{Et}_4\text{N})_2[\text{Co}_2(\text{L}^{i\text{Pr}})_2]$ and $(\text{Et}_4\text{N})_2[\text{Co}(\text{HL}^{i\text{Pr}})_2]$ complexes catalytically oxidize triphenylphosphine (PPh_3) to triphenylphosphine oxide (PPh_3O) with much higher efficiencies than those previously observed for cobalt(II) complexes of chelating ligands. These complexes exhibit catalytic TONs on par with $\text{Pd}(\text{OAc})_2$ (Table 3-1). More importantly, these reactions proceed in the presence of known radical inhibitors such as 2,6-di-*tert*-butyl-4-methylphenol, ruling out possible radical chain mechanism pathways. Additionally, control reactions show that cobalt(II) bromide (CoBr_2) and cobalt(II) acetate ($\text{Co}(\text{OAc})_2$) salts are not efficient catalysts in this process. With such efficient cobalt(II) systems in hand, we sought to explore the mechanism of dioxygen activation. This chapter will explore the reaction of cobalt(II) complexes with dioxygen through mechanistic, spectroscopic, and structural studies.

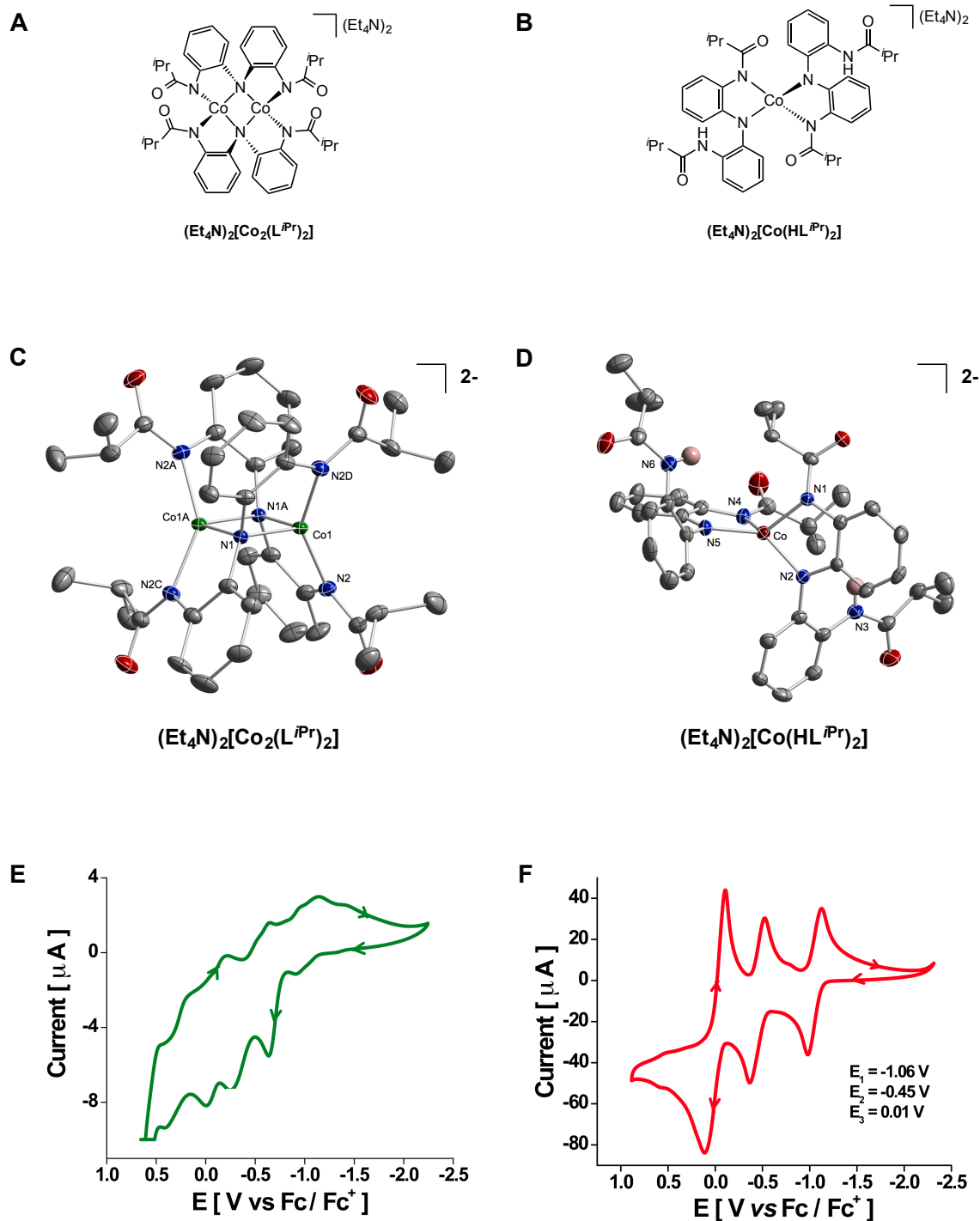
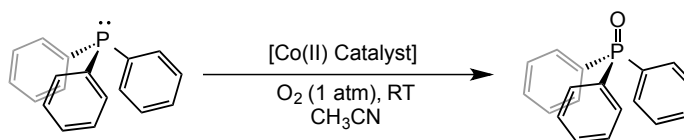


Figure 3-2. A) Dinuclear and B) mononuclear cobalt(II) complexes supported by the bis(phenylamido)amine ligand $\text{NH}(o\text{-PhNHC(O)}^i\text{Pr})_2$ ($\text{H}_3\text{L}^{\text{iPr}}$), and their solid-state X-ray structures (C and D) and electrochemical profiles (E and F), respectively.³¹

Table 3-1. Catalytic aerobic O-atom transfer to triphenylphosphine carried out by $(\text{Et}_4\text{N})_2[\text{Co}_2(\text{L}^{\text{iPr}})_2]$ and $(\text{Et}_4\text{N})_2[\text{Co}(\text{HL}^{\text{iPr}})_2]$.³¹



Entry	[Catalyst]	mol%	Time (h)	TON ^a
1	$(\text{Et}_4\text{N})_2[\text{Co}(\text{HL}^{\text{iPr}})_2]$	0.2	6	185
2	$(\text{Et}_4\text{N})_2[\text{Co}_2(\text{L}^{\text{iPr}})_2]$	0.2	6	345

^a Rates on par with $\text{Pd}(\text{OAc})_2$.

The aforementioned work by Sharma et al. led us to investigate the mechanism by which both $(\text{Et}_4\text{N})_2[\text{Co}_2(\text{L}^{\text{iPr}})_2]$ and $(\text{Et}_4\text{N})_2[\text{Co}(\text{HL}^{\text{iPr}})_2]$ react with dioxygen. We hypothesized that the comprehensive understanding of each complex's operative mechanism would aid in designing novel and more reactive aerobic oxidation cobalt(II) catalysts. Additionally, identifying possible reactive intermediates throughout the path of these reactions would allow for the reactivity of these catalysts to be attenuated for a wider substrate scope. The results presented herein represent a collaborative effort initiated by Dr. Savita K. Sharma, a postdoctoral fellow in our laboratory.

Section 3-3-1. Stoichiometric Oxygenation and Oxygen-atom Transfer Reaction Studies

At the onset of this project, the possibility of isolating and identifying possible reactive intermediates in the reaction of $(\text{Et}_4\text{N})_2[\text{Co}_2(\text{L}^{i\text{Pr}})_2]$ and $(\text{Et}_4\text{N})_2[\text{Co}(\text{HL}^{i\text{Pr}})_2]$ was called into question. For this purpose, stoichiometric reactions with dioxygen were carried out. Exposure of an acetonitrile (CH_3CN) solution of the dinuclear complex, $(\text{Et}_4\text{N})_2[\text{Co}_2(\text{L}^{i\text{Pr}})_2]$, to two equivalents of dioxygen gas at room temperature and 1 atmosphere (atm) of pressure caused a rapid color change of the solution from the dark-green color of $(\text{Et}_4\text{N})_2[\text{Co}_2(\text{L}^{i\text{Pr}})_2]$ to dark burgundy. This dark burgundy species proves stable at room temperature for days as an anhydrous CH_3CN solution and its UV-visible absorption spectrum displays intense bands at $\lambda_{\text{max}} = 390$ nm, 500 nm and 785 nm (Figure 3-3A). Remarkably, degassing the oxygenated mixture does not regenerate the initial spectra of $(\text{Et}_4\text{N})_2[\text{Co}_2(\text{L}^{i\text{Pr}})_2]$ ($\lambda_{\text{max}} = 596$ nm), confirming this oxygenation reaction to be irreversible.

Similarly, one equivalent of dioxygen was added to a CH_3CN solution of the mononuclear complex, $(\text{Et}_4\text{N})_2[\text{Co}(\text{HL}^{i\text{Pr}})_2]$, under similar reaction conditions. This resulted in a color change from the dark-red color of $(\text{Et}_4\text{N})_2[\text{Co}(\text{HL}^{i\text{Pr}})_2]$ to dark burgundy. Likewise, degassing the oxygenated mixture did not regenerate the initial spectra of $(\text{Et}_4\text{N})_2[\text{Co}(\text{HL}^{i\text{Pr}})_2]$ ($\lambda_{\text{max}} = 575$ nm), confirming the irreversible oxygenation of the metal complex. The burgundy species displays intense bands at $\lambda_{\text{max}} = 390$ nm, 525 nm and 785 nm (Figure 3-3B). Both species were isolated as a powder in an inert atmosphere. The results shown in Figure 3-2 indicate that both $(\text{Et}_4\text{N})_2[\text{Co}(\text{HL}^{i\text{Pr}})_2]$ and

$(\text{Et}_4\text{N})_2[\text{Co}_2(\text{L}^{i\text{Pr}})_2]$ form very similar oxygenated species with dioxygen. More importantly, detailed gas uptake experiments indicate that a 1:1 Cobalt to O_2 stoichiometric ratio is achieved.

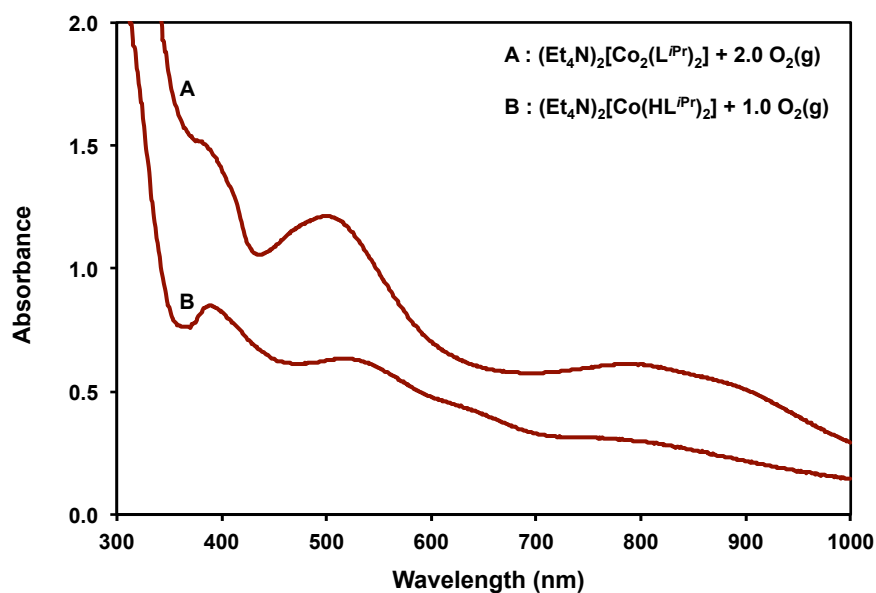
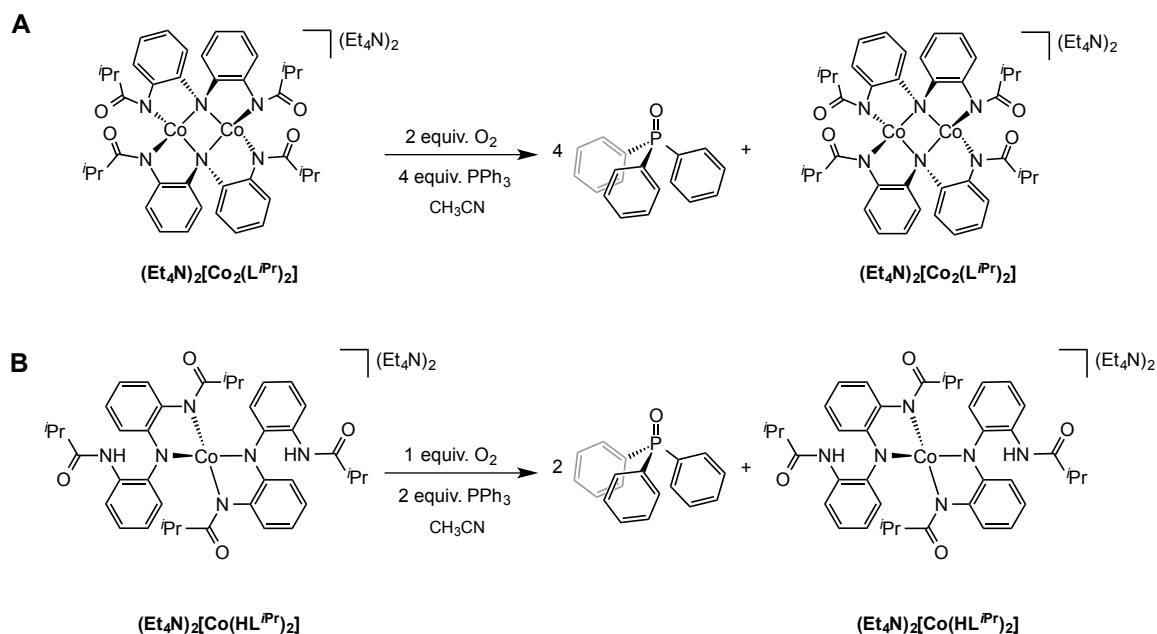


Figure 3-3. UV-Visible absorption spectra of the products isolated from the reaction of **A**) $(\text{Et}_4\text{N})_2[\text{Co}_2(\text{L}^{i\text{Pr}})_2]$ with two equivalents of dioxygen gas and **B**) $(\text{Et}_4\text{N})_2[\text{Co}(\text{HL}^{i\text{Pr}})_2]$ with one equivalent of dioxygen gas. Both spectra recorded at room temperature in CH_3CN from isolated oxygenated compounds.

To gain further insight into the oxygenation stoichiometry in the reaction of both $(\text{Et}_4\text{N})_2[\text{Co}_2(\text{L}^{i\text{Pr}})_2]$ and $(\text{Et}_4\text{N})_2[\text{Co}(\text{HL}^{i\text{Pr}})_2]$ with dioxygen, stoichiometric O-atom transfer reactions were carried out in the presence of a substrate (Scheme 3-7). For instance, a CH_3CN solution of the dinuclear complex, $(\text{Et}_4\text{N})_2[\text{Co}_2(\text{L}^{i\text{Pr}})_2]$, was treated with two equivalents of dioxygen gas, to generate the dark burgundy oxygenated species. Once generated, this oxygenated species was isolated as a powder, and treated with four

equivalents of PPh_3 in CH_3CN under anaerobic conditions (two equivalents of PPh_3 per cobalt metal). After 24 hours, ^{31}P NMR analysis confirmed full conversion of PPh_3 to OPPh_3 . More impressively, ^1H NMR analysis of the reaction mixture revealed the regeneration of $(\text{Et}_4\text{N})_2[\text{Co}_2(\text{L}^{i\text{Pr}})_2]$. Following the same procedure, the mononuclear complex, $(\text{Et}_4\text{N})_2[\text{Co}(\text{HL}^{i\text{Pr}})_2]$, was treated with two equivalents of dioxygen gas; the oxygenated species was isolated as a powder, and two equivalents of PPh_3 in CH_3CN was added under anaerobic conditions. Similarly, ^{31}P NMR analysis of the reaction mixture confirmed full conversion of PPh_3 to OPPh_3 and ^1H NMR analysis revealed the regeneration of $(\text{Et}_4\text{N})_2[\text{Co}(\text{HL}^{i\text{Pr}})_2]$. The results outlined in Scheme 3-7 further support the gas uptake experiments indicating that a 1:1 cobalt to O_2 ratio takes place.



Scheme 3-7. Stoichiometric O-atom transfer reactions by **A**) $(\text{Et}_4\text{N})_2[\text{Co}_2(\text{L}^{i\text{Pr}})_2]$ and **B**) $(\text{Et}_4\text{N})_2[\text{Co}(\text{HL}^{i\text{Pr}})_2]$ to PPh_3 .

Section 3-3-2. Spectroscopic Studies on the Activation of Dioxygen by Cobalt Complexes

To investigate the nature of the intermediates formed upon the reaction of $(\text{Et}_4\text{N})_2[\text{Co}_2(\text{L}^{\text{iPr}})_2]$ and $(\text{Et}_4\text{N})_2[\text{Co}(\text{HL}^{\text{iPr}})_2]$ with dioxygen, *in situ* reactions were monitored via UV-visible absorption spectroscopy. An acetonitrile solution of the dinuclear complex, $(\text{Et}_4\text{N})_2[\text{Co}_2(\text{L}^{\text{iPr}})_2]$, was exposed to excess dioxygen at room temperature. The UV-visible absorption traces of this reaction are shown in Figure 3-3. Interestingly, addition of excess dioxygen to a solution of $(\text{Et}_4\text{N})_2[\text{Co}_2(\text{L}^{\text{iPr}})_2]$ resulted in the disappearance of the band ($\lambda_{\text{max}} = 596 \text{ nm}$) corresponding to $(\text{Et}_4\text{N})_2[\text{Co}_2(\text{L}^{\text{iPr}})_2]$ with the concomitant growth of three intense absorption bands ($\lambda_{\text{max}} = 400 \text{ nm}$, 525 nm , and 800 nm) corresponding to an intermediate (Figure 3-4, *Intermediate 1*—orange trace). As the oxygenation reaction progressed, this intermediate species ultimately transformed into the oxygenated species (Figure 3-4, species *C*—burgundy trace) with absorption bands at $\lambda_{\text{max}} = 390 \text{ nm}$, 500 nm , and 785 nm . The UV-visible absorption spectrum of species *C* matches the oxygenated species in which $(\text{Et}_4\text{N})_2[\text{Co}_2(\text{L}^{\text{iPr}})_2]$ reacts with two equivalents of dioxygen.

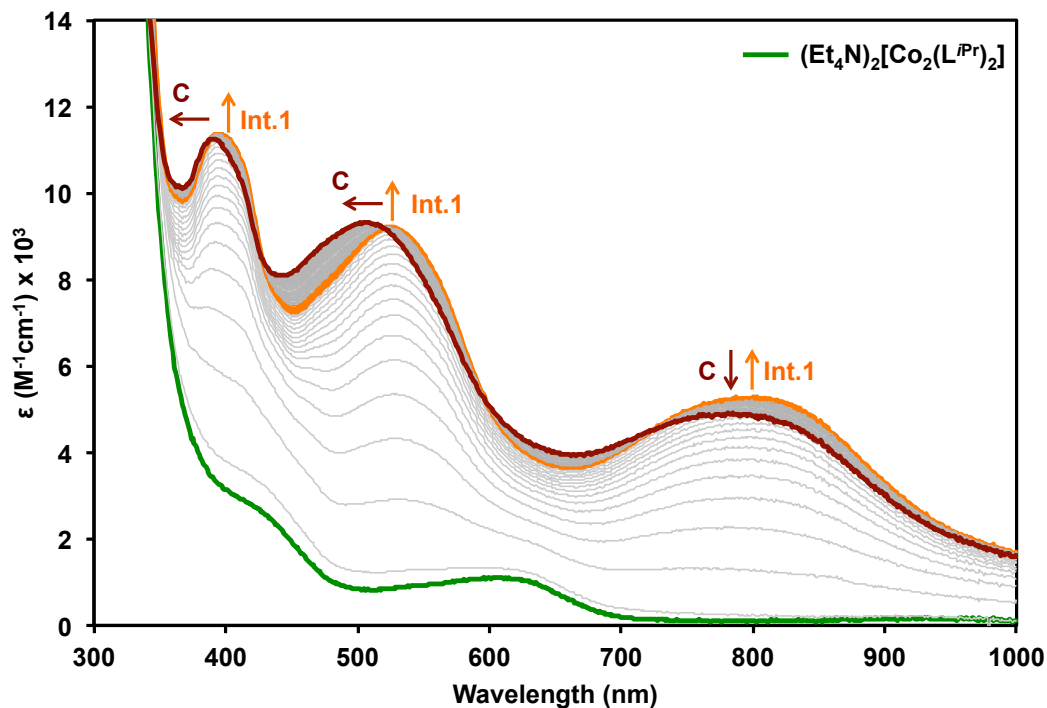


Figure 3-4. Changes in the UV-visible absorption spectrum of $(\text{Et}_4\text{N})_2[\text{Co}_2(\text{L}^{i\text{Pr}})_2]$ (green trace, prior to oxygenation) upon addition of dioxygen into the headspace above a solution of $(\text{Et}_4\text{N})_2[\text{Co}_2(\text{L}^{i\text{Pr}})_2]$ in CH_3CN at $25\text{ }^\circ\text{C}$. Scan rate of 1 scan/min. Orange trace corresponds to *Intermediate 1* and burgundy trace corresponds to the final oxygenated species *C* upon reaction with dioxygen.

The reaction of the mononuclear cobalt(II) complex $(\text{Et}_4\text{N})_2[\text{Co}(\text{HL}^{i\text{Pr}})_2]$ with dioxygen was also followed using UV-visible absorption spectroscopy. The UV-visible absorption traces of this reaction are shown in Figure 3-5. Remarkably, addition of excess dioxygen to a solution of $(\text{Et}_4\text{N})_2[\text{Co}(\text{HL}^{i\text{Pr}})_2]$ resulted in the disappearance of the band ($\lambda_{\text{max}} = 575\text{ nm}$) corresponding to $(\text{Et}_4\text{N})_2[\text{Co}(\text{HL}^{i\text{Pr}})_2]$ with the simultaneous growth of a new and intense absorption band ($\lambda_{\text{max}} = 434\text{ nm}$) corresponding to a very short-lived (~ 1 - 2 minutes) intermediate (Figure 3-5, *Intermediate 1* – blue trace). The spectral band at

$\lambda_{\text{max}} = 434$ nm, corresponding to *Intermediate 1*, decays as the oxygenation reaction proceeds to form a new species with three notably different absorption bands ($\lambda_{\text{max}} = 400$ nm, 525 nm, and 800 nm) corresponding to *Intermediate 2* (Figure 3-5, *Intermediate 2*–orange trace). In this reaction, *Intermediate 2* shows absorption bands very similar to *Intermediate 1* observed in the reaction between the dinuclear complex $(\text{Et}_4\text{N})_2[\text{Co}_2(\text{L}^{i\text{Pr}})_2]$ and dioxygen. *Intermediate 2* ultimately becomes a final oxygenated species (Figure 3-5, Species C–burgundy trace) with absorption bands at $\lambda_{\text{max}} = 390$ nm, 500 nm, and 785 nm. The UV-visible absorption spectrum of species C matches the oxygenated species in which $(\text{Et}_4\text{N})_2[\text{Co}(\text{HL}^{i\text{Pr}})_2]$ reacts with two equivalents of dioxygen.

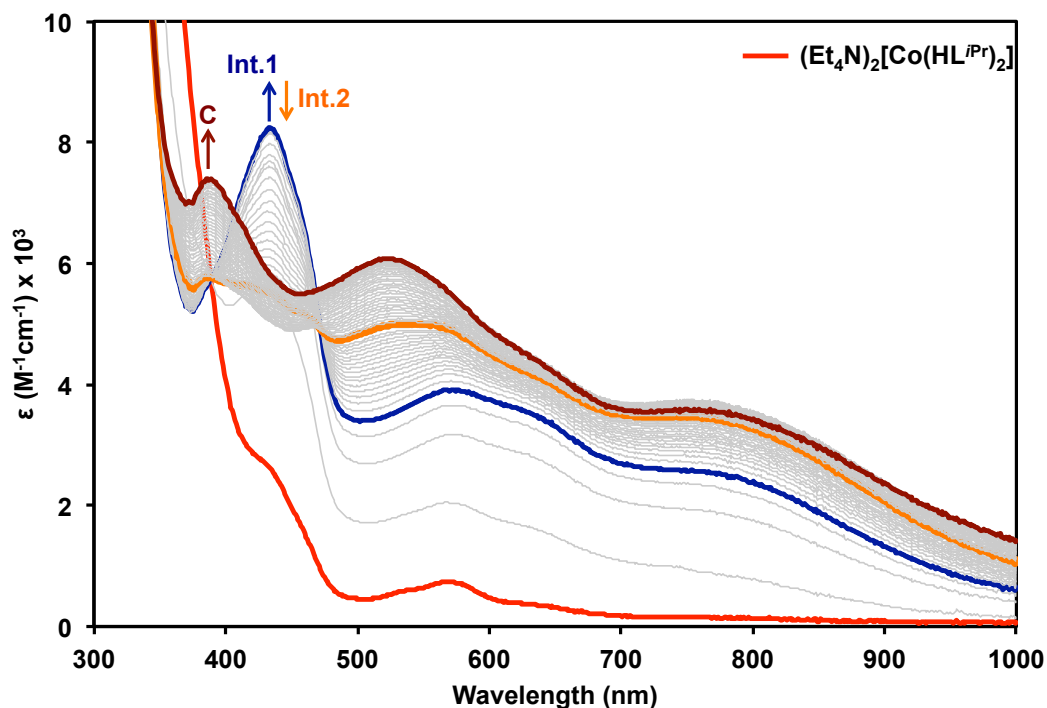


Figure 3-5. Changes in the UV-visible absorption spectrum of $(\text{Et}_4\text{N})_2[\text{Co}(\text{HL}^{i\text{Pr}})_2]$ (red trace, prior to oxygenation) upon addition of dioxygen into the headspace above a solution of $(\text{Et}_4\text{N})_2[\text{Co}(\text{HL}^{i\text{Pr}})_2]$ in CH_3CN at $25\text{ }^\circ\text{C}$. Scan rate of 1 scan/min. Blue trace corresponds to *Intermediate 1* and orange trace corresponds to *Intermediate 2*. Burgundy trace corresponds to the final oxygenated species *C* upon reaction with dioxygen.

To further investigate the origin of *Intermediate 1* in the reaction between the mononuclear complex $(\text{Et}_4\text{N})_2[\text{Co}(\text{HL}^{i\text{Pr}})_2]$ and dioxygen, the oxygenation reaction was monitored via UV-visible near-infrared (UV-vis NIR) spectroscopy. The spectral traces of this reaction are shown in Figure 3-6. Similar absorption peaks are observed in the UV-visible region. Notably, the absorption band corresponding to *Intermediate 1* exhibited a weak-energy absorption at $\lambda_{\text{max}} = 1700\text{ nm}$, characteristic of an intervalence charge-transfer (IVCT) band. The UV-vis NIR of the reaction of the dinuclear complex $(\text{Et}_4\text{N})_2[\text{Co}_2(\text{L}^{i\text{Pr}})_2]$

and dioxygen did not exhibit any absorption features in the NIR region. The spectral traces for that reaction are shown in Figure 3-7 for comparison. The UV-visible and UV-visible NIR absorption spectroscopy studies shown in this work suggest that $(\text{Et}_4\text{N})_2[\text{Co}_2(\text{L}^{i\text{Pr}})_2]$ and $(\text{Et}_4\text{N})_2[\text{Co}(\text{HL}^{i\text{Pr}})_2]$ initially react with dioxygen to form distinct intermediates but ultimately form similar final oxygenated species (species C).

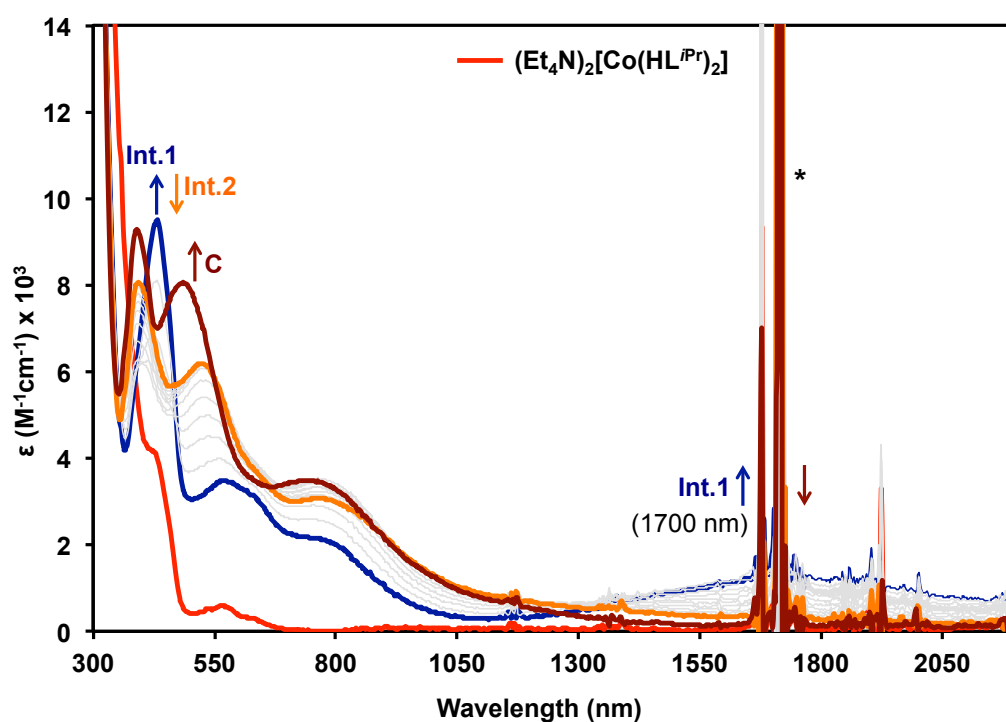


Figure 3-6. Changes in the UV-visible NIR absorption spectrum of $(\text{Et}_4\text{N})_2[\text{Co}(\text{HL}^{i\text{Pr}})_2]$ (red trace, prior to oxygenation) upon addition of dioxygen into the headspace above a solution of $(\text{Et}_4\text{N})_2[\text{Co}(\text{HL}^{i\text{Pr}})_2]$ in CH_3CN at $25\text{ }^\circ\text{C}$. Scan rate of 1 scan/ 3 min. Blue trace corresponds to *Intermediate 1* and orange trace corresponds to *Intermediate 2*. Burgundy trace corresponds to the final oxygenated species *C* upon reaction with dioxygen. Quartz from cuvette is marked by an asterisk (*).

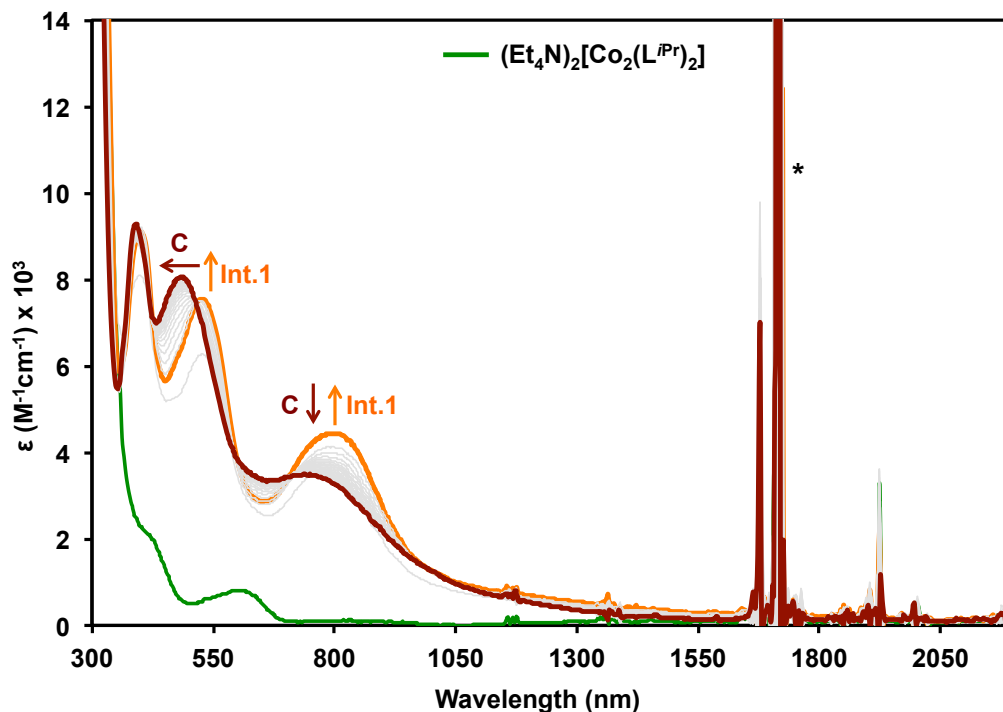


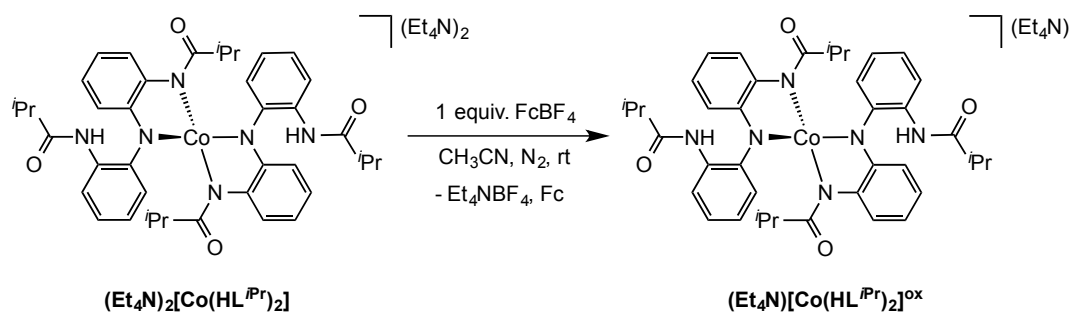
Figure 3-7. Changes in the UV-visible NIR absorption spectrum of $(\text{Et}_4\text{N})_2[\text{Co}_2(\text{L}^{\text{iPr}})_2]$ (green trace, prior to oxygenation) upon addition of dioxygen into the headspace above a solution of $(\text{Et}_4\text{N})_2[\text{Co}_2(\text{L}^{\text{iPr}})_2]$ in CH_3CN at $25\text{ }^\circ\text{C}$. Scan rate of 1 scan/3 min. Orange trace corresponds to *Intermediate 1*. Burgundy trace corresponds to the final oxygenated species *C* upon reaction with dioxygen. Quartz from cuvette is marked by an asterisk (*).

Section 3-3-3. Chemical Oxidation of Mononuclear Complex $(\text{Et}_4\text{N})_2[\text{Co}(\text{HL}^{\text{iPr}})_2]$

To further understand the nature of *Intermediate 1* observed in the reaction between mononuclear complex $(\text{Et}_4\text{N})_2[\text{Co}(\text{HL}^{\text{iPr}})_2]$ and dioxygen, the one-electron oxidized complex $(\text{Et}_4\text{N})[\text{Co}(\text{HL}^{\text{iPr}})_2]^{\text{ox}}$ was investigated. Treating a CH_3CN solution of complex $(\text{Et}_4\text{N})_2[\text{Co}(\text{HL}^{\text{iPr}})_2]$ with one equivalent of ferrocenium tetrafluoroborate (FcBF_4) at room

temperature resulted in the almost instantaneous color change from the dark red color of $(\text{Et}_4\text{N})_2[\text{Co}(\text{HL}^{i\text{Pr}})_2]$ to deep blue.³¹ This deep blue species corresponds to the formally one-electron oxidized complex $(\text{Et}_4\text{N})[\text{Co}(\text{HL}^{i\text{Pr}})_2]^{\text{ox}}$ (Scheme 3-8). This complex is stable at room temperature as an anhydrous CH_3CN solution and its UV-visible NIR absorption spectrum exhibits intense bands at λ_{max} ($\epsilon, \text{M}^{-1}\text{cm}^{-1}$) = 482 nm (2913), 592 nm (3277), 785 nm (2093) (sh), and 1700 nm (1318) (Figure 3-8). Most notably, the intense band at 1700 nm in its NIR spectrum is consistent with the absorption band of *Intermediate 1* observed in the reaction between mononuclear complex $(\text{Et}_4\text{N})_2[\text{Co}(\text{HL}^{i\text{Pr}})_2]$ and dioxygen. We tentatively assign the absorption band at $\lambda_{\text{max}} = 1700$ nm to be an intervalence charge-transfer band (IVCT) consistent with a species containing a ligand radical.³²

Deep blue X-ray diffraction quality crystals of $(\text{Et}_4\text{N})[\text{Co}(\text{HL}^{i\text{Pr}})_2]^{\text{ox}}$ were obtained by the slow diffusion of diethyl ether into a CH_3CN solution of the complex at room temperature. The solid-state structure of $(\text{Et}_4\text{N})[\text{Co}(\text{HL}^{i\text{Pr}})_2]^{\text{ox}}$ shows that the cobalt ion remains four-coordinate and confirms the overall charge of the complex to be (-1).³¹ Due to the poor diffraction quality of the data, the specific location of the ligand-localized radical is unclear. To date, attempts to obtain higher quality X-ray diffraction data have been unsuccessful. However, the results obtained from the UV-visible NIR absorption data of $(\text{Et}_4\text{N})[\text{Co}(\text{HL}^{i\text{Pr}})_2]^{\text{ox}}$ indicate that the first step involved in the binding of dioxygen to $(\text{Et}_4\text{N})_2[\text{Co}(\text{HL}^{i\text{Pr}})_2]$ could be the generation of a short-lived cobalt(II)-superoxide ligand radical species (*Intermediate 1*).



Scheme 3-8. One-electron chemical oxidation of $(\text{Et}_4\text{N})_2[\text{Co}(\text{HL}^{\text{iPr}})_2]$ to generate $(\text{Et}_4\text{N})[\text{Co}(\text{HL}^{\text{iPr}})_2]^{\text{ox}}$.

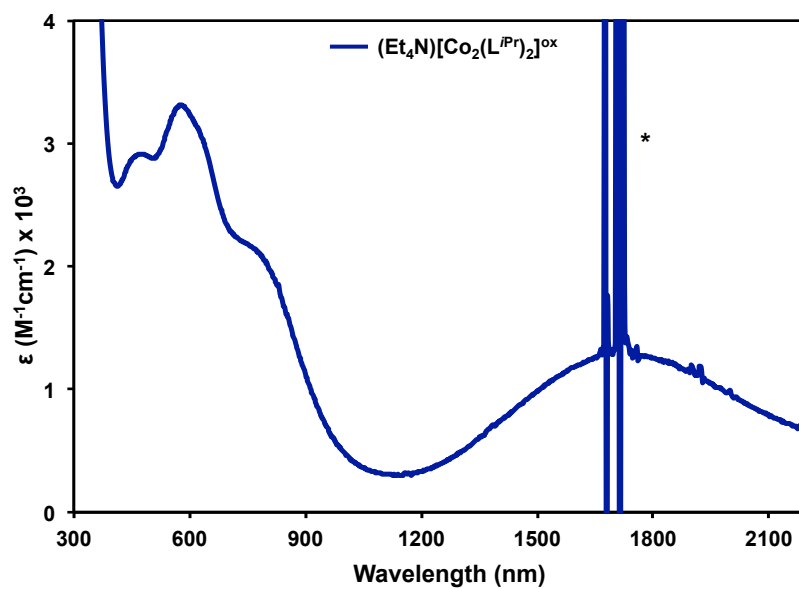
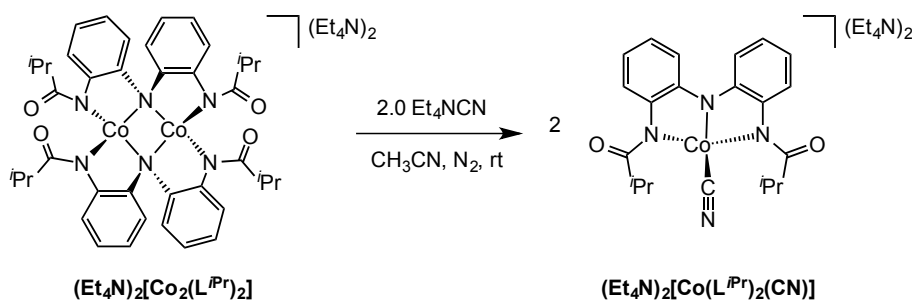


Figure 3-8. UV-visible NIR absorption spectrum of $(\text{Et}_4\text{N})[\text{Co}(\text{HL}^{\text{iPr}})_2]$. Recorded in CH_3CN at room temperature. Quartz from cuvette is marked by an asterisk (*).

Section 3-3-4. Synthetic Studies to Probe Possible Catalyst Structure

The spectroscopic studies presented in this work unambiguously demonstrate that both $(\text{Et}_4\text{N})_2[\text{Co}_2(\text{L}^{\text{iPr}})_2]$ and $(\text{Et}_4\text{N})_2[\text{Co}(\text{HL}^{\text{iPr}})_2]$ can undergo significant structural rearrangement during their respective oxygenation reactions. To probe the propensity of $(\text{Et}_4\text{N})_2[\text{Co}_2(\text{L}^{\text{iPr}})_2]$ to undergo rearrangement upon reaction with an exogenous ligand, it was reacted with cyanide. The cyanide anion is a strong-field ligand and is commonly used in both biochemical and synthetic studies to probe dioxygen coordination.³³ The dinuclear cobalt(II) complex reacts readily with two equivalents (one equivalent per cobalt center) of tetraethylammonium cyanide ($[\text{Et}_4\text{N}]\text{CN}$) to produce a deep burgundy-colored solution. The product of this reaction corresponds to a mononuclear cobalt(II)-cyano complex, $(\text{Et}_4\text{N})_2[\text{Co}(\text{L}^{\text{iPr}})(\text{CN})]$ (Scheme 3-9). $(\text{Et}_4\text{N})_2[\text{Co}(\text{L}^{\text{iPr}})(\text{CN})]$ exhibits a cyanide stretch in the solid-state FTIR spectrum at 2109 cm^{-1} , consistent with a terminally bound cyanide ligand.³⁴



Scheme 3-9. Synthesis of mononuclear cobalt(II)-cyano complex, $(\text{Et}_4\text{N})_2[\text{Co}(\text{L}^{\text{iPr}})(\text{CN})]$.

Dark burgundy-colored crystals of $(\text{Et}_4\text{N})_2[\text{Co}(\text{L}^{\text{tr}})(\text{CN})]$ were obtained by diffusion of diethyl ether (Et_2O) into a CH_3CN solution of the complex at room temperature in 70% yield. Its molecular structure was determined by X-ray diffraction studies (Figure 3-9) and the metrical parameters for this complex are listed in Table 3-2. This complex crystallizes in the monoclinic $\text{P}2(1)/n$ space group with four crystallographically independent but geometrically similar molecules in its asymmetric unit. The solid-state structure of $(\text{Et}_4\text{N})_2[\text{Co}(\text{L}^{\text{tr}})(\text{CN})]$ reveals that the cobalt(II) ion is coordinated by one tridentate, trianionic ligand in a meridional fashion and is situated in a distorted trigonal pyramidal geometry ($\tau_4 = 0.61$).³⁵ The average C–N bond lengths and angles observed in its solid-state structure are consistent with a cobalt(II) center coordinated to a trianionic ligand. The $\text{N}_{\text{Amido}}\text{--Co--C}_{\text{CN}}$ angle is observed to be $134.87(7)^\circ$.

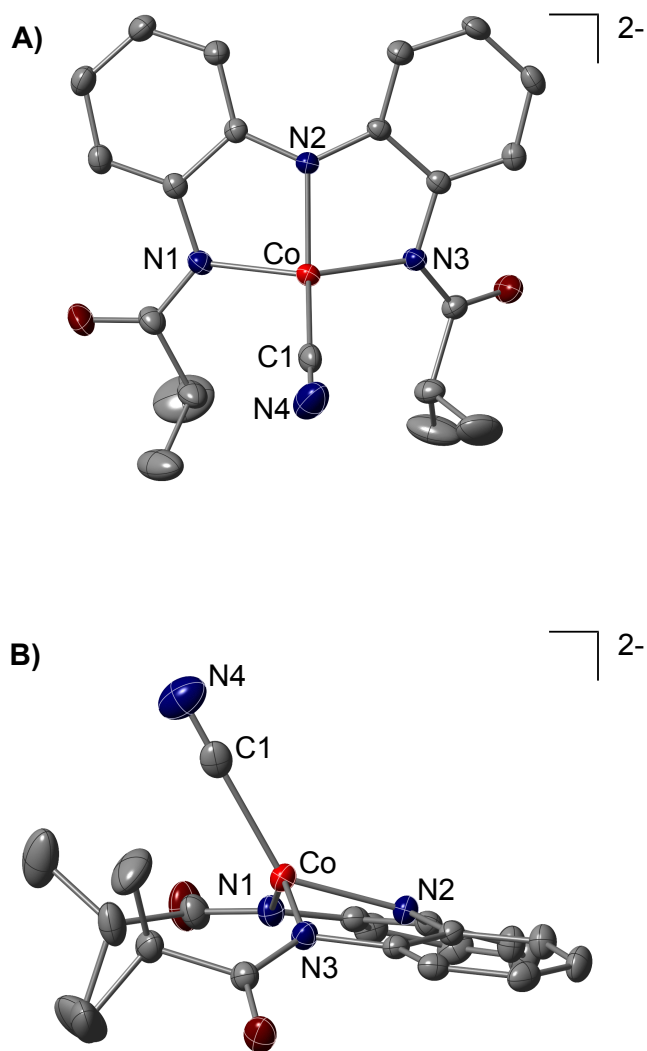


Figure 3-9. A) Solid-state structure of $(\text{Et}_4\text{N})_2[\text{Co}(\text{L}^{i\text{Pr}})(\text{CN})]$. B) Side view of $(\text{Et}_4\text{N})_2[\text{Co}(\text{L}^{i\text{Pr}})(\text{CN})]$ showing the orientation of the cyano ligand with respect to the tridentate ligand. Thermal ellipsoids are drawn at 40% probability. Hydrogen atoms and tetraethylammonium counteranions have been omitted for clarity.

Table 3-2. Selected bond lengths (Å) and angles (°) for (Et₄N)₂[Co(L^{iPr})(CN)].

Bond Lengths (Å) and Angles (°)	
(Et ₄ N) ₂ [Co(L ^{iPr})(CN)]	
Co–N2	1.9505(15)
Co–N1/N3	1.9985(16)/2.0096(15)
Co–C1	2.089(2)
N1/N3–Co–C1	107.93(7)/109.32(6)
N2–Co–C1	134.87(7)
N1–Co–N3	139.0(6)
N1/N3–Co–N2	83.14(6)/82.36(6)
τ_4	0.61

The complex, (Et₄N)₂[Co(L^{iPr})(CN)], displays paramagnetically-shifted peaks in its ¹H NMR spectrum and exhibits a μ_{eff} value of 4.27(3) μ_{B} at 298K in CDCl₃, indicative of a cobalt(II) high-spin system ($S = 3/2$). As a CH₃CN solution, this complex exhibits a high-energy, high-intensity broad shoulder at $\lambda_{\text{max}} = 502$ nm ($\epsilon = 1070$ M⁻¹cm⁻¹) followed by a low-energy low intensity broad band at $\lambda_{\text{max}} = 740$ nm ($\epsilon = 390$ M⁻¹cm⁻¹) in its UV-visible absorption spectrum (Figure 3-10). We assign the shoulder at $\lambda_{\text{max}} = 502$ nm to be a metal-to-ligand charge transfer (MLCT) band promoted by the cyanide ligand bound to the cobalt(II) center and the broad band at $\lambda_{\text{max}} = 740$ nm to correspond to a d–d transition.

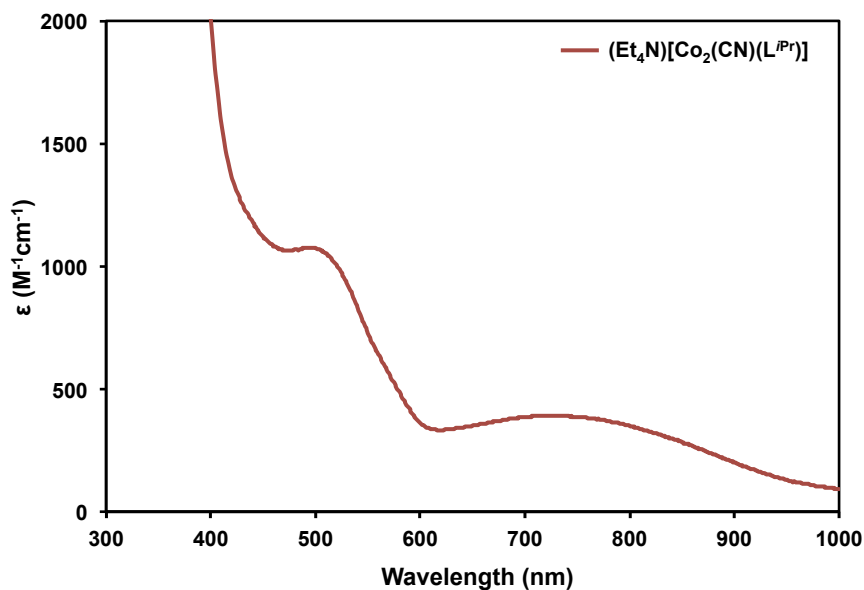


Figure 3-10. UV-visible absorption spectrum of $(\text{Et}_4\text{N})_2[\text{Co}(\text{L}^{i\text{Pr}})(\text{CN})]$ in CH_3CN . Recorded at room temperature.

The electrochemical properties of $(\text{Et}_4\text{N})_2[\text{Co}(\text{L}^{i\text{Pr}})(\text{CN})]$ were investigated by cyclic voltammetry in dichloromethane (CH_2Cl_2). This complex displays a single, one-electron reversible event. As shown in Figure 3-11, this is an oxidation event centered at $E_{1/2} = -1.164$ V vs. Fc/Fc^+ . These results demonstrate that $(\text{Et}_4\text{N})_2[\text{Co}(\text{L}^{i\text{Pr}})(\text{CN})]$ is unable to promote catalytic dioxygen activation. Given these results, we sought to investigate its reactivity with dioxygen. Reaction of a CH_3CN solution of $(\text{Et}_4\text{N})_2[\text{Co}(\text{L}^{i\text{Pr}})(\text{CN})]$ with excess dioxygen gas in the presence of PPh_3 (100 equivalents) at room temperature did not result in O-atom transfer. Performing the oxidation reactions with stoichiometric amounts of substrate yielded similar results. These observations are in accordance with the electrochemical results obtained and indicate that the cobalt(II)-cyano complex, $(\text{Et}_4\text{N})_2[\text{Co}(\text{L}^{i\text{Pr}})(\text{CN})]$, is not a catalyst for aerobic O-atom transfer reactions.

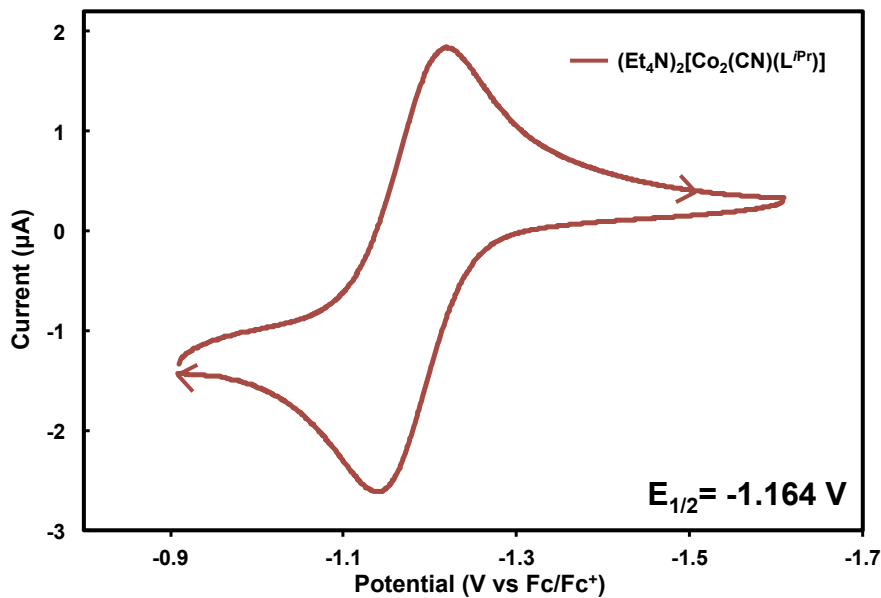
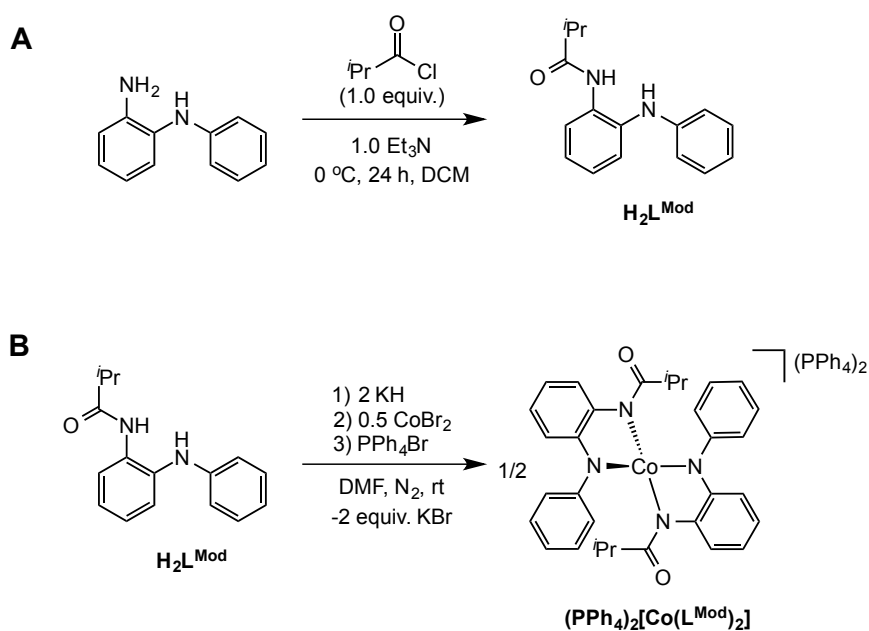


Figure 3-11. Cyclic voltammogram of $(\text{Et}_4\text{N})_2[\text{Co}(\text{L}^{i\text{Pr}})(\text{CN})]$. Conditions: 10 mV/s, with 0.1 M $\text{TBAPF}_6/\text{TBA}$ in CH_2Cl_2 as the supporting electrolyte, referenced vs. Fc/Fc^+ , Ag/Ag^+ as the reference electrode, using a glassy carbon working electrode, with scans initially negative.

Section 3-3-5. Synthetic Studies to Probe the Role of The Ligand Backbone

In order to observe if the tridentate coordination mode of this ligand is key for the catalytic reactivity exhibited by both $(\text{Et}_4\text{N})_2[\text{Co}_2(\text{L}^{i\text{Pr}})_2]$ and $(\text{Et}_4\text{N})_2[\text{Co}(\text{HL}^{i\text{Pr}})_2]$ with dioxygen, additional synthetic work was carried out. For this purpose, a bidentate potentially-dianionic ligand, *N*-(2-(phenylamino)-phenyl)isobutyramide [$\text{HN}(\text{Ph})(o\text{-PhNHC}(\text{O})^i\text{Pr}]$, or $(\text{H}_2\text{L}^{\text{Mod}})$, was prepared according to Scheme 3-10A. This ligand can be isolated as an air-stable, off-white powder in 90% yield directly from the acylation of

commercially available *N*-Phenyl-*o*-phenylenediamine with isobutyryl chloride in the presence of Et₃N at 0°C in CH₂Cl₂. Metalation of H₂L^{Mod} with cobalt(II) was carried out by deprotonating a dimethylformamide (DMF) solution of this ligand with two equivalents of potassium hydride (KH), followed by the addition of 0.5 equivalents of cobalt(II) bromide (CoBr₂) at room temperature under a nitrogen atmosphere. Subsequent *in situ* salt metathesis with tetraphenylphosphonium bromide (PPh₄Br) affords (PPh₄)₂[Co(L^{Mod})₂] (Scheme 3-10b).



Scheme 3-10. **A)** Synthesis of bidentate ligand [HN(Ph)(*o*-PhNHC(O)^{*i*}Pr] (H₂L^{Mod}) and **B)** its metalation with cobalt(II) to form mononuclear cobalt(II) complex (PPh₄)₂[Co(L^{Mod})₂].

Dark red-colored X-ray diffraction quality crystals of (PPh₄)₂[Co(L^{Mod})₂] were obtained by slow diffusion of Et₂O into a CH₃CN solution of the complex at room

temperature in 75% yield. The molecular structure of $(\text{PPh}_4)_2[\text{Co}(\text{L}^{\text{Mod}})_2]$ was obtained by X-ray diffraction studies (Figure 3-12) and the metrical parameters are listed in Table 3-3. This complex crystallizes in the $P2(1)$ space group with four geometrically similar but crystallographically independent molecules in its asymmetric unit. The solid-state structure of $(\text{PPh}_4)_2[\text{Co}(\text{L}^{\text{Mod}})_2]$ shows that the coordination about the cobalt(II) ion is in a distorted trigonal pyramidal geometry ($\tau_4 = 0.74$).³⁵ More importantly, the molecular structure of $(\text{PPh}_4)_2[\text{Co}(\text{L}^{\text{Mod}})_2]$ shows that the bond lengths and angles about the cobalt(II) ion are nearly identical to the structural parameters observed in the solid-state structure of mononuclear cobalt(II) complex, $(\text{Et}_4\text{N})_2[\text{Co}(\text{HL}^{\text{Pr}})_2]$,³¹ supported by the tridentate ligand $(\text{H}_3\text{L}^{\text{Pr}})$.

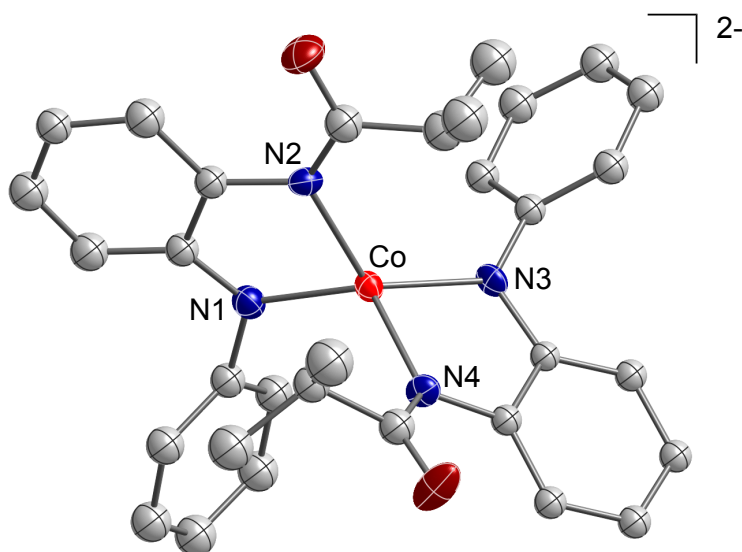


Figure 3-12. Solid-state structure of $(\text{PPh}_4)_2[\text{Co}(\text{L}^{\text{Mod}})_2]$. Thermal ellipsoids are drawn at 40% probability. Hydrogen atoms and tetraphenylphosphonium counterions have been omitted for clarity.

Table 3-3. Selected bond lengths (Å) and angles (°) for $(\text{PPh}_4)_2[\text{Co}(\text{L}^{\text{Mod}})_2]$.

Bond Lengths (Å) and Angles (°)	
$(\text{PPh}_4)_2[\text{Co}(\text{L}^{\text{Mod}})_2]$	
Co–N1/N4	2.031(5)/2.005(5)
Co–N2/N3	1.962(5)/1.980(5)
N2–Co–N3	125.0(2)
N1–Co–N3	131.2(2)
N2–Co–N4	121.8(2)
N1–Co–N2	82.4(2)
N1–Co–N4	118.6(2)
τ_4	0.74

The complex $(\text{PPh}_4)_2[\text{Co}(\text{L}^{\text{Mod}})_2]$ displays 11 paramagnetically-shifted peaks in its ^1H NMR spectrum (CD_3CN , 400 MHz), corresponding to a C_2 -symmetric complex in solution. The magnetic and spectral properties exhibited by the complex $(\text{PPh}_4)_2[\text{Co}(\text{L}^{\text{Mod}})_2]$ are very similar to those observed in $(\text{Et}_4\text{N})_2[\text{Co}(\text{HL}^{i\text{Pr}})_2]$.³¹ For example, $(\text{PPh}_4)_2[\text{Co}(\text{L}^{\text{Mod}})_2]$ displays an absorption band at $\lambda_{\text{max}} = 570$ nm, ($\epsilon = 812 \text{ M}^{-1}\text{cm}^{-1}$) in its UV-visible absorption spectrum in CH_3CN , indicative of a d–d transition (Figure 3-13). Furthermore, $(\text{PPh}_4)_2[\text{Co}(\text{L}^{\text{Mod}})_2]$ exhibits a μ_{eff} value of $4.93(6) \mu_{\text{B}}$ (Evan's Method, CD_3CN 400 MHz, 298K),³⁶ indicative of a cobalt(II) center in high-spin state system ($S = 3/2$).

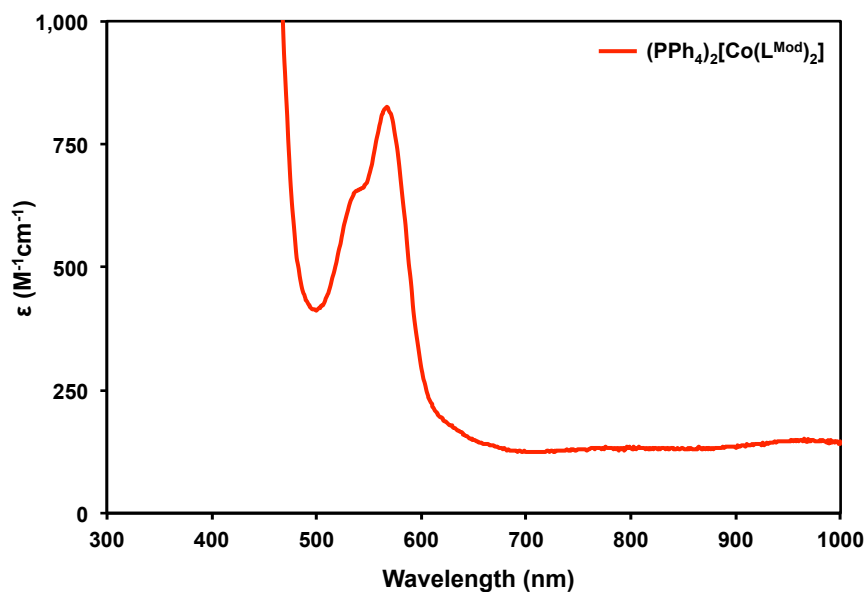


Figure 3-13. UV-visible absorption of $(\text{PPh}_4)_2[\text{Co}(\text{L}^{\text{Mod}})_2]$. Spectrum recorded in CH_3CN at room temperature.

The electrochemical properties of $(\text{PPh}_4)_2[\text{Co}(\text{L}^{\text{Mod}})_2]$ were investigated using cyclic voltammetry in CH_2Cl_2 . Interestingly, the cyclic voltammogram of $(\text{PPh}_4)_2[\text{Co}(\text{L}^{\text{Mod}})_2]$ varies significantly with respect to the cyclic voltammogram of $(\text{Et}_4\text{N})_2[\text{Co}(\text{HL}^{i\text{Pr}})_2]$. The mononuclear complex $(\text{Et}_4\text{N})_2[\text{Co}(\text{HL}^{i\text{Pr}})_2]$, supported by the tridentate ligand $(\text{H}_3\text{L}^{i\text{Pr}})$, displays three reversible oxidation events in its cyclic voltammogram,³¹ whereas $(\text{PPh}_4)_2[\text{Co}(\text{L}^{\text{Mod}})_2]$ displays only two one-electron oxidation events centered at $E_{1/2} = -1.126\text{V}$ and $E_{1/2} = -0.666\text{V}$ vs. Fc/Fc^+ in its cyclic voltammogram (Figure 3-14).

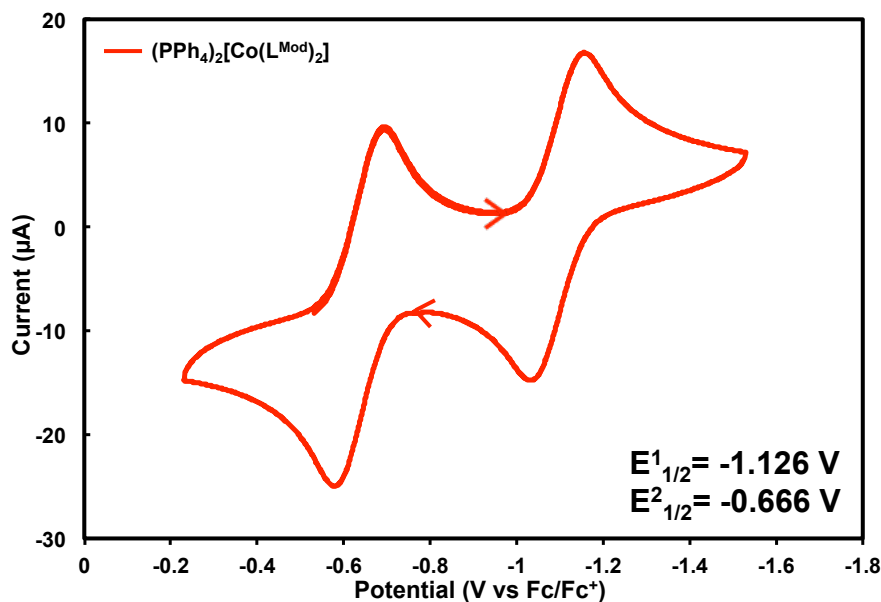
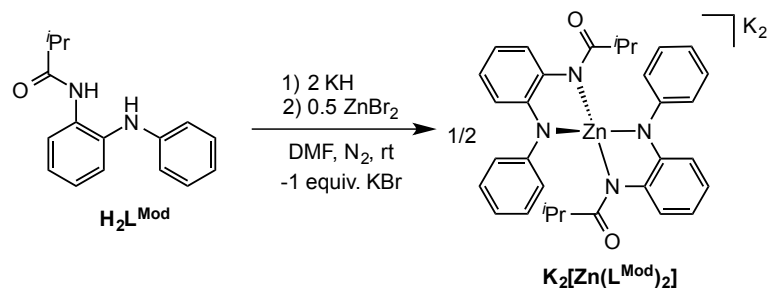


Figure 3-14. Cyclic voltammogram of $(\text{PPh}_4)_2[\text{Co}(\text{L}^{\text{Mod}})_2]$. Conditions: 10 mV/s, with 0.1M TBAPF₆TBA in CH₂Cl₂ as the supporting electrolyte, referenced vs. Fc/Fc⁺, Ag/Ag⁺ as the reference electrode, using a glassy carbon working electrode, with scans initially negative.

To further understand the role of the second carboxamide moiety of the tridentate ligand ($\text{H}_3\text{L}^{\text{iPr}}$) in catalysis, the complex $(\text{PPh}_4)_2[\text{Co}(\text{L}^{\text{Mod}})_2]$ was tested for its ability to catalytically activate dioxygen and oxidize PPh_3 under aerobic conditions. When a CH₃CN solution of $(\text{PPh}_4)_2[\text{Co}(\text{L}^{\text{Mod}})_2]$ was treated with 100 equivalents of PPh_3 and exposed to a continuous flow of dioxygen gas, only 18% of PPh_3 was converted to OPPh_3 after 20 hours, as determined by gas chromatography (GC). Contrary to the high oxidation rates for aerobic PPh_3 oxidation exhibited by both $(\text{Et}_4\text{N})_2[\text{Co}_2(\text{L}^{\text{iPr}})_2]$ and $(\text{Et}_4\text{N})_2[\text{Co}(\text{HL}^{\text{iPr}})_2]$,³¹ the complex $(\text{PPh}_4)_2[\text{Co}(\text{L}^{\text{Mod}})_2]$ proves to be an ineffective catalyst for this transformation.

Section 3-3-5. Synthetic Studies to Establish the Redox Non-innocence of Tridentate, Trianionic Ligand $[L^{iPr}]^{3-}$

In order to establish the redox non-innocence of the tridentate, trianionic ligand $[L^{iPr}]^{3-}$, attempts were made to synthesize zinc(II) complexes isostructural to $(Et_4N)_2[Co_2(L^{iPr})_2]$ and $(Et_4N)_2[Co(HL^{iPr})_2]$. It was hypothesized that any reversible electrochemical events displayed in the cyclic voltammograms of these isostructural complexes would originate from the ligand scaffolds, as zinc(II) is a redox-inactive metal ion. Unfortunately, only a dinuclear zinc(II) complex, $(Et_4N)_2[Zn_2(L^{iPr})_2]$ isostructural to $(Et_4N)_2[Co_2(L^{iPr})_2]$, was isolated regardless of the metalation route utilized (discussed in Chapter 2). However, the dinuclear zinc(II) complex $(Et_4N)_2[Zn_2(L^{iPr})_2]$, gives rise to a number of irreversible responses in its cyclic voltammogram we were not able to assign. A mononuclear zinc(II) complex was synthesized using the bidentate ligand $[HN(Ph)(o-PhNHC(O)^iPr)]$ (H_2L^{Mod}). Using the same synthetic approach as with $(PPh_4)_2[Co(L^{Mod})_2]$, a DMF solution of the ligand $[HN(Ph)(o-PhNHC(O)^iPr)]$ (H_2L^{Mod}) was treated with two equivalents of KH and metalated with 0.5 equivalents of $ZnBr_2$ to obtain the mononuclear four-coordinate zinc(II) complex, $K_2[Zn(L^{Mod})_2]$ (Scheme 3-11).



Scheme 3-11. Synthesis of mononuclear zinc(II) complex, $K_2[Zn(L^{Mod})_2]$.

Light yellow-colored X-ray diffraction quality crystals of $K_2[Zn(L^{Mod})_2]$ were obtained by diffusion of Et_2O into a solution of CH_3CN of the complex at room temperature in 72 % yield. Its molecular structure was obtained by X-ray diffraction studies (Figure 3-15). This complex crystallizes in the $P2(1)/c$ space group and the metrical parameters, shown in Table 3-4, show that the complex is isostructural to its cobalt(II) analogue, $(PPh_4)_2[Co(L^{Mod})_2]$. The zinc(II) ion sits in a distorted trigonal pyramidal geometry ($\tau_4 = 0.73$)³⁵ and the $Zn-N_{Amido}$ and $Zn-N_{Amidate}$ are consistent with a dianionic ligand bound to a zinc(II) ion. The slight differences between $(PPh_4)_2[Co(L^{Mod})_2]$ and $K_2[Zn(L^{Mod})_2]$ could be attributed to the differences in ionic radii size between Co^{2+} and Zn^{2+} , which resultantly induces slight changes in the bond lengths and angles of the overall structure.

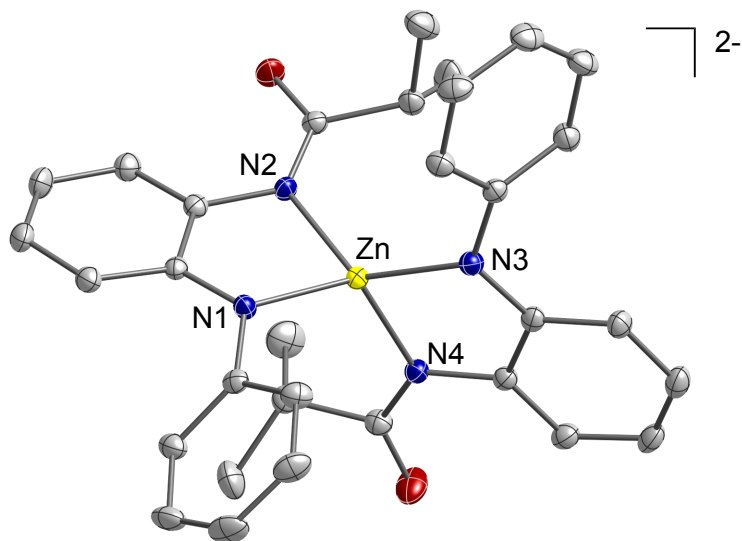


Figure 3-15. Solid-state structure of $K_2[Zn(L^{Mod})_2]$. Thermal ellipsoids are drawn at 40% probability. Hydrogen atoms and potassium counterions have been omitted for clarity.

Table 3-4. Selected bond lengths (Å) and angles (°) for $K_2[Zn(L^{Mod})_2]$.

Bond Lengths (Å) and Angles (°)	
$K_2[Zn(L^{Mod})_2]$	
Zn–N1/N4	1.999(2)/2.042(2)
Zn–N2/N3	2.047(2)/1.982(2)
N2–Zn–N3	128.44(8)
N1–Zn–N3	128.66(8)
N2–Zn–N4	117.34 (8)
N1–Zn–N2	83.66(9)
N1–Zn–N4	117.92 (8)
τ_4	0.73

The electrochemical properties of $K_2[Zn(L^{Mod})_2]$ were investigated by cyclic voltammetry to establish the redox non-innocence of this ligand. The cyclic voltammogram of $K_2[Zn(L^{Mod})_2]$ in CH_2Cl_2 , shown in Figure 3-16, displays two quasi-reversible events centered at $E_{1/2} = -0.894V$ and $E_{1/2} = -0.590V$ vs. Fc/Fc^+ . These events are assigned as two one-electron oxidation events. We interpret the redox-inactive zinc(II) data to imply that the observed sequential oxidations are predominantly ligand-centered. These results are further supported by the comparable, yet shifted oxidation potentials of the cobalt(II) complex, $(PPh_4)_2[Co(L^{Mod})_2]$ ($E_{1/2} = -1.126V$ and $-0.666V$ vs. Fc/Fc^+).

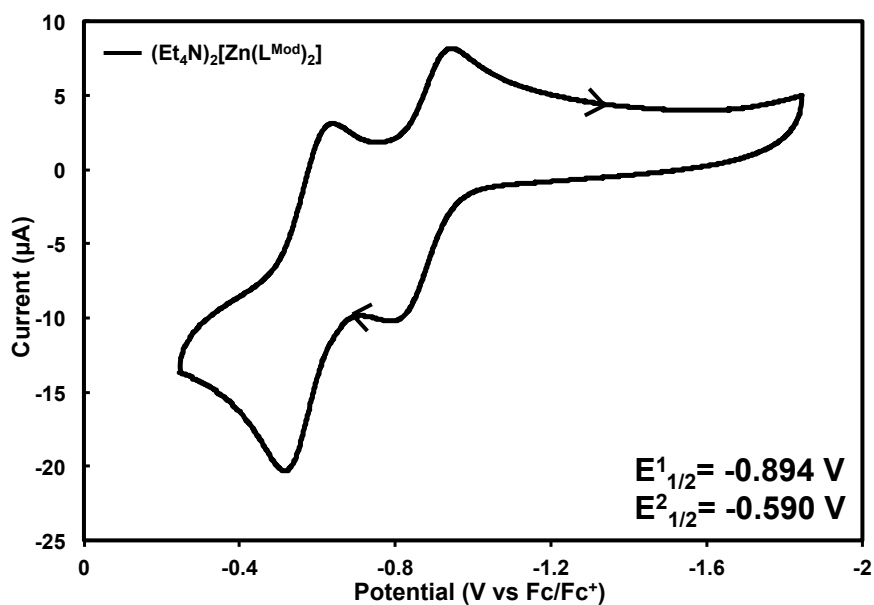
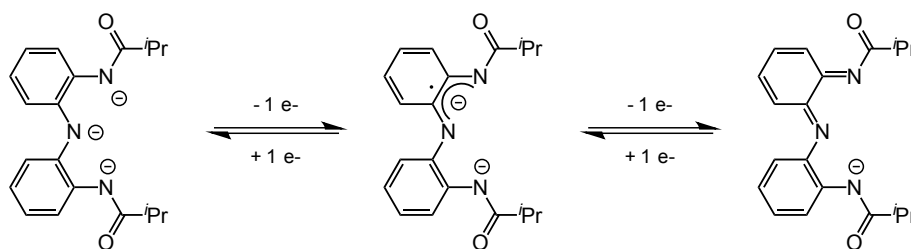


Figure 3-16. Cyclic voltammogram of $K_2[Zn(L^{Mod})_2]$. Conditions: 10 mV/s, with 0.1M TBAPF₆TBA in CH_2Cl_2 as the supporting electrolyte, referenced vs. Fc/Fc^+ , Ag/Ag^+ as the reference electrode, using a glassy carbon working electrode, with scans initially negative.

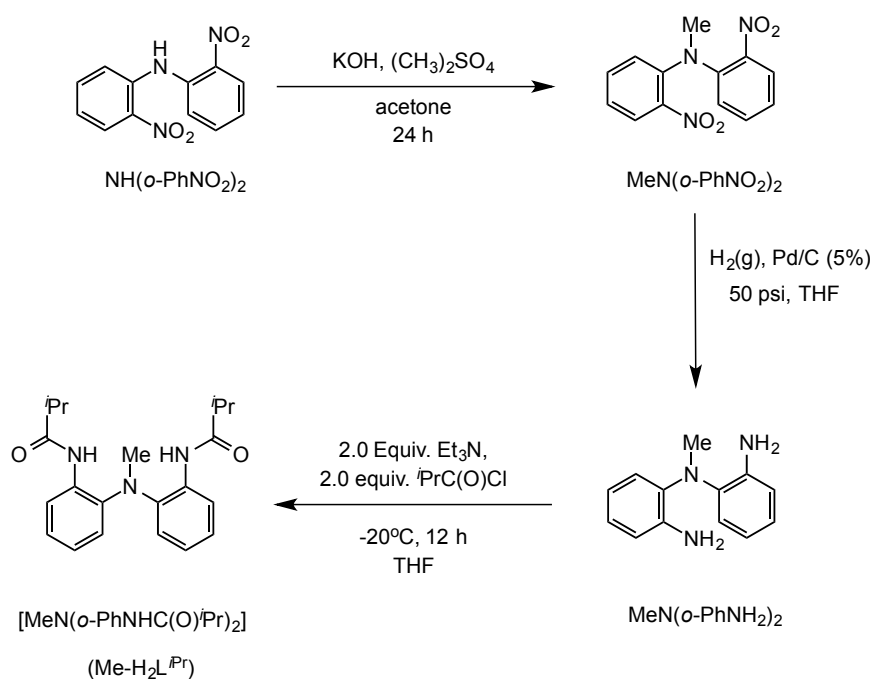
Section 3-3-6. Synthetic Studies to Establish the Redox Non-innocence of Tridentate, Trianionic Ligand $[L^{iPr}]^{3-}$

The results presented above establish the redox activity of the bidentate, dianionic ligand $[N(Ph)(o\text{-PhNC}(O)^iPr)]^{2-}$ ($[L^{Mod}]^{2-}$). However, further evidence for the redox non-innocence of the tridentate, trianionic ligand $[N(o\text{-PhNC}(O)^iPr)_2]^{3-}$ ($[L^{iPr}]^{3-}$) was obtained by structural and synthetic studies involving its structural modification. It was envisaged that when coordinated, the trianionic ligand backbone $[L^{iPr}]^{3-}$ acts as a redox-active ligand by undergoing two successive oxidations, as proposed for triamido platforms that incorporate *o*-phenylenediamine backbones (Scheme 3-12).³⁷ In order to test this hypothesis, a ligand was designed in where the central nitrogen atom would be tertiary by placing a methyl group, which was speculated to yield several effects. Notably, the alkylation of this position would remove an acidic proton from the ligand backbone, reducing the number of deprotonation sites. Although the alkylated amine would still be available to coordinate metal ions as neutral, two-electron donor, this modification would significantly impact the ligand's ability to act as a redox-active scaffold by shutting down the redox pathway outlined in Scheme 3-12.



Scheme 3-12. Possible oxidation states of the trianionic ligand platform $[L^{iPr}]^{3-}$.

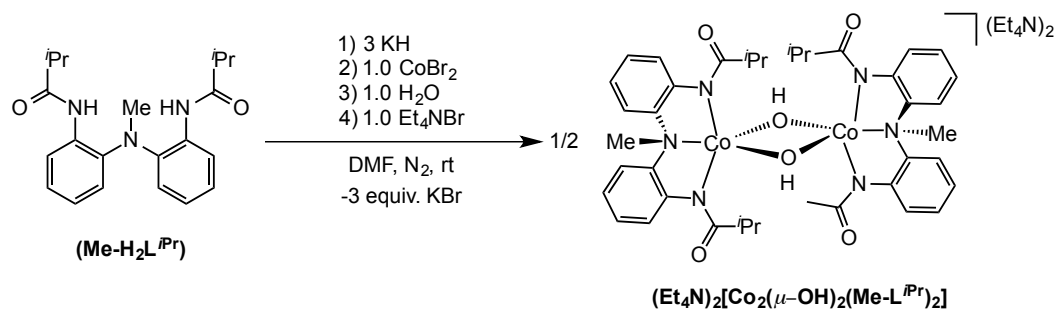
With this hypothesis in mind, the ligand $\text{MeN}(o\text{-PhNHC(O)}^i\text{Pr})_2$ ($\text{Me-H}_2\text{L}^{i\text{Pr}}$) was synthesized according to Scheme 3-13. In the synthesis of this ligand, the bis(nitro)amine ligand $\text{HN}(o\text{-PhNO}_2)_2$ ³¹ is first methylated with dimethyl sulfate in the presence of equivalent amounts of potassium hydroxide (KOH) in acetone to obtain $\text{MeN}(o\text{-PhNO}_2)_2$. A reduction of $\text{MeN}(o\text{-PhNO}_2)_2$ was followed by Palladium-catalyzed hydrogenation to yield $\text{MeN}(o\text{-PhNH}_2)_2$. Lastly, acylation of $\text{MeN}(o\text{-PhNH}_2)_2$ with isobutyryl chloride at low temperature ($-20\text{ }^\circ\text{C}$) in the presence of Et_3N yields the desired product ($\text{Me-H}_2\text{L}^{i\text{Pr}}$) as an off-white and air-stable solid in 96 % yield.



Scheme 3-13. Synthesis of the ligand $\text{MeN}(o\text{-PhNHC(O)}^i\text{Pr})_2$ ($\text{Me-H}_2\text{L}^{i\text{Pr}}$).

Given the nature of $\text{MeN}(o\text{-PhNHC(O)}^i\text{Pr})_2$ ($\text{Me-H}_2\text{L}^{i\text{Pr}}$), with only two available sites for deprotonation, metalation of this ligand was approached by deprotonating a DMF solution of this ligand with two equivalents of KH followed by addition of one

equivalent of CoBr_2 . Unexpectedly, the isolated product of this reaction proved to be a dimeric cobalt(II) species containing two bridging hydroxide ligands, $[\text{Co}_2(\mu\text{-OH})_2(\text{Me-L}^{i\text{Pr}})_2]^{2-}$. It was rationalized that the bridging hydroxide ligands originated from residual H_2O molecules in the solvents. This led us to systematically design an approach to purposefully synthesize this bis(μ -hydroxo) bridged complex. Thus, as seen in Scheme 3-14, the $[\text{Co}_2(\mu\text{-OH})_2(\text{Me-L}^{i\text{Pr}})_2]^{2-}$ dimer can be readily synthesized by treating a DMF solution of the ligand ($\text{Me-H}_2\text{L}^{i\text{Pr}}$) with three equivalents of KH (two for deprotonation of the ligand and one extra equivalent for the deprotonation of water to form the bridging hydroxide ligands). Subsequent addition of one equivalent of CoBr_2 and one equivalent of H_2O to the reaction mixture followed by an *in situ* salt metathesis of one equivalent of Et_4NBr leads to the isolation of the tetraethylammonium salt of $(\text{Et}_4\text{N})_2[\text{Co}_2(\mu\text{-OH})_2(\text{Me-L}^{i\text{Pr}})_2]$ in 76 % yield.



Scheme 3-14. Synthesis of dinuclear cobalt(II) complex $(\text{Et}_4\text{N})_2[\text{Co}_2(\mu\text{-OH})_2(\text{Me-L}^{i\text{Pr}})_2]$.

Magenta-colored X-ray diffraction quality crystals of $(\text{Et}_4\text{N})_2[\text{Co}_2(\mu\text{-OH})_2(\text{Me-L}^{i\text{Pr}})_2]$ were obtained by slow diffusion of Et_2O into a DMF solution of the complex at room temperature. Its molecular structure was determined by X-ray diffraction studies

(Figure 3-17) and the metrical parameters for this complex are listed in Table 3-5. This complex is bridged by two hydroxide ligands that separate the two crystallographically equivalent cobalt(II) ions by a through-space distance of 3.087(1) Å, ruling out a possible Co–Co bond. The O··O through-space distance between the two μ -bridging-hydroxo ligands in this complex is 2.569(1) Å, confirming the absence of an O–O bond. Additionally, the solid-state structure of $(\text{Et}_4\text{N})_2[\text{Co}_2(\mu\text{-OH})_2(\text{Me-L}^{\text{Pr}})_2]$ shows that each cobalt(II) ion is five-coordinate and displays a very slightly distorted square pyramidal geometry ($\tau_5 = 0.02$). The τ_5 value is a parameter used to measure trigonality in five-coordinate complexes. A τ_5 value of 0.0 corresponds to perfect square-pyramidal geometries while a τ_5 value of 1.0 is indicative of a perfect trigonal-bipyramidal geometry.³⁸

This complex is interesting from both a synthetic and structural standpoint. Synthetic cobalt(II) bis- μ -hydroxo dimers are very rare, and only few of them have been reported in the literature.³⁹ Specifically, Moro-oka and co-workers have reported on these rare species with a primary focus on their synthesis and characterization as synthetic models of various metalloenzymes capable of carrying out C–H oxidation reactions.⁴⁰

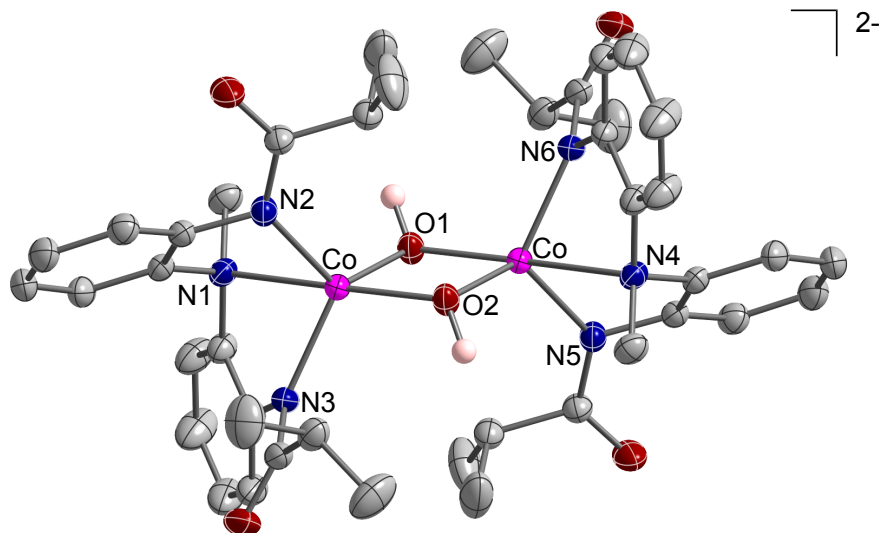


Figure 3-17. Solid-state structure of $(\text{Et}_4\text{N})_2[\text{Co}_2(\mu\text{-OH})_2(\text{Me-L}^{i\text{Pr}})_2]$. Thermal ellipsoids are drawn at 40% probability. Hydrogen atoms (with the exception of the hydrogen atoms on two μ -bridging-hydroxo ligands) and tetraethylammonium counteranions have been omitted for clarity.

Table 3-5. Selected bond lengths (\AA) and angles ($^\circ$) for $(\text{Et}_4\text{N})_2[\text{Co}_2(\mu\text{-OH})_2(\text{Me-L}^{i\text{Pr}})_2]$.

Bond Lengths (\AA) and Angles ($^\circ$)	
$(\text{Et}_4\text{N})_2[\text{Co}_2(\mu\text{-OH})_2(\text{Me-L}^{i\text{Pr}})_2]$	
Co–O1/O2	1.9813(12)/2.0274(13)
Co–N1/N4	2.0436(14)
Co–N2/N5	2.0493(14)
Co–N3/N6	2.3588(6)
Co \cdots Co	3.087(1)
O \cdots O	2.569(1)
O1–Co–O2	79.58(6)
N1–Co–N2/N3	75.63(5)/73.96(5)
N2–Co–O1/O2	121.91(11)/111.22(11)
N3–Co–O1/O2	120.57(11)/107.83(10)
τ_5	0.02

Solution-state characterization of $(\text{Et}_4\text{N})_2[\text{Co}_2(\mu\text{-OH})_2(\text{Me-L}^{i\text{Pr}})_2]$ was carried out utilizing UV-visible absorption spectroscopy, ^1H NMR, and room temperature magnetic susceptibility studies. As seen in Figure 3-18, the complex exhibits an absorption band corresponding to a d–d transition with λ_{max} at 632 nm ($\epsilon = 296 \text{ M}^{-1} \text{ cm}^{-1}$) in DMF. The ^1H NMR spectrum of this complex exhibits paramagnetically shifted resonances. Solution-state magnetic moment determination indicates that this complex is low-spin ($S = \frac{1}{2}$) with a magnetic moment of $4.01(2) \mu_{\text{B}}$ (Evan's Method, CD_3CN , 400 MHz, 298K).³⁶

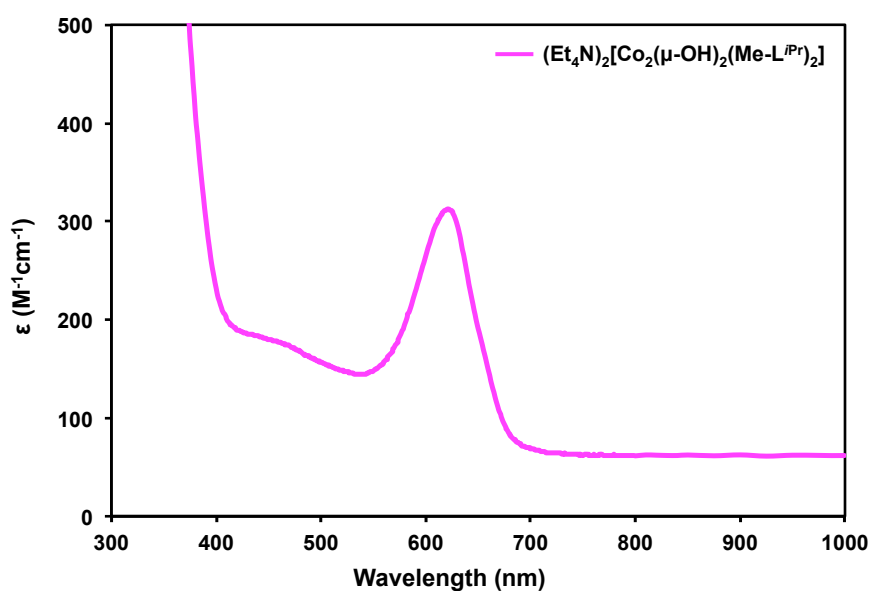


Figure 3-18. UV-visible absorption of $(\text{Et}_4\text{N})_2[\text{Co}_2(\mu\text{-OH})_2(\text{Me-L}^{i\text{Pr}})_2]$. Spectrum recorded in DMF at room temperature.

The electrochemical properties of $(\text{Et}_4\text{N})_2[\text{Co}_2(\mu\text{-OH})_2(\text{Me-L}^{i\text{Pr}})_2]$ were investigated using cyclic voltammetry in DMF. The cyclic voltammogram of this complex displays no reversible electrochemical responses (Figure 3-19). More

importantly, $(\text{Et}_4\text{N})_2[\text{Co}_2(\mu\text{-OH})_2(\text{Me-L}^{i\text{Pr}})_2]$ is unreactive toward aerobic PPh_3 oxidation evidenced when a CH_3CN solution of $(\text{Et}_4\text{N})_2[\text{Co}_2(\mu\text{-OH})_2(\text{Me-L}^{i\text{Pr}})_2]$ was exposed to excess dioxygen in the presence of 100 equivalents of PPh_3 , only traces of OPPh_3 were observed after 48 hours according to GC and ^{31}P NMR analysis. Similar results were observed when only 10 equivalents of PPh_3 were used under similar reaction conditions. These results support our hypothesis concerning the important role of the central nitrogen atom of the tridentate ligand ($\text{H}_3\text{L}^{i\text{Pr}}$). Additionally, this methylated ligand ($\text{Me-H}_2\text{L}^{i\text{Pr}}$) explicitly illustrates the cruciality of the redox-active ligand framework in $\text{H}_3\text{L}^{i\text{Pr}}$ to undergo successive oxidation events outlined in Scheme 3-12 when coordinated to cobalt(II) ions.

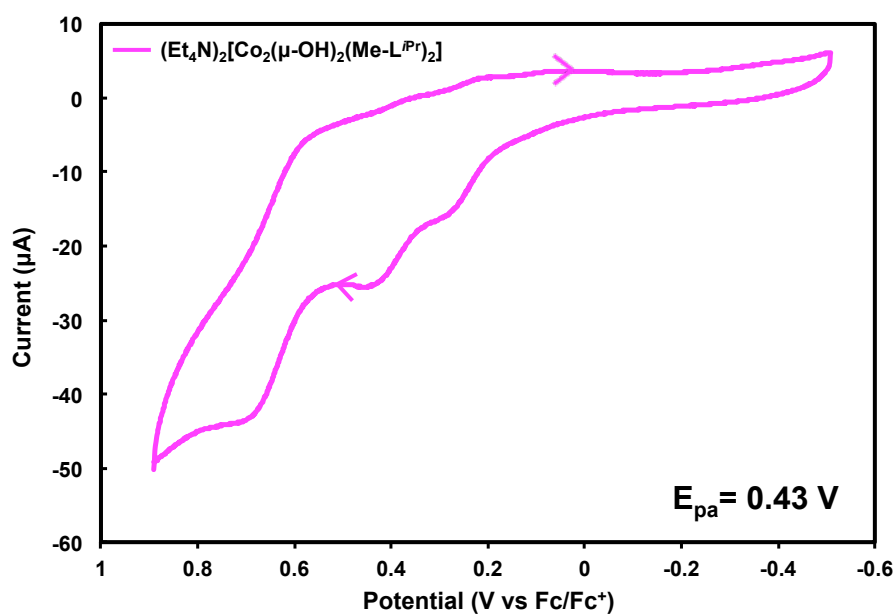


Figure 3-19. Cyclic voltammogram of $(\text{Et}_4\text{N})_2[\text{Co}_2(\mu\text{-OH})_2(\text{Me-L}^{i\text{Pr}})_2]$. Conditions: 25 mV/s, with 0.1M $\text{TBAPF}_6/\text{TBA}$ in DMF as the supporting electrolyte, referenced vs.

Fc/Fc⁺, Ag/Ag⁺ as the reference electrode, using a glassy carbon working electrode, with scans initially negative.

Section 3-3-7. Synthetic and Spectroscopic Studies Using Zinc(II) To Probe Possible Decomposition Pathway of Bidentate, Dianionic Ligand [L^{Mod}]²⁻

The negative oxidation potentials displayed by K₂[Zn(L^{Mod})₂] ($E_{1/2} = -0.894\text{V}$ and $E_{1/2} = -0.590\text{V}$ vs. Fc/Fc⁺) in its cyclic voltammogram (Figure 3-16) indicate that this complex is capable of reacting with dioxygen.⁴¹ Exposing an anhydrous light yellow-colored CH₃CN solution of K₂[Zn(L^{Mod})₂] to excess dioxygen gas resulted in the rapid formation of a dark emerald green solution. This emerald green species is stable at room temperature for days as an anhydrous CH₃CN solution. Its UV-visible absorption spectrum exhibits a band at $\lambda_{\text{max}} = 615\text{ nm}$ (Figure 3-20). Remarkably, degassing this solution mixture does not regenerate the initial spectra of K₂[Zn(L^{Mod})₂], suggesting the reaction to be irreversible. This species was isolated as an emerald green powder. Various attempts to obtain X-ray diffraction quality crystals of this species proved unsuccessful. More interestingly, when a CH₃CN solution of this emerald green species was allowed to slowly evaporate open to air overnight, a deep red-colored solution formed. This red species is stable for days at room temperature in CH₃CN and its UV-visible absorption spectrum exhibits a band at $\lambda_{\text{max}} = 500\text{ nm}$ (Figure 3-20).

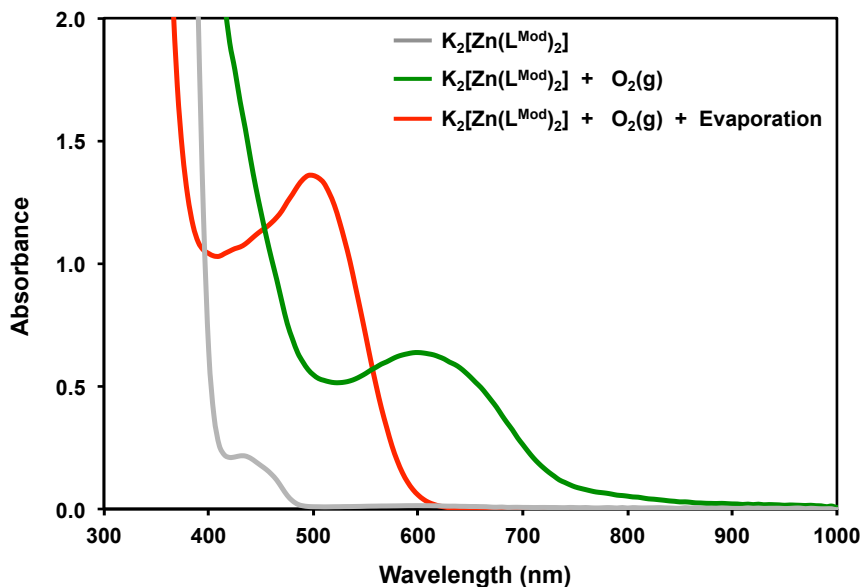
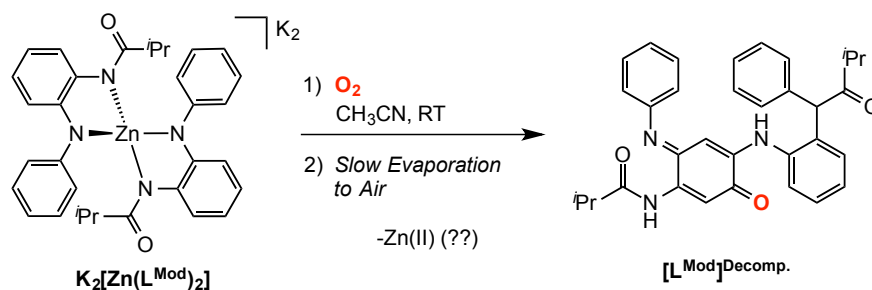


Figure 3-20. UV-visible absorption spectra of $K_2[Zn(L^{Mod})_2]$ (gray line), $K_2[Zn(L^{Mod})_2]$ after its reaction with dioxygen gas (green line), and $K_2[Zn(L^{Mod})_2]$ after its reaction with dioxygen gas followed by slow evaporation in air (red line). All spectra were recorded from isolated compounds in CH_3CN at room temperature.

With the observations that $K_2[Zn(L^{Mod})_2]$ was able to react with dioxygen, its ability to catalyze aerobic PPh_3 oxidation was investigated. Exposing a CH_3CN solution of $K_2[Zn(L^{Mod})_2]$ to dioxygen in the presence of PPh_3 (100 equivalents) resulted in a maximum 11 TON for the conversion of $OPPh_3$ after 48 hours. Experiments carried out with lower loadings of PPh_3 (50 and 10 equivalents) gave similar results, suggesting that $K_2[Zn(L^{Mod})_2]$ is a poor catalyst for aerobic PPh_3 oxidation.

The poor catalytic reactivity of $K_2[Zn(L^{Mod})_2]$ led us to further investigate its reactivity with dioxygen. These studies have provided key results about potential ligand decomposition pathways. When a solution of the fully oxidized emerald green species was exposed to air and allowed to slowly evaporate, a red X-ray diffraction quality

crystalline material resulted. This species, characterized by X-ray diffraction, ^1H NMR, solid-state FTIR, and mass spectrometry corresponds to an organic product displaying significant ligand rearrangement (Scheme 3-15). The molecular structure of this product is shown in Figure 3-21, and reveals that one oxygen atom (presumably from dioxygen) was inserted into one of the aromatic rings of the $[\text{L}^{\text{Mod}}]^{2-}$ ligand unit forming a quinone. This decomposed ligand ($[\text{L}^{\text{Mod}}]^{\text{Decomp.}}$) exhibits an N-H stretching frequency in its solid-state FTIR spectrum at 3300 and 3270 cm^{-1} . The parent peak in the mass spectrum (ESI-MS, negative mode) of this compound has an $m/z = 519.3$, consistent with a negatively charged fragment of this molecule. Intriguingly, the identity of the zinc(II) byproduct in this transformation remains unknown.



Scheme 3-15. Decomposition pathway of $\text{K}_2[\text{Zn}(\text{L}^{\text{Mod}})_2]$ observed after exposing a solution of the fully oxidized complex to air.

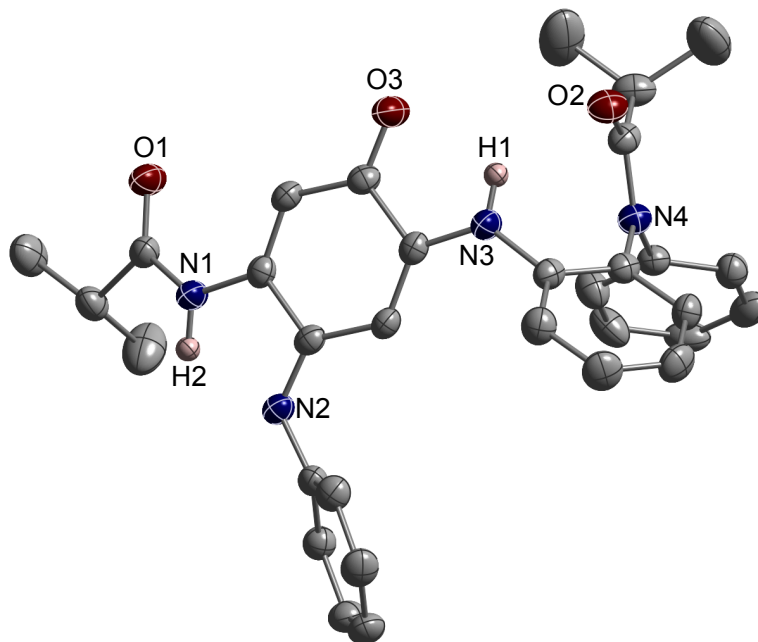


Figure 3-21. Solid-state structure of the ligand decomposition product, $[L^{\text{Mod}}]^{\text{Decomp}}$, obtained from the reaction of $K_2[Zn(L^{\text{Mod}})_2]$ with dioxygen after open-air evaporation. Thermal ellipsoids are drawn at 40 % probability.

With these results in mind, the one- and two-electron chemical oxidations of $K_2[Zn(L^{\text{Mod}})_2]$ were examined. Treating a CH_3CN solution of $K_2[Zn(L^{\text{Mod}})_2]$ with one equivalent of $FcBF_4$ at room temperature results in the almost instantaneous color change from the colorless solution of $K_2[Zn(L^{\text{Mod}})_2]$ to deep purple. The UV-visible NIR absorption spectrum of this purple species exhibits intense bands at λ_{max} ($M^{-1}cm^{-1}$) = 538 nm (2347), 680 nm (497), and 1356 nm (2099) (Figure 3-22, purple line). This species is stable at room temperature as an anhydrous CH_3CN solution. Additionally, treating a CH_3CN solution of complex $K_2[Zn(L^{\text{Mod}})_2]$ with two equivalents of $FcBF_4$ at room temperature results in the almost instantaneous color change from the colorless solution

of $K_2[Zn(L^{Mod})_2]$ to green. The UV-visible NIR absorption spectrum of this green species exhibits intense bands at λ_{max} ($M^{-1}cm^{-1}$) = 422 nm (1300) and 720 nm (3187) (Figure 3-22, green line).

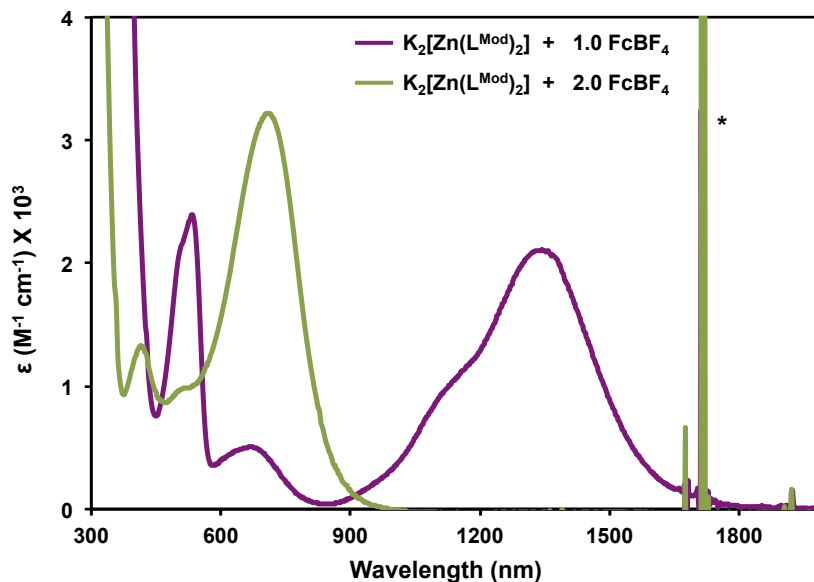


Figure 3-22. UV-visible absorption spectra of the products from one-electron (purple line) and two-electron (green line) oxidations of $K_2[Zn(L^{Mod})_2]$ resulting from treatment with one and two equivalents of $FcBF_4$, respectively. Spectra were recorded from isolated compounds in CH_3CN at room temperature.

The products from the one- and two-electron oxidations of $K_2[Zn(L^{Mod})_2]$ were investigated using X-band electron paramagnetic resonance (EPR) spectroscopy. The X-band EPR spectrum of one-electron oxidized product was recorded at room temperature in toluene. As seen in Figure 3-23A, this species exhibits typical $S = 1/2$ signals with well-defined nitrogen hyperfine structure. Its EPR spectrum displays a signal at $g=2.006$,

typical of a delocalized π -radical. The EPR spectrum of the two-electron oxidized species was recorded in frozen toluene glass at 10K and displays a signal at $g=2.002$ showing nitrogen hyperfine coupling (Figure 3-23B). More interestingly, the EPR spectrum in frozen toluene glass at 10K of the deep emerald green product formed from the reaction of $K_2[Zn(L^{Mod})_2]$ and dioxygen also displays a signal at $g = 2.002$ with hyperfine coupling that is different from the one-electron oxidized product (Figure 3-23C). However, this spectrum of this species matches that of the two-electron chemically oxidized species. This data suggests that dioxygen acts as an outer sphere oxidant to oxidize $K_2[Zn(L^{Mod})_2]$ by two electrons. The EPR spectra obtained collectively provide evidence suggesting that the redox chemistry of $K_2[Zn(L^{Mod})_2]$ is ligand-based.

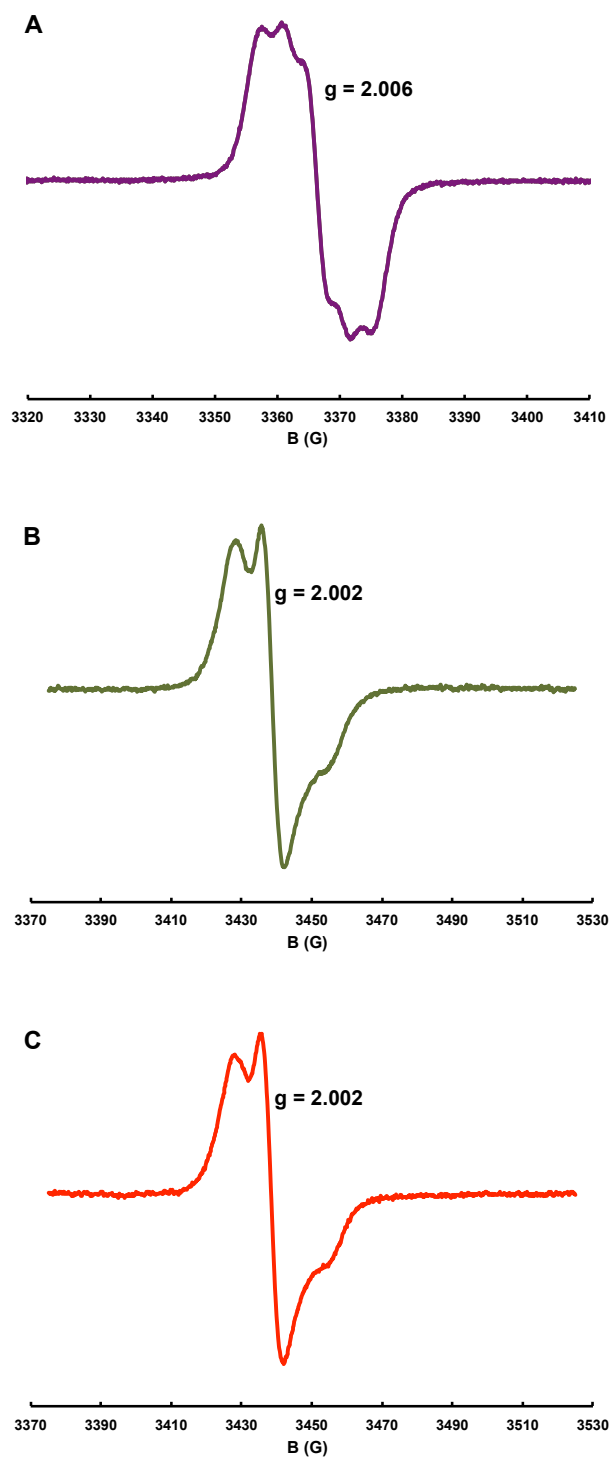


Figure 3-23. EPR spectra of **A)** one-electron oxidized species, $\text{K}[\text{Zn}(\text{L}^{\text{Mod}})_2]^{\text{ox}}$ (room temperature, toluene), **B)** two-electron oxidized species, $\text{K}[\text{Zn}(\text{L}^{\text{Mod}})_2]^{\text{ox}}$ (Toluene glass,

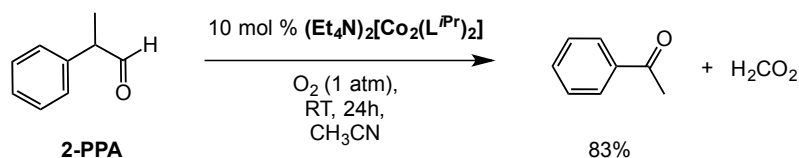
10K), and C) the product isolated from the reaction of $K_2[Zn(L^{Mod})_2]$ with dioxygen gas. Spectra recorded at room temperature in toluene (10K).

Section 3-3-8. Expanding The Aerobic Oxidation Reactivity Profile of Dinuclear Cobalt(II) Complex, $(Et_4N)_2[Co_2(L^{iPr})_2]$

As part of our effort to develop robust homogenous oxidation catalysts, the reactivity of the dinuclear cobalt(II) complex $(Et_4N)_2[Co_2(L^{iPr})_2]$ towards other substrates were explored. With strong evidence supporting the ability of this complex to neatly rearrange into a monomeric species in solution after exposure to an exogenous ligand, it was hypothesized that its aerobic oxidation chemistry could be applied to substrates that undergo variable oxidation mechanisms. These studies led us to discover that the dinuclear cobalt(II) complex $(Et_4N)_2[Co_2(L^{iPr})_2]$ is capable of performing aerobic aldehyde deformylation and aerobic catechol oxidation reactions under ambient conditions.

With precedents that metal(III)-peroxo complexes with heme and non-heme ligands can perform the deformylation of aldehydes to yield the corresponding deformylated products, the ability of $(Et_4N)_2[Co_2(L^{iPr})_2]$ to react with aldehydes under aerobic conditions was investigated.^{30a} GC and 1H NMR analysis of the reaction product of 2-phenylpropionaldehyde (2-PPA) with 10 mol% of $(Et_4N)_2[Co_2(L^{iPr})_2]$ revealed the formation of acetophenone in 83 % yield (Scheme 3-16). A control reaction under exact reaction conditions utilizing cobalt(II) bromide ($CoBr_2$) as the catalyst was conducted;

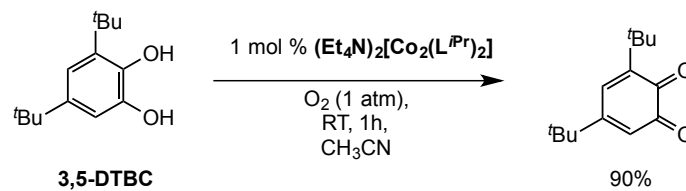
however, GC and ^1H NMR analysis of this reaction show that 2-PPA remains intact after 24 hours, illustrating that $(\text{Et}_4\text{N})_2[\text{Co}_2(\text{L}^{i\text{Pr}})_2]$ is indeed the catalyst for this transformation. These results suggest that in its oxygenation reaction with dioxygen, $(\text{Et}_4\text{N})_2[\text{Co}_2(\text{L}^{i\text{Pr}})_2]$ forms an oxygenated species with nucleophilic character.



Scheme 3-16. Catalytic aerobic deformylation of 2-phenylpropionaldehyde (2-PPA) by $(\text{Et}_4\text{N})_2[\text{Co}_2(\text{L}^{i\text{Pr}})_2]$.

The ability of $(\text{Et}_4\text{N})_2[\text{Co}_2(\text{L}^{i\text{Pr}})_2]$ to carry out different aerobic oxidation reactions was investigated by exploring catechol oxidations. Recent work by Hikichi and co-workers has shown that cobalt(II)-semiquinonato complexes are capable of dioxygen activation and subsequent catechol oxidation.⁴² The aerobic catechol oxidation ability of $(\text{Et}_4\text{N})_2[\text{Co}_2(\text{L}^{i\text{Pr}})_2]$ was investigated using 3,5-di-*tert*-butylcatechol (3,5-DTBC), a commonly utilized substrate in the catecholase reactivity of tyrosinase.⁴³ Exposing a CH_3CN solution of $(\text{Et}_4\text{N})_2[\text{Co}_2(\text{L}^{i\text{Pr}})_2]$ (1 mol %) to dioxygen in the presence of 3,5-DTBC resulted in the formation of the corresponding oxidized product, 3,5-di-*tert*-butyl-*o*-quinone (3,5-DTBQ), in 90 % yield after 1 hr (Scheme 3-17), which was confirmed by ^1H NMR spectroscopy and GC. Additionally, the formation of product, 3,5-DTBQ, was monitored via UV-visible absorption spectroscopy. The absorption band corresponding to 3,5-DTBQ ($\lambda_{\text{max}} = 400 \text{ nm}$)⁴⁴ was monitored from a solution containing 3,5-DTBC and 1

mol % $(\text{Et}_4\text{N})_2[\text{Co}_2(\text{L}^{\text{iPr}})_2]$ upon exposure to 1 mL of dioxygen. The UV-visible absorption traces for the formation of 3,5-DTBQ are shown in Figure 3-24. These results demonstrate that within minutes, the reaction is complete, illustrating the rapid oxidation efficiency of $(\text{Et}_4\text{N})_2[\text{Co}_2(\text{L}^{\text{iPr}})_2]$. Control experiments under exact reaction conditions were carried out using CoBr_2 as the catalyst, as well as exposure of 3,5-DTBC to dioxygen in the absence of no catalyst. Notably, GC and ^1H NMR analysis of these control reactions showed only trace amounts ($< 2\%$ via ^1H NMR and GC) of 3,5-DTQ, confirming that $(\text{Et}_4\text{N})_2[\text{Co}_2(\text{L}^{\text{iPr}})_2]$ is needed for this oxidation reaction. These results highlight the ability of $(\text{Et}_4\text{N})_2[\text{Co}_2(\text{L}^{\text{iPr}})_2]$ to carryout efficient catecholase-type reactivity, a reaction previously unattained using cobalt(II) and dioxygen in the absence of co-reductants.



Scheme 3-17. Catalytic aerobic oxidation of 3,5-di-*tert*-butylcatechol (3,5-DTBC) carried out by dinuclear cobalt(II) complex, $(\text{Et}_4\text{N})_2[\text{Co}_2(\text{L}^{\text{iPr}})_2]$.

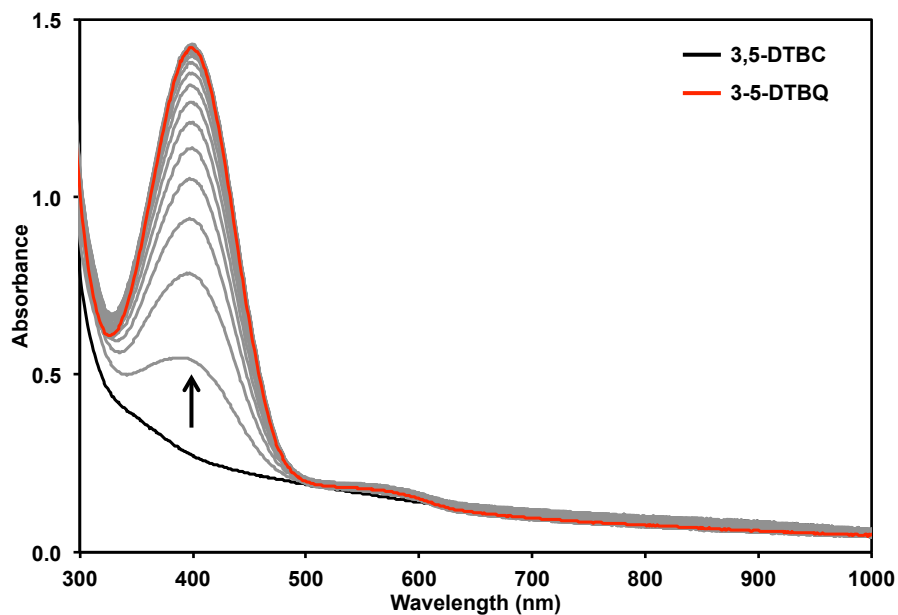


Figure 3-24. Increase in absorbance band at $\lambda_{\text{max}} = 400$ nm, after addition of dioxygen into the headspace above a $[7.192 \times 10^{-4}]$ M solution of 3,5-DTBC (initial black trace) containing 1 mol% of $(\text{Et}_4\text{N})_2[\text{Co}_2(\text{L}^{\text{iPr}})_2]$ in CH_3CN at 25 °C. Scan rate of 1 scan/min. Final red trace corresponds to 3,5-DTBQ ($\lambda_{\text{max}} = 400$ nm).

Section 3-4. Discussion

The results described herein reveal that the tridentate, trianionic redox-active ligand ($[L^{iPr}]^{3-}$) is capable of promoting novel reactivity at cobalt(II) metal ions. In the absence of co-reductants, this ligand platform drives forward the reaction between cobalt(II) and dioxygen, previously regarded as a reversible process.

Both dinuclear and mononuclear cobalt(II) complexes supported by the tridentate ligand scaffold (H_3L^{iPr}), $(Et_4N)_2[Co_2(L^{iPr})_2]$ and $(Et_4N)_2[Co(HL^{iPr})_2]$, respectively, react irreversibly with dioxygen to form stable and isolable oxygenated species capable of carrying out O-atom transfer reactions. Gas uptake experiments and stoichiometric O-atom transfer reactions to PPh_3 indicate that the oxygenation stoichiometry is one cobalt(II) per every O_2 molecule (1:1, Co: O_2). The cobalt-oxygenated species is a very stable species in solution. For example, the UV-visible absorption spectrum of a CH_3CN solution of this species shown in Figure 3-2 remains unchanged even when heated to 40 °C for 24 hours in the absence of dioxygen. Similarly, its UV-visible absorption spectrum remains unchanged when the temperature is lowered to -40 °C for 24 hours in the absence of dioxygen. These results suggest that this cobalt-oxygenated species is not in thermal equilibrium between two different types of cobalt-oxygenated species in solution.

The *in situ* UV-visible absorption and UV-visible NIR absorption studies indicate that both $(Et_4N)_2[Co_2(L^{iPr})_2]$ and $(Et_4N)_2[Co(HL^{iPr})_2]$ react with dioxygen to generate the similar oxygenated species. These studies, however, revealed that both $(Et_4N)_2[Co_2(L^{iPr})_2]$ and $(Et_4N)_2[Co(HL^{iPr})_2]$ form distinct intermediates in their respective oxygenation reaction with dioxygen. The dinuclear complex, $(Et_4N)_2[Co_2(L^{iPr})_2]$, generates one

intermediate, while the mononuclear complex, $(\text{Et}_4\text{N})_2[\text{Co}(\text{HL}^{\text{iPr}})_2]$, generates two intermediates before ultimately forming the same final cobalt-oxygenated species.

The one-electron chemical oxidation of mononuclear complex $(\text{Et}_4\text{N})_2[\text{Co}(\text{HL}^{\text{iPr}})_2]$ was carried out using one equivalent of FcBF_4 to obtain the formally one-electron oxidized mononuclear complex $(\text{Et}_4\text{N})[\text{Co}(\text{HL}^{\text{iPr}})_2]^{\text{ox}}$. Though the X-ray diffraction data is of low quality, the solid-state structure of $(\text{Et}_4\text{N})[\text{Co}(\text{HL}^{\text{iPr}})_2]^{\text{ox}}$ shows that the cobalt ion remains four-coordinate. The one-electron oxidized complex $(\text{Et}_4\text{N})[\text{Co}(\text{HL}^{\text{iPr}})_2]^{\text{ox}}$ exhibits an IVCT band in its NIR spectrum ($\lambda_{\text{max}} = 1700 \text{ nm}$, $\epsilon = 1318 \text{ M}^{-1}\text{cm}^{-1}$) which is consistent with the IVCT band exhibited by *Intermediate 1* observed in the reaction between mononuclear complex $(\text{Et}_4\text{N})_2[\text{Co}(\text{HL}^{\text{iPr}})_2]$ and dioxygen. These results demonstrate that $(\text{Et}_4\text{N})[\text{Co}(\text{HL}^{\text{iPr}})_2]^{\text{ox}}$ and *Intermediate 1* observed in the reaction between mononuclear complex $(\text{Et}_4\text{N})_2[\text{Co}(\text{HL}^{\text{iPr}})_2]$ and dioxygen have similar electronic properties.

Cyanide was used to better understand the ability of the dinuclear complex $(\text{Et}_4\text{N})_2[\text{Co}_2(\text{L}^{\text{iPr}})_2]$ to rearrange in the presence of exogenous ligands. As a result, the mononuclear cobalt(II)-cyano complex, $(\text{Et}_4\text{N})_2[\text{Co}(\text{L}^{\text{iPr}})(\text{CN})]$, was isolated and has provided insights into possible coordination modes that may be relevant to the intermediate(s) that are formed in the oxygenation reactions of the complexes with dioxygen. This result indicates that the dinuclear complex, $(\text{Et}_4\text{N})_2[\text{Co}_2(\text{L}^{\text{iPr}})_2]$, is able to undergo significant rearrangement. The formation of $(\text{Et}_4\text{N})_2[\text{Co}(\text{L}^{\text{iPr}})(\text{CN})]$ directly from mononuclear complex $(\text{Et}_4\text{N})_2[\text{Co}(\text{HL}^{\text{iPr}})_2]$ was also attained, however, the loss of one coordinating ligand and deprotonation of the uncoordinated carboxamide ($[\text{NHC}(\text{O})^{\text{iPr}}]$) moiety was necessary. These results highlight the ability for the tridentate, trianionic ligand $[\text{L}^{\text{iPr}}]^{3-}$ in $(\text{Et}_4\text{N})_2[\text{Co}_2(\text{L}^{\text{iPr}})_2]$ and $(\text{Et}_4\text{N})_2[\text{Co}(\text{HL}^{\text{iPr}})_2]$ to rearrange and adopt a possible meridional

coordination mode with dioxygen. More importantly, this rearrangement and tridentate coordination mode was shown to be an essential requirement for catalytic aerobic oxidation.

In its oxygenation reaction, the mononuclear complex $(\text{Et}_4\text{N})_2[\text{Co}(\text{HL}^{\text{iPr}})_2]$ loses one of its coordinating ligands. When $(\text{Et}_4\text{N})_2[\text{Co}(\text{HL}^{\text{iPr}})_2]$ is treated with dioxygen and the cobalt-oxygenated species is isolated as a powder, a residual organic compound corresponding to the deprotonated ligand $[\text{HL}^{\text{iPr}}]^{2-}$ was confirmed via ^1H NMR. Attempts to obtain X-ray diffraction quality crystals of $[\text{HL}^{\text{iPr}}]^{2-}$ were unsuccessful, however, a similar species was isolated using the phenyl-substituted ligand scaffold system, $\text{H}_3\text{L}^{\text{Ph}}$. The phenyl-substituted mononuclear cobalt(II) complex, $(\text{Et}_4\text{N})_2[\text{Co}(\text{HL}^{\text{Ph}})_2]$ (discussed in Chapter 2), reacts similarly with dioxygen as $(\text{Et}_4\text{N})_2[\text{Co}(\text{HL}^{\text{iPr}})_2]$. X-ray diffraction quality crystals of the organic byproduct, $(\text{Et}_4\text{N})_2[\text{HL}^{\text{Ph}}]$, formed in the oxygenation reaction of $(\text{Et}_4\text{N})_2[\text{Co}(\text{HL}^{\text{Ph}})_2]$ with dioxygen were obtained by slow diffusion of Et_2O into a CH_3CN solution of the reaction mixture (Figure 3-26). The solid-state structure of this species is shown in Figure 3-26 and confirms this species to be a doubly-deprotonated, dianionic ligand stabilized by two tetraethylammonium counterions. This result indicates that during the oxygenation reaction, $(\text{Et}_4\text{N})_2[\text{Co}(\text{HL}^{\text{iPr}})_2]$, kicks off one of its ligands, followed by a rearrangement of the other trianionic ligand to adopt a possible meridional coordination mode with cobalt and dioxygen.

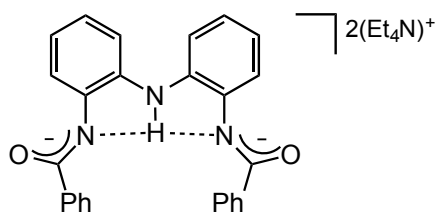


Figure 3-25. Deprotonated ligand, $(\text{Et}_4\text{N})_2[\text{HL}^{\text{Ph}}]$, obtained as a byproduct from the reaction of $(\text{Et}_4\text{N})_2[\text{Co}(\text{HL}^{\text{iPr}})_2]$ and dioxygen gas.

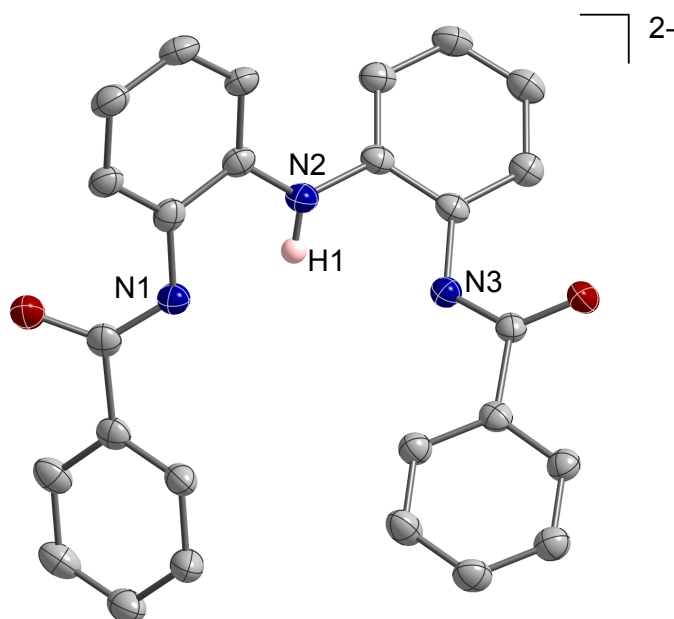


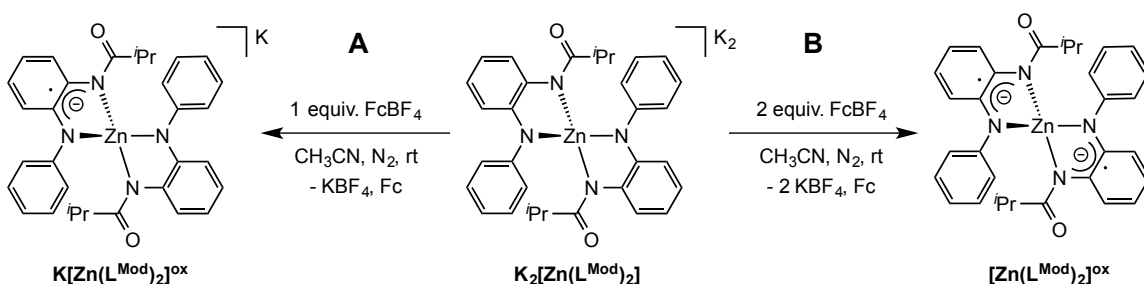
Figure 3-26. Solid-state structure of $(\text{Et}_4\text{N})_2[\text{HL}^{\text{Ph}}]$. Thermal ellipsoids are drawn at 40 % probability. Hydrogen atoms (with the exception of central amide hydrogen) and tetraethylammonium counterions have been omitted for clarity.

With these observations in hand, we aimed to understand the role of the uncoordinated carboxamide moiety in the mononuclear complex $(\text{Et}_4\text{N})_2[\text{Co}(\text{HL}^{\text{iPr}})_2]$. The

bidentate ligand (H_2L^{Mod}) and its cobalt(II) complex, $(PPh_4)_2[Co(L^{Mod})_2]$ has allowed us to conclude that the uncoordinated carboxamide ($[NHC(O)^iPr]$) moiety found in $(Et_4N)_2[Co(HL^{iPr})_2]$ is essential for promoting efficient dioxygen activation. First, by comparing the electrochemical profiles of $(Et_4N)_2[Co(HL^{iPr})_2]$ ³¹ and $(PPh_4)_2[Co(L^{Mod})_2]$, we illustrated that the two-electron redox event observed in $(Et_4N)_2[Co(HL^{iPr})_2]$ is no longer present in $(PPh_4)_2[Co(L^{Mod})_2]$. This could be the result of a proton-coupled electron transfer (PCET) process taking place at the pendant proton of the uncoordinated carboxamide ($[NHC(O)^iPr]$) moiety. Recent work Nocera and co-workers have shown that pendant protons on synthetic systems provide significant catalytic enhancement when compared to their non-pendant analogues.⁴⁵ Additionally, the Nocera group has demonstrated that proton-coupled electron transfer processes promoted by pendant protons can significantly have an effect on dioxygen bond activation.⁴⁶ The drastic decrease in TON exhibited by $(PPh_4)_2[Co(L^{Mod})_2]$ in aerobic PPh_3 oxidation compared to both $(Et_4N)_2[Co_2(L^{iPr})_2]$ and $(Et_4N)_2[Co(HL^{iPr})_2]$ indicates that the second carboxamide moiety of the tridentate ligand is necessary for efficient catalytic reactivity. These results indicate that the ability of the tridentate ligand (H_3L^{iPr}) in complexes $(Et_4N)_2[Co_2(L^{iPr})_2]$ and $(Et_4N)_2[Co(HL^{iPr})_2]$ to rearrange during oxygenation reactions is essential to induce catalytic dioxygen activation and carry out efficient catalytic O-atom transfer reactions.

The chemical oxidations of mononuclear zinc(II) complex $K_2[Zn(L^{Mod})_2]$ have provided strong evidence for ligand-centered reactivity. The purple species generated from the one-electron chemical oxidation of $K_2[Zn(L^{Mod})_2]$ corresponds to a formally one-electron oxidized mononuclear zinc(II) species, $K[Zn(L^{Mod})_2]^{ox}$, in which one ligand is oxidized by one electron (Scheme 3-18A). The intense band at $\lambda_{max} = 1356$ nm in the UV-

vis NIR spectrum of this species corresponds to an IVCT band indicative of a ligand-localized radical species. We assign the green species generated from the two-electron chemical oxidation of $K_2[Zn(L^{Mod})_2]$ as a formally two-electron oxidized mononuclear zinc(II) species, $[Zn(L^{Mod})_2]^{ox}$, whereby each ligand is oxidized by one electron (Scheme 3-18B). These assignments are collectively based on the UV-visible NIR absorption and EPR data obtained for these two species. This data is in accordance with similar zinc(II) complexes hosting ligand-centered radicals previously reported by Wieghardt and co-workers.²⁰



Scheme 3-18. A) One- and B) two-electron chemical oxidations of mononuclear zinc(II) complex $K_2[Zn(L^{Mod})_2]$ using $FcBF_4$.

The mechanistic, spectroscopic, and structural studies allowed us to understand the redox-activity and role of the ligand backbone and led us to explore our cobalt(II) system in deformylation reactions. Due to its biological relevance, metal-mediated aerobic deformylation of aldehydes remains an important type of oxidation reaction.^{29a} In this work, we show that $(Et_4N)_2[Co_2(L^{iPr})_2]$ is capable of carrying out the catalytic aerobic deformylation of 2-PPA under ambient conditions. The work presented herein, to our

knowledge, would represent the first example of a cobalt(II)-catalyzed aerobic aldehyde deformylation without the use of external co-reductants.

To expand the oxidation scope of the dinuclear complex $(\text{Et}_4\text{N})_2[\text{Co}_2(\text{L}^{\text{iPr}})_2]$ its catecholase activity was investigated. Catechol oxidation by metal-oxygen species has been recognized as an important biological transformation carried out by tyrosinases for over 50 years.⁴⁷ We demonstrate that $(\text{Et}_4\text{N})_2[\text{Co}_2(\text{L}^{\text{iPr}})_2]$ is capable of oxidizing 3,5-di-*tert*-butylcatechol to 3,5-di-*tert*-butylquinone using dioxygen as the terminal oxidant. Functional models for catechol oxidase using first-row transition metal complexes with chelating ligands are known, however, few are capable of carrying out this transformation under aerobic conditions without the use of co-reductants and at this rate.⁴²

Section 3-5. Conclusion

Through a series of mechanistic, spectroscopic, and synthetic studies that the oxidatively robust, tridentate and trianionic redox-active ligand $[\text{N}(o\text{-PhNC}(\text{O})^{\text{iPr}})_2]^{3-}$ is a good scaffold for promoting aerobic oxidation catalysis at cobalt(II). Under ambient conditions in the presence of excess dioxygen and in the absence of co-reductants, cobalt(II) complexes supported by this ligand are capable of carrying out rapid O-atom transfer,³¹ aldehyde deformylation, and catechol oxidation reactions. These results signify a landmark innovation in cobalt(II)-catalyzed aerobic oxidation catalysis. Ongoing spectroscopic studies currently being pursued in collaboration with Berry and co-workers at the University of Wisconsin-Madison, include resonance Raman (rR), EPR spectroscopy, and density functional theory (DFT) to give insights into the identity of the

cobalt-oxygenated species and the intermediates formed in the oxygenation of both $(\text{Et}_4\text{N})_2[\text{Co}_2(\text{L}^{i\text{Pr}})_2]$ and $(\text{Et}_4\text{N})_2[\text{Co}(\text{HL}^{i\text{Pr}})_2]$.

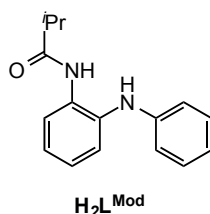
Section 3-6. Experimental Section

Section 3-6-1. General Considerations and Materials

All manipulations were carried out using standard Schlenk techniques or conducted in an MBraun Labmaster 130 drybox under a nitrogen atmosphere. All reagents used were purchased from commercial vendors and used as received unless otherwise noted. Anhydrous solvents were purchased from Sigma-Aldrich and further purified by sparging with Ar gas followed by passage through activated alumina columns. Elemental analyses were performed by Midwest Microlab, LLC. ^1H and ^{13}C spectra were recorded on a Mercury 300 MHz or an Inova 400 MHz spectrometer at ambient temperature. ^1H and ^{13}C chemical shifts were referenced to residual solvent peaks. Infrared spectra were recorded as KBr pellets on a Varian Scimitar 800 Series FT-IR spectrophotometer. UV-visible absorption spectra were recorded on a Cary50 spectrophotometer using 1.0 cm quartz cuvettes. UV-visible near-infrared absorption spectra were recorded on a UV-3101PC Shimadzu UV-vis NIR scanning spectrophotometer using 1.0 cm quartz cuvettes. All UV-vis and UV-vis NIR *in situ* oxygenation reactions were run in 1.0 cm quartz cuvettes (ES Quartz Glass, 45 x 12.5 x 12.5 mm, 3.50 mL in volume) by monitoring the UV-vis and UV-vis NIR spectral changes of the solutions. EPR at room temperature was collected at Emory University in the Warnke laboratory by using a Bruker ER200D EPR spectrometer equipped with a Bruker 4102ST/9216 TE102 cavity. X-band (9.28 GHz) EPR spectra at 10K were collected as frozen solutions using a Bruker EMX spectrometer equipped with an ER041XG microwave bridge in the Borovik laboratory at the University of California, Irvine by Ms. Sarah Cook. 2-phenylpropionaldehyde (2-PPA) and 3,5-di-*tert*butylcatechol (3,5-

DTBC) were purchased from Sigma-Aldrich and the purity of these substrates were checked by GC and ^1H NMR prior to use. Solution-state magnetic moments were measured using the Evans' method.³⁶ Mass spectra were recorded in the Mass Spectrometry Center at Emory University on a JEOL JMS-SX102/SX102A/E mass spectrometer. X-ray diffraction studies were carried out in the X-ray Crystallography Laboratory at Emory University on a Bruker Smart 1000 CCD diffractometer. Cyclic voltammetry experiments were carried out using a CH Instruments (Austin, TX) Model 660C potentiostat. All experiments were conducted in CH_2Cl_2 with 0.10 M tetrabutylammonium hexafluorophosphate as the supporting electrolyte. Electrochemical experiments were conducted in a three-component cell consisting of a Pt auxiliary electrode, a non-aqueous reference electrode (Ag/AgNO_3), and a glassy carbon-working electrode. All electrochemical measurements are referenced and reported versus the ferrocene/ferrocenium couple.

Section 3-6-2. Ligand Syntheses



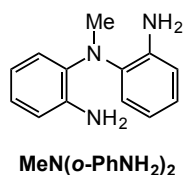
***N*-(2-(phenylamino)-phenyl)isobutyramide ($\text{HN}(\text{Ph})(o\text{-PhNHC}(\text{O})^i\text{Pr})$) [$\text{H}_2\text{L}^{\text{Mod}}$]:** A suspension of *N*-Phenyl-*o*-phenylenediamine (3.75 g, 20.35 mmol) in dichloromethane (DCM, 200 mL) was lowered to 0 °C under an atmosphere of N_2 . Triethylamine (2.85 mL, 20.35 mmol) was then added, followed by the drop-wise addition isobutyryl chloride (2.15 mL, 14.74 mmol) via a dropper funnel. The mixture was stirred at 0 °C for 1 h. The reaction

mixture was slowly warmed to room temperature and stirred for an additional 24 h. The resulting pale brown-colored solution was extracted with saturated aqueous NaHCO_3 (3 x 30 mL) and brine (2 x 20 mL), and the organic layer was dried over magnesium sulfate for 30 minutes, filtered, and concentrated in vacuo. The crude solid was recrystallized by layering of diethyl ether on top of a concentrated DCM solution of the product (4.66 g, 90 %). ^1H NMR (δ , CDCl_3 , 400 MHz): (ppm) 8.02 (dd, $J = 9.2$ Hz, 6.8 Hz, 1H, ArH), 7.66 (s, 1H, NH(CO)), 7.25 - 7.09 (m, 5H, ArH), 6.87 (t, $J = 14.8$ Hz, 1H, ArH), 6.76 (d, $J = 7.6$ Hz, 2H, ArH), 5.68 (s, 1H, NH), 2.46 (q, $J = 6.8$ Hz, 1H, CH), 1.15 (d, $J = 9.2$ Hz, 6H, CH_3); ^{13}C NMR (δ , CDCl_3 , 75.5 MHz): (ppm) 176.26, 145.11, 133.97, 132.36, 129.62, 125.61, 124.96, 124.14, 122.96, 120.39, 116.26, 36.63, 19.74; HRESI-MS: $\text{C}_{16}\text{H}_{19}\text{N}_2\text{O}$ m/z Calcd. 255.1497 Found 255.1499 $[\text{M} + \text{H}]^+$; FTIR (KBr, cm^{-1}): $\nu(\text{NH})_{\text{Amine}}$ 3309, $\nu(\text{NH})_{\text{Amide}}$ 3347, $\nu(\text{CO})$ 1651.

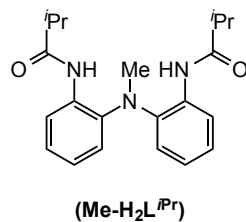


MeN(o-PhNO₂)₂: (Prepared using a modified literature procedure).⁴⁸ To an acetone (50.0 mL) solution of $\text{HN}(o\text{-PhNO}_2)_2$ ³¹ (2.0 g, 7.72 mmol) was added solid potassium hydroxide (KOH) (1.9g, 32.2 mmol). The reaction mixture was heated until reflux (80 °C). After color of solution changed to dark purple, Me_2SO_4 (2.4 mL, 24.17 mmol) was added to solution via a syringe slowly as an acetone solution (10 mL). Reaction flask was sealed under N_2 (g) and heated for an additional 20 min. After 20 min, addition of 400 mL distilled H_2O was added to reaction mixture to form a yellow-brown precipitate which was collected in a medium

porosity frit. Crystallization with ethyl alcohol at -32 °C overnight gave a yellow-brown crystalline material (1.78 g, 84.3 %). ^1H NMR (δ , CDCl_3 , 300 MHz): 7.75 (m, 2H, ArH), 7.52 (m, 2H, ArH), 7.24 (m, 2H, ArH), 7.13 (m, 2H, ArH), 3.38 (s, 3H, CH_3); ^{13}C NMR (δ , CDCl_3 , 75.5 MHz): 143.24, 142.03, 124.11, 126.49, 124.94, 123.91, 42.71. HRMS(ESI): $\text{C}_{13}\text{H}_{12}\text{N}_3\text{O}_4$ m/z Calcd. 274.082, Found 274.083 $[\text{M}+1]^+$.

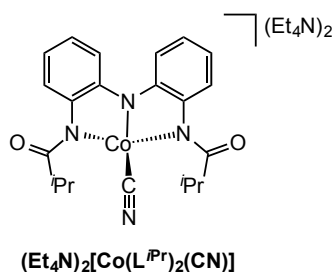


MeN(o-PhNH₂)₂: (Prepared using a modified literature procedure).⁴⁹ To a THF (50.0 mL) solution of MeN(o-PhNO₂)₂ (2.0 g, 7.32 mmol) was added 5 wt.% Pd/C (1.0 g, 0.5 mmol, 6 mol %). The reaction mixture was placed in a pressure-safe reaction vessel and shaken under H₂ at 50 psi for 45 min. The reaction mixture was filtered through a pad of Celite, and the filtrate was concentrated in vacuo to obtain a thick, colorless oil. Crystalline product can be obtained by layering a concentrated ether solution of the compound with hexanes (1.40 g, 90 %). ^1H NMR (δ , CDCl_3 , 300 MHz): 6.96 (m, 4H, ArH), 6.76 (m, 4H, ArH), 3.82 (s, 4H, NH), 3.08 (s, 3H, CH_3); ^{13}C NMR (δ , CDCl_3 , 75.5 MHz): (ppm) 140.808, 136.689, 125.024, 122.311, 119.019, 116.090, and 40.115. HRMS(ESI): $\text{C}_{13}\text{H}_{16}\text{N}_3$ m/z Calcd. 214.1344, Found 214.1338 $[\text{M}+1]^+$. FTIR (KBr, cm^{-1}): $\nu(\text{NH})$ 3448 and 3354

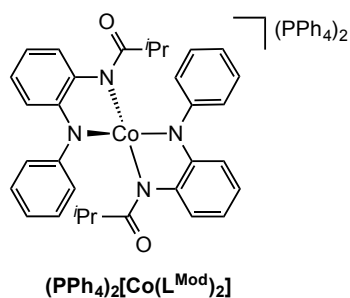


MeN(*o*-PhNHC(O)^{*i*Pr})₂ (Me-H₂L^{*i*Pr}): A suspension of MeN(*o*-PhNH₂)₂ (1.70 g, 7.97 mmol) in THF (50 mL) was lowered to -20.0 °C under an atmosphere of N₂. Triethylamine (2.45 mL, 17.5 mmol) was then added, followed by drop wise addition of isobutyryl chloride (1.85 mL, 17.5 mmol) using a dropper funnel over the course of 1 h. The mixture stirred at -20.0 °C for an additional 1 h. The reaction mixture was slowly warmed to room temperature and stirred for an additional 20 h. The resulting pale brown solution was extracted with saturated aqueous NaHCO₃ (3 x 30 mL) and brine (2 x 20 mL), and the organic layer was dried over magnesium sulfate for 30 min, filtered, and concentrated in vacuo. The crude solid was recrystallized by layering hexanes over a concentrated DCM solution of the product (2.70 g, 96 %). ¹H NMR (δ, CDCl₃, 300 MHz): (ppm) 7.93 (s, 2H, NH(CO)), 7.88 (d, 2H, ArH), 7.01 (m, 4H, ArH), 6.99 (d, 2H, ArH), 3.12 (s, 3H, CH₃), 2.39 (m, 2H, CH), 1.08 (d, 12H, CH₃); ¹³C NMR (δ, CDCl₃, 75.5 MHz): (ppm) 154.26, 130.96, 129.86, 129.02, 125.60, 124.18, 121.740, 40.12, 37.89, 20.86. HRESI-MS: C₂₁H₂₈N₃O₂ *m/z* Calcd. 354.2182 Found 354.21699 [M+1]⁺. FTIR (KBr, cm⁻¹): ν(NH_{amide}) 3230, ν(NH_{amine}) 3241, ν(CO) 1655.

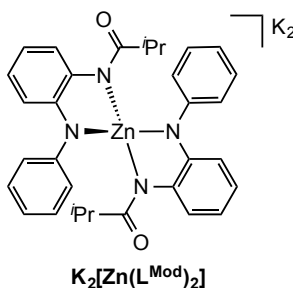
Section 3-6-3. Complex Syntheses



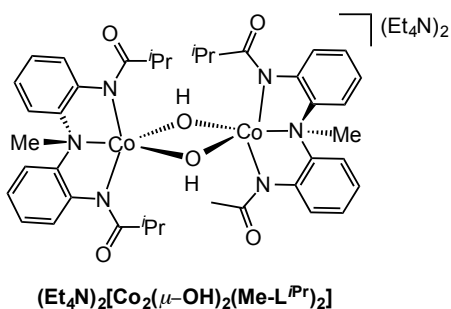
Synthesis of $(\text{Et}_4\text{N})_2[\text{Co}(\text{CN})(\text{L}^{\text{iPr}})_2]$: Under an inert atmosphere, to a CH_3CN (10 mL) solution of $(\text{Et}_4\text{N})_2[\text{Co}_2(\text{L}^{\text{iPr}})_2]$ (120 mg, 0.1142 mmol) was added Et_4NCN (35.7 mg, 0.2285 mmol) as a solid at 25 °C. Color of the solution changed from deep green to a deep burgundy solution within 30 min. After stirring for 4 h, CH_3CN solution was filtered through a medium porosity frit, and the filtrate was concentrated to dryness. Dark burgundy X-ray diffraction quality crystals of $(\text{Et}_4\text{N})_2[\text{Co}(\text{L}^{\text{iPr}})_2(\text{CN})]$ were obtained by slow diffusion of diethyl ether into a concentrated CH_3CN solution of the product (109 mg, 70 %). ^1H NMR (δ , CD_3CN , 400 MHz): (ppm) -30.80 (s), -46.55 (s), -37.18 (s), -31.30 (s), -2.744 (s), 26.91 (s), 37.06 (s), 47.04 (s), 60.58 (s). FTIR (KBr, cm^{-1}): $\nu(\text{CO})$ 1663, $\nu(\text{CN})$ 2109. $\mu_{\text{eff}} = 4.27(3) \mu_{\text{B}}$ (Evans Method, CD_3CN , 298K). λ_{max} , nm (ϵ , $\text{M}^{-1}\text{cm}^{-1}$) (CH_3CN): 502 (1070), 740 (390). HRESI-MS: for $[\text{Co}(\text{CN})(\text{L}^{\text{iPr}})_2]$: Calcd (m/z): 421.1075, Found 421.10965.



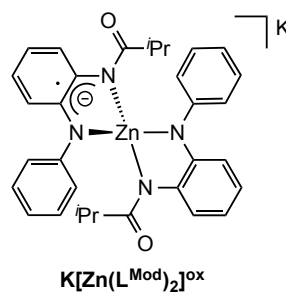
Synthesis of $(\text{PPh}_4)_2[\text{Co}(\text{L}^{\text{Mod}})_2]$: To a solution of $(\text{HN}(\text{Ph})(o\text{-PhNHC}(\text{O})\text{iPr}) (\text{H}_2\text{L}^{\text{Mod}})$ (200 mg, 0.7864 mmol) in DMF, (10 mL) was added potassium hydride (63.1 mg, 1.573 mmol). When gas evolution ceased, CoBr_2 (86.0 mg, 0.3932 mmol) was added as a solid. When the reaction mixture became homogenous, tetraphenylphosphonium bromide (330.0 mg, 0.7864 mmol) was added to the red solution. After stirring for 8 h, the DMF was removed under high vacuum and the resulting solid was dissolved in CH_3CN (10 mL), filtered through a medium porosity frit, and the filtrate was concentrated to dryness. Bulk recrystallization was obtained by diffusing diethyl ether into a concentrated CH_3CN solution containing the product. Dark red-colored X-ray diffraction quality crystals were obtained by slow diffusion of diethyl ether into a concentrated CH_2Cl_2 solution of $(\text{PPh}_4)_2[\text{Co}(\text{L}^{\text{Mod}})_2]$ (366 mg, 75 %). ^1H NMR (δ , CD_3CN , 400 MHz): (ppm) -65.92 (d), -59.30 (s), -1.825 (s), 56.565 (s), 55.07 (s), 72.04 (s), 80.52 (s), 90.04 (s). FTIR (KBr, cm^{-1}): $\nu(\text{CO})$ 1588. $\mu_{\text{eff}} = 4.93(6)$ μ_{B} (Evans Method, CD_3CN , 298K). λ_{max} , nm (ϵ , $\text{M}^{-1}\text{cm}^{-1}$) (CH_3CN): 570 (812). HRESI-MS: for $[[\text{Co}(\text{L}^{\text{Mod}})_2]+1]^{1-}$ Calcd (m/z): 563.1863, Found 563.1854.



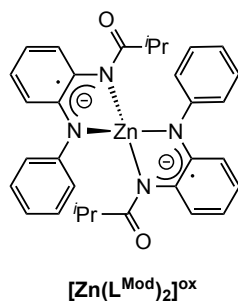
Synthesis of $(\text{Et}_4\text{N})_2[\text{Zn}(\text{L}^{\text{Mod}})_2]$: To a solution of $(\text{HN}(\text{Ph})(o\text{-PhNHC}(\text{O})^i\text{Pr})$ ($\text{H}_2\text{L}^{\text{Mod}}$) (180.0 mg, 0.7077 mmol) in DMF, (10 mL) was added potassium hydride (56.8 mg, 1.415 mmol). When gas evolution ceased, ZnBr_2 (79.7 mg, 0.3539 mmol) was added as a solid resulting in a completely homogeneous light yellow-colored solution. After stirring for 8 h, the DMF was removed under high vacuum and the resulting solid was dissolved in CH_3CN (10 mL), filtered through a medium porosity frit, and the filtrate was concentrated to dryness. Bulk recrystallization was obtained by layering diethyl ether into a concentrated CH_3CN solution containing the product. Light yellow-colored, X-ray quality crystals were obtained by slow diffusion of diethyl ether into a concentrated CH_3CN solution of $\text{K}_2[\text{Zn}(\text{L}^{\text{Mod}})_2]$ (165 mg, 72.0 %). ^1H NMR (δ , CD_3CN , 400 MHz): (ppm) 0.758 (d, 24H, $-\text{CH}_3$), 1.163 (s, 12H, $-\text{CH}_3$), 2.689 (b, 2H, $-\text{CH}-$), 3.101 (s, 8H, $-\text{CH}_2$), 6.276 (d, 3H, ArH), 6.474 (s, 2H, ArH), 7.044 (m, 11H, ArH), 8.687 (s, 2H, ArH); ^{13}C NMR (δ , CDCl_3 , 75.5 MHz): (ppm) 180.12, 155.04, 147.36, 139.56, 128.35, 121.40, 120.80, 119.93, 117.70, 112.66, 109.88, 38.615, 20.82. FTIR (KBr, cm^{-1}): $\nu(\text{CO})$ 1668. λ_{max} , nm (ϵ , $\text{M}^{-1}\text{cm}^{-1}$) (CH_3CN): 460 (2290). HRESI-MS: for $[\text{Zn}(\text{L}^{\text{Mod}})_2 + 1]^-$ (m/z) Calcd. 569.1895 Found 569.1905.



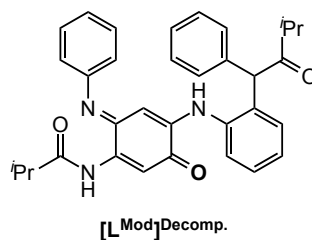
Synthesis of $(\text{Et}_4\text{N})_2[\text{Co}_2(\mu\text{-OH})_2(\text{Me-L}^{\text{iPr}})_2]$: To a solution of $\text{MeN}(\text{HL}^{\text{iPr}})_2$ (132.4 mg, 0.374 mmol) in DMF (10 mL) was added potassium hydride (45.10 mg, 1.124 mmol). CoBr_2 (81.90 mg, 0.3774 mmol) was added as a solid. Color became dark blue. Degassed $\text{H}_2\text{O}(l)$ (6.0 μL , 0.374 mmol) was then added changing the solution color to purple. When the reaction mixture became homogenous, tetraethylammonium bromide (78.50 mg, 0.374 mmol) was added to the purple solution. After stirring for 3 h, the DMF was removed under high vacuum and the resulting solid was dissolved in CH_3CN (15 mL), filtered through a medium porosity frit, and the filtrate was concentrated to dryness. Magenta, X-ray diffraction quality crystals were obtained by slow diffusion of diethyl ether into a concentrated DMF solution of $(\text{Et}_4\text{N})_2[\text{Co}_2(\mu\text{-OH})_2(\text{Me-L}^{\text{iPr}})_2]$ (120 mg, 76 %). ^1H NMR (δ , CD_3CN , 400 MHz): (ppm) -39.94 (s), -37.67 (s), 5.74 (s), 17.50 (s), 25.48 (s), 59.86 (s). FTIR (KBr, cm^{-1}): $\nu(\text{CO})$ 1596, $\nu(\text{OH})$ 3632. $\mu_{\text{eff}} = 4.01(2) \mu_{\text{B}}$ (Evans Method, DMSO-d_6 , 298K). λ_{max} , nm (ϵ , $\text{M}^{-1}\text{cm}^{-1}$) (DMF): 632 (296). HRESI-MS: for $[(\text{Et}_4\text{N})[\text{Co}(\text{Me-N}(\text{L}^{\text{iPr}})_2)(\mu\text{-OH})_2]+1]^+$ (m/z) Calcd. 957.423 Found 957.401



Synthesis of $\text{K}[\text{Zn}(\text{L}^{\text{Mod}})_2]^{\text{ox}}$: To a light yellow-colored solution of $\text{K}_2[\text{Zn}(\text{L}^{\text{Mod}})_2]$ (80.0 mg, 0.1234 mmol) in acetonitrile (CH_3CN , 6 mL) was added ferrocenium tetrafluoroborate (FcBF_4) (33.7 mg, 0.1234 mmol) as a CH_3CN solution (2 mL) dropwise. After stirring for 4 h, the solvent was removed under vacuum, and the resulting solid was dissolved in THF and filtered to remove KBF_4 . The deep purple filtrate was then concentrated to dryness. The deep purple solid that resulted was washed with hexanes (3 x 5 mL) to remove ferrocene, and the crude solid was collected on a frit. Micro crystalline compound can be obtained by layering diethyl ether onto a CH_3CN solution of the product (66.9 mg, 89%). ^1H NMR (δ , CD_3CN , 400 MHz): (ppm) 8.82 (s), 8.34 (s), 7.18 - 6.83 (m), 6.45 (s), 3.64 (s), 0.83 (s), 0.63 (s). FTIR (KBr, cm^{-1}): $\nu(\text{CO})$ 1669; $\lambda_{\text{max}}(\epsilon, \text{M}^{-1}\text{cm}^{-1})$ (CH_3CN): 538 (2347), 680 (497), 1356 (2099).



Synthesis of $[\text{Zn}(\text{L}^{\text{Mod}})_2]^{\text{ox}}$: To a light yellow solution of $\text{K}_2[\text{Zn}(\text{L}_{\text{EF}}^{\text{iPr}})_2]$ (119 mg, 0.1670 mmol) in acetonitrile (CH_3CN , 10 mL) was added ferrocenium tetrafluoroborate (FcBF_4) (92.6 mg, 0.3340 mmol) as an CH_3CN solution (2 mL). After stirring for 4 h, the solvent was removed under vacuum, and the resulting solid was dissolved in THF and filtered to remove KBF_4 . The deep green filtrate was then concentrated to dryness. The deep green solid that resulted was washed with hexanes (3 x 5 mL) to remove ferrocene, and the crude solid was collected on a frit. Microcrystalline compound can be obtained by layering hexanes onto a diethyl ether solution of the product (92.5 mg, 96 %). ^1H NMR (δ , CD_3CN , 400 MHz): (ppm) 8.64 (s), 7.57 (s), 7.25 - 6.69 (m), 6.47 (d, $J = 19.6$ Hz), 5.08 (s), 2.56 (s), -1.83 (s), 0.93 (d, $J = 19.6$ Hz). FTIR (KBr, cm^{-1}): $\nu(\text{CO})$ 1656; $\lambda_{\text{max}}(\epsilon, \text{M}^{-1}\text{cm}^{-1})$ (CH_3CN): 422 (1300), 720 (3187).



Generation and Isolation of [L^{Mod}]Decomp.: Under an inert atmosphere, a 25 mL round bottom schlenk flask was charged with a stir bar, K₂[Zn(L^{Mod})₂] (0.150 g, 0.2314 mmol), and 10 mL of CH₃CN. Once the solution was homogeneous, the flask was fitted with a septum, sealed with electrical tape and removed from the dry box. While stirring at room temperature, a constant slow purge of O₂ gas (1 atm) was introduced to the flask by connecting it, via 18-gauge needles inserted through the septum, to an O₂ line and to a mineral oil gas bubbler. Color of solution changed from light yellow to deep emerald green. After 4 hours, O₂ gas purge was removed from reaction flask and reaction was transferred to a 20 mL scintillation vial. Solution was left to evaporate open to air for 2 days. Color of solution changed from deep emerald green to deep red. Red X-ray diffraction quality crystals were obtained as the solvent evaporated. ¹H NMR (δ, CD₃CN, 400 MHz): (ppm) 7.95 (dd, J = 2.4 Hz, J = 2.0 Hz, ArH, 1H), 7.17 (t, J = 8.8 Hz, ArH, 4H), 7.07 - 7.04 (m, ArH, 4H), 6.81 (d, J = 7.6 Hz, ArH, 6H), 2.54 (q, 2H, J = 6.8 Hz, CH), 1.11 (d, J = 6.8 Hz, CH₃, 12H). FTIR (KBr, cm⁻¹): ν(CO) 1705, 1642, ν(NH) 3300, 3270. HRESI-MS: C₃₃H₃₃N₃O₃ *m/z* Calcd. 519.25 Found 519.25 [M+1]⁺. λ_{max} (nm) = 500.

Section 3-6-4. Reactivity Studies

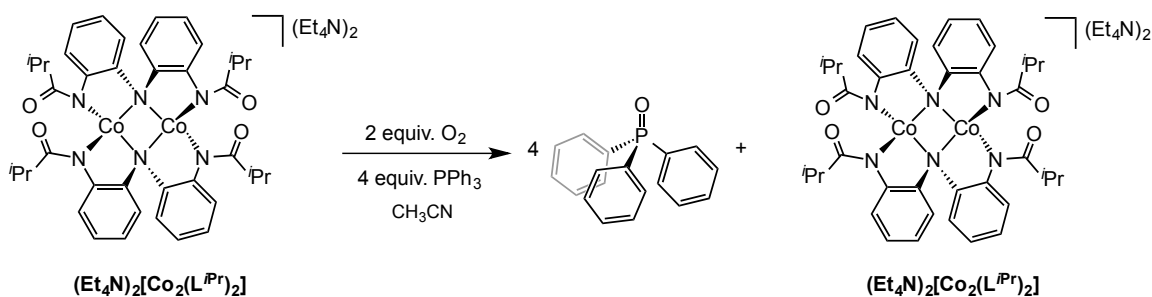
I. Stoichiometric Oxygenation and Stoichiometric Oxygen-atom Transfer Reactions

Typical Procedure for $(\text{Et}_4\text{N})_2[\text{Co}_2(\text{L}^{\text{iPr}})_2] + 2.0$ equivalents of $\text{O}_2(\text{g})$: Under an inert atmosphere, a 25 mL round bottom schlenk flask was charged with a stir bar, $(\text{Et}_4\text{N})_2[\text{Co}_2(\text{L}^{\text{iPr}})_2]$ (0.200 g, 0.1904 mmol), and 10 mL of CH_3CN . Once the solution was homogeneous, the flask was fitted with a septum, sealed with electrical tape, and removed from the dry box. While stirring at room temperature, O_2 gas (9.30 mL, 0.3808 mmol) was injected to the flask via a gas-tight syringe (inserted through the septum). Solution color changed from deep green to deep burgundy within minutes (~ 4 min). After stirring for 12 hours, the solvent was removed under vacuum, and the resulting solid was brought back into the dry box. The solid was washed with Et_2O (3 x 3 mL) and the crude solid was collected on a frit. λ_{max} (CH_3CN): 390 nm, 500 nm, and 785 nm.

Typical Procedure for $(\text{Et}_4\text{N})_2[\text{Co}(\text{HL}^{\text{iPr}})_2] + 1.0$ equivalent of $\text{O}_2(\text{g})$: Under an inert atmosphere, a 25 mL round bottom schlenk flask was charged with a stir bar, $(\text{Et}_4\text{N})_2[\text{Co}(\text{HL}^{\text{iPr}})_2]$ (0.200 g, 0.2011 mmol), and 10 mL of CH_3CN . Once the solution was homogeneous, the flask was fitted with a septum, sealed with electrical tape, and removed from the dry box. While stirring at room temperature, O_2 gas (4.90 mL, 0.2011 mmol) was injected to the flask via a gas-tight syringe (inserted through the septum). Solution color changed from deep red to deep burgundy within minutes (~ 4 min). After stirring for 12 hours, the solvent was removed under vacuum, and the resulting solid was

brought back into the dry box. The solid was washed with Et₂O (3 x 3 mL) and the crude solid was collected on a frit. λ_{max} (CH₃CN): 390 nm, 500 nm, and 785 nm.

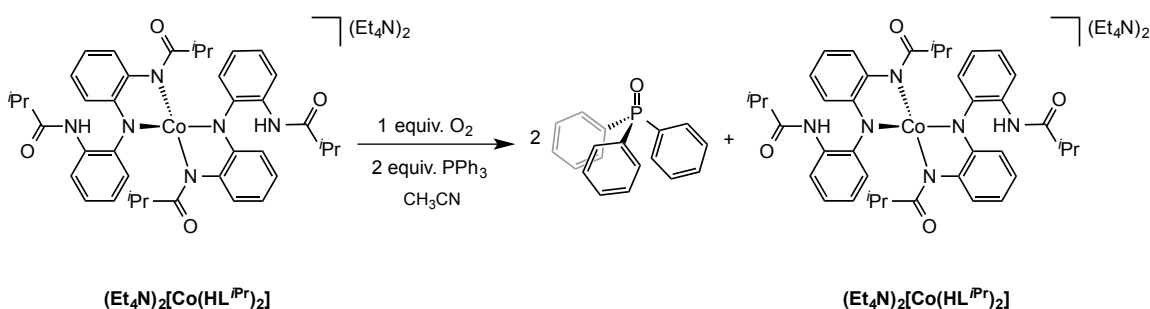
Typical Procedure for (Et₄N)₂[Co₂(L^{iPr})₂] + 2.0 equivalents of O₂(g) + 4.0 equivalents of PPh₃:



Under an inert atmosphere, a 25 mL round bottom schlenk flask was charged with a stir bar, (Et₄N)₂[Co(HL^{iPr})₂] (0.150 g, 0.1428 mmol), and 10 mL of CH₃CN. Once the solution was homogeneous, the flask was fitted with a septum, sealed with electrical tape and removed from the dry box. While stirring at room temperature, O₂ gas (7.00 mL, 0.1428 mmol) was injected to the flask via a gas-tight syringe (inserted through the septum). Solution color changed from deep green to deep burgundy within minutes (~ 4 min). After stirring for 12 hours, the solvent was removed under vacuum, and the resulting solid was brought back into the dry box. Triphenylphosphine (0.150 g, 0.5712 mmol) in 3 mL of CH₃CN was added to a dark burgundy solution of oxygenated cobalt-species in 3 mL CH₃CN. The solution was allowed to stir for 4 hours. Color changed from deep burgundy to deep green. After 4 h, solvent was removed. ¹H analysis of reaction mixture revealed (Et₄N)₂[Co₂(L^{iPr})₂] and OPPh₃. ¹H NMR (δ, CDCl₃, 400 MHz): (ppm) -46.29 (s), -38.97 (s), -1.44 (s), 0.52 (s), 1.19 (t, Et₄N⁺) 3.44 (m, Et₄N⁺), 7.64 - 7.27 (m, OPPh₃), 7.71

(m, OPh₃), 11.29 (s), 25.90 (s), 28.90 (s), 65.59 (s); ³¹P NMR (δ, CDCl₃, 400 MHz): (ppm) 24.71 (s, OPh₃).

Typical Procedure for (Et₄N)₂[Co(HL^{iPr})₂] + 1.0 equivalent of O₂(g) + 2.0 equivalents of PPh₃:



Under an inert atmosphere, a 25 mL round bottom schlenk flask was charged with a stir bar, (Et₄N)₂[Co(HL^{iPr})₂] (0.200 g, 0.2011 mmol), and 10 mL of CH₃CN. Once the solution was homogeneous, the flask was fitted with a septum, sealed with electrical tape and removed from the dry box. While stirring at room temperature, O₂ gas (4.90 mL, 0.2011 mmol) was injected to the flask via a gas-tight syringe (inserted through the septum). Solution color changed from deep red to deep burgundy within minutes (~ 4 min). After stirring for 12 hours, the solvent was removed under vacuum, and the resulting solid was brought back into the dry box. Triphenylphosphine (0.105 g, 0.4022 mmol) in 3 mL of CH₃CN was added to a dark burgundy solution of oxygenated cobalt-species in 3 mL CH₃CN. The solution was allowed to stir for 4 hours. Color changed from deep burgundy to deep red. After 4 h, solvent was removed. ¹H analysis (CDCl₃, 400 MHz) of the

reaction mixture revealed $(\text{Et}_4\text{N})_2[\text{Co}(\text{HL}^{i\text{Pr}})_2]$ and OPPh_3 . ^{31}P NMR (δ , CDCl_3 , 400 MHz): (ppm) 24.71 (s, OPPh_3).

II. Gas Uptake Experiment Using $(\text{Et}_4\text{N})_2[\text{Co}_2(\text{L}^{i\text{Pr}})_2]$

An O_2 gas uptake experiment was conducted following a previously reported manometric gas uptake method.⁵⁰ Under an inert atmosphere, a 25 mL round bottom schlenk flask was charged with a stir bar, $(\text{Et}_4\text{N})_2[\text{Co}_2(\text{L}^{i\text{Pr}})_2]$ (0.500 g, 0.4760 mmol), and 25.0 mL of CH_3CN . Once the solution was homogeneous, the flask was fitted with a septum, sealed with electrical tape and removed from the dry box. The schlenk flask was then connected to the manometric set up and entire system was sealed against air and removed from the inert-atmosphere. O_2 gas was then added through the system and into the flask containing the deep green solution. A rapid color change from deep green to dark burgundy took place within minutes (~ 4 min). The system was allowed to equilibrate and the amount of O_2 was measured directly from the displacement of the volume change in the manometer (23.25 mL, 0.952 mmol).

III. *In Situ* Oxygenation Reactions – UV-vis and UV-vis NIR Monitoring Experiments

Typical Procedure for $(\text{Et}_4\text{N})_2[\text{Co}_2(\text{L}^{i\text{Pr}})_2] + \text{O}_2(\text{g})$: Under an inert atmosphere, a 6.755×10^{-5} M CH_3CN solution of $(\text{Et}_4\text{N})_2[\text{Co}_2(\text{L}^{i\text{Pr}})_2]$ was placed inside a 1.0 cm quartz cuvette (45 x 12.5 x 12.5 mm, 3.50 mL in volume) with a stir bar. The cuvette was fitted with a septum, sealed with electrical tape and removed from the dry box. While stirring at room temperature, O_2 gas (1.0 mL) was injected into the headspace above the solution in the cuvette via a gas-tight syringe (inserted through the septum). Solution color changed from deep green to deep burgundy within minutes (~ 2 min). The changes in the UV-visible absorption spectrum of $(\text{Et}_4\text{N})_2[\text{Co}_2(\text{L}^{i\text{Pr}})_2]$ were recorded at a scan rate of 1 scan per minute. The same procedure was carried out for recording the changes in the UV-visible NIR absorption spectrum of $(\text{Et}_4\text{N})_2[\text{Co}_2(\text{L}^{i\text{Pr}})_2]$ and O_2 gas at a scan rate of 1 scan per every three minutes.

Typical Procedure for $(\text{Et}_4\text{N})_2[\text{Co}(\text{HL}^{i\text{Pr}})_2] + \text{O}_2(\text{g})$: Under an inert atmosphere, a 1.030×10^{-4} M CH_3CN solution of $(\text{Et}_4\text{N})_2[\text{Co}(\text{HL}^{i\text{Pr}})_2]$ was placed inside a 1.0 cm quartz cuvette (45 x 12.5 x 12.5 mm, 3.50 mL in volume) with a stir bar. The cuvette was fitted with a septum, sealed with electrical tape and removed from the dry box. While stirring at room temperature, O_2 gas (1.0 mL) was injected into the headspace above the solution in the cuvette via a gas-tight syringe (inserted through the septum). Solution color changed from deep red to deep burgundy within minutes (~ 2 min). The changes in the UV-visible absorption spectrum of $(\text{Et}_4\text{N})_2[\text{Co}(\text{HL}^{i\text{Pr}})_2]$ were recorded at a scan rate of 1 scan per minute. The same procedure was carried out for recording the changes in the UV-visible

NIR absorption spectrum of $(\text{Et}_4\text{N})_2[\text{Co}(\text{HL}^{\text{iPr}})_2]$ and O_2 gas at a scan rate of 1 scan per every three minutes.

IV. Catalytic O-atom Transfer Procedures

Typical Procedure for Catalytic Aerobic O-atom Transfer to PPh_3 : Under an inert atmosphere, a 25 mL round bottom schlenk flask was charged with a stir bar, metal complex (0.01 mmol), PPh_3 (1.0 mmol), and 10 mL of CH_3CN . Once the solution was homogeneous, the flask was fitted with a septum, sealed with electrical tape and removed from the dry box. While stirring at room temperature, a constant slow purge of O_2 gas (1 atm) was introduced to the flask by connecting it, via 18-gauge needles inserted through the septum, to an O_2 line and to a mineral oil gas bubbler. The reactions were monitored using GC analysis by taking small (0.1 mL) aliquots of the reaction mixture (PPh_3 and OPPh_3 were compared to authentic samples). OPPh_3 yields were calculated based on catalyst TONs. Products from the reaction were confirmed using ^{31}P NMR.

Catalytic Aerobic PPh_3 Oxidation using $(\text{PPh}_4)_2[\text{Co}(\text{L}^{\text{Mod}})_2]$: Typical procedure for catalytic aerobic O-atom transfer to PPh_3 was carried out using $(\text{PPh}_4)_2[\text{Co}(\text{L}^{\text{Mod}})_2]$ (0.040 g, 0.0321 mmol), PPh_3 (0.8445 g, 3.21 mmol), and 10 mL of CH_3CN . After 20 hours, 18 % of PPh_3 was converted to OPPh_3 (0.5778 mmol). Reaction showed similar product conversions after 48 hours.

Catalytic Aerobic PPh₃ Oxidation using K₂[Zn(L^{Mod})₂]: Typical procedure for catalytic aerobic O-atom transfer to PPh₃ was carried out using K₂[Zn(L^{Mod})₂] (0.050 g, 0.0880 mmol), PPh₃ (2.31 g, 0.8800 mmol), and 10 mL of CH₃CN. After 48 hours, 0.9 % of PPh₃ was converted to OPPh₃ (0.0080 mmol). Reaction showed similar product conversions when PPh₃ loading was lowered to 50 and 10 equivalents.

Catalytic Aerobic PPh₃ Oxidation using (Et₄N)₂[Co₂(μ-OH)₂(Me-L^{iPr})₂]: Typical procedure for catalytic aerobic O-atom transfer to PPh₃ was carried out using (Et₄N)₂[Co₂(μ-OH)₂(Me-L^{iPr})₂] (0.0450 g, 0.0414 mmol), PPh₃ (1.10 g, 0.4139 mmol), and 10 mL of CH₃CN. After 48 hours, only trace amounts of OPPh₃ (2 % by GC) were detected. Reaction showed similar results when PPh₃ loading was lowered to 50 and 10 equivalents.

V. Catalytic Substrate Oxidation Reactions

Typical Procedure for Catalytic Aerobic Substrate Oxidation: Under an inert atmosphere, a 25 mL round bottom flask was charged with a stir bar, metal complex, substrate, and 10 mL of CH₃CN. The mixture was stirred until homogeneous for about 5 minutes. Reaction flask was sealed and taken outside the dry box. While stirring at room temperature, a constant slow purge of O₂ (1 atm) was then introduced to the reaction flask by connecting it, via 18-gauge needles inserted through the septum, to an O₂ line and to a mineral oil gas bubbler. After stirring for the indicated time, O₂ gas was removed from

reaction flask. The reactions were monitored using GC analysis by taking small (0.1 mL) aliquots of the reaction mixture before removing CH₃CN solvent. Once dried, precipitate was brought back into the dry box and suspended in a 9:1 (hexane to ethyl acetate) solvent mixture (3 x 5 mL) to extract organic product. Suspension was passed through a pack of silica and filtrate was concentrated to dryness. Isolated yields are reported as the average of three different reaction trials. Known products were confirmed using ¹H NMR.

Catalytic Aerobic Oxidation of 2-phenylpropionaldehyde (2-PPA) Using (Et₄N)₂[Co₂(L^{iPr})₂]: Typical procedure for catalytic aerobic substrate oxidation was carried out using (Et₄N)₂[Co₂(L^{iPr})₂] (0.200 mg, 0.1904 mmol), 2-PPA (255 μL, 1.904 mmol), and 20 mL of CH₃CN. After 24 hours reaction was removed from O₂ gas and acetophenone was isolated as the organic product as a clear oily-liquid (83 % yield, 190 mg).

Catalytic Aerobic Oxidation of 2-phenylpropionaldehyde (2-PPA) Using CoBr₂: Typical procedure for catalytic aerobic substrate oxidation was carried out using CoBr₂ (0.194 mg, 0.8869 mmol), 2-PPA (1.10 mL, 8.869 mmol), and 25 mL of CH₃CN. GC analysis of the reaction mixture after 48 hours showed only 6 % conversion of 2-PPA to acetophenone.

Catalytic Aerobic Oxidation of 3,5-ditertbutylcatechol (3,5-DTBC) Using (Et₄N)₂[Co₂(L^{iPr})₂]: Typical procedure for catalytic aerobic substrate oxidation was carried out using (Et₄N)₂[Co₂(L^{iPr})₂] (0.055 mg, 0.0523 mmol), 3,5-DTBC (1.2 g, 5.23 mmol), and 20 mL of CH₃CN. After 1 hour reaction was removed from O₂ gas and 3,5-

diterbutylquinone (3,5-DTBQ) was isolated as the organic product as a yellow solid (83 % yield, 1.05 g).

Catalytic Aerobic Oxidation of 3,5-diterbutylcatechol (3,5-DTBC) Using CoBr₂:

Typical procedure for catalytic aerobic substrate oxidation was carried out using CoBr₂ (0.194 mg, 0.8869 mmol), 3,5-DTBC (1.10 mL, 8.869 mmol), and 25 mL of CH₃CN. GC analysis of the reaction mixture after 1 hour showed traces 3,5-DTBQ (< 2 %).

Monitoring The Catalytic Aerobic Oxidation of 3,5-diterbutylcatechol (3,5-DTBC)

Via UV-visible Absorption Experiments: Under an inert atmosphere, 3.0 mL of a [7.192 x 10⁻⁴] M solution of 3,5-DTBC containing 1 mol % of (Et₄N)₂[Co(HL^{iPr})₂] was placed inside a 1.0 cm quartz cuvette (45 x 12.5 x 12.5 mm, 3.50 mL in volume) with a stir bar. The cuvette was fitted with a septum, sealed with electrical tape and removed from the dry box. While stirring at room temperature, O₂ (1.0 mL) was injected into the headspace above the solution in the cuvette via a gas-tight syringe (inserted through the septum). Increase in absorbance band at λ_{max} = 400 nm corresponding to 3,5-DTBQ, after addition of O₂ into the headspace above were recorded at a scan rate of 1 scan per minute.

VI. Additional Experiments

Typical Procedure for K₂[Zn(L^{Mod})₂] + O₂(g): Under an inert atmosphere, a 25 mL round bottom schlenk flask was charged with a stir bar, K₂[Zn(L^{Mod})₂] (0.050 g, 0.0880 mmol), and 10 mL of CH₃CN. Once the solution was homogeneous, the flask was fitted

with a septum, sealed with electrical tape and removed from the dry box. While stirring at room temperature, a constant slow purge of O₂ (1 atm) was introduced to the flask by connecting it, via 18-gauge needles inserted through the septum, to an O₂ line and to a mineral oil gas bubbler. Within the course of 15 minutes, the yellow solution became deep emerald green in color. After 4 hours of additional stirring, the solvent was removed in vacuo and the resulting emerald green solid was brought back into the dry box to be isolated on a medium porosity frit after several rinses with Et₂O (3 x 3 mL). $\lambda_{\text{max}} = 500$ nm (CH₃CN).

Section 3-6-5 Crystallographic Data

Data were collected using a Bruker APEX-II CCD diffractometer equipped with an Oxford cryosystems low-temperature apparatus operating at the indicated temperature. All structures were solved in their respective space groups and crystal systems by direct methods using the XT (Sheldrick, 2008) structure solution program and refined by Least Squares using version of ShelXL-97 (Sheldrick, 2008). All non-hydrogen atoms were refined anisotropically. Hydrogen atom positions were calculated geometrically and refined using the riding model.

Table 3-6. Crystal data and structure refinement parameters for $(\text{Et}_4\text{N})_2[\text{Co}(\text{CN})(\text{L}^{\text{iPr}})_2]$ and $(\text{Et}_4\text{N})_2[\text{Co}_2(\text{m-OH})_2(\text{Me-L}^{\text{iPr}})_2]$.

	$(\text{Et}_4\text{N})_2[\text{Co}(\text{CN})(\text{L}^{\text{iPr}})_2]$	$(\text{Et}_4\text{N})_2[\text{Co}_2(\text{m-OH})_2(\text{Me-L}^{\text{iPr}})_2]$
Formula	$\text{C}_{37}\text{H}_{62}\text{CoN}_6\text{O}_2$	$\text{C}_{29}\text{H}_{46}\text{CoN}_4\text{O}_3$
Form. Wt. (g/mol)	681.86	557.63
T (K)	173(2)	446(2)
Crystal system	Monoclinic	Monoclinic
Space group	$P2(1)/n$	$P2(1)/n$
<i>a</i> (Å)	11.150(5)	10.302(4)
<i>b</i> (Å)	16.151(7)	19.375(7)
<i>c</i> (Å)	22.239(10)	15.734(5)
α (°)	90	90
β (°)	104.421(7)	96.534(5)
γ (°)	90	90
<i>V</i> (Å³)	3879(3)	3120.3(18)
<i>Z</i>	4	4
ρ, calcd (g/cm³)	1.168	1.187
<i>m/mm</i>-1	0.48	0.583
Unique reflns.	1476	1196
Crystal size (mm³)	0.69 x 0.43 x 0.40	0.44 x 0.43 x 0.41
Theta range	2.27 to 32.46°	1.67 to 32.44°
Reflns. Collected	81156	65256
Data/rest./par.	13326/1/436	10712/12/365
<i>GOF</i>	1.033	1.035
Final R indexes		
[<i>I</i>>2σ (<i>I</i>)]	R1 = 0.0533	R1 = 0.0461
All data	wR2 = 0.1355	wR2 = 0.1180

Table 3-7. Crystal data and structure refinement parameters for $(\text{PPh}_4)_2[\text{Co}(\text{L}^{\text{Mod}})_2]$ and $\text{K}_2[\text{Zn}(\text{L}^{\text{Mod}})_2]$ complexes.

	$(\text{PPh}_4)_2[\text{Co}(\text{L}^{\text{Mod}})_2]$	$\text{K}_2[\text{Zn}(\text{L}^{\text{Mod}})_2]$
Formula	$\text{C}_{80}\text{H}_{72}\text{CoN}_4\text{O}_2\text{P}_2$	$\text{C}_{42}\text{H}_{51}\text{KN}_6\text{O}_2\text{Zn}$
Form. Wt. (g/mol)	1242.29	776.36
T (K)	173(2)	173(2)
Crystal system	Monoclinic	Monoclinic
Space group	P2(1)	P2(1)/c
<i>a</i> (Å)	19.3903(5)	10.748(8)
<i>b</i> (Å)	13.3308(4)	14.152(10)
<i>c</i> (Å)	25.2189(7)	27.39(2)
α (°)	90	90
β (°)	98.642(2)	98.798(11)
γ (°)	90	90
<i>V</i> (Å³)	6444.8(3)	4118(5)
<i>Z</i>	4	4
ρ, calcd (g/cm³)	1.28	1.252
<i>m</i>/mm-1	2.96	0.739
Unique reflns.	2612	1640
Crystal size (mm³)	0.27 x 0.09 x 0.03	0.36 x 0.30 x 0.19
Theta range	1.77 to 69.35°	1.92 to 29.13°
Reflns. Collected	41676	72650
Data/rest./par.	18893/1/886	11089/0/469
<i>GOF</i>	1.049	1.087
Final R indexes [<i>I</i>>2σ (<i>I</i>)]	R1 = 1.049	R1 = 0.0492
All data	wR2 = 0.1636	wR2 = 0.1280

Table 3-8. Crystal data and structure refinement parameters for $[\text{L}^{\text{Mod}}]^{\text{Decomp.}}$ and $(\text{Et}_4\text{N})_2[\text{L}^{\text{Ph}}]$.

	$[\text{L}^{\text{Mod}}]^{\text{Decomp.}}$	$(\text{Et}_4\text{N})_2[\text{L}^{\text{Ph}}]$
Formula	$\text{C}_{32}\text{H}_{32}\text{N}_4\text{O}_3$	$\text{C}_{49}\text{H}_{59}\text{N}_5\text{O}_2$
Form. Wt. (g/mol)	520.62	665.94
T (K)	173(2)	173(2)
Crystal system	Monoclinic	Monoclinic
Space group	$P2(1)/n$	$P2(1)/n$
<i>a</i> (Å)	9.2161(11)	11.6361(3)
<i>b</i> (Å)	16.439(2)	26.6964(8)
<i>c</i> (Å)	18.984(2)	13.4599(4)
α (°)	90	90
β (°)	98.052(2)	113.168(2)
γ (°)	90	90
<i>V</i> (Å³)	2847.8(6)	3844.02(19)
<i>Z</i>	4	4
ρ, calcd (g/cm³)	1.214	1.151
<i>m</i>/mm-1	0.079	0.550
Unique reflns.	1104.0	1448
Crystal size (mm³)	0.54 x 0.15 x 0.06	0.15 x 0.10 x 0.08
Theta range	4.34 to 50.24°	3.31 to 69.97°
Reflns. Collected	38637	26084
Data/rest./par.	5072/0/360	6992/0/442
<i>GOF</i>	1.033	1.008
Final R indexes		
[<i>I</i>>2σ (<i>I</i>)]	R1 = 0.0533	R1 = 0.0677
All data	wR2 = 0.1355	wR2 = 0.1798

References

1. Stahl, S. S., *Science*. **2005**, *309* (5742), 1824.
2. (a) Smidt, J.; Hafner, W.; Jira, R.; Sieber, R.; Sedlmeier, J.; Sabel, A., *Angewandte Chemie International Edition in English*. **1962**, *1* (2), 80; (b) Keith, J. A.; Henry, P. M., *Angewandte Chemie International Edition*. **2009**, *48* (48), 9038.
3. J. Sheehan, R., Terephthalic Acid, Dimethyl Terephthalate, and Isophthalic Acid. In *Ullmann's Encyclopedia of Industrial Chemistry*, Wiley-VCH Verlag GmbH & Co. KGaA: 2000.
4. Luzzio, F. A.; Guziec, F. S., *Organic Preparations and Procedures International*. **1988**, *20* (6), 533.
5. Dash, S.; Patel, S.; Mishra, B. K., *Tetrahedron*. **2009**, *65* (4), 707.
6. *Vision 2020 Catalysis Report; The Council for Chemical Research*.
7. McDonald, R. I.; Liu, G.; Stahl, S. S., *Chem Rev*. **2011**, *111* (4), 2981.
8. (a) Stahl, S. S., *Angewandte Chemie International Edition*. **2004**, *43* (26), 3400; (b) Sigman, M. S.; Jensen, D. R., *Accounts Chem Res*. **2006**, *39* (3), 221.
9. (a) Weinstein, A. B.; Stahl, S. S., *Catalysis Science & Technology*. **2014**, *4* (12), 4301; (b) Kotov, V.; Scarborough, C. C.; Stahl, S. S., *Inorg Chem*. **2007**, *46* (6), 1910.
10. Costas, M.; Mehn, M. P.; Jensen, M. P.; Que, L., *Chem Rev*. **2004**, *104* (2), 939.
11. Friedle, S.; Reisner, E.; Lippard, S. J., *Chem Soc Rev*. **2010**, *39* (8), 2768.

12. (a) Klinman, J. P., *Chem Rev.* **1996**, *96* (7), 2541; (b) Solomon, E. I.; Heppner, D. E.; Johnston, E. M.; Ginsbach, J. W.; Cirera, J.; Qayyum, M.; Kieber-Emmons, M. T.; Kjaergaard, C. H.; Hadt, R. G.; Tian, L., *Chem Rev.* **2014**, *114* (7), 3659.
13. Punniyamurthy, T.; Velusamy, S.; Iqbal, J., *Chem Rev.* **2005**, *105* (6), 2329.
14. (a) Tshuva, E. Y.; Lippard, S. J., *Chem Rev.* **2004**, *104* (2), 987; (b) Kim, E.; Chufán, E. E.; Kamaraj, K.; Karlin, K. D., *Chem Rev.* **2004**, *104* (2), 1077.
15. Holm, R. H.; Solomon, E. I., *Chem Rev.* **2004**, *104* (2), 347.
16. Borovik, A. S., *Accounts Chem Res.* **2004**, *38* (1), 54.
17. Chirik, P. J.; Wieghardt, K., *Science.* **2010**, *327* (5967), 794.
18. (a) Stubbe, J.; van der Donk, W. A., *Chem Rev.* **1998**, *98* (2), 705; (b) Whittaker, J. W., *Chem Rev.* **2003**, *103* (6), 2347; (c) Chen, Y.-R.; Gunther, M. R.; Mason, R. P., *Journal of Biological Chemistry.* **1999**, *274* (6), 3308; (d) Whittaker, M. M.; Kersten, P. J.; Nakamura, N.; Sanders-Loehr, J.; Schweizer, E. S.; Whittaker, J. W., *Journal of Biological Chemistry.* **1996**, *271* (2), 681; (e) Wachter, R. M.; Montague-Smith, M. P.; Branchaud, B. P., *Journal of the American Chemical Society.* **1997**, *119* (33), 7743.
19. Lyons, C. T.; Stack, T. D. P., *Coordin Chem Rev.* **2013**, *257* (2), 528.
20. Chaudhuri, P.; Hess, M.; Müller, J.; Hildenbrand, K.; Bill, E.; Weyhermüller, T.; Wieghardt, K., *Journal of the American Chemical Society.* **1999**, *121* (41), 9599.
21. Carter, M. J.; Rillema, D. P.; Basolo, F., *Journal of the American Chemical Society.* **1974**, *96* (2), 392.
22. Tsumaki, T., *Bulletin of the Chemical Society of Japan.* **1938**, *13* (2), 252.
23. Hikichi, S.; Akita, M.; Moro-oka, Y., *Coordin Chem Rev.* **2000**, *198* (1), 61.

24. Tiné, M. R., *Coordin Chem Rev.* **2012**, 256 (1–2), 316.
25. Cho, J.; Sarangi, R.; Nam, W., *Accounts Chem Res.* **2012**, 45 (8), 1321.
26. (a) Ray, K.; Pfaff, F. F.; Wang, B.; Nam, W., *Journal of the American Chemical Society.* **2014**, 136 (40), 13942; (b) Givaja, G.; Volpe, M.; Edwards, M. A.; Blake, A. J.; Wilson, C.; Schröder, M.; Love, J. B., *Angewandte Chemie International Edition.* **2007**, 46 (4), 584; (c) Pfaff, F. F.; Kundu, S.; Risch, M.; Pandian, S.; Heims, F.; Pryjomska-Ray, I.; Haack, P.; Metzinger, R.; Bill, E.; Dau, H.; Comba, P.; Ray, K., *Angewandte Chemie International Edition.* **2011**, 50 (7), 1711; (d) Hong, S.; Pfaff, F. F.; Kwon, E.; Wang, Y.; Seo, M.-S.; Bill, E.; Ray, K.; Nam, W., *Angewandte Chemie International Edition.* **2014**, 53 (39), 10403.
27. (a) Kim, D.; Cho, J.; Lee, Y.-M.; Sarangi, R.; Nam, W., *Chemistry – A European Journal.* **2013**, 19 (42), 14112; (b) Fukuzumi, S.; Mandal, S.; Mase, K.; Ohkubo, K.; Park, H.; Benet-Buchholz, J.; Nam, W.; Llobet, A., *Journal of the American Chemical Society.* **2012**, 134 (24), 9906.
28. Schaefer, W. P.; Huie, B. T.; Kurilla, M. G.; Ealick, S. E., *Inorg Chem.* **1980**, 19 (2), 340.
29. (a) Patra, T.; Manna, S.; Maiti, D., *Angewandte Chemie International Edition.* **2011**, 50 (51), 12140; (b) LeCloux, D. D.; Barrios, A. M.; Lippard, S. J., *Bioorganic & Medicinal Chemistry.* **1999**, 7 (5), 763; (c) Wertz, D.; Valentine, J., Nucleophilicity of Iron-Peroxo Porphyrin Complexes. In *Metal-Oxo and Metal-Peroxo Species in Catalytic Oxidations*, Meunier, B., Ed. Springer Berlin Heidelberg: 2000; Vol. 97, pp 37; (d) Selke, M.; Valentine, J. S., *Journal of the American Chemical Society.* **1998**, 120 (11), 2652.

30. (a) Jo, Y.; Annaraj, J.; Seo, M. S.; Lee, Y.-M.; Kim, S. Y.; Cho, J.; Nam, W., *Journal of Inorganic Biochemistry*. **2008**, *102* (12), 2155; (b) Cho, J.; Sarangi, R.; Kang, H. Y.; Lee, J. Y.; Kubo, M.; Ogura, T.; Solomon, E. I.; Nam, W., *Journal of the American Chemical Society*. **2010**, *132* (47), 16977.
31. Sharma, S. K.; May, P. S.; Jones, M. B.; Lense, S.; Hardcastle, K. I.; MacBeth, C. E., *Chem Commun*. **2011**, *47* (6), 1827.
32. (a) Kurahashi, T.; Fujii, H., *Journal of the American Chemical Society*. **2011**, *133* (21), 8307; (b) Pavlova, N. A.; Poddelsky, A. I.; Bogomyakov, A. S.; Fukin, G. K.; Cherkasov, V. K.; Abakumov, G. A., *Inorganic Chemistry Communications*. **2011**, *14* (10), 1661.
33. Hanusa, T. P., Cyanide Complexes of the Transition Metals. In *Encyclopedia of Inorganic Chemistry*, John Wiley & Sons, Ltd: 2006.
34. Nakamoto, K., *Infrared and Raman Spectra of Inorganic and Coordination Compounds*. Wiley: New York, 1997.
35. Yang, L.; Powell, D. R.; Houser, R. P., *Dalton T*. **2007**, (9), 955.
36. Evans, D. F., *Journal of the Chemical Society (Resumed)*. **1959**, (0), 2003.
37. (a) Nguyen, A. I.; Blackmore, K. J.; Carter, S. M.; Zarkesh, R. A.; Heyduk, A. F., *Journal of the American Chemical Society*. **2009**, *131* (9), 3307; (b) Nguyen, A. I.; Zarkesh, R. A.; Lacy, D. C.; Thorson, M. K.; Heyduk, A. F., *Chemical Science*. **2011**, *2* (1), 166.
38. Addison, A. W.; Rao, T. N.; Reedijk, J.; Vanrijn, J.; Verschoor, G. C., *J Chem Soc Dalton*. **1984**, (7), 1349.

39. Hikichi, S.; Yoshizawa, M.; Sasakura, Y.; Akita, M.; Moro-Oka, Y., *Journal of the American Chemical Society*. **1998**, *120* (40), 10567.
40. (a) Brunold, T. C.; Tamura, N.; Kitajima, N.; Moro-oka, Y.; Solomon, E. I., *Journal of the American Chemical Society*. **1998**, *120* (23), 5674; (b) Hikichi, S.; Komatsuzaki, H.; Akita, M.; Moro-oka, Y., *Journal of the American Chemical Society*. **1998**, *120* (19), 4699; (c) Kosugi, M.; Hikichi, S.; Akita, M.; Moro-oka, Y., *Inorg Chem*. **1999**, *38* (11), 2567; (d) Akita, M.; Takahashi, Y.; Hikichi, S.; Moro-oka, Y., *Inorg Chem*. **2001**, *40* (1), 169; (e) Miyaji, T.; Kujime, M.; Hikichi, S.; Moro-oka, Y.; Akita, M., *Inorg Chem*. **2002**, *41* (20), 5286.
41. Zanello, P., *Metal Complexes Containing Redox-Active Ligands. Inorganic Electrochemistry: Theory, Practice, and Application*. Royal Society of Chemistry: Cambridge, U.K., 2003.
42. Ikeda, A.; Hoshino, K.; Komatsuzaki, H.; Satoh, M.; Nakazawa, J.; Hikichi, S., *New Journal of Chemistry*. **2013**, *37* (8), 2377.
43. Monzani, E.; Quinti, L.; Perotti, A.; Casella, L.; Gullotti, M.; Randaccio, L.; Geremia, S.; Nardin, G.; Faleschini, P.; Tabbì, G., *Inorg Chem*. **1998**, *37* (3), 553.
44. Ackermann, J.; Meyer, F.; Kaifer, E.; Pritzkow, H., *Chemistry – A European Journal*. **2002**, *8* (1), 247.
45. (a) Bediako, D. K.; Solis, B. H.; Dogutan, D. K.; Roubelakis, M. M.; Maher, A. G.; Lee, C. H.; Chambers, M. B.; Hammes-Schiffer, S.; Nocera, D. G., *Proceedings of the National Academy of Sciences*. **2014**, *111* (42), 15001; (b) Helm, M. L.; Stewart, M. P.; Bullock, R. M.; DuBois, M. R.; DuBois, D. L., *Science*. **2011**, *333* (6044), 863; (c) Horvath, S.; Fernandez, L. E.; Soudackov, A.

- V.; Hammes-Schiffer, S., *Proceedings of the National Academy of Sciences*. **2012**, *109* (39), 15663.
46. Rosenthal, J.; Nocera, D. G., *Accounts Chem Res*. **2007**, *40* (7), 543.
47. (a) Dawson, C. R.; Tarpley, W. B., *Annals of the New York Academy of Sciences*. **1963**, *100* (2), 937; (b) Siegbahn, P. M., *J Biol Inorg Chem*. **2004**, *9* (5), 577.
48. Hey, D. H.; Mulley, R. D., *Journal of the Chemical Society (Resumed)*. **1952**, (0), 2276.
49. (a) Black, D. S.; Rothnie, N. E., *Aust J Chem*. **1983**, *36* (6), 1141; (b) Black, D. S.; Rothnie, N. E., *Aust J Chem*. **1983**, *36* (6), 1149.
50. Sorrell, T. N.; Malachowski, M. R., *Inorg Chem*. **1983**, *22* (13), 1883.

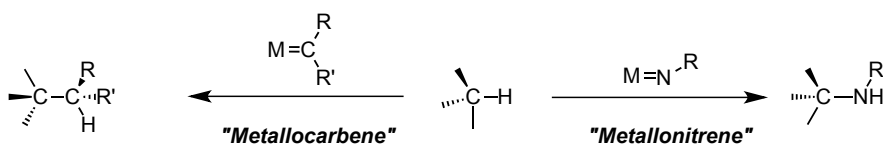
Chapter 4:

Intramolecular sp^3 C–H Amination of Aryl Azides Catalyzed by a Cobalt(II) Complex

Section 4-1. Introduction

The quest for catalyst systems that predictably convert petroleum feedstocks into value added functional groups has become a global research theme in catalysis. Future advances in this area require predictable methods to selectively functionalize C–H bonds for both the fine chemicals and materials production industry.¹ C–H functionalization remains a rapid-growing area of research that is revolutionizing the way chemical synthesis is approached. Traditionally, the functionalization of unreactive C–H bonds has been restricted to reactions at sp^2 -hybridized sites driven primarily by proximal directing groups for positional selectivity. Major developments in this area over the past two decades, however, have led to the discovery of a comprehensive landscape of methodologies that make the selective functionalization of C–H bonds possible.

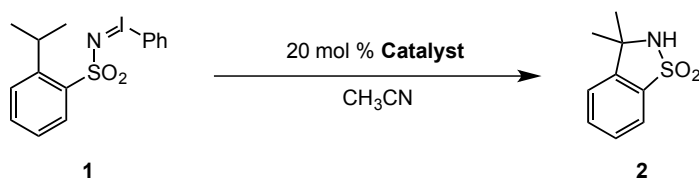
The most efficient and widely used strategies for C–H functionalization is the use of transition metal-catalyzed reactions. Two of the most employed methods in transition metal-catalyzed C–H functionalization are C–H insertion carried out by metallocarbenes² and metallonitrenes.³ Both are highly attractive because of their rapid application to a wide range of substrates. This has allowed for the diversification of biologically relevant compounds (Scheme 4-1).



Scheme 4-1. C–H insertion by metallocarbenes and metallonitrenes.⁴

The ubiquity of nitrogen-containing compounds in both natural products and pharmaceutical compounds has driven organic chemists to pursue new methods for making C–N bonds. Specifically, a central focus of C–H amination has been catalyst design. In collaboration with the inorganic synthetic community, the design of new catalysts for C–H amination has led to improved selectivity with dramatically lower catalyst loadings. More importantly, the development of novel catalysts for C–H amination has allowed for the substrate scope to expand beyond traditional benzylic C–N bond formation to aryl, vinyl, primary, secondary, and tertiary C–H bonds.⁵ While both metallocarbene- and metallonitrene-catalyzed reactions are changing the way we conduct and envision chemical synthesis, metallonitrene reactions remain far less developed.

Early examples of metal-catalyzed C–H amination began emerging in the literature during the 1960s. Reports by Kwart and Kahn,⁶ Sloan,⁷ and Turner⁸ demonstrated the ability of metal complexes or metal salts to perform C–H amination. In the early 80s work by Breslow and co-workers observed that iron(III)- and manganese(III)-porphyrin analogues of cytochrome P-450, as well as dirhodium(II) acetate, were capable of catalytically performing the intramolecular C–H amination of 2,5-diisopropyl(imidoiodo)benzene **1**.⁹ As a result, they were able to synthesize C–H insertion product **2** (Scheme 4-2).



Entry	[Catalyst]	2 yield, %
1	Mn^{III}(TPP)Cl	17
2	Fe^{III}(TPP)Cl	85
3	Rh₂(OAc)₄	94

Scheme 4-2. Catalytic intramolecular C–H amination by Mn(III)- and Fe(III)-porphyrins and dirhodium(II) acetate.⁹

The generally accepted mechanism for C–H amination involves the binding of a transition metal complex to a nitrene-source. This is generally followed by the extrusion of a leaving group (from the nitrene source) and with the concomitant formation of a highly reactive metallonitrene intermediate. Once generated, the metallonitrene intermediate inserts into a C–H bond followed by the formation of a new C–N bond (Figure 4-1). Mechanistic studies leading to the discovery of this insertion mechanism have allowed for the significant and rapid advances in C–H amination for numerous applications.^{5,10} These studies have given fundamental insight into the type of mechanism by which a C-H insertion takes place (concerted versus hydrogen-atom radical abstraction mechanisms).¹¹

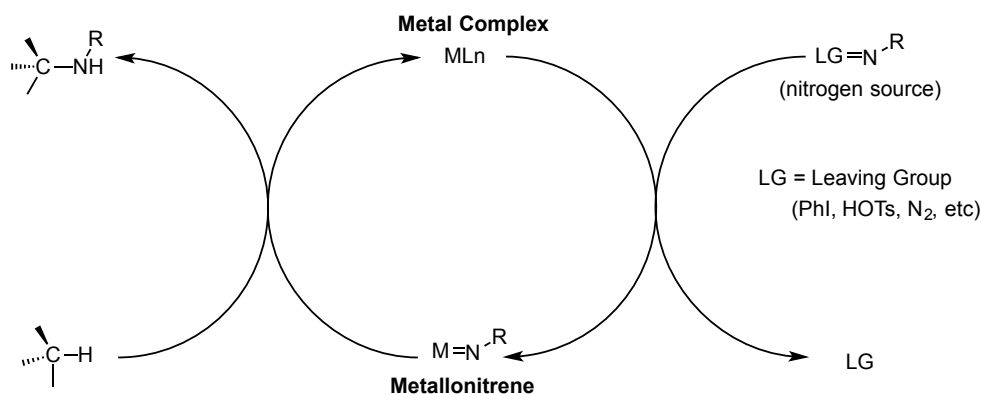


Figure 4-1. Mechanism for the formation of a metallonitrene and its insertion into a C–H bond.⁴

The most widely used sources of nitrene precursors are carbamates, sulfamates, sulfamides, and sulfonamides (Figure 4-2).¹² These nitrene sources are typically chosen because of their facile oxidation by a hypervalent iodine reagent such as iodobenzene diacetate ($PhI(OAc)_2$). Upon oxidation, iminoiodinanes are generated *in situ*. In the presence of a transition metal, the iminoiodinanes promote the formation of the highly reactive metallonitrene.

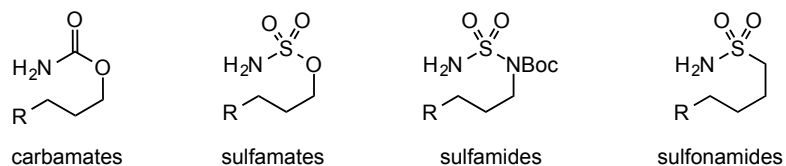
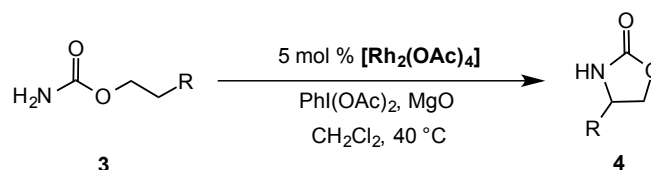


Figure 4-2. Commonly used sources of nitrene precursors.¹²

Some of the most notable examples of C–H amination have been conducted by Du Bois and co-workers. They have demonstrated that dirhodium(II) complexes are capable of converting carbamates (**3**), to the corresponding five-membered oxazolidinone

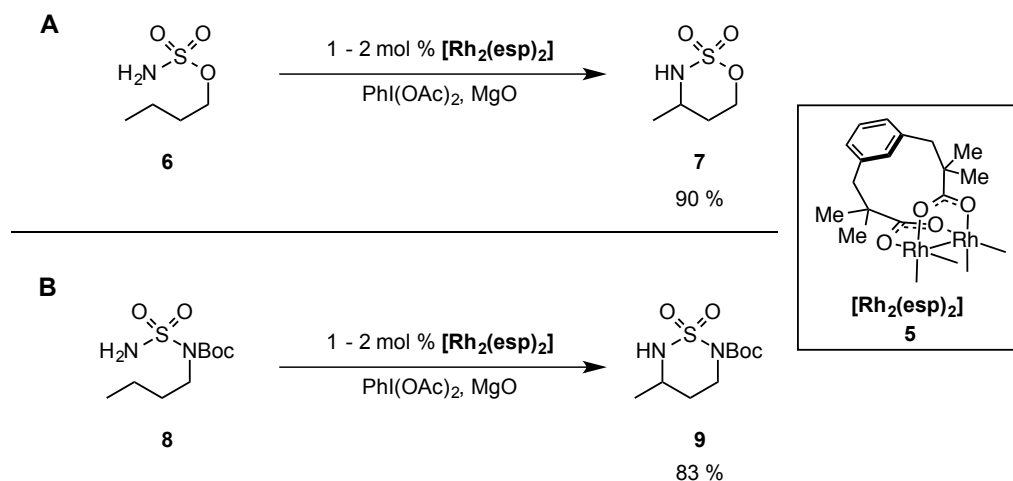
products (**4**) (Scheme 4-3).¹³ In this reaction system, a series of carbamates are readily oxidized using $\text{PhI}(\text{OAc})_2$, generating the iminoiodinane *in situ* necessary to form a rhodium-nitrene. Their work was considered a landmark in C–H amination, as simple carbamate compounds were not previously explored as potential precursors for the synthesis of substituted oxazolidinones.



Scheme 4-3. C–H amination of carbamates by dirhodium(II) tetracarboxylate.¹³

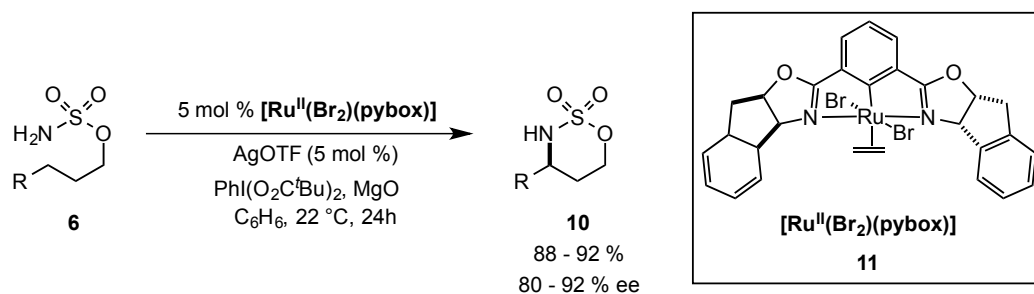
Mechanistic studies by Du Bois and co-workers suggested that rhodium(II) acetate catalyst underwent rapid ligand exchange and catalyst degradation in the presence of $\text{PhI}(\text{OAc})_2$; therefore, they focused on developing catalysts that would avoid such issues.¹⁴ They proposed that by replacing bidentate chelating tetracarboxylate ligands with bridging ligands the ligand exchange processes could be avoided or inhibited, leading to a more stable catalyst. With the multi-carboxylate chelating ligands stabilizing complex **5** ($[\text{Rh}_2(\text{esp})_2]$), the Du Bois group observed efficient catalysis of intramolecular C–H amination with sulfamate **6** and sulfamide **8**. In comparison to the original dirhodium(II) tetracarboxylate catalysts, higher yields were observed (Scheme 4-4).¹⁴ It was reported that catalyst **5** could also efficiently carry out the intramolecular C–H amination of guanidines and ureas under similar reaction conditions, a process that was

previously unattainable using dirhodium(II) systems. These results elegantly highlight how catalyst design approaches can dramatically impact substrate scope.



Scheme 4-4. Intramolecular rhodium(II)-catalyzed C–H amination of **A**) sulfamates and **B**) sulfamides.

The ability to carry out C–H amination transformations enantioselectively is of great significance for the synthesis of natural products and biologically active compounds. Based on the work by Du Bois and co-workers, attempts were made to carry out intramolecular C–H amination of sulfamate esters enantioselectively.¹⁴⁻¹⁵ One example in particular was presented by Blakey and co-workers reported the enantioselective C–H amination of sulfamate ester **6** with ruthenium(II)-pybox complex **10** (Scheme 4-5).¹⁵ In their work, silver triflate (AgOTf) abstraction of the proximal bromide halide from the catalyst proved to be essential in obtaining high yields and enantioselectivities. This work illustrated the ability to perform these reactions enantioselectively increased the applicability of this methodology.



Scheme 4-5. Ruthenium(II)-catalyzed enantioselective intramolecular C–H amination of sulfamate esters.¹⁵

Porphyrin ligand systems have also been widely used in C–H amination. These ligand frameworks have played a crucial role in nitrene transfer reactions into aliphatic and benzylic C–H bonds from first-row metal ions. Reports by Berslow and co-workers in 1982 provided evidence that iron and manganese porphyrins systems were good catalysts for performing C–H amination reactions.^{9, 16} Since then, few porphyrin-catalyzed C–H amination processes have been reported. White and co-workers reported a seminal example of an iron-catalyzed intramolecular allylic C–H amination process.¹⁷ In this work, it was observed that an iron porphyrin system could be used to selectively C–H aminate allylic positions over the expected aziridination displayed by rhodium- and ruthenium-catalyzed systems.¹⁸

Although the reactions mentioned thus far demonstrated a new approach to synthesizing heterocyclic nitrogen containing compounds, the use of external oxidants to generate reactive metallonitrene species is needed. In the midst of the efficiency of these reactions, from an environmental and atom-economy standpoint, the stoichiometric byproduct from the oxidant is a limitation facing these types of reactions. An alternative sources for nitrene precursors emerging in the field of intra- and intermolecular C–H

amination reactions are organic azides. Azides are attractive sources of nitrene precursor mainly because nitrogen gas is the only byproduct of the reaction. The reaction of organic azides with transition metals have been explored since the early 1960s, primarily from the perspective of understanding different coordination modes to metal complexes and much interest was placed on the ability of these compounds to form isolable nitrene (or imido) metal complex species.¹⁹ Recent advances in continuous flow systems have made organic azides amenable for large-scale industrial reactions.²⁰ The electronic nature of the azide group, as well as the labile $N_{\beta}-N_{\gamma}$ bond, makes it an ideal ligand for metal complexes to form metallonitrenes. In this mechanism, nitrogen is the only byproduct, making this an ideal atom-economical and environmentally friendly process (Figure 4-4).²¹

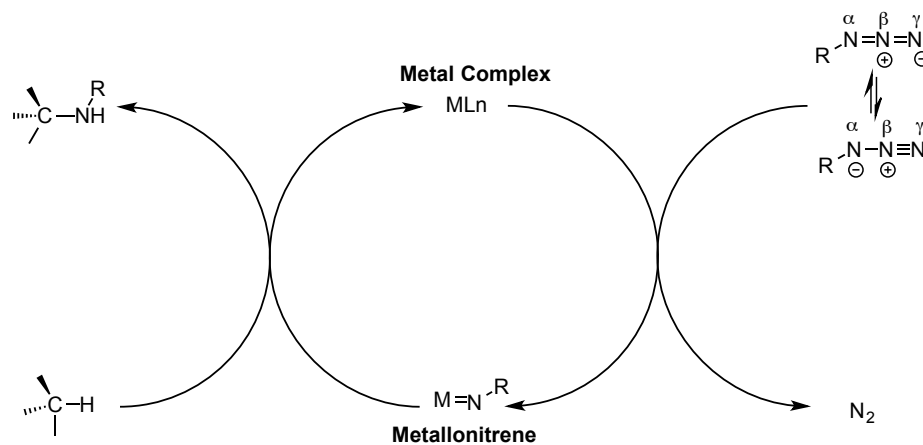
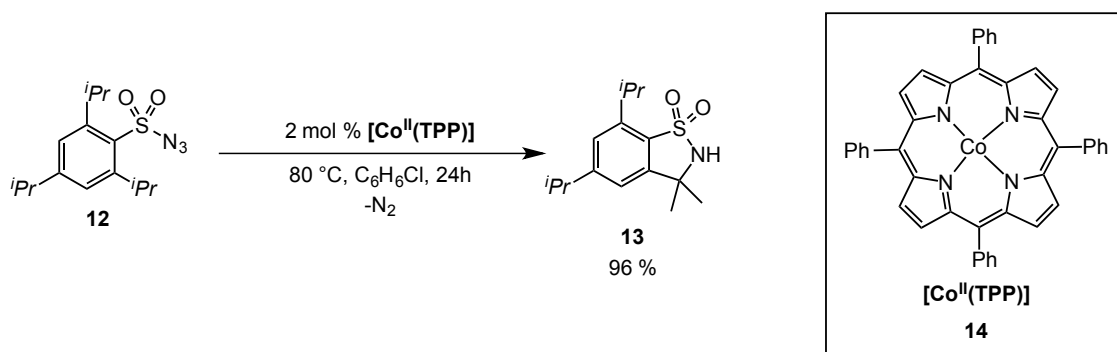


Figure 4-4. General scheme for the formation of a metallonitrene and its insertion into a C–H bond using an organic azide (resonance formulas for RN_3 are shown).²¹

Work reported by Zhang and co-workers in 2007 was among the first reports of intramolecular C–H amination using aryl sulfonyl azides.²² They observed that cobalt(II)-tetraphenylporphyrin **14**, was an effective catalyst for intramolecular C–H amination with

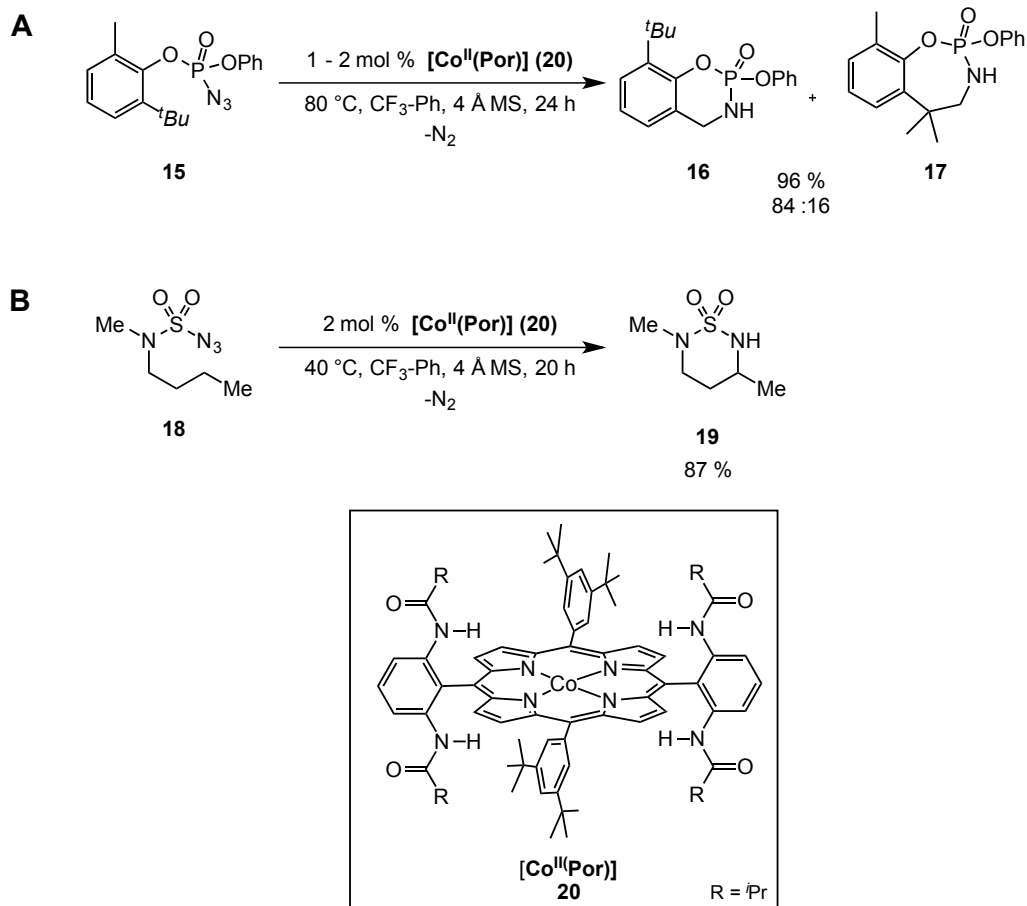
2,4,6-triisopropylbenzenesulfonyl azide (**12**) to obtain **13** in 96 % yield in the absence of additives or oxidants (Scheme 4-6). This result demonstrated both the ability of sulfonyl azides to act as nitrene sources and metallonitrene radical systems to promote C–H amination using first-row transition metals. The most promising classes of catalysts for C–H amination with organic azides have been those that contain second- and third-row metals. These systems are among the most efficient C–H amination catalysts available to date.²³ As can be expected, wide arrays of catalyst design strategies have emerged to better tune these catalysts for efficient C–H amination reactions. For sustainability purposes, however, first-row transition metals are attractive candidates for the synthesis of nitrogen-containing compounds because they are highly abundant, making the C–H amination methodology with organic azides even more economical.



Scheme 4-6. Cobalt(II)-porphyrin catalyzed C–H amination with sulfonyl azides.²²

In 2010, Zhang and co-workers reported on the primary, secondary, and tertiary benzylic and homobenzylic C–H amination of phosphoryl azides (Scheme 4-7).²⁴ Systematically designing cobalt(II)-porphyrin **20**, Zhang and co-workers observed conversion of phosphoryl azide **15** to six- and seven- membered cyclophosphoramidates

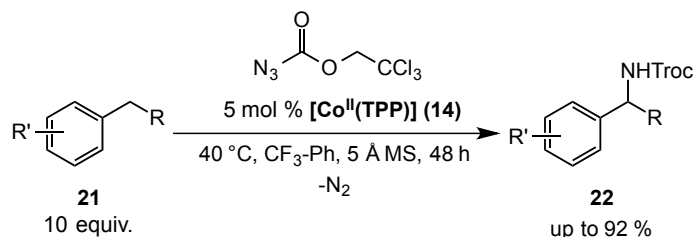
16 and **17**, respectively. The unique reactivity cobalt(II) catalyst **20** is suggested to be due in part from proposed hydrogen-bonding interaction between the P=O and N–H units of a possible nitrene intermediate, as suggested by MM2 energy minimization calculations. These results established that cobalt(II)-porphyrin systems are capable of effectively carrying out C–H aminations with phosphoryl azides, substrates that for the past 30 years were only seen as sources of nitrenes via photolysis.²⁵ The possible hydrogen-bonding interaction found in cobalt(II)-porphyrin **20** led Zhang and co-workers to attempt C–H amination reactions using sulfamoyl azides in a subsequent study.^{24b} In that work, cobalt(II)-porphyrin **20** was found to catalyze the C–H amination of a series of sulfamoyl azides (**18**) to obtain the corresponding cyclic sulfamides **19** (Scheme 4-7, B). The cyclic sulfamides obtained in these results demonstrated a synthetic strategy for conveniently forming 1,3-diamines, compounds that previously could not be formed directly through C–H functionalization.



Scheme 4-7. Cobalt(II)-porphyrin catalyzed C–H amination with **A**) sulfonyl^{24a} and **B**) sulfamoyl^{24b} azides.

Zhang and co-workers have postulated cobalt(II)-porphyrin catalyst **20** to have radical character. The stable radical nature of the cobalt(II)-porphyrin **20** has allowed for significant broadening of the substrate scope. In addition to intramolecular C–H aminations, these systems were found useful in intermolecular C–H aminations using 2,2,2-trichloroethoxycarbonyl azide (TrocN₃).²⁶ Among the many cobalt(II)-porphyrin systems designed by Zhang and co-workers, Co^{II}(TPP) **14** was observed to be a good

catalyst for the C–H insertion into various benzylic C–H bonds of compounds **21** to obtain the corresponding Troc-protected amines **22** (Scheme 4-8).



Scheme 4-8. Intramolecular C–H amination catalyzed by $\text{Co}^{\text{II}}(\text{TPP})$ **14** using azide Troc- N_3 .²⁶

It is proposed that upon reaction of Troc N_3 with cobalt(II)-porphyrin systems, a cobalt(III)-N intermediate with a nitrogen-based radical forms along with the extrusion of nitrogen gas. This cobalt(III)-N intermediate carries out hydrogen-atom abstraction followed by radical recombination to form the C–N bond and regenerate the active catalyst. Figure 4-5 depicts the proposed mechanism for cobalt(II)-porphyrin catalyzed intermolecular C–H amination using Troc- N_3 .

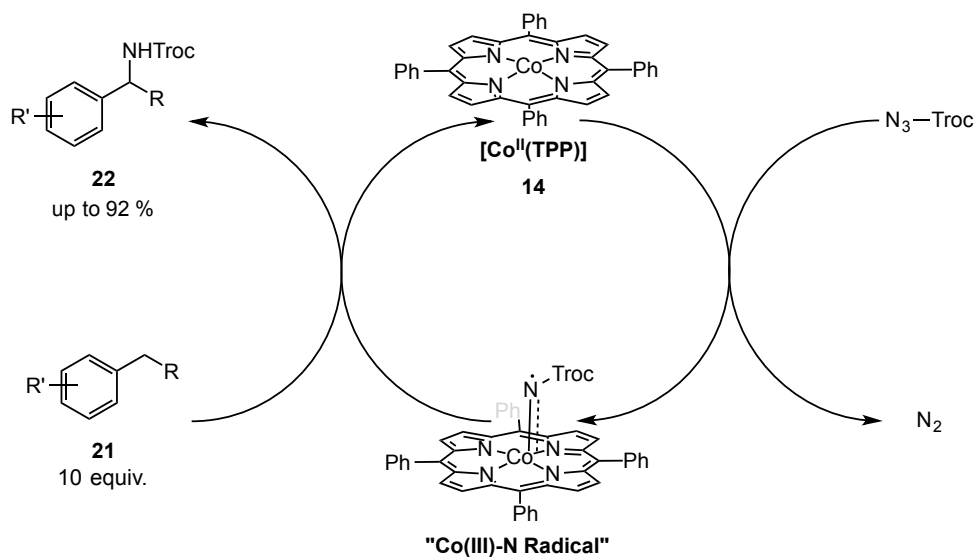
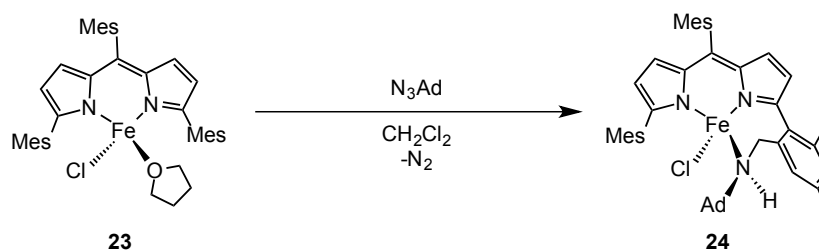


Figure 4-5. Proposed mechanism for catalytic intermolecular cobalt(II)-catalyzed nitrene insertion with TrocN.²⁶

A long-term challenge in metallonitrene-catalyzed C–H amination is the development of practical and sustainable methods for conducting these reactions. The use of first-row transition metals to replace second- and third-row metal catalysts is a slowly emerging and challenging concept. As presented above, cobalt(II) porphyrin systems are among the first pioneering examples of first-row transition metal-catalyzed C–H amination reactions using organic azides. Although the use of porphyrins as supporting ligands has proven to be efficient at promoting cobalt(II)-catalyzed nitrene transfer processes, non-heme cobalt(II)-catalyzed C–H aminations with azides have not been explored. As discussed in Chapter 1, redox-active ligands have been widely used to enhance the reactivity of first-row transition metal catalyst in the past decade.²⁷

In 2009, Betley and co-workers reported the intramolecular C–H amination by an iron(II) dipyrromethene complex.²⁸ In this work, an arylated dipyrromethene ligand was

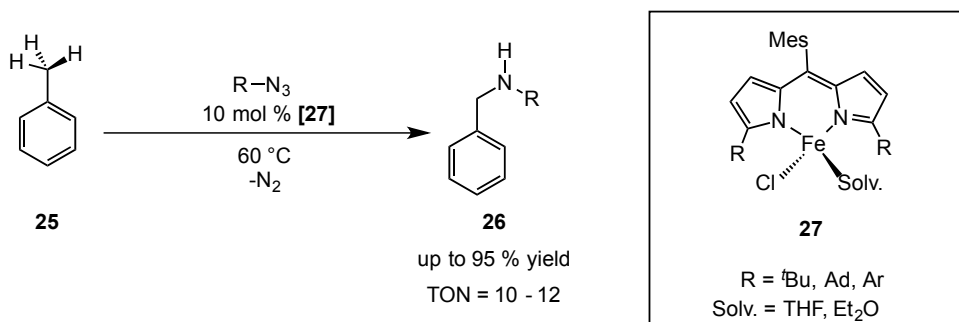
proven to stabilize high-spin iron(II) complex **23** with an open coordination site. The cyclic voltammogram of the zinc(II) analogue complex of this ligand revealed a fully reversible, one-electron event originating from the ligand platform, indicating that this ligand is redox-active. Treating iron(II) complex **23** with a stoichiometric amount of 1-azidoadamantane (N_3Ad) resulted in the formation of the new high-spin iron(II) complex **24**, whereby an [NAd] fragment was inserted into the benzylic C–H bond in one of the mesityl aryl groups of the pyrrole ligand (Scheme 4-9). This result demonstrated that the dipyrromethene ligand system developed by Betley and co-workers could mediate intramolecular C–H bond amination at first-row transition metal centers using organic azides.



Scheme 4-9. Stoichiometric intramolecular C–H amination by an iron(II) dipyrromethene complex.²⁸

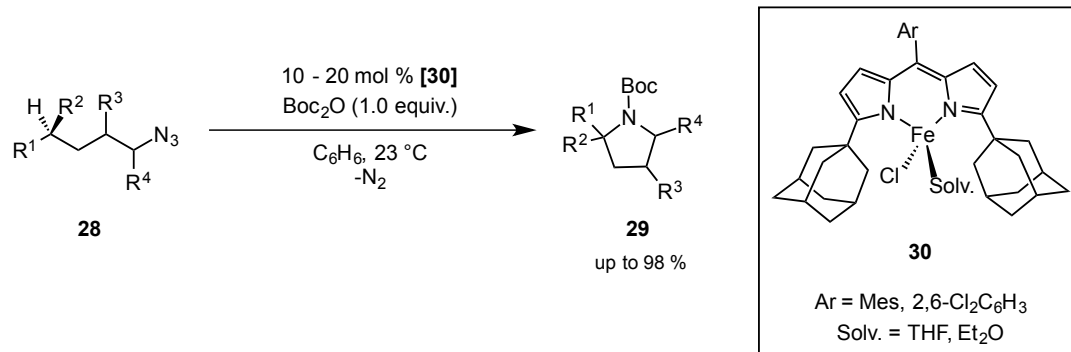
With this result at hand, Betley and co-workers explored the ability of iron(II) dipyrromethene complexes to perform C–H amination in intermolecular reactions. In 2011, the group reported the intermolecular C–H amination of primary C–H bonds from alkyl azides catalyzed by iron(II) complex **27** of the dipyrromethene ligand system (Scheme 4-10).²⁹ Although catalytic C–H amination reactivity was observed at room

temperature into toluene, optimal yields and turn over numbers (TONs) were observed at 60 °C.



Scheme 4-10. Catalytic intermolecular C–H amination by an iron(II) dipyrromethene complex.²⁹

Betley's dipyrromethene ligand system continues to be the most notable example of incorporating redox-active ligands for catalytic C–H amination to date. In a 2013 report, the efficient catalytic amination of aliphatic C–H bonds with linear alkyl azides **28** to form pyrrolidines **29** was carried out by iron(II)-dipyrinato catalyst **30** (Scheme 4-11).^{27o} This work elegantly demonstrated the ability of iron(II) dipyrromethene complexes to use alkyl azides to form the Boc-protected cyclic amines, a reaction that was previously unattainable even via alkyl azide photolysis or Hoffmann-Löffler-Freytag methods. This work exemplified the ability of non-heme redox-active ligands to promote catalytic C–H aminations reactions, representing a major innovation in C–H amination; however, the need to use other first-row transition metals that can utilize organic azides for C–H amination transformations remains an unexplored topic in C–H functionalization.



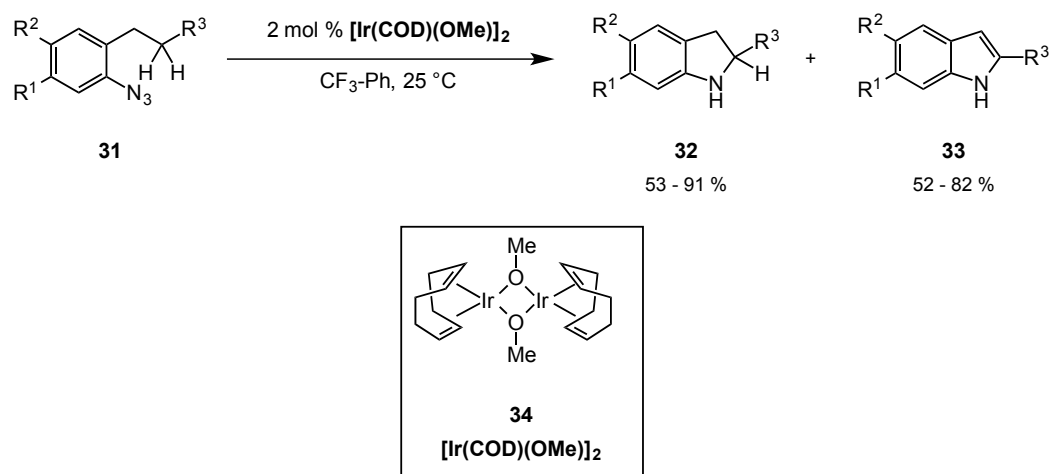
Scheme 4-11. Catalytic intramolecular C–H amination of linear alkyl azides by an iron(II) dipyrromethene complex.^{27o}

Section 4-2. Background and Significance

Our group became interested in expanding beyond dioxygen activation and directed our focus to C–H functionalization reactions. It was hypothesized that using first-row transition metal catalysts that can efficiently and selectively facilitate C–H amination using organic azides would fulfill both economic and environmental demands for the synthesis of nitrogen-containing heterocyclic compounds. In particular, we became interested in C–H amination reactions utilizing organic aryl azides. Recent advances in this field have made metallonitrene-catalyzed N-atom transfer reactions from aryl azides a more practical method for selectively making new C–N bonds.²³

Recently, Driver and co-workers reported that $[\text{Ir}(\text{cod})(\text{OMe})_2]$ was an effective catalyst for intramolecular benzylic C–H amination using aryl azides, a reaction which was unattainable under rhodium catalysis.³⁰ In their work, iridium(I) complex **34** catalyzed the

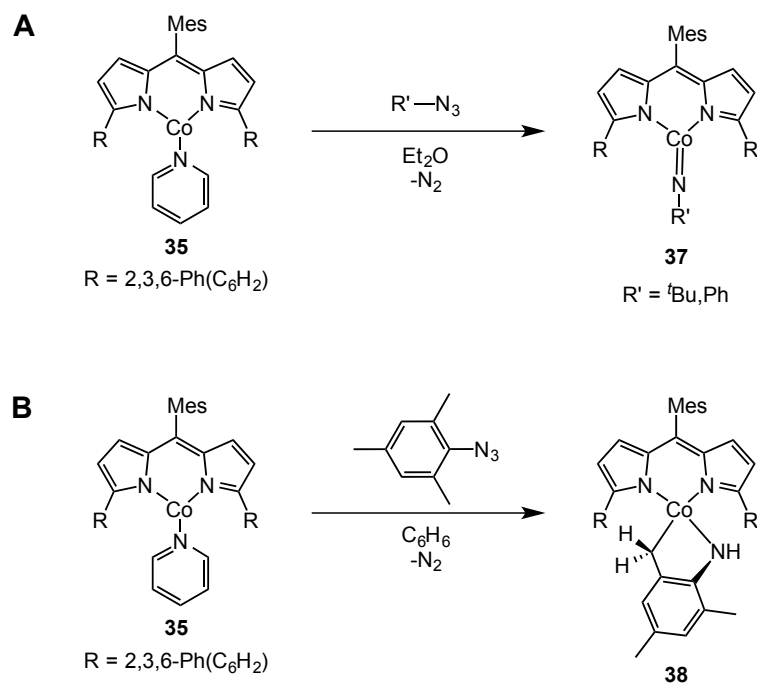
intramolecular benzylic C–H amination of a wide scope of aryl substituted azides **31** to obtain the corresponding indoline **32** and indole **33** in fairly good yields (Scheme 4-12). In this work, it was observed that electron-poor azides resulted in higher yields whereas electron-rich azides gave no reaction with iridium(I) catalyst **34**. These results highlighted a new method for obtaining functionalized indoles and indolines directly from aryl azides. The discovery of new routes for synthesizing indoles and indolines is highly attractive, as both nitrogen-containing heterocyclic compounds are ubiquitous in a number of biologically active compounds.



Scheme 4-12. Iridium(I)-catalyzed C–H amination of aryl azides to form indolines and indoles.³⁰

Betley and co-workers recently demonstrated precedent for nitrene reactivity with non-heme cobalt complexes. In 2012 it was demonstrated that cobalt(I) complexes of the dipyrromethene ligand system reacted with alkyl and aryl azides to stabilize cobalt(III)-imidos that showed spin crossover.³¹ In this work, the stoichiometric addition of a *tert*-butyl-

or phenyl-substituted azide to an ethereal solution of cobalt(I) complex **35** gave rise to three-coordinate cobalt(III)-imido complexes **37** (Scheme 4-13, A). In contrast, using mesityl azide resulted in the formation of a metallacycloindoline **38** (Scheme 4-13, B). ^1H NMR experiments using deuterated mesityl azide suggested that a cobalt(III)-imido forms upon the reaction of **35** with mesityl azide followed by H-atom abstraction from one of the methylene groups by the imido, which subsequently performs radical recombination between the cobalt metal center and a benzylic radical. These results suggested that both aryl and alkyl azides could be used to generate cobalt imido species capable of carrying out intramolecular C–H activation. Although these cobalt(III) imidos were isolable and well characterized by a number of spectroscopic techniques and X-ray crystallography, the authors did not report on their ability to perform C–H amination catalysis. In the midst of the results presented above, the reactivity of aryl azides by cobalt(II) complexes of non-heme ligand systems remains uninvestigated. Therefore, in order to promote inter- and intramolecular C–H amination, new ligand systems have to be explored. Work by Driver and Betley led us to think that first-row transition metal complexes could catalyze the C–H amination of aryl azides. Specifically, we were interested in using cobalt(II) complexes. Cobalt(II)-catalyzed C–H amination of aryl azides, to date, has been unexplored. More importantly, the use of non-heme redox-active ligands for catalytic C–H amination reactions remains an unexplored topic.



Scheme 4-13. Reactions of cobalt(I) dipyrromethene complex **35** with **A**) alkyl and **B**) aryl azides.³¹

Section 4-3. Results

Despite recent advances in this area, cobalt(II) catalysts that utilize redox-active ligands for intramolecular C–H amination reactions with aryl azides are presently unknown. Inspired by the ability of cobalt(II) complexes supported by the tridentate, trianionic NNN redox-active ligand, $[\text{N}(o\text{-PhNC(O)}^{i\text{Pr}})_2]^{3-}$ ($[\text{L}^{i\text{Pr}}]^{3-}$) to promote catalytic dioxygen activation (discussed in Chapter 3), C–H amination reactions using aryl azides were targeted. In collaboration with Blakey and co-workers at Emory University, the reactivity of the dinuclear complex, $(\text{Et}_4\text{N})_2[\text{Co}_2(\text{L}^{i\text{Pr}})_2]$ shown in Figure 4-6, with aryl azides was investigated. During the course of this study, all aryl azides were synthesized and fully characterized by Mrs. Nina Weldy, a graduate student in the Blakey laboratory.

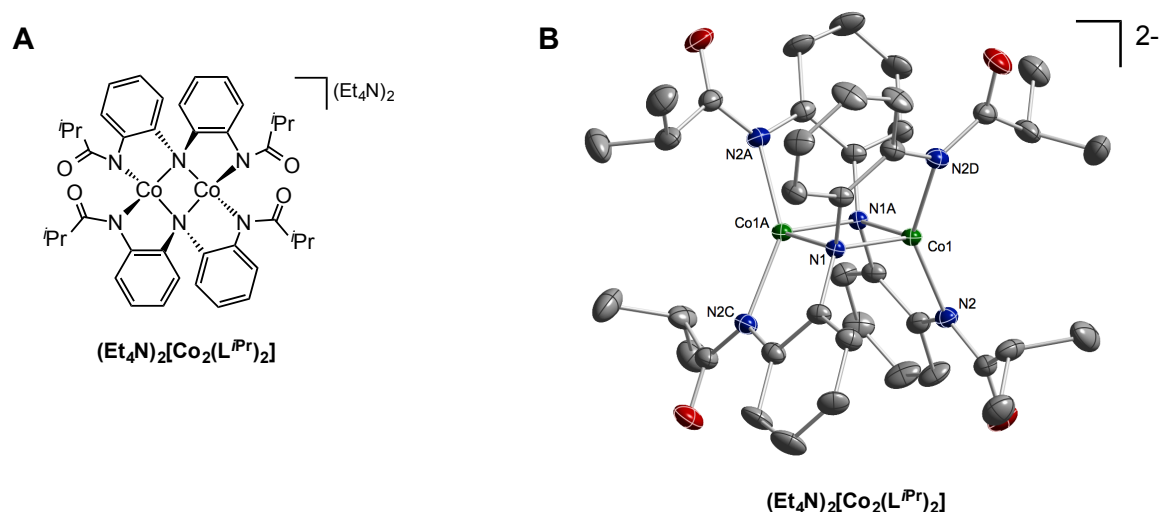


Figure 4-6. A) Dinuclear cobalt(II) complex, $(\text{Et}_4\text{N})_2[\text{Co}_2(\text{L}^{i\text{Pr}})_2]$, used in the investigation for C–H amination reactions with aryl azides and B) its solid-state X-ray structure.²⁷ⁱ

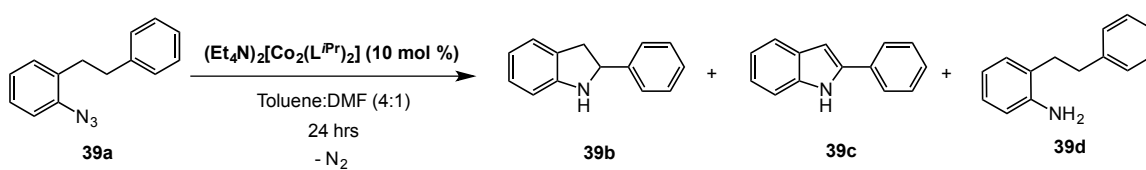
Section 4-3-1. Initial Investigations on the C–H Amination of an Aryl Azide by Dinuclear Cobalt(II) Complex $(\text{Et}_4\text{N})_2[\text{Co}_2(\text{L}^{\text{iPr}})_2]$

At the onset of this project, the ortho-homobenzyl- aryl azide **39a** was selected as a test substrate to explore the possibility of the cobalt(II)-catalyzed intramolecular amination of aryl azides and establish effective reaction conditions. Additionally, precedent work by Driver and co-workers showed the ability of iridium(I) to drive this reaction. Addition of aryl azide **39a** to a 4:1 mixture of toluene and dimethylformamide (DMF) solution of 10 mol % $(\text{Et}_4\text{N})_2[\text{Co}_2(\text{L}^{\text{iPr}})_2]$ at room temperature gave no reaction over the course of 24 hours, and the starting azide **39a** remained fully intact as determined by ^1H NMR analysis of the crude mixture (Table 4-1, entry 1). Typically these types of reactions are carried out in highly nonpolar organic solvents (e.g. toluene, benzene, or trifluorotoluene); however, DMF was used in these reactions to solubilize the dianionic $[\text{Co}_2(\text{L}^{\text{iPr}})_2]^{2-}$ complex.

Our next attempt to perform the intramolecular C–H amination of aryl azide **39a** with cobalt(II) complex $(\text{Et}_4\text{N})_2[\text{Co}_2(\text{L}^{\text{iPr}})_2]$ led us to perform reactions at elevated temperatures. Heating the reaction mixture to 110 °C for 24 hours resulted in the formation of indoline **39b**, indole **39c**, and aniline **39d** in 26 : 8 : 55 ratio, respectively, without full consumption of the starting azide **39a** as determined by ^1H NMR analysis (Table 4-1, entry 2). We were pleased to observe these initial C–H amination results shown in Scheme 4-14; however, the predominant formation of aniline **39d** was highly disparaging. In an attempt to suppress aniline formation, the reaction was performed in the presence of 4Å molecular sieves (MS) to remove adventitious water from the reaction. This was to prevent any residual water in the

solvents to initiate aniline formation. Remarkably, doing this produced indoline **39b** as the only product in 73 % yield (Table 4-1, entry 3), according to ¹H NMR analysis.

Table 4-1. Initial reaction conditions of cobalt(II) complex, $(\text{Et}_4\text{N})_2[\text{Co}_2(\text{L}^{\text{iPr}})_2]$, with aryl azide **39a**.



Entry	Temperature	Molecular Sieves	NMR Ratios ^a 39a : 39b : 39c : 39d	indoline 39b yield, % ^b
1	25 °C	—	100 : 0 : 0 : 0	—
2	110 °C	—	(11 : 26 : 8 : 55)	—
3	110 °C	4Å	27 : 73 : 0 : 0	73

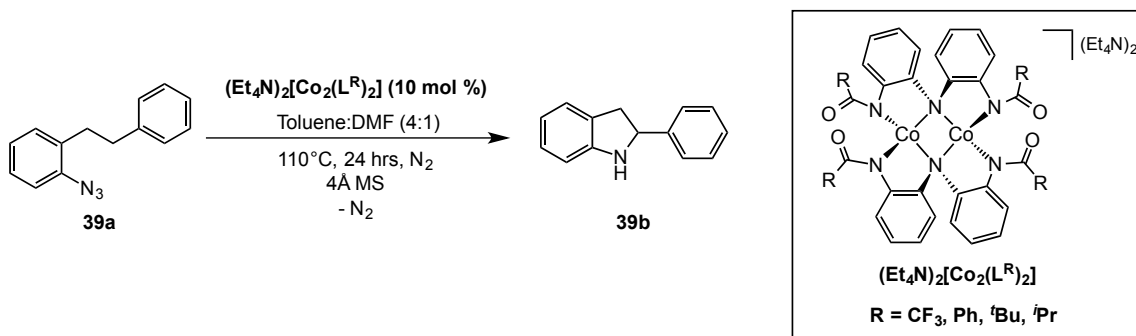
^a As determined from integration of peaks from crude ¹H NMR.

^b As determined by ¹H NMR using 1,3,5-trimethoxybenzene as an internal standard.

Section 4-3-2. C–H Amination of An Aryl Azide Using Dinuclear Cobalt(II) Complexes With Varying Acyl Substituents

One of the key advantages in utilizing the tridentate, trianionic NNN redox-active ligand, $[N(o\text{-PhNC(O)}^{i\text{Pr}})_2]^{3-}$ ($[L^{i\text{Pr}}]^{3-}$), lies in its highly modular nature. To take advantage of the modularity of the ligand, dinuclear cobalt(II) complexes with varying acyl substituents on the carboxamide arms of the ligand ($R = \text{CF}_3, \text{Ph}, \text{tBu}$), discussed in Chapter 2, were evaluated for their catalytic activity for intramolecular C–H amination using aryl azide **39a** (Table 4-2). Using trifluoro-acyl substituted cobalt(II) complex $(\text{Et}_4\text{N})_2[\text{Co}_2(\text{L}^{\text{CF}_3})_2]$ resulted in only trace amount of indoline **39b** (Table 4-2, entry 1). Conversely, phenyl- and *tert*-butyl-substituted cobalt(II) complexes, $(\text{Et}_4\text{N})_2[\text{Co}_2(\text{L}^{\text{Ph}})_2]$ and $(\text{Et}_4\text{N})_2[\text{Co}_2(\text{L}^{\text{tBu}})_2]$, furnished indoline yields of 10 % (Table 4-2, entry 2) and 20 % (Table 4-2, entry 3), respectively.

Table 4-2. Performance of cobalt(II) dinuclear complexes bearing redox-active ligands with varying acyl substituents for intramolecular C–H amination of aryl azide **39a**.



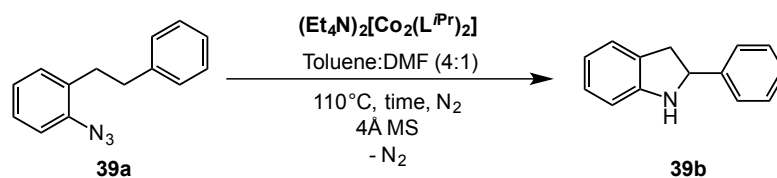
Entry	[Catalyst]	indoline yield, % ^a
1	$(\text{Et}_4\text{N})_2[\text{Co}_2(\text{L}^{\text{CF}_3})_2]$	traces
2	$(\text{Et}_4\text{N})_2[\text{Co}_2(\text{L}^{\text{Ph}})_2]$	10
3	$(\text{Et}_4\text{N})_2[\text{Co}_2(\text{L}^{\text{tBu}})_2]$	20
4	$(\text{Et}_4\text{N})_2[\text{Co}_2(\text{L}^{\text{iPr}})_2]$	73

^a As determined by ^1H NMR using 1,3,5-trimethoxybenzene as an internal standard.

Section 4-3-3. Optimization of Cobalt(II)-Catalyzed C–H amination Reaction

With the observation that $(\text{Et}_4\text{N})_2[\text{Co}_2(\text{L}^{\text{iPr}})_2]$ was the best catalyst for the intramolecular C–H amination of aryl azide **39a**, attempts to optimize the reaction under lower catalyst loadings of $(\text{Et}_4\text{N})_2[\text{Co}_2(\text{L}^{\text{iPr}})_2]$ and different reaction times were examined (Table 4-3). Shorter reaction time (15 hours) only afforded 44 % of indoline **39b** (Table 4-3, entry 1). Increasing the reaction time to 24 hours increased the yield of indoline **39b** to 73 % (Table 4-3, entry 2). Lower catalyst loadings (1 mol%) resulted in the formation of 11 % of indoline **39b** over the course of 24 hours (Table 4-3, entry 3). Remarkably, the yield increased to 83 % over the course of 48 hours (Table 4-3, entry 4). These observations indicated to us that the catalyst $(\text{Et}_4\text{N})_2[\text{Co}_2(\text{L}^{\text{iPr}})_2]$ has an induction period. With these results at hand, we explored whether the formation of indoline **39b** from aryl azide **39a** was a thermally induced process, a commonly observed behavior of aryl azides.³² Under optimized conditions, no reaction was observed in the absence of $(\text{Et}_4\text{N})_2[\text{Co}_2(\text{L}^{\text{iPr}})_2]$ (Table 4-3, entry 5). Additionally, it was observed that using cobalt(II) bromide salt as the catalyst resulted in no product formation (Table 4-3, entry 6).

Table 4-3. Optimization for the conversion of aryl azide **39a** to indoline **39b** catalyzed by $(\text{Et}_4\text{N})_2[\text{Co}_2(\text{L}^{\text{iPr}})_2]$.



Entry	[Catalyst]	mol%	Time (h)	indoline yield, % ^a
1	$(\text{Et}_4\text{N})_2[\text{Co}_2(\text{L}^{\text{iPr}})_2]$	10	15	44
2	$(\text{Et}_4\text{N})_2[\text{Co}_2(\text{L}^{\text{iPr}})_2]$	10	24	73
3	$(\text{Et}_4\text{N})_2[\text{Co}_2(\text{L}^{\text{iPr}})_2]$	1	24	11
4	$(\text{Et}_4\text{N})_2[\text{Co}_2(\text{L}^{\text{iPr}})_2]$	1	48	83
5	—	—	48	0
6	CoBr_2	1	48	0

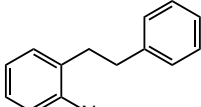
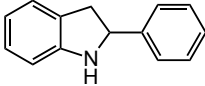
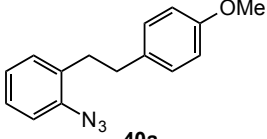
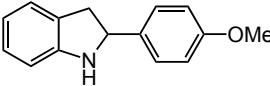
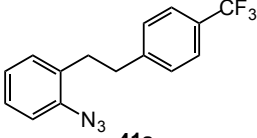
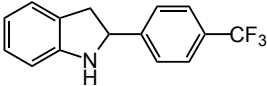
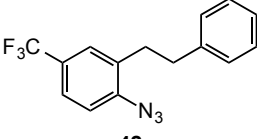
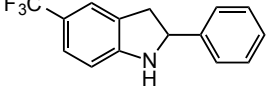
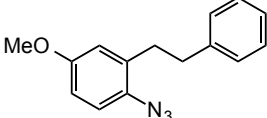
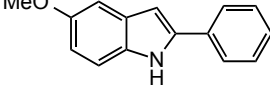
^a As determined by ^1H NMR using 1,3,5-trimethoxybenzene as an internal standard.

Section 4-3-4. Substrate Scope and Limitations.

After determining the optimal reaction conditions to achieve C–H amination, the substrate scope and limitations of this reaction were explored. We initiated these efforts by investigating the electronic effect on the reaction yield by substituting the parent azide **39a** at positions R¹ and R² with an electron-donating group, OMe, and an electron-withdrawing group, CF₃ (Table 4-4). Changing the electronic identity of the homobenzylic aryl group at position R² with an electron-donating group using azide **40a** (Table 4-4, entry 2) and an electron-withdrawing group using azide **41a** (Table 4-4, entry 3) gave comparable yields of the corresponding indolines **40b** and **41b** of 81 % and 83 %, respectively. Placing the electron-withdrawing group CF₃ using azide **42a**, gave slightly lower yield (72 %) of the corresponding indoline **42b** (Table 4-4, entry 4). Moreover, electron-rich aryl azide **43a** yielded 60 % of indole **43b** (Table 4-4, entry 5) and 30 % of starting azide **43a** was recovered from the reaction. ¹H NMR analysis of the crude reaction mixture, revealed a 1:2 ratio of indole to indoline; however, oxidation of the indoline occurred upon purification over SiO₂.

Table 4-4. Electronic effect on the cobalt(II)-catalyzed benzylic C–H bond amination of aryl azides.

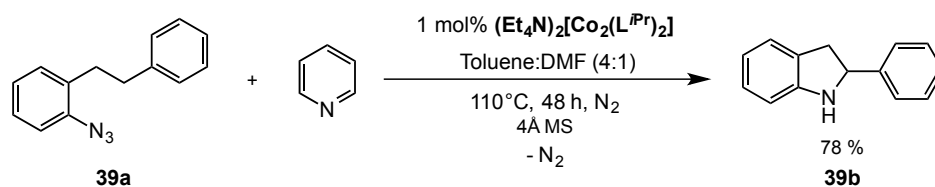
1 mol% $(\text{Et}_4\text{N})_2[\text{Co}_2(\text{L}^{\text{Pr}})_2]$
Toluene:DMF (4:1)
110°C, 48 h, N_2
4Å MS
- N_2

Entry	Substrate	Product	yield, % ^a
1	 39a	 39b	80
2	 40a	 40b	81
3	 41a	 41b	83
4	 42a	 42b	72
5	 43a	 43b	60 ^b

^a Isolated yield after chromatography over SiO_2

^bYield is that of isolated indole after indoline fully oxidizes to indole over SiO_2

In order to explore the ability of the cobalt(II) catalyst, $(\text{Et}_4\text{N})_2[\text{Co}_2(\text{L}^{\text{iPr}})_2]$, to carry out the C–H amination reaction in the presence of an exogenous coordinating ligand, the reaction was performed in the presence of pyridine. Azide **39a** was reacted with 1 mol% of $(\text{Et}_4\text{N})_2[\text{Co}_2(\text{L}^{\text{iPr}})_2]$ in the presence of an equivalent amount of pyridine (Scheme 4-14). Indoline **39b** was obtained in 78 % yield from this reaction.



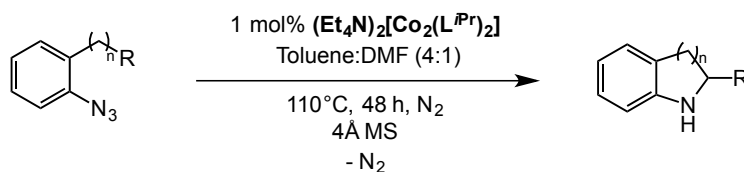
Scheme 4-14. C–H amination reaction in the presence of pyridine using azide **39a**.

Encouraged by these results, we explored additional substrates to better understand the scope of this reaction. Heteroaromatic-containing azides **44a** and **45a** substrates were investigated. Reaction of aryl azide **44a** with 1 mol% $(\text{Et}_4\text{N})_2[\text{Co}_2(\text{L}^{\text{iPr}})_2]$ resulted in the formation of the corresponding indoline **44b** in 80 % yield (Table 4-5, entry 1). Azide **45a** was used to investigate the amination alpha to a protected indole. Reaction of aryl azide **45a** with 1 mol% $(\text{Et}_4\text{N})_2[\text{Co}_2(\text{L}^{\text{iPr}})_2]$ resulted in the formation of the corresponding indoline **45b** in 85 % yield (Table 4-5, entry 2). Extension of the alkyl linker by one carbon atom using azide **46a**, demonstrated that the reaction is selective for benzylic insertion, forming only the six-membered ring. Reaction of aryl azide **46a** with $(\text{Et}_4\text{N})_2[\text{Co}_2(\text{L}^{\text{iPr}})_2]$ resulted in the formation of the corresponding tetrahydroquinoline **46b** in 70 % yield (Table 4-5, entry 3).

Azide **47a** was targeted to test the ability of this system to aminate tertiary positions. Unfortunately, reaction of aryl azide **47a** with $(\text{Et}_4\text{N})_2[\text{Co}_2(\text{L}^{\text{iPr}})_2]$ did not result in the

formation of the corresponding indoline **47b** (Table 4-5, entry 4). Under standard reaction conditions, ^1H NMR spectroscopy showed starting material aryl azide **47a** as the only product. Indoline **47b** was not observed. Starting material, azide **47a**, was recovered in 90 % yield. This result, however, led us to investigate tertiary insertion by synthesizing azide **48a**, in which the alkyl linker is extended by one carbon atom. Reaction of aryl azide **48a** with 1 mol% $(\text{Et}_4\text{N})_2[\text{Co}_2(\text{L}^{\text{Pr}})_2]$ resulted in the formation of the corresponding six-membered N-heterocycle **48b**, whereby tertiary insertion was successfully attained, in 85 % yield (Table 4-5, entry 5). Extending the alkyl chain of azide **46a**, by utilizing azide **49a**, the seven-membered tetrahydrobenzoazepine **49b** is formed in 30 % (Table 4-5, entry 6). Though this yield is moderate, this result illustrates the ability of $(\text{Et}_4\text{N})_2[\text{Co}_2(\text{L}^{\text{Pr}})_2]$ to form seven-membered azepines from aryl azides.

Table 4-5. Substrate scope on the cobalt(II)-catalyzed benzylic C–H bond amination of aryl azides to form N-heterocycles.



Entry	Aryl Azide	N-heterocycle	yield, % ^a
1			80
2			85
3			70
4			0 ^b
5			85
6			30 ^c

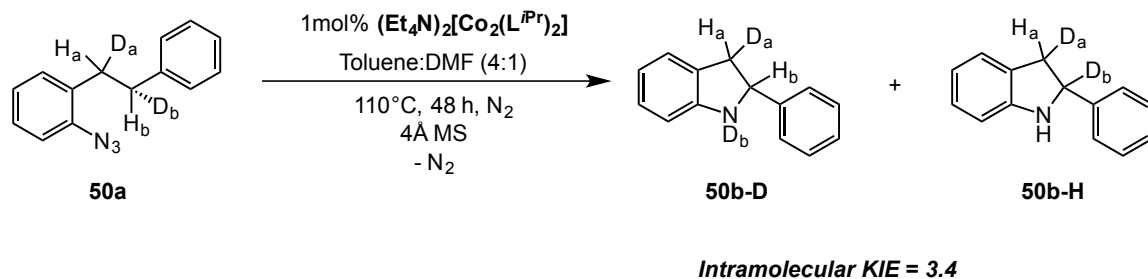
^a Isolated yield after chromatography over SiO₂

^b 90 % of starting aryl azide **9a** was recovered from the reaction mixture.

^c 5 mol % catalyst loading.

Section 4-3-5. Kinetic Isotope Effect Study

In order to probe the reaction mechanism pathway, the kinetic isotope effect (KIE) of the C–H amination reaction was measured. Azide **49a**, in which one of two benzylic H-atoms is replaced with a deuterium atom, was synthesized for this purpose.³³ When azide **49a** was subjected to standard catalytic conditions with $(\text{Et}_4\text{N})_2[\text{Co}_2(\text{L}^{\text{iPr}})_2]$, a mixture of indolines **49b-D** and **49b-H** were generated as a result from C–H and C–D amination, respectively. ^1H NMR analysis of the product mixture provided an intramolecular KIE of 3.4 (Scheme 4-15). Zhang and co-workers report slightly higher isotope effects (KIE = 6.2) for cobalt(II)-based metalloradical C–H amination of sulfonyl azides that undergo through a H-atom abstraction, radical recombination mechanism.³⁴ Similarly, Driver and co-workers report KIE values of 5.06 and 6.02 for iridium(I)-³⁰ and rhodium(II)-catalyzed³³ C–H amination of benzylic C–H bonds, respectively, for the same type of mechanism. The magnitude of the KIE exhibited in the C–H amination carried out by $(\text{Et}_4\text{N})_2[\text{Co}_2(\text{L}^{\text{iPr}})_2]$ is much higher than that of Rh_2 -catalyzed intramolecular amination of benzylic C–H bonds that operate through a concerted C–H insertion mechanism reported by Du Bois and co-workers (KIE = 1.9).^{11b} These observations indicate that the C–H amination carried out by $(\text{Et}_4\text{N})_2[\text{Co}_2(\text{L}^{\text{iPr}})_2]$ is in agreement with a H-atom abstraction/radical recombination mechanism.



Scheme 4-15. Intramolecular KIE for the C–H amination of benzylic C–H bonds of aryl azide **50a** carried out by $(\text{Et}_4\text{N})_2[\text{Co}_2(\text{L}^{\text{iPr}})_2]$.

Section 4-4. Discussion

This work demonstrates the dinuclear cobalt(II) complex $(\text{Et}_4\text{N})_2[\text{Co}_2(\text{L}^{\text{iPr}})_2]$ to be an effective and selective catalyst for C–H amination reactions to selectively form indolines from aryl azides. Indolines are an important class of molecules ubiquitous in nature. Their presence in many natural products and pharmaceutical materials make the discovery of new routes for the synthesis of indolines highly attractive.³⁵

We use the modularity of the tridentate, trianionic NNN redox-active ligand, $[\text{N}(o\text{-PhNC}(\text{O})^{\text{R}})_2]^{3-}$ ($[\text{L}^{\text{R}}]^{3-}$, $\text{R} = \text{iPr, Bu, Ph, and CF}_3$), and examine the C–H amination profiles of dinuclear cobalt(II) complexes of these ligands, $(\text{Et}_4\text{N})_2[\text{Co}_2(\text{L}^{\text{R}})_2]$ where $\text{R} = \text{iPr, Bu, Ph, and CF}_3$. The results obtained from these studies show that the isopropyl-substituted cobalt(II) complex $(\text{Et}_4\text{N})_2[\text{Co}_2(\text{L}^{\text{iPr}})_2]$, furnished the highest indoline formation out of these complexes. On the basis of these results, it is inferred that both steric and electronic factors play a key role in the C–H amination reaction pathway carried out by this type of cobalt(II) catalyst system with aryl azide **39a**. The fact that no

indoline formation was observed (nor decomposition of the aryl azide **39a**) with trifluoromethyl-substituted complex $(\text{Et}_4\text{N})_2[\text{Co}_2(\text{L}^{\text{CF}_3})_2]$, implies that electron withdrawing substituents on the ligand essentially shut down reactivity towards azides.

Initial reaction optimizations indicated that optimal reactions conditions consisted of high temperatures (110 °C), the use of 4Å molecular sieves to remove any traces of water from the solvents, and using 1 mol % of cobalt(II) catalyst, $(\text{Et}_4\text{N})_2[\text{Co}_2(\text{L}^{\text{iPr}})_2]$ over the course of 24 hours. Water in these reactions promotes aniline formation, which leads to deactivation of the catalyst due to possible aniline coordination. Several examples, including those by Driver and co-workers, have shown that aniline formation during a catalytic reaction can deactivate catalysts.³⁰ A control reaction with CoBr_2 as the catalyst without the formation of indoline product, indicates that cobalt salts alone do not carry out this reaction.

The results in Table 4-3 reveal that the amination is not sensitive to the electronic nature of the aryl azide. These results are in contrast with the observations of Driver and co-workers with these substrates.³⁰ Driver observed that placing electron-poor CF_3 -substituted azide **42a** group *para* to the azide resulted in the highest yield of indoline product while electron-donating substituents on the aromatic ring at the azide gave no products (azide **43a**). These results place an emphasis on the versatility of cobalt(II) complex, $(\text{Et}_4\text{N})_2[\text{Co}_2(\text{L}^{\text{iPr}})_2]$, to perform C–H amination reactions with electron-rich aryl azides. It also suggests that an electron-rich cobalt center is necessary to generate a highly reactive nitrene intermediate capable of performing the C–H amination.

Remarkably, exogenous coordinating ligands do not outcompete azide binding. This is observed when the formation of indoline **39b** was obtained in good yield (78%) in

the presence of pyridine. Pyridine coordination has been shown promote catalyst deactivation in C–H amination reactions by outcompeting azide binding to the metal catalyst.^{27o, 29-30} These results led us to carry out the C–H amination of azide **44a**, containing a pyridine moiety. More importantly, these results suggest that the C–H amination is tolerant to pyridine functionalities, a privileged capability for targets of pharmaceutical interest.³⁶

Notable, the intramolecular C–H amination reaction is applicable to benzylic positions alpha to activated indoles. This demonstrates the reaction to be tolerant of oxidation-sensitive substrates. Remarkably, extending the alkyl linker by one carbon using azide **46a** results in the selective formation of tetrahydroquinoline **46b**. Tetrahydroquinolines are prevalent in pharmaceutical compounds and in the structural fragments of many alkaloids.³⁷ Considerable efforts have been made in the past decade to find alternative paths to synthesize functionalized tetrahydroquinolines by efficient and sustainable routes. Tetrahydroquinoline **46b** was recently reported by Che and co-workers directly from **46a**, however, this work consisted of using an iron(III)-porphyrin system to carry out this reaction.³⁸ To the best of our knowledge the results presented herein represent the first example for the synthesis of a tetrahydroquinoline by a non-heme system using an aryl azide as the nitrogen source.

The intramolecular C–H amination is not limited to only benzylic and alpha to aromatic C–H insertions. Azide **47a** as a test substrate does not afford indoline **47b** or an indole. This result parallels those seen by Driver and co-workers, whereby $[\text{Ir}(\text{cod})(\text{OMe})_2]$ was not able to carry out a reaction with azide **47a** to afford product formation.³⁰ ¹H NMR analysis of the crude mixture showed only starting azide **47a**,

which was recovered in 90 % yield from the reaction mixture. Azide **48a** was used as a second test substrate to insert into a tertiary C–H bond by extension of the alky chain. This led us to isolate the tertiary C–H insertion product **48b**.

The insertion into tertiary C–H position with azide **48a** and not with **47a** indicate that azide **47a** is possibly facing a highly sterically hindered interaction with the active cobalt catalyst, which is preventing product formation, as evidenced by the recovery of only 90 % of starting material. This thought motivated us to perform a stoichiometric reaction with $(\text{Et}_4\text{N})_2[\text{Co}_2(\text{L}^{\text{iPr}})_2]$ and azide **47a**. Addition of two equivalents of azide **47a** to a solution of $(\text{Et}_4\text{N})_2[\text{Co}_2(\text{L}^{\text{iPr}})_2]$ under standard reaction conditions resulted in the formation of a deep teal-green species with an electronic absorption band at $\lambda_{\text{max}} = 773$ nm (Figure 4-7). Solid-state FT-IR analysis reveals the absence of an azide (ν_{N_3}) stretch, suggesting that $(\text{Et}_4\text{N})_2[\text{Co}_2(\text{L}^{\text{iPr}})_2]$ consumes azide **47a**. More importantly, this species gives rise to new paramagnetically-shifted ^1H NMR peaks with low symmetry indication, compared to the spectra of $(\text{Et}_4\text{N})_2[\text{Co}_2(\text{L}^{\text{iPr}})_2]$. This indicates that the dimeric species $(\text{Et}_4\text{N})_2[\text{Co}_2(\text{L}^{\text{iPr}})_2]$ undergoes a significant structural transformation upon addition of azide **47a**, whereby a new organic fragment from azide **47a** is now coordinated to the paramagnetic cobalt metal center. Further evidence was obtained when this deep teal-green species is subjected to electrospray ionization mass spectrometry (ESI-MS). The negative mode ESI-mass spectrum exhibits a parent peak with m/z ratio of 605.23, which is consistent with the formulation of $[\text{Co}(\text{L}^{\text{iPr}})(\text{NHR})]^-$ (where R = the organic fragment of azide **47a** without N_2) (Figure 4-8). These results collectively suggest that the deep teal-green species could possibly be a cobalt-amido species resulting from the conversion of a cobalt-imido species by the formal transfer of a H-atom. Similar results have been

demonstrated with iron(II) complexes by Borovik and co-workers, whereby iron(III)-amido complexes were formed and isolated from high valent species by H-atom abstraction from an external species.³⁹

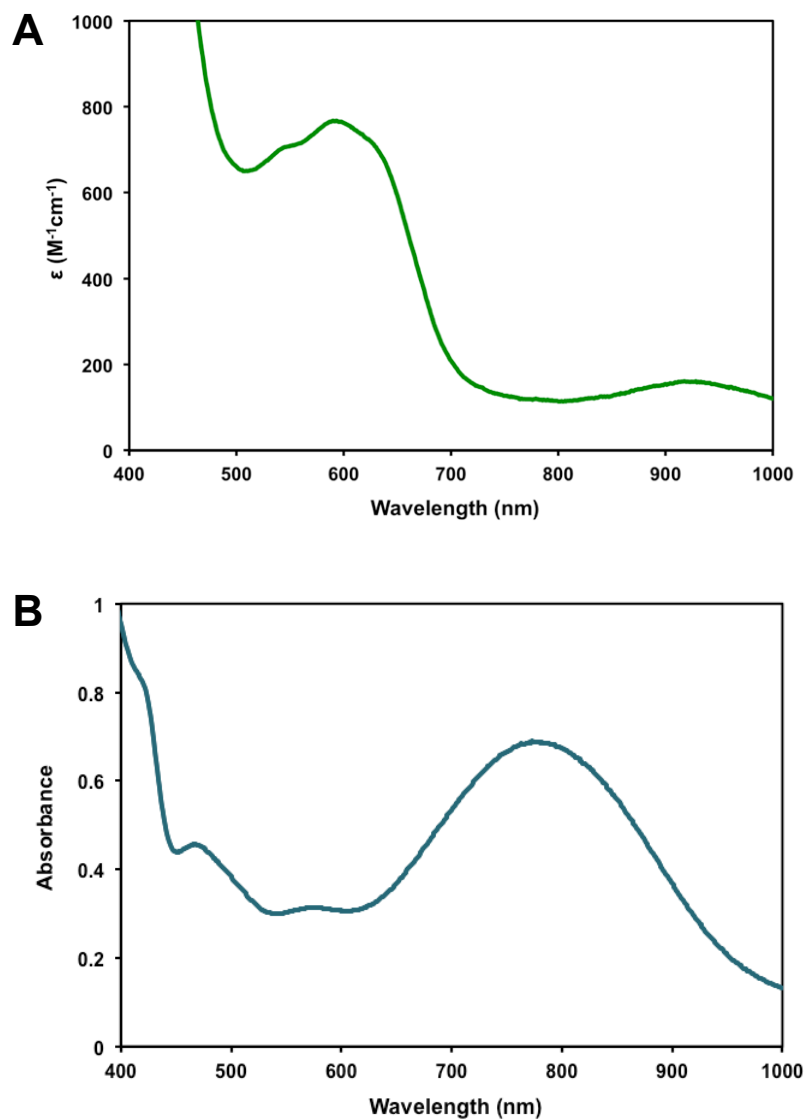


Figure 4-7. UV-visible absorption spectrum of **A)** $(\text{Et}_4\text{N})_2[\text{Co}_2(\text{L}^{\text{iPr}})_2]$ ($\lambda_{\text{max}} = 596 \text{ nm}$) and **B)** product formed from the reaction of $(\text{Et}_4\text{N})_2[\text{Co}_2(\text{L}^{\text{iPr}})_2]$ with 2.0 equivalents of azide **47a** ($\lambda_{\text{max}} = 773 \text{ nm}$). Both spectra recorded in CH_3CN at 25°C .

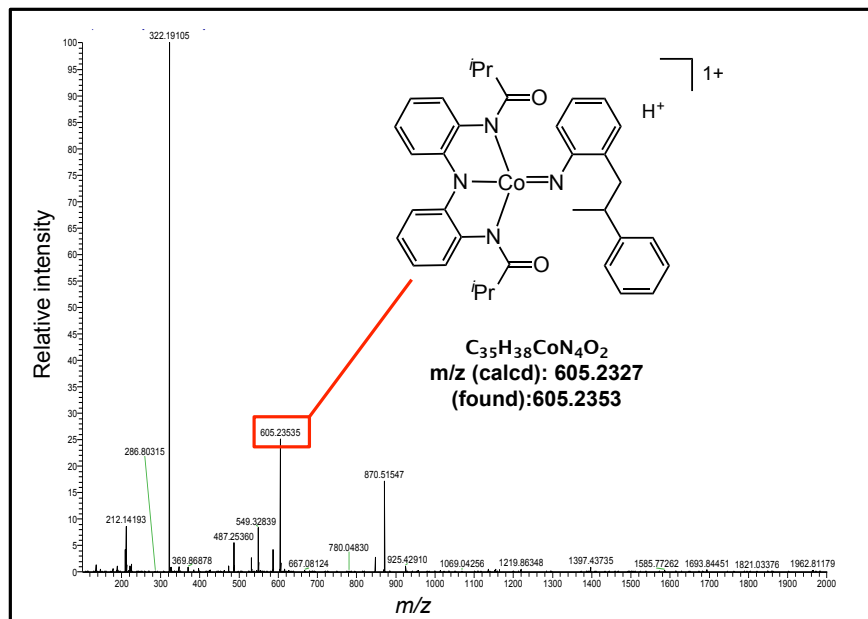


Figure 4-8. ESI-MS (positive mode) spectrum of the product formed from the reaction of $(Et_4N)_2[Co_2(L^{iPr})_2]$ with 2.0 equivalents of azide **47a**.

Recrystallization by vapor diffusion of diethyl ether into a concentrated methyl-tetrahydrofuran (Me-THF) solution of this species produces small, dark teal-green crystals. The crystals obtained, however are of poor quality to obtain diffraction data. Efforts to structurally and spectroscopically characterize this species through single-crystal X-ray crystallography and electron paramagnetic resonance (EPR) spectroscopy are currently underway in the MacBeth laboratory. The results obtained from those studies could be of indispensable importance in addressing the nature of a potential reactive intermediate and gain structural insight into the mechanism of our cobalt(II)-catalyzed C–H amination reaction using aryl azides.

While performing reactions in which aniline was being observed as a major product, an unusual side product was observed. This product was identified by ^1H NMR spectroscopy, mass spectrometry, and X-ray crystallography to be a modified ligand from our cobalt catalyst. X-ray quality crystals of this product were obtained by diffusing hexanes into a toluene solution of the product. The solid-state structure of this product was obtained by X-ray diffraction studies and the results are shown in Figure 4-9. This product, L^{Cyc} , corresponds to a cyclized ligand, whereby the carbon from one carboxamide arm is now connected to the amido nitrogen of the ligand, forming a five-membered imine ring. While these types of amine condensations to form five-membered imines are not uncommon, we speculate that in the presence of water, aniline formation initiates this acid-catalyzed process. These results have provided us with important information about potential ligand decomposition pathways.

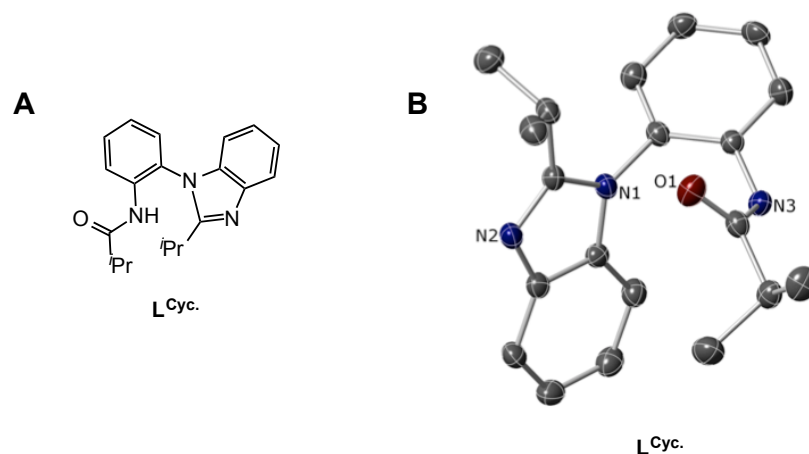


Figure 4-9. A) Cyclized ligand L^{Cyc} and B) its solid-state X-ray structure (thermal ellipsoids drawn at 40 % probability. Hydrogen atoms omitted for clarity).

Section 4-5. Conclusion

In conclusion, this study supports the use of redox-active ligands for the development of efficient cobalt(II) catalysts for C–H amination. The tridentate, trianionic NNN redox-active ligand, $[N(o\text{-PhNC(O)}^{iPr})_2]^{3-}$ demonstrates to be an excellent scaffold for this type of reactivity. This constitutes a major landmark in the field of C–H amination considering all major advances that have been made over the past decade. Future studies in our laboratory will explore the substrate scope of these reactions with aims to carry out intermolecular C–H bond amination with this ligand system.

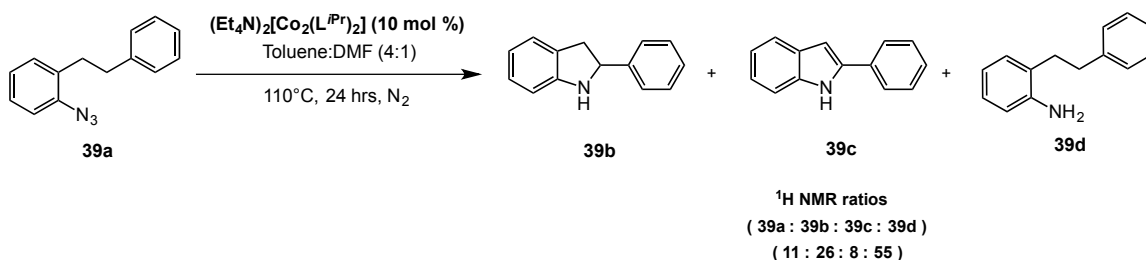
Section 4-6. Experimental Section

Section 4-6-1. General Considerations and Materials

All manipulations were carried out using standard Schlenk techniques or conducted in an MBraun Labmaster 130 drybox under a nitrogen atmosphere. All reagents used were purchased from commercial vendors and used as received unless otherwise noted. Anhydrous solvents were purchased from Sigma-Aldrich and further purified by sparging with Ar gas followed by passage through activated alumina columns. Additionally, anhydrous solvents were stored inside an inert atmosphere dry box under freshly activated 4Å molecular sieves. ^1H and ^{13}C NMR spectra were recorded on a VNMR 400 MHz or Inova 400 MHz spectrometers at ambient temperature. ^1H and ^{13}C chemical shifts were referenced to residual solvent peaks. Solid-state Infrared spectra were recorded as KBr pellets on a Varian Scimitar 800 Series FT-IR spectrophotometer. UV-Visible absorption spectra were recorded on a Cary50 spectrophotometer using 1.0 cm quartz cuvettes. Mass spectra were recorded in the Mass Spectrometry Center at Emory University on a JEOL JMS-SX102/SX102A/E mass spectrometer. X-ray diffraction studies were carried out in the X-ray Crystallography Laboratory at Emory University on a Bruker Smart 1000 CCD diffractometer. Mrs. Nina Weldy, a graduate student in the Blakey laboratory at Emory University carried out the syntheses for all aryl azides according to their respective literature procedures (cited within the experimental). The synthesis of $(\text{Et}_4\text{N})_2[\text{Co}_2(\text{L}^{\text{iPr}})_2]$ was carried out according to its literature procedure.²⁷ⁱ Syntheses of $(\text{Et}_4\text{N})_2[\text{Co}_2(\text{L}^{\text{CF}_3})_2]$, $(\text{Et}_4\text{N})_2[\text{Co}_2(\text{L}^{\text{tBu}})_2]$, and $(\text{Et}_4\text{N})_2[\text{Co}_2(\text{L}^{\text{Ph}})_2]$ were carried out according to procedures outlined in Chapter 2.

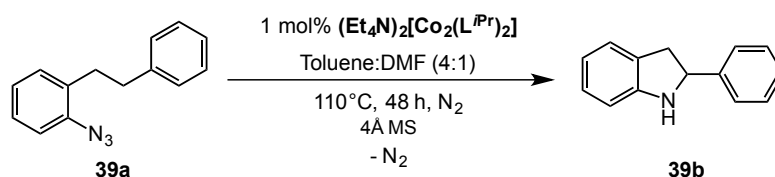
Section 4-6-2. General Procedures

I. Initial procedure for cobalt(II)-catalyzed Azide Decomposition.

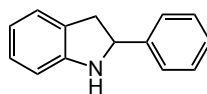


Inside a nitrogen-filled atmosphere dry box, a 20 mL scintillation vial was charged with a magnetic stir bar, 0.100 g of aryl azide **39a** (0.448 mmol), 0.047 g of $(\text{Et}_4\text{N})_2[\text{Co}_2(\text{L}^{\text{iPr}})_2]$ (10 mol%), and 5.0 mL of a 4:1 mixture of toluene and DMF, respectively. The reaction vial was sealed with a Teflon cap and the reaction mixture was stirred while heated at 110°C for 24 hours inside the dry box on a DynaBloc heating block. After 24 hours, the reaction vial was removed from the heating block and was allowed to stir at room temperature for 30 minutes. After reaction mixture cooled to room temperature, the solvent was removed under vacuum. The resulting oil was stirred in 5.0 mL of hexanes. The heterogeneous mixture was filtered through Celite and filtrate was concentrated *in vacuo* and the resulting solid (oil) was analyzed for ^1H NMR. The spectral data match the literature.³⁰

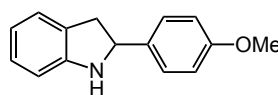
II. Optimized General Procedure for Synthesis of Indolines from Aryl Azides



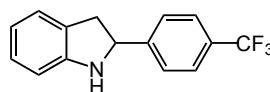
Inside a nitrogen-filled atmosphere dry box, a 20 mL scintillation vial was charged with a magnetic stir bar, 0.150 g of aryl azide **39a** (0.672 mmol), 0.0071 g of $(\text{Et}_4\text{N})_2[\text{Co}_2(\text{L}^{\text{iPr}})_2]$ (1 mol%), and 5.0 mL of a 4:1 mixture of toluene and DMF, respectively. To the reaction mixture was added freshly activated 4 Å molecular sieves and capped with a Teflon cap. The reaction vial was sealed with a Teflon cap and the reaction mixture was stirred while heated at 110 °C for 24 hours inside the dry box on a DynaBloc heating block. After 24 hours, the reaction vial was removed from the heating block and was allowed to stir at room temperature for 30 minutes. After reaction mixture cooled to room temperature, the molecular sieves were removed by filtration and the solvent was removed under vacuum. The filtrate was concentrated *in vacuo* and the resulting solid (oil) was analyzed for ^1H NMR. Indoline product **39b** was purified by column chromatography (SiO_2 , 1:7 EtOac:Hexanes) for which the yield is reported (0.105 g, 80 % yield). The spectral data match the literature.³⁰

**39b**

Indoline 39b.³⁰ ¹H NMR (400 MHz; CDCl₃): δ (ppm) 7.44 - 7.28 (m, 5H), 7.12 - 7.04 (m, 2H), 6.76 (td, J = 7.4 Hz, 1.0, 1H), 6.69 (d, J = 7.3 Hz, 1H), 4.97 (t, J = 9.0 Hz, 1H), 4.17 (s, 1H), 3.47 (dd, J = 15.7 Hz, 9.2 Hz, 1H), 3.00 (dd, J = 15.7 Hz, 8.8 Hz, 1H)

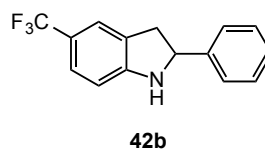
**40b**

Indoline 40b.³⁰ The general optimized procedure was followed with 0.1750 g of azide **40a** (0.6908 mmol) and 0.0073 g of (Et₄N)₂[Co₂(L^{iPr})₂] (0.0069 mmol) in 5.0 mL of a 4:1 mixture of toluene and DMF, respectively. Indoline **40b** was purified by column chromatography (SiO₂, 1:7 EtOAc:Hexanes) for which the yield is reported (0.1264 g, 81 % yield). The spectral data match the literature. ¹H NMR (400 MHz; CDCl₃): δ (ppm) 7.35 (d, J = 8.4 Hz, 2H), 7.11 - 7.06 (m, 2H), 6.88 (d, J = 8.0 Hz, 2H), 6.76 - 6.73 (m, 1H), 6.67 (d, J = 8 Hz, 1H) 4.91 (t, J = 9.0 Hz, 1H), 4.11 (s, 1H), 3.81 (s, 3H), 3.41 (dd, J = 16.8 Hz, 6.4 Hz, 1H), 2.97 (dd, J = 17.6 Hz, 6.8, 1H).

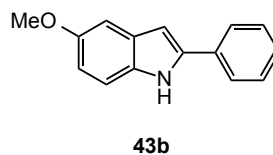
**41b**

Indoline 41b.³⁰ The general optimized procedure was followed with 0.150 g of azide **41a** (0.515 mmol) and 0.005 g of (Et₄N)₂[Co₂(L^{iPr})₂] (0.005 mmol) in 5.0 mL of a 4:1 mixture of toluene and DMF, respectively. Indoline **41b** was purified by column chromatography

(SiO₂, 1:7 EtOac:Hexanes) for which the yield is reported (0.113 g, 83 % yield). The spectral data match the literature. ¹H NMR (400 MHz; CDCl₃): δ (ppm) 7.63 - 7.50 (m, 4H), 7.08 (m, 2H), 6.74 (tdd, J = 7.4 Hz, 3.6 Hz, 1.1 Hz, 1H), 6.69 (d, J = 7.6 Hz, 1H), 5.01 (t, J = 9.3 Hz, 1H), 4.16 (s, 1H), 3.47 (dd, J = 15.6 Hz, 9.1 Hz, 1H), 2.93 (dd, J = 15.6 Hz, 9.1 Hz, 1H).

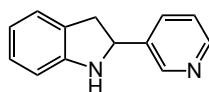


Indoline 42b.³⁰ The general optimized procedure was followed with 0.170 g of azide **42a** (0.5836 mmol) and 0.0061 g of (Et₄N)₂[Co₂(L^{iPr})₂] (0.0058 mmol) in 5.0 mL of a 4:1 mixture of toluene and DMF, respectively. Indoline **42b** was purified by column chromatography (SiO₂, 1:7 EtOac:Hexanes) for which the yield is reported (0.110 g, 72 % yield). The spectral data match the literature. ¹H NMR (400 MHz; CDCl₃): δ (ppm) 7.50 - 7.59 (m, 7H), 6.69 (d, J = 8.0 Hz, 1H), 5.04 (t, J = 9.0 Hz, 1H), 4.40 (s, 1H), 3.50 (dd, J = 15.6 Hz, 9.4 Hz, 1H), 3.00 (dd, J = 15.8 Hz, 8.4 Hz, 1H).

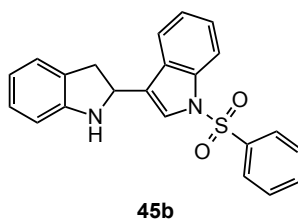


Indole 43b. The general optimized procedure was followed with 0.160 g of azide **43a**³⁰ (0.632 mmol) and 0.006 g of (Et₄N)₂[Co₂(L^{iPr})₂] (0.006 mmol) in 5.0 mL of a 4:1 mixture of toluene and DMF, respectively. After filtration through Celite and removal of solvent *in vacuo*, the product mixture was analyzed using ¹H NMR spectroscopy. Analysis of

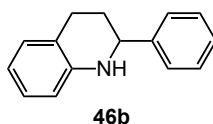
spectral data revealed that indoline and indole **43b** were formed in a 2 : 1 ratio. Upon purification by column chromatography (SiO₂, 1:7 EtOac:Hexanes), indoline product oxidized to indole **43b** (0.085 g, 60 % yield). 0.048 g 30 % of azide **43a** was recovered from the reaction after column chromatography. The spectral data for indole **43a** matches the literature data.⁴⁰ ¹H NMR (400 MHz; CDCl₃): δ (ppm) 8.22 (bs, 1H), 7.63 (dd, *J* = 10 Hz, 2H) 7.47 - 7.37 (m, 2H), 7.08 (d, *J* = 2.5 Hz, 1H), 6.85 (td, *J* = 8.8 Hz, 2.4 Hz, 1H), 6.75 (dt, *J* = 2.3 Hz, 1.2 Hz, 1H), 3.86 (s, 3H).

**44b**

Indoline 44b. The general optimized procedure was followed with 0.150 g of azide **44a** (0.669 mmol) and 0.007 g of (Et₄N)₂[Co₂(L^{iPr})₂] (0.007 mmol) in 5.0 mL of a 4:1 mixture of toluene and DMF, respectively. Indoline **44b** was purified by column chromatography (SiO₂, 1:7 EtOac:Hexanes) for which the yield is reported (0.105 g, 80 % yield). ¹H R_f (7:3 EtOac/hexanes) 0.25; IR (thin film, cm⁻¹) 3677, 2851, 2370, 2277, 2037, 1483, 1249, 901, 753; ¹H NMR (CDCl₃, 400 MHz) δ 8.63 (bs, 1H), 8.52 (d, *J* = 8.5 Hz, 1H), 7.79 (d, *J* = 7.9 Hz, 1H), 7.27-7.24 (m, 1H), 7.07 (dd, *J* = 15.4, 13.6, 2H), 6.74 (t, *J* = 7.2 Hz, 1H), 6.67 (d, *J* = 7.5 Hz, 1H), 4.97 (t, *J* = 9.2 Hz, 1H), 4.14 (bs, 1H), 3.46 (dd, *J* = 15.4, 9.2 Hz, 1H), 2.95 (dd, *J* = 15.8, 9.2 Hz, 1H); ¹³C NMR (CDCl₃, 100 MHz) δ 150.4, 148.0, 147.3, 134.9, 127.8, 127.4, 124.6, 123.9, 119.4, 109.2, 60.9, 39.5, 29.7; HRMS (+ESI) calculated for C₁₃H₁₃N₂ 197.1073, found 197.1074 [M+H]⁺.

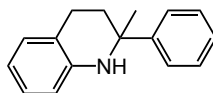


Indoline 45b. The general optimized procedure was followed with 0.150 g of azide **8a** (0.373 mmol) and 0.004 g of $(\text{Et}_4\text{N})_2[\text{Co}_2(\text{L}^{\text{iPr}})_2]$ (0.004 mmol) in 5.0 mL of a 4:1 mixture of toluene and DMF, respectively. Purification by flash chromatography (7:1 hexanes/EtOAc) afforded the title compound as a yellow oil (120 mg, 85 % yield). R_f 0.18 (7:1 hexanes/EtOAc); IR (thin film, cm^{-1}) 3369, 3030, 1608, 1484, 1246, 1033, 747; ^1H NMR (CDCl_3 , 400 MHz) δ 8.01 (d, $J = 8.4$, 1.1 Hz, 1H), 7.91 - 7.84 (m, 2H), 7.57 (s, 1H), 7.55 - 7.48 (m, 2H), 7.47 - 7.38 (m, 2H), 7.36 - 7.27 (m, 1H), 7.26 - 7.17 (m, 1H), 7.16 - 7.03 (m, 2H), 6.76 (td, $J = 7.4$, 1.1 Hz, 1H), 6.69 (d, $J = 7.7$ Hz, 1H), 5.16 (tdd, $J = 9.2$, 3.3, 0.9 Hz, 1H), 4.12 (s, 1H), 3.48 (dd, $J = 15.6$, 9.3 Hz, 1H), 3.14-3.03 (m, 1H); ^{13}C NMR (CDCl_3 , 100 MHz) δ 150.5, 138.1, 135.8, 133.8, 129.3, 129.0, 128.1, 127.7, 126.8, 125.8, 124.9, 124.7, 123.2, 122.7, 120.2, 119.1, 113.9, 109.3, 56.0, 37.3; HRMS (+ESI) calculated for $\text{C}_{22}\text{H}_{19}\text{N}_2\text{O}_2\text{S}$ 375.1167, found 375.1162 $[\text{M}+\text{H}]^+$.



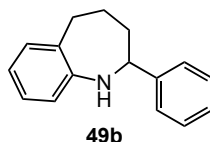
Tetrahydroquinoline 46b.⁴¹ The general optimized procedure was followed with 0.0150 g of azide **46a**⁴² (0.6321 mmol) and 0.0066 g of $(\text{Et}_4\text{N})_2[\text{Co}_2(\text{L}^{\text{iPr}})_2]$ (0.0063 mmol) in 5.0 mL of a 4:1 mixture of toluene and DMF, respectively. Tetrahydroquinoline **46b** was purified by column chromatography (SiO_2 , 1:7 EtOac:Hexanes) for which the yield is reported (0.0931 g, 70 % yield). The spectral data of **46b** match the literature.⁴¹ ^1H

NMR (400 MHz; CDCl₃): δ (ppm) 7.26-7.39 (m, 5H), 6.97-6.99 (m, 2H), 6.64 (td, $J = 7.6$ Hz, 0.8 Hz, 1H), 6.51 (d, $J = 7.6$ Hz, 1H), 4.41 (dd, $J = 9.2$ Hz, 3.2 Hz, 1H), 2.88-2.90 (m, 1H), 2.74 (dt, $J = 16.4$ Hz, 4.8 Hz, 1H), 2.08-2.10 (m, 1H), 1.96-2.02 (m, 1H)



48b

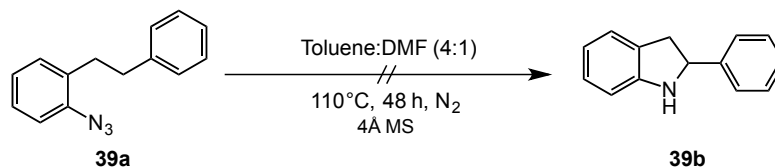
48b. The general optimized procedure was followed with 0.150 g (0.5968 mmol) of azide **48a** and 0.0063 g of (Et₄N)₂[Co₂(L^{iPr})₂] (0.0060 mmol) in 5.0 mL of a 4:1 mixture of toluene and DMF, respectively. Purification by flash chromatography (9:1 hexanes/EtOAc) afforded the title compound as a yellow oil (120 mg, 85 % yield). R_f 0.8 (9:1 hexanes/EtOAc); IR (thin film, cm⁻¹) 3402, 3052, 3023, 2924, 2843, 2358, 2345; ¹H NMR (CDCl₃, 400 MHz) δ 7.38 (dd, $J = 8.8, 1.2$ Hz, 2H), 7.28 (t, $J = 7.9$ Hz, 2H), 7.19 (td, $J = 7.6, 1.2$ Hz, 1H), 7.02 (t, $J = 7.6$ Hz, 1H), 6.9 (d, $J = 7.6$ Hz, 1H), 6.61-6.58 (m, 2H), 4.11 (bs, 1H), 2.59 (dt, $J = 16.4, 4.7$ Hz, 1H), 2.31 (ddd, $J = 16.2, 11.3, 5.3$ Hz, 1H), 2.20 (dt, $J = 12.9, 5.0$ Hz, 1H) 1.9 (ddd, $J = 12.9, 11.1, 4.7$ Hz, 1H), 1.57 (s, 3H); ¹³C NMR (CDCl₃, 100 MHz) δ 148.2, 143.8, 129.2, 128.3, 126.9, 126.3, 125.4, 120.4, 116.6, 113.4, 55.5, 35.4, 30.6, 24.3; HRMS (+ESI) calculated for C₁₆H₁₈N 224.1434, found 224.1436 [M+H]⁺.



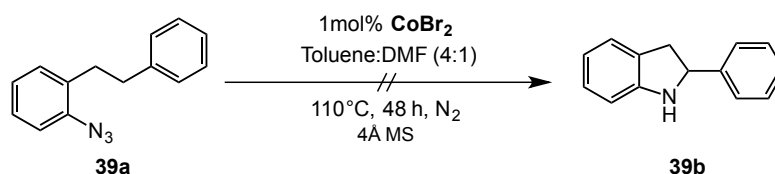
2-phenyl-2,3,4,5-tetrahydro-1H-benzo[b]azepine, 49b. A mixture of 1-azido-2-(4-phenylbutyl)benzene **49a** (75 mg, 0.299 mmol) and 5 mol % $(\text{Et}_4\text{N})_2[\text{Co}_2(\text{L}^{\text{ipr}})_2]$ (16 mg, 0.0076 mmol) was stirred in a 5.0 mL of a 4:1 mixture of toluene and DMF, respectively. Purification by flash chromatography (9:1 hexanes/EtOAc) afforded the title compound as a light orange oil (20 mg, 30 % yield). R_f (9:1 hexanes/EtOAc) 0.3; IR (thin film, cm^{-1}) 3840, 3648, 2924, 2702, 2356, 2157, 1935, 903, 721; ^1H NMR (CDCl_3 , 400 MHz) δ 7.29-7.17 (m, 5H), 7.07-7.05 (m, 1H), 6.99 (t, $J = 7.6$ Hz, 1H), 6.67 (t, $J = 7.3$ Hz, 1H), 6.58 (d, $J = 7.6$ Hz, 1H), 3.89-3.84 (m, 2H), 3.14 (dd, $J = 15.5, 8.5$ Hz, 1H), 2.75-2.68 (m, 3H), 1.96-1.92 (m, 2H); ^{13}C NMR (CDCl_3 , 100 MHz) δ 141.7, 128.4, 128.3, 127.2, 125.9, 124.6, 118.5, 109.1, 59.5, 38.4, 36.1, 32.9, 14.2. HRMS (+ESI) calculated for $\text{C}_{16}\text{H}_{18}\text{N}$ 224.14338, found 224.14303 $[\text{M}+\text{H}]^+$.

Section 4-6-3. Additional Experiments

I. Control Reactions:

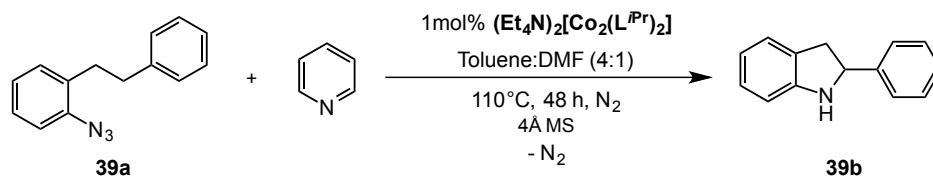


The general optimized procedure was followed with 0.100 g of azide **39a** in 5.0 mL of a 4:1 mixture of toluene and DMF (no catalyst was used). After filtration through Celite and removal of solvent *in vacuo*, analysis of the resulting oil using ^1H NMR spectroscopy showed starting material aryl azide **39a** as the only product (0.095 g, 95 % yield of azide **39a**). The spectral data for **39a** match the literature.³⁰



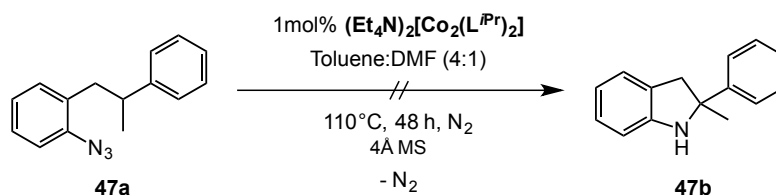
The general optimized procedure was followed with 0.400 g (1.79 mmol) of azide **39a** and 0.004 g of CoBr_2 (0.002 mmol) in 5.0 mL of a 4:1 mixture of toluene and DMF. After filtration through Celite and removal of solvent *in vacuo*, analysis of the resulting oil using ^1H NMR spectroscopy showed starting material aryl azide **39a** as the only product (0.384 g, 96 % yield of azide **39a**). The spectral data for **39b** match the literature.³⁰

II. C–H Amination Reaction in the Presence of Pyridine:



The general optimized procedure was followed with 0.1700 g (0.7614 mmol) of azide **39a**, 0.0080 g of $(\text{Et}_4\text{N})_2[\text{Co}_2(\text{L}^{\text{iPr}})_2]$ (0.0076 mmol), 60.00 μL (0.7614 mmol) of pyridine in 5.0 mL of a 4:1 mixture of toluene and DMF, respectively. Indoline **39b** was purified by column chromatography (SiO_2 , 1:7 EtOac:Hexanes) (0.1331 g, 78 % yield). The spectral data match the literature.³⁰

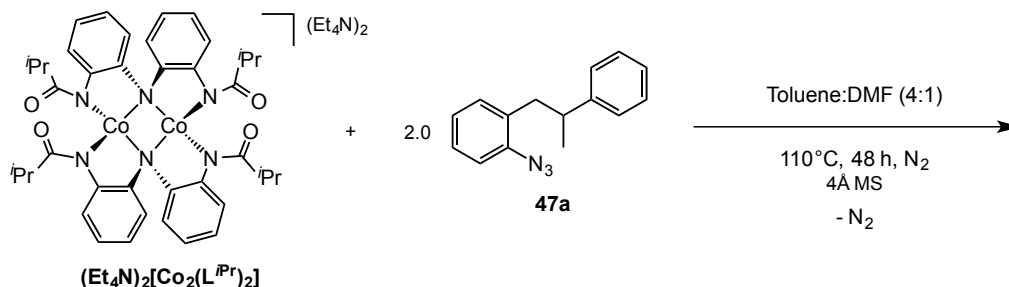
III. Catalytic Reaction of Cobalt(II) Complex $(\text{Et}_4\text{N})_2[\text{Co}_2(\text{L}^{\text{iPr}})_2]$ With Azide **47a**:



The general optimized procedure was followed with 0.1150 g (0.4210 mmol) of azide **47a** and 0.0045 g of $(\text{Et}_4\text{N})_2[\text{Co}_2(\text{L}^{\text{iPr}})_2]$ (0.0043 mmol) in 5.0 mL of a 4:1 mixture of toluene and DMF. After filtration through Celite and removal of solvent *in vacuo*, analysis of the resulting oil using ^1H NMR spectroscopy showed starting material aryl azide **47a** as the only product. Indoline **47b** was not observed. Starting material, azide **47a**, was re-isolated and purified by column chromatography (SiO_2 , 1:7 EtOac:Hexanes) (0.1035 g, 90 % yield). The spectral data for **47a** match the literature.³⁰

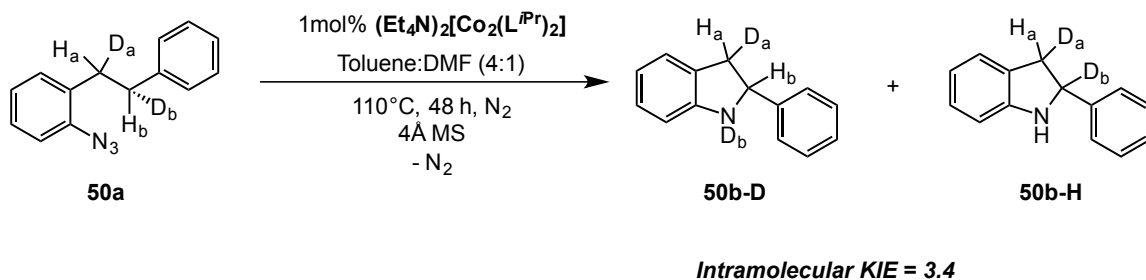
IV. Stoichiometric Reaction of cobalt(II) complex $(\text{Et}_4\text{N})_2[\text{Co}_2(\text{L}^{\text{iPr}})_2]$ with azide

47a:



Treatment of $(\text{Et}_4\text{N})_2[\text{Co}_2(\text{L}^{\text{iPr}})_2]$ (50.0 mg, 0.0476 mmol) with 2.0 equivalents of azide **47a** (26.0 mg, 0.0952 mmol) in 5.0 mL of a 4:1 mixture of toluene and DMF was carried out using the general optimized procedure. After stirring for 48 h at 100 °C, solution was allowed to cool to room temperature and was concentrated to dryness. Crude solid compound (deep green in color) was collected on a medium porosity frit and rinsed with multiple washes of hexanes (3x). ^1H NMR analysis of hexanes filtrate did not contain any free/unreacted azide **47a**. Deep green microcrystals can be obtained by slow diffusion of diethyl ether into a concentrated methyl-tetrahydrofuran (Me-THF) solution of the product, however crystals were not suitable for X-ray diffraction studies. ^1H NMR (δ , CD_3CN , 400 MHz): -76.205 (s), -76.003 (s), -66.592 (s), -65.864 (s), -51.807 (s), -51.139 (s), -44.252 (s), -38.120 (s), -34.942 (s), -33.752 (s), -34.942 (s), -33.752 (s), -33.187 (s), -31.966 (s), -20.551 (s), -13.085 (s), -10.972 (s), -9.573 (s), -5.00 (s), 17.022 (s), 18.314 (s), 25.433 (s), 26.499 (s), 26.780 (s), 46.612 (s), 59.822 (s), 60.472 (s). λ_{max} , nm (CH_3CN): 472, 772. HRESI-MS: for $\text{C}_{35}\text{H}_{38}\text{CoN}_4\text{O}_2$, Calcd (m/z): 605.2327, Found: 605.2353.

V. Intramolecular Kinetic Isotope Experiment for Indoline Formation.



Deuterated azide **50a** was synthesized according to its literature procedure.³³ The general optimized procedure was followed with 0.1500 g (0.6658 mmol) of azide **50a** and 0.0070 g of $(\text{Et}_4\text{N})_2[\text{Co}_2(\text{L}^{\text{iPr}})_2]$ (0.0067 mmol) in 5.0 mL of a 4:1 mixture of toluene and DMF, respectively. After filtration through Celite and removal of solvent *in vacuo*, ¹H NMR indicated that indolines **50b-D** and **50b-H** were present as a mixture from the reaction. The mixture of indolines **50b-D** and **50b-H** were purified over SiO₂ chromatography. The kinetic isotope effect (KIE) was determined from the ratio of **50b-D** and **50b-H**. Spectral data of the mixture matches the previously reported data.³³ ¹H NMR (400 MHz; CDCl₃): δ 7.43 – 7.37 (m, 2H), 7.36 – 7.29 (m, 2H), 7.29 – 7.22 (m, 2H), 7.10 – 7.02 (m, 2H), 6.75 – 6.68 (m, 1H), 6.66 (d, J = 7.6 Hz, 1H), 4.94 (d, J = 8.9 Hz), 4.12 (s, 1H), 3.41 (s, 0H), 2.96 (s, 1H).

V. Intramolecular Kinetic Isotope Experiment for Indoline Formation (continued).

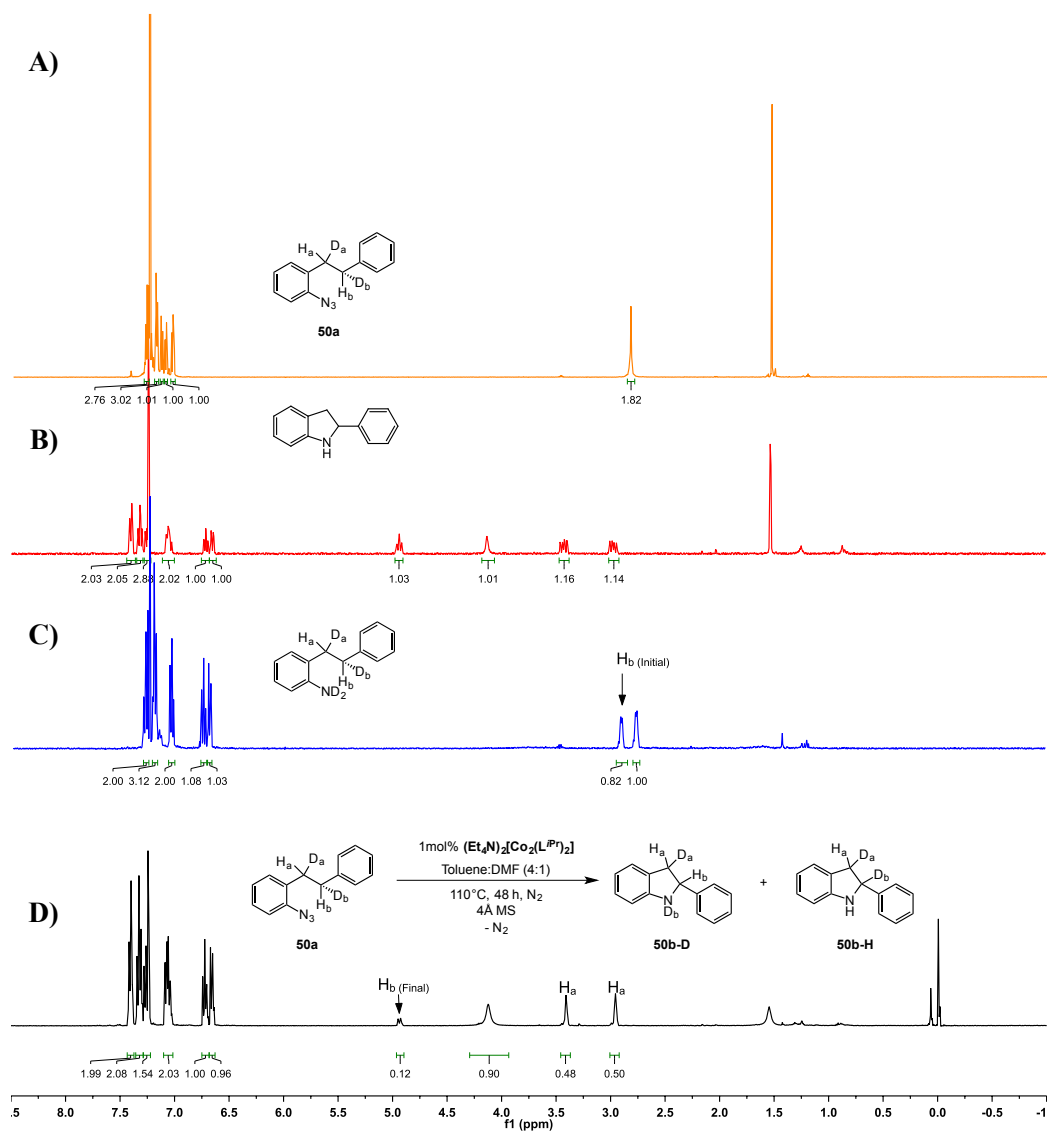


Figure 4-10. ^1H NMR spectra for **A)** deuterated azide **50a**, **B)** indoline product **50b**, **C)** aniline precursor to azide **50a**,³³ and **D)** reaction mixture of indoline products **50b-D** and **50b-H**.

V. Intramolecular Kinetic Isotope Experiment for Indoline Formation (continued).

Calculations used for the determination of KIE value from ^1H NMR analysis found in Figure 4-10:

Before Reaction (H_b initial): 0.82 H_b
After Reaction (H_b final): 0.12 H_b

H_b consumed : (H_b initial) - (H_b final) = (0.82 - 0.12) = 0.70
% of H_b consumed = (0.70/0.82) x 100% = 85%

Before Reaction (D_b initial): 2.0 - (H_b initial) = 2.0 - 0.82 = 1.18 D_b
After Reaction (D_b final): 1 - (H_b final) = 1.0 - 0.12 = 0.88

D_b consumed : (D_b initial) - (D_b final) = (1.18 - 0.88) = 0.30
% of D_b consumed = (0.30 / 1.18) x 100% = 25%

$$\text{KIE} = \text{KH} / \text{KD} = 0.85 / 0.25 = \mathbf{3.4}$$

Section 4-6-4. Crystallographic Data

Table 4-6. Data refinement for the solid-state structure of cycled ligand (**L^{Cyc.}**).^a

L^{Cyc.}	
Formula	C ₄₀ H ₄₆ N ₆ O ₂
Form. Wt. (g/mol)	642.83
T (K)	173(2)
Crystal system	monoclinic
Space group	P21/c
<i>a</i> (Å)	8.8762(18)
<i>b</i> (Å)	13.892(3)
<i>c</i> (Å)	14.471
α (°)	90
β (°)	100.77(3)
γ (°)	90
<i>V</i> (Å³)	1753.0(6)
<i>Z</i>	2
ρ, calcd (g/cm³)	1.218
m/mm-1	0.077
Unique reflns.	4760
Crystal size (mm³)	0.188 × 0.137 × 0.064
Theta range	4.1 to 58.5°
Reflns. Collected	32111
Data/rest./par.	4760/0/221
<i>GOF</i>	0.97
Final R indexes [<i>I</i>>2σ (<i>I</i>)]	R1 = 0.0606
All data	wR2 = 0.1179

^aData for this structure was collected using a Bruker APEX-II CCD diffractometer equipped with an Oxford cryosystems low-temperature apparatus operating at the indicated temperature. Structure was solved in the monoclinic P21/c space group by direct methods using the XT (Sheldrick, 2008) structure solution program and refined by Least Squares using version of ShelXL-97 (Sheldrick, 2008). All non-hydrogen atoms were refined anisotropically. Hydrogen atom positions were calculated geometrically and refined using the riding model.

References

1. *Vision 2020 Catalysis Report; The Council for Chemical Research.*
2. Doyle, M. P.; Duffy, R.; Ratnikov, M.; Zhou, L., *Chem Rev.* **2010**, *110* (2), 704.
3. Du Bois, J., *Org Process Res Dev.* **2011**, *15* (4), 758.
4. Davies, H. M. L.; Manning, J. R., *Nature.* **2008**, *451* (7177), 417.
5. Collet, F.; Dodd, R. H.; Dauban, P., *Chem Commun.* **2009**, (34), 5061.
6. Kwart, H.; Khan, A. A., *Journal of the American Chemical Society.* **1967**, *89* (8), 1951.
7. Breslow, D. S.; Sloan, M. F., *Tetrahedron Letters.* **1968**, *9* (51), 5349.
8. Carr, D.; Seden, T. P.; Turner, R. W., *Tetrahedron Letters.* **1969**, *10* (6), 477.
9. Breslow, R.; Gellman, S. H., *Journal of the American Chemical Society.* **1983**, *105* (22), 6728.
10. (a) Wehn, P. M.; Du Bois, J., *Angewandte Chemie International Edition.* **2009**, *48* (21), 3802; (b) Andresen, B. M.; Du Bois, J., *Journal of the American Chemical Society.* **2009**, *131* (35), 12524.
11. (a) Intrieri, D.; Zardi, P.; Caselli, A.; Gallo, E., *Chem Commun.* **2014**, *50* (78), 11440; (b) Fiori, K. W.; Espino, C. G.; Brodsky, B. H.; Du Bois, J., *Tetrahedron.* **2009**, *65* (16), 3042.
12. (a) Espino, C. G.; Du Bois, J., *Modern Rhodium-Catalyzed Organic Reactions.* **2005**, 379; (b) Esteoule, A.; Duran, F.; Retailleau, P.; Dodd, R. H.; Dauban, P., *Synthesis-Stuttgart.* **2007**, (8), 1251.
13. Espino, C. G.; Du Bois, J., *Angewandte Chemie International Edition.* **2001**, *40* (3), 598.

14. Espino, C. G.; Fiori, K. W.; Kim, M.; Du Bois, J., *Journal of the American Chemical Society*. **2004**, *126* (47), 15378.
15. Milczek, E.; Boudet, N.; Blakey, S., *Angewandte Chemie International Edition*. **2008**, *47* (36), 6825.
16. Breslow, R.; Gellman, S. H., *Journal of the Chemical Society, Chemical Communications*. **1982**, (24), 1400.
17. Paradine, S. M.; White, M. C., *Journal of the American Chemical Society*. **2012**, *134* (4), 2036.
18. Harvey, M. E.; Musaev, D. G.; Du Bois, J., *Journal of the American Chemical Society*. **2011**, *133* (43), 17207.
19. (a) Cenini, S.; La Monica, G., *Inorg Chim Acta*. **1976**, *18* (0), 279; (b) Cenini, S.; Fantucci, P.; Pizzotti, M.; Lamonica, G., *Inorg Chim Acta*. **1975**, *13* (3), 243.
20. Delville, M. M. E.; Nieuwland, P. J.; Janssen, P.; Koch, K.; van Hest, J. C. M.; Rutjes, F. P. J. T., *Chemical Engineering Journal*. **2011**, *167* (2–3), 556.
21. Cenini, S.; Gallo, E.; Caselli, A.; Ragaini, F.; Fantauzzi, S.; Piangiolino, C., *Coordin Chem Rev*. **2006**, *250* (11–12), 1234.
22. Ruppel, J. V.; Kamble, R. M.; Zhang, X. P., *Org Lett*. **2007**, *9* (23), 4889.
23. Driver, T. G., *Organic & Biomolecular Chemistry*. **2010**, *8* (17), 3831.
24. (a) Lu, H.; Tao, J.; Jones, J. E.; Wojtas, L.; Zhang, X. P., *Org Lett*. **2010**, *12* (6), 1248; (b) Lu, H.; Jiang, H.; Wojtas, L.; Zhang, X. P., *Angewandte Chemie International Edition*. **2010**, *49* (52), 10192.
25. (a) Breslow, R.; Feiring, A.; Herman, F., *Journal of the American Chemical Society*. **1974**, *96*, 5937; (b) Breslow, R.; Herman, F.; Schwabacher, A. W.,

- Journal of the American Chemical Society*. **1984**, *106*, 5359; (c) Maslak, P.; Szczepanski, J. J.; Minard, R. D.; Collins, L. A., *Tetrahedron Lett.* **1990**, *31*, 4261; (d) Maslak, P., *Journal of the American Chemical Society*. **1989**, *111*, 8201.
26. Lu, H.; Subbarayan, V.; Tao, J.; Zhang, X. P., *Organometallics*. **2009**, *29* (2), 389.
27. (a) Luca, O. R.; Crabtree, R. H., *Chem Soc Rev.* **2013**, *42* (4), 1440; (b) Lyaskovskyy, V.; de Bruin, B., *ACS Catalysis*. **2012**, *2* (2), 270; (c) Bill, E.; Bothe, E.; Chaudhuri, P.; Chlopek, K.; Herebian, D.; Kokatam, S.; Ray, K.; Weyhermüller, T.; Neese, F.; Wieghardt, K., *Chemistry – A European Journal*. **2005**, *11* (1), 204; (d) Chun, H.; Verani, C. N.; Chaudhuri, P.; Bothe, E.; Bill, E.; Weyhermüller, T.; Wieghardt, K., *Inorg Chem*. **2001**, *40* (17), 4157; (e) Pierpont, C. G., *Coordin Chem Rev.* **2001**, *216–217* (0), 99; (f) Wile, B. M.; Trovitch, R. J.; Bart, S. C.; Tondreau, A. M.; Lobkovsky, E.; Milsmann, C.; Bill, E.; Wieghardt, K.; Chirik, P. J., *Inorg Chem*. **2008**, *48* (9), 4190; (g) Vlcek, A., *Coordin Chem Rev.* **2010**, *254* (13–14), 1357; (h) Mukherjee, C.; Pieper, U.; Bothe, E.; Bachler, V.; Bill, E.; Weyhermüller, T.; Chaudhuri, P., *Inorg Chem*. **2008**, *47* (19), 8943; (i) Sharma, S. K.; May, P. S.; Jones, M. B.; Lense, S.; Hardcastle, K. I.; MacBeth, C. E., *Chem Commun.* **2011**, *47* (6), 1827; (j) Manuel, T. D.; Rohde, J.-U., *Journal of the American Chemical Society*. **2009**, *131* (43), 15582; (k) Atienza, C. C. H.; Diao, T.; Weller, K. J.; Nye, S. A.; Lewis, K. M.; Delis, J. G. P.; Boyer, J. L.; Roy, A. K.; Chirik, P. J., *Journal of the American Chemical Society*. **2014**, *136* (34), 12108; (l) Tondreau, A. M.; Milsmann, C.; Patrick, A. D.; Hoyt, H. M.; Lobkovsky, E.; Wieghardt, K.; Chirik, P. J., *Journal of the American Chemical*

- Society*. **2010**, *132* (42), 15046; (m) Darmon, J. M.; Stieber, S. C. E.; Sylvester, K. T.; Fernández, I.; Lobkovsky, E.; Semproni, S. P.; Bill, E.; Wiegardt, K.; DeBeer, S.; Chirik, P. J., *Journal of the American Chemical Society*. **2012**, *134* (41), 17125; (n) Smith, A. L.; Hardcastle, K. I.; Soper, J. D., *Journal of the American Chemical Society*. **2010**, *132* (41), 14358; (o) Hennessy, E. T.; Betley, T. A., *Science*. **2013**, *340* (6132), 591.
28. King, E. R.; Betley, T. A., *Inorg Chem*. **2009**, *48* (6), 2361.
29. King, E. R.; Hennessy, E. T.; Betley, T. A., *Journal of the American Chemical Society*. **2011**, *133* (13), 4917.
30. Sun, K.; Sachwani, R.; Richert, K. J.; Driver, T. G., *Org Lett*. **2009**, *11* (16), 3598.
31. King, E. R.; Sazama, G. T.; Betley, T. A., *Journal of the American Chemical Society*. **2012**, *134* (43), 17858.
32. L'Abbe, G., *Chem Rev*. **1969**, *69* (3), 345.
33. Nguyen, Q.; Sun, K.; Driver, T. G., *Journal of the American Chemical Society*. **2012**, *134* (17), 7262.
34. Lu, H.; Jiang, H.; Hu, Y.; Wojtas, L.; Zhang, X. P., *Chemical Science*. **2011**, *2* (12), 2361.
35. Lopchuk, J. M., Chapter 5.2 - Five-Membered Ring Systems: Pyrroles and Benzo Analogs. In *Progress in Heterocyclic Chemistry*, Gordon, W. G.; John, A. J., Eds. Elsevier: 2014; Vol. Volume 26, pp 151.
36. Carey, J. S.; Laffan, D.; Thomson, C.; Williams, M. T., *Organic & Biomolecular Chemistry*. **2006**, *4* (12), 2337.

37. Sridharan, V.; Suryavanshi, P. A.; Menéndez, J. C., *Chem Rev.* **2011**, *111* (11), 7157.
38. Liu, Y.; Wei, J.; Che, C.-M., *Chem Commun.* **2010**, *46* (37), 6926.
39. Lucas, R. L.; Powell, D. R.; Borovik, A. S., *Journal of the American Chemical Society.* **2005**, *127* (33), 11596.
40. Bartoli, G.; Palmieri, G.; Petrini, M., *Tetrahedron.* **1990**, *46* (4), 1379.
41. Han, Z.-Y.; Xiao, H.; Chen, X.-H.; Gong, L.-Z., *Journal of the American Chemical Society.* **2009**, *131* (26), 9182.
42. Murata, S.; Yoshidome, R.; Satoh, Y.; Kato, N.; Tomioka, H., *The Journal of Organic Chemistry.* **1995**, *60* (5), 1428.